Design and Fabrication of a Miniature Silicon Microphone

Edward Pallett
(BEng. Hons. Electronic Engineering)

A thesis submitted in partial fulfilment of the requirements of De Montfort University for the degree of Doctor of Philosophy

April 1995

De Montfort University

School of Engineering & Manufacture

Department of Mechanical & Manufacturing Engineering

Sponsored by the Science and Engineering Research Council

TEXT
CUT OFF IN THE
ORIGINAL

ABSTRACT

Silicon micromachining techniques were developed and used to batch fabricate a new type of heavily doped p-type (or p^+) silicon etch stop structure on glass that could be suitable for implementation of a condenser microphone. This involved study, development and use of techniques such as mask design, lithography, oxidation, diffusion, thin film deposition, electrostatic bonding, many different etching techniques, freeze drying, packaging/interfacing and testing.

The condenser microphone structure consisted of a thin conductive diaphragm suspended above a back plate electrode in order to form a capacitive device. A narrow gap between the two plates constituted the capacitor plate separation and the air occupying the gap was the dielectric material. Two versions of this condenser microphone structure were fabricated with over all dimensions of $2mm^2$ x 8-12 μm, air gap sizes of 0.5-1.5 μm and 1μm thick diaphragms. The first design utilised a square diaphragm with an area of $1mm^2$ while the second incorporated a circular diaphragm with a diameter of 1mm. Fabrication of the back chambers was implemented with an innovative double thermal oxidation technique.

Signals of up to 1 mV/Pa were obtained in the audio range for one of the circular p^+ silicon microphone structures, but the frequency response measured was not consistent with the desired frequency response for a condenser microphone.

Thin film thicknesses, silicon etch rates and electrode metallisation conductivity were characterised using specially designed test structures and innovative electrical and optical

measurement techniques so that fabrication accuracy and reproducibility could be monitored.

As a result of the investigations carried out to develop novel p^+ silicon microphone structures, this thesis also identifies important areas which warrant further research, and provides a foundation, in terms of theory and fabrication, for future development of more advanced and appropriate p^+ microstructures for application as condenser microphones.

ACKNOWLEDGEMENTS

This work has been funded by SERC and forms part of the near field acoustic holography groups activities.

I would like to thank my supervisors Professor Jeffery Knight, Dr. Colin Horley and Dr. Robert Adama Acquah for their support and encouragement during this project.

I would also like to thank Professor R. Linford and Dr. R. Pritchard for allowing the use of silicon fabrication facilities in the Applied Physics Department.

Special thanks go to N. Bevan for his invaluable experience and knowledge of thin film deposition techniques and other practicalities of silicon fabrication.

Thanks are also due to D. Bazeley and T. Woodford for their technician support for various aspects of the work.

An important acknowledgement must be given to Ashley Lees for his excellent finite element simulation work using ALGOR, which was used to support microphone modelling work for this thesis.

Finally, I would like to thank all members of the Department of Mechanical and Manufacturing Engineering who have contributed or helped with this work.

SAFETY WARNING

Some of the procedures detailed in this thesis involve the use of extremely hazardous chemicals such as hydrofluoric acid. Use of such dangerous chemicals must only be undertaken by trained personnel using appropriate facilities and safety precautions. Such personnel must have completed the appropriate risk assessment COSHH regulation documents for all chemicals used and be fully aware of all handling procedures and hazards regarding the chemicals and their use in a specific process.

CONTENTS

1.0 INTRODUCTION

This chapter outlines the need for miniature silicon microphones and introduces silicon microengineering technology. A summary of the different types of microphone transduction principles are described as a suitable prelude to the literature survey of chapter 2.

1.1 Aims and objectives

The aim of this project was to design and develop techniques for producing sub miniature ($<2mm^2$) microphones with closely matched audio frequency and voltage sensitivity characteristics for use in large $1m^2$ acoustic imaging arrays that employ up to 256 microphones. Commercially available microphones are unsuitable for this purpose because they are not sufficiently miniature and are difficult to obtain with matched characteristics in high quantities due to manufacturing limitations. This thesis investigates the possibility of fabricating miniature microphones using the emerging technology of silicon microengineering since it can be highly suited for batch fabrication of miniature sensors which have good stability and performance characteristics.

It is widely recognised that the integrated circuit (IC) industry has a knowledge base and infra structure that already supports the requirements for batch fabrication of silicon chips. If this is coupled with the fact that silicon has excellent physical properties [1] suitable for the construction of sensors, then it is quite clear that silicon technology is very well suited for the design and manufacture of sensors. Therefore the aim of this project was to fabricate a silicon microphone sensor using some of the same principles found in IC manufacturing and to include extended techniques developed for silicon micromachining.

Silicon microengineering a new microsensor from scratch with no prior experience and limited resources represented a considerable undertaking due to the complexity of silicon fabrication and the multidisciplinary requirements for design, implementation and characterisation. Working across the disciplines of chemistry, physics, mechanical and electronic engineering placed a significant burden on the scope of the project and what could be achieved during the available research period. The emphasis of this thesis is placed on the development and understanding of suitable techniques required for reproducible batch fabrication of silicon microstructures and the problems that have been observed and solved as a result of implementing a devised fabrication scheme. Microphone design details are discussed for the sake of completeness, but a complete detailed formal design specification and comparison with completed structures was not possible due to the lack of detailed accurate models, low fabrication yields and the physical difficulties of electrically testing and characterising new miniature microstructures.

1.2 Background

Silicon micromachining is an area of engineering that involves the sculpting of micron sized three dimensional structures from silicon [2]. These structures can be designed for use in a variety of sensor or actuator applications and are now beginning to play an increasing role in micro systems technology [3].

Many silicon micromachining techniques tend to be an extension of existing fabrication technologies for integrated circuit manufacture [4], but very often micromachined structures themselves have sequences of processing that are incompatible with IC manufacture. This problem has been widely recognised and so current research effort is focused on trying to

integrate micromachining processes for a given structure with standard industrial IC fabrication techniques.

The two main types of silicon micromachining will now be discussed as they are central to the fabrication of microphone structures in the literature.

1.2.1 Bulk micromachining

This form of micromachining uses both sides of a silicon wafer and usually requires special alignment facilities. Generally a masked wafer is used with a suitable etching technique to etch away the bulk of the exposed silicon and leave thin silicon structure(s) remaining. Very often etch stops are used in conjunction with this technique to give precise control of structure dimensions.

Anisotropic etching [5] can be used for bulk micromachining purposes and indeed for making three dimensional structures, since the etchants involved etch different crystal planes in the silicon at different rates. For example a 40 % KOH solution can produce up to a 40:1 etch ratio between the (100) and the close packed(111) planes respectively.

1.2.2 Surface micromachining

Surface micromachining is carried out on one side of a wafer and involves the use of sacrificial layers, which can be etched away to leave free standing silicon structures on the surface of a wafer. Various types of film deposition techniques can be employed to deposit the sacrificial layer and the desired structure material(s).[6]

1.3 Silicon microphones

There are many types of microphones [7] including electromagnetic, electrodynamic, contact carbon, piezo electric, piezo resistive and the electrostatic or condenser microphone. The last three types have been realised in many different forms by silicon micromachining over the last decade. In view of this, the rest of this section and the literature survey chapter will concentrate on these three. These types of microphones require a diaphragm to detect acoustic waves. Amplitude modulation of the diaphragm caused by impinging sound waves is converted to an electrical signal, the methods for this conversion will now be discussed.

1.3.1 Optical acoustic

Incident sound waves modulate the light guided in an optical fibre. An example could be intensity modulation of a fibre optic guided light beam from a shiny moving membrane surface or interferometric techniques with a membrane surface. [8, 9]

1.3.2 Piezo electric

The deformation of piezo electric material, usually deposited on a silicon diaphragm, caused by strain due to diaphragm movement generates a voltage [24].

1.3.3 Piezo resistive

Strain gauges, consisting of four small piezo resistors diffused into a silicon diaphragm, will produce an output voltage dependent on diaphragm deflection when connected in a wheatstone bridge circuit configuration [10].

1.3.4 Electrostatic or condenser microphone

The movement of one of the plates of a capacitor, usually made of a conductive silicon diaphragm, causes a change in the value of capacitance. If a large D.C electric field is present between the two plates, a change in voltage can be measured for a change in capacitance. This field can be provided by an electret or an external voltage source. A condenser microphone was implemented for this work.

2.0 LITERATURE SURVEY AND PREVIOUS WORK

This chapter will summarise the literature on the three types of microphones discussed in section 1.3 with respect to their silicon micromachined implementations, since they are of the greatest relevance to this work. The structures reviewed will be classified into the three sections that follow.

2.1 Dual chip structures

Most of the structures in this section are fabricated by bulk micromachining techniques. The first silicon subminiature condenser microphone was presented in 1984 by Hohm and Gerhard-Multhaupt [11] using silicon dioxide as an electret [12] charged by corona charging [13]. A layer of 2μm SiO_2 was thermally grown on the silicon backplate and charged up to 350V. The diaphragm was made of 13μm thick mylar coated with aluminium on the air gap side and had an area of 50 mm^2. A 30 μm air gap was provided by a 30 μm polymer ring between the diaphragm and the backplate. A 1mm diameter acoustic hole was present in the centre of the backplate. The capacitance of the microphone was 9pF and the sensitivity 3mV/Pa. A resonance peak of 5 dB occurred at 8.5 kHz.

Hohm presented a second silicon microphone in 1986 with a 150 nm silicon nitride diaphragm [14]. The microphone was constructed of two silicon pieces, one containing the diaphragm 0.8 x 0.8 mm and the other acting as the backplate. Cosmetic nail varnish was used to join the two pieces giving an air gap of 2 μm. With such a small air gap an electret was not required and the structure could be biased from an external source of 28 V. The diaphragm tension was manipulated by the implantation of nitrogen ions. The higher the

dose, the lower the initial tensile stress of the diaphragm. For the given external bias the microphones gave sensitivities between 0.2 and 4.3 mV/Pa, depending on the implantation dose, and bandwidths between 20 kHz and 2 kHz respectively.

More recently in 1991 and 1992 this microphone design has been improved by Kuhnel and Hess [15,16] by making deep acoustic cavities or grooves in the back chambers to reduce damping losses and improve frequency response. Both techniques improved the microphone sensitivities, with the grooves adding the most significant contribution. Sensitivities of up to 10 mV/Pa were achieved for a 28 V bias. Highly perforated backplates with up to 144 holes were tried and gave a sensitivity of 3 mV/Pa and resonance peak at 16 kHz.

Some microphones with larger area and air gaps have been made with silicon backchambers and mylar diaphragms containing a metallisation electrode, the mylar was attached to the silicon backchamber using commercial glue and a special jig. Sprenkels in 1988 presented a design incorporating an electret [17,18] with an open circuit sensitivity of 25mV/Pa and 20 Hz to 15 kHz bandwidth. Murphy et al.[19] extended this work by gluing the mylar on a separate piece of silicon which was then glued onto a silicon back plate. Teflon and SiO_2 electrets were used.

Backplate chips with more ventilation holes have been investigated due to the improved frequency response that this technique gives. In 1990 Berqvist and Rudolf [20] presented a condenser microphone without an electret and a 2 x 2 mm silicon diaphragm with a thickness of between 5 and 8 μm. This diaphragm was attached to a backplate chip with 100 ventilation holes occupying 20% of its area. The air gap was 4 μm thick giving a

microphone capacitance of about 3.5 pF. Sensitivities of the designs ranged from 1.4 mV/Pa to 13 mV/Pa and bandwidths from 4 kHz to 16 kHz respectively depending on the diaphragm thickness. Later designs by Bergvist et al.[21] had between 2500 and 4000 ventilation holes in the backplate. A flat frequency response between 2 Hz and 20 kHz was obtained with 1.6 mV/Pa sensitivity, 27 kHz resonant peak and a 40 dBA sound pressure level (SPL) noise level.

Kuhnel designed a microphone which incorporated a FET [22]. The diaphragm, made of silicon nitride, acted as a movable gate above a backchamber chip containing an unusual FET structure that had two large grooves either side to reduce air damping. The distance between the FET gate oxide and the diaphragm was just 2 μm. A drain resistor of 10 kΩ was used with a supply voltage of 30V, the source was grounded and the drain bias current was adjusted to 2 mA. The output signal from the drain had a maximum sensitivity of 5mV/Pa and a flat frequency response up to 30 kHz. The FET contributed to a relatively high noise level of 62 dBA SPL.

Stoffel et. al. have also designed a microphone with a built in FET (1993). The p-n etch stop technique was employed to produce a slotted membrane with a central boss. The boss covered the active gate area of a second FET chip. The air gap in this region was 460 nm which gave a large gate working capacitance. The highest reported sensitivity was 38 mV/Pa at 5.8 kHz for a 2.3 mm^2 x 5 μm membrane with a high noise level of 58 dBA attributed to FET gate leakage.

2.2 Single chip structures

Surface micromachining is used extensively for the diaphragms of the microphones described in this section, but bulk micromachining is used for structuring the back chambers. Surface micromachining has played a very important role in more recent structures in the literature.

An integrated 2 mm^2 microphone with CMOS circuits on a single chip was presented by Muller et al. in 1989 [23]. The 1.4 μm thick diaphragm was made of LPCVD silicon nitride with a thin film of ZnO deposited on the top for piezoelectric transduction. Annular electrodes were used to obtain the microphone signal for the CMOS circuitry. The first resonant frequency was around 30 kHz and there was poor response below 800 Hz. At 3 kHz the sensitivity was about 0.8mV/Pa with an amplifier gain of 20 dB. In 1991 Muller published a paper [24] on an improved version of the IC compatible Piezoelectric microphone. The unamplified sensitivity was roughly 1mV/Pa over the audio range with an equivalent noise level of 50 dB SPL.

There are very few piezo-resistive microphones given in the literature, probably due to the fact that diffusing usable piezo resistors into very thin diaphragm structures is difficult. Schillin et al. [25] fabricated a microphone (1991) with four polysilicon resistors diffused in the diaphragm to form a bridge configuration and obtained a maximum sensitivity of 0.025 mV/Pa for a supply voltage of 6 V. Piezo-resistive techniques are more suited to pressure sensor fabrication, Kensall D.Wise has carried out much work in this area [26].

Scheeper et al. in 1991 [27] and 1992 [28] published papers on two types of microphones made by surface micromachining on a single wafer. A sacrificial layer technique was used

whereby the sacrificial layer was covered with silicon nitride as the diaphragm material. Etching of the sacrificial layer through acoustic holes in the backplate resulted in an air gap between the diaphragm and the backplate substrate. The diaphragm of the first microphone was 1 x 1 mm^2 and 1 μm thick, the air gap was approximately 1 μm. A sensitivity of 1.4mV was measured with a bias voltage of only 2 V. The upper cut off frequency was below 40 Hz due the backchamber having three acoustic holes in the shape of slits.

The second microphone diaphragm was 1.5 x 1.5 mm^2 and 1μm thick, it had a silicon nitride backplate and diaphragm and the air gap was 3 μm. A flat frequency response of up to 14kHz was measured and attributable to the provision of 392 acoustic holes in the backplate. The sensitivity was 2 mV/Pa for a bias of 16V.

Bergqvist and Gobet (1994) [29] have recently presented a microphone with an electroplated surface micromachined backplate. The diaphragm is 1.8 x 1.8 mm^2 and has a reported sensitivity of 1.4 mV/Pa for a bias voltage of 28 V and a bandwidth of up to 14 kHz.

2.3 Structures fabricated on glass

These types of structures are bulk micromachined by using a selective wafer dissolution process. The selectivity results from heavily doped regions of silicon acting as etch stops. In this instance, glass is used as the substrate for the heavily doped structures. Kensall D.Wise et. al. fabricated a silicon tactile imager [30] in 1984 and later some pressure sensors [31] that were made of highly doped (p^+) silicon on glass.

In 1992, after this research was initiated, Bourouina et al. fabricated a microphone [32] with

a 1 μm thick boron doped silicon diaphragm and a glass backplate with an aluminium electrode. A range of these microphones had a diaphragm area that varied between 0.25 mm^2 and 1 mm^2 with an air gap thickness between 5 μm and 7.5 μm. Depending on the dimensions used and a bias voltage of 20 V, sensitivities measured were between 0.4 and 3.5 mV/Pa. The best frequency response of 20 kHz was obtained for a microphone that was 0.25mm^2 in area and had an air gap of 5 μm.

2.4 Conclusions

Miniaturised silicon condenser microphones of about 1 mm^2 can give a high sensitivity and a flat frequency response in the audio range with good noise performance. However these characteristics do not match those of microphones made by other techniques commercially such as Bruel & Kjaer [33], who used a 130 mm^2 metal diaphragm to achieve a sensitivity of 50 mv/Pa. The disadvantage of these types of microphones is that they are not miniature and do not benefit from the advantages of silicon batch fabrication. However, sensitivity and noise performance decrease with miniaturization.

The microphones considered, with a thin air gap of the order of microns, no longer require the use of an electret, since a small bias voltage can be used instead. The disadvantage that a small air gap can bring is a reduced frequency response due to significant air damping.

The optimal design of a silicon condenser microphone will depend on the application, but it is important to realise that trade offs must be made between bandwidth, sensitivity and the microphone dimensions.

The other types of microphones discussed do not have the same advantages as condenser microphones and usually present more complexity in the design and fabrication to yield inferior results.

3.0 DESIGN CONSIDERATIONS OF A SILICON CONDENSER MICROPHONE

This chapter details the background theory and some modelling aspects of the condenser microphone in order to present an understanding of the important parameters required for design. Some of the graphs shown in this chapter to illustrate evaluation of the models are simulation results from the design used for fabrication in this project.

The main design parameters for an audio condenser microphone are sensitivity, frequency response and noise. These parameters are affected by different attributes of the condenser structure employed for the design and are discussed in this chapter. This chapter also discusses condenser microphone theory in conjunction with appropriate available models. These models were evaluated with devised computer programs in order to determine some of the characteristics of miniature microphones. The results of evaluations are given in this chapter for heavily p-type (or p^+ , see ch. 4) silicon microphones with a 1 μm thick diaphragm and a 1 μm air gap between the diaphragm and the back chamber. Models for square and circular diaphragms are evaluated with dimensions of 1mm x 1mm and 1mm diameter diaphragms respectively. The dimensions that were chosen are similar to the dimensions of the miniature microphones given in the literature survey, yield appropriate design requirements (Discussed in this chapter) from simulation and are realistic dimensions for fabrication with the resources that were available. Since development of the fabrication technology was evolutionary, the microphone design was not optimised for the best possible performance characteristics because design issues regarding the fabrication implementation were not fully known at the initial microphone design phase. The design issues that became clear at the end of the project as a result of fabrication and test experiments form part of the discussion in chapter 8.

3.1 Condenser microphone theory

The condenser microphone, schematically shown in fig. 3.1 consists of a diaphragm that is made of a conducting material, or metal on insulator, to form a moveable plate of a capacitor. The other conducting plate must be fixed and usually has acoustic holes, or suitable geometry, to reduce streaming losses and hence improve the microphone sensitivity at higher audio frequencies. The equation for the capacitance C of a parallel plate capacitor can be stated as

$$C=\frac{\epsilon_o\epsilon_r A}{d} \tag{3.1}$$

which shows that the size of the capacitance is directly proportional to the area A of the plates and inversely proportional to the plate separation d. For the condenser microphone, d would be the distance between the diaphragm and the backplate and A would be the diaphragm area, assuming the backplate electrode has the same area as the diaphragm. The permittivity of the dielectric ϵ for air is given by $\epsilon_o\epsilon_r$ where ϵ_o is the permittivity of free space and ϵ_r is the relative permittivity or dielectric constant of air. ($\epsilon_r \simeq 1$ for air)

Some condenser microphones have an electret between the backplate and the diaphragm to supply the required D.C. electric field in the air gap [12]. This is not a requirement for the silicon microphone in this project because the air gap is a few microns, allowing the use of a low voltage external bias in conjunction with a suitable bias resistor. A disadvantage of such a narrow air gap can be increased air damping of the diaphragm movement.

Figure 3.2 shows a simple electrical model of the condenser microphone where C_m is the microphone capacitance, C_p is a parasitic capacitance due to microphone connections, C_i is

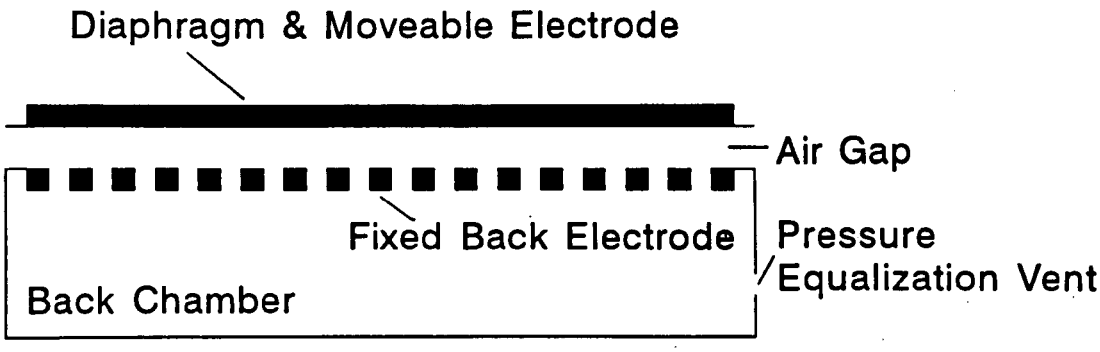

Figure 3.1 : Unconnected condenser microphone structure.

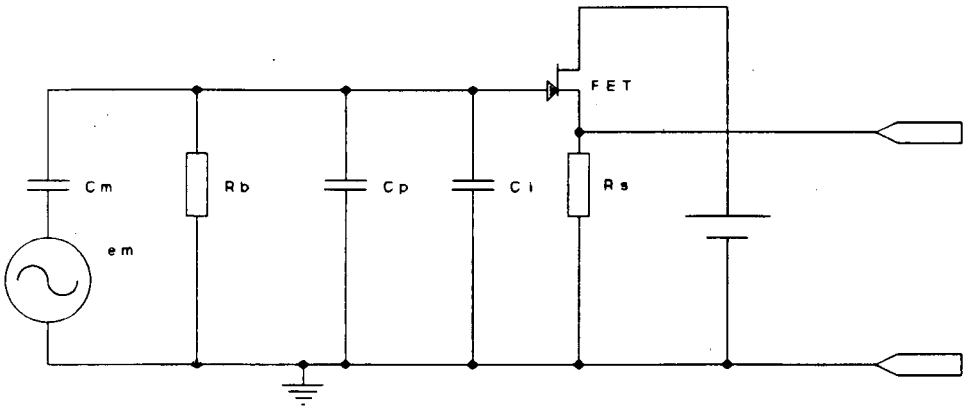

Figure 3.2 : Electrical model of a condenser microphone with impedance conversion circuitry.

the input capacitance of the impedance conversion amplification stage (or source follower) and R_b is the bias resistor for the microphone. The stray capacitance C_s is equal to the sum of C_i and C_p. The external bias or polarisation voltage V_b must have a high impedance so that the time constant $R_b(C_m+C_s)$ is long compared to the lowest frequency of sound to be measured. This also ensures that the charge Q stored on the capacitor (C_m+C_s) is approximately constant. From the formula $Q=(C_m+C_s)e_m$ it is seen that if the charge is constant and the capacitance C_m varies due to an impinging sound wave on the diaphragm, a varying microphone voltage e_m will appear across the plates. This voltage is then fed to an amplifier which has a high input impedance, but low output impedance, in order to drive subsequent amplification circuitry and prevent loading of the microphone signal.

If the sound pressure acting on the diaphragm causes a capacitance change ΔC_m, then the changing output of the microphone is given as

$$\Delta e_m = \frac{\Delta C_m V_O}{(C_m + C_s)} \qquad (3.2)$$

The above equation shows that the microphone sensitivity is proportional to the bias voltage V_o and inversely proportional to (C_m+C_s).

The microphone open circuit sensitivity S (V/Pa) is given by

$$S = \frac{\Delta e_m}{\Delta p} \qquad (3.3)$$

where Δp is the small changing sound pressure on the diaphragm. Substituting equation 3.2 into equation 3.3, leads to an expression given as

$$S = V_o \frac{\Delta C_m / C_m}{\Delta P} \frac{1}{1 + C_s / C_m} \tag{3.4}$$

It is apparent from this expression that in order to obtain a good sensitivity and signal to noise ratio, ΔC_m should be large and C_m should be large in comparison to C_s.

3.1.1 Plate deflection theory

Understanding the response of diaphragms to an applied pressure is very important for microphone design. There are two types of diaphragm which will now be defined in order to distinguish between the stress free and stressed cases.

Thin Plate

A diaphragm without any initial stress whose deflection is determined by the flexural rigidity of the diaphragm if it is loaded.

Membrane

A diaphragm with large initial stress and a deflection that is mainly determined by stress when loaded.

Diaphragms are usually square or circular for microphones and a comparison of the two has shown that the static deflection of a circular diaphragm, due to a homogeneous load, is maximally 20 % larger than the deflection of a square diaphragm with the same load, if both have the same area [34]. Models have been derived by Timoshenko [35], for the membrane and the plate, to relate a homogeneous load to the centre deflection w_o for values of Young's modulus, diaphragm thickness h and radius R for a circular diaphragm. Appendix A1.1

shows the results of such derivations for a circular membrane and plate for an applied homogeneous pressure under static conditions. These models were used for the basis of computer numerical calculations of diaphragm deflection given in this thesis (Section 3.3)

3.1.2 Electrostatic forces

The bias voltage causes electrostatic forces between the plates of the capacitor, which for a deflecting diaphragm, turn out to be non homogeneous. If the diaphragm is considered to have piston movement ie the plates remain parallel for diaphragm movement, then the forces are homogeneous as in the parallel plate case. (Ignoring edge effects of the plates) Additionally, the air gap size of the microphone is limited by dielectric breakdown of the electrostatic field between the plates.

If the diaphragm movement for dynamic behaviour is large in comparison to its thickness, the non homogeneous electrostatic forces will affect the diaphragm movement in a non linear way and introduce distortion in the output signal of the microphone. The relationship between the static deflection w_o and the corresponding voltage for values of Young's modulus E_d, diaphragm thickness h and radius R is given in appendix A1.1 for a circular diaphragm. Both cases of a stress free diaphragm and a diaphragm with a large initial tensile stress are given.

3.1.3 Frequency response and noise characteristics

For a flat frequency response such as that shown in fig. 3.3 for a typical condenser microphone, ΔC_m and hence the deflection of the diaphragm for a given sound pressure must be independent of frequency. It is also very important for the natural frequency of the

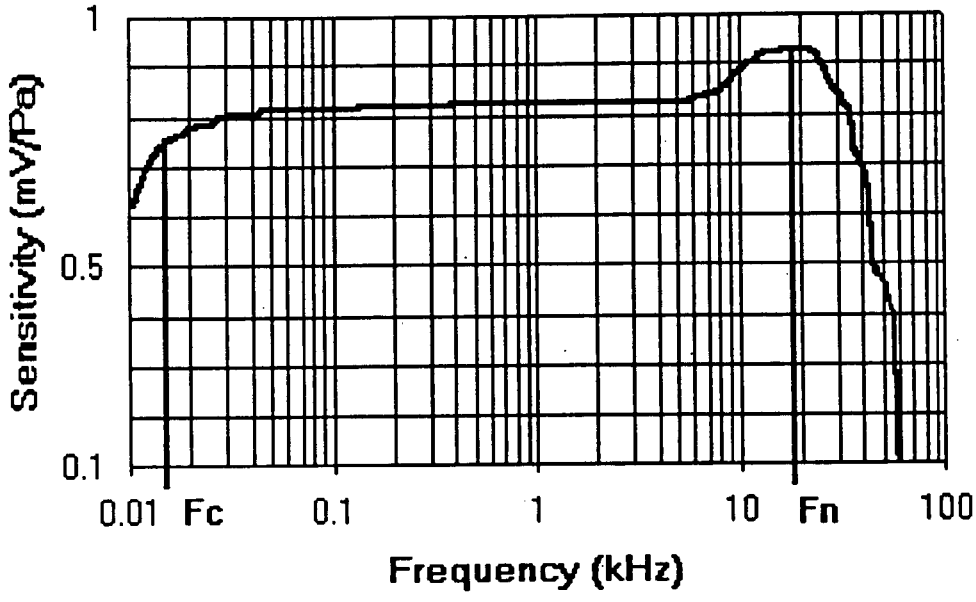

Figure 3.3 : Typical frequency response of a wideband condenser microphone structure.

diaphragm to be well above the highest frequency of sound to be measured. The natural frequency f_n for a circular diaphragm with a large initial tension T is given by [36].

$$f_n \propto \sqrt{\frac{T}{M}} \tag{3.5}$$

It can be seen that if the mass M is large, the resonant frequency is lower. Beyond resonance the motion of the diaphragm becomes mass controlled so that the average diaphragm displacement is no longer constant for a given sound pressure level (SPL), but decreases inversely with frequency.

Viscous damping in the air gap can cause the diaphragm movement to be attenuated at higher frequencies in the audio range, especially for thin air gaps. (Aside : With careful design, this effect can be used to compensate for the rise in response at resonance, by adjusting the slots sizes in the fixed backing plate in order to affect the motion of the air to and from the region adjacent to the diaphragm)

Noise performance is another important parameter of a condenser microphone and its preamplifier. Signal to noise ratio (SNR) is used to specify this characteristic and it is usually defined as the ratio of the signal e_m and the A-weighted value of the equivalent input noise Ni. (Noise voltage source Ni in series with the signal source e_m) [37]. The A-weighting function is defined by the frequency characteristic of the human ear, so to obtain the total audible noise, Ni is filtered by the A-weighting function. SNR has to be given for a specified sound pressure level SPL for comparison purposes, this is because e_m will change for different sound pressure changes p, causing change of the SNR. This SPL has been defined as 2×10^{-5} Pa, which is the lowest detectable sound by the human ear and it allows

e_m to be calculated from eqn. 3.2. This leads to the definition for the noise level of a microphone being the ratio of the A-weighted equivalent input noise Ni to the SPL microphone signal (calculated e_m), usually given in dBA SPL. This is a figure of merit for microphones and the smaller the magnitude of the figure, the less audible noise is detected.

The most significant contributors to the noise are the bias resistor, pre-amplifier and packaging of microphone and amplifier. Fig. 3.4(a) indicates the most important noise source. If it is assumed that the amplifier and packaging noise can be neglected and that the input resistance of the amplifier is much higher than the bias resistor R_b, then the total noise voltage density u_n^2 at the output can be approximated by [38]

$$u_n^2 = \frac{4kT}{4\pi^2 f^2 (C_m + C_s)^2 R_b} \tag{3.6}$$

for an amplifier gain of unity. Where k is the Boltzmann constant, T the absolute temperature (293°C at room temperature) and f the frequency. From this expression it is clear that the larger the bias resistance, the lower the noise contribution at higher frequencies. In general the dominant thermal noise shows a 1/f characteristic, that is to say, the noise increases with decreasing frequency. The units of the noise voltage u_n are nV/√Hz and fig. 3.4(b) shows the u_n relationship with frequency for three different bias resistor values at room temperature.

It is interesting to note that the ultimate limit of pressure sensitivity of the microphone diaphragm is caused by the background Brownian noise [39], where Brownian motion of the diaphragm is set up by local variations of the air surrounding the diaphragm. These variations are caused by thermal agitation of the air molecules.

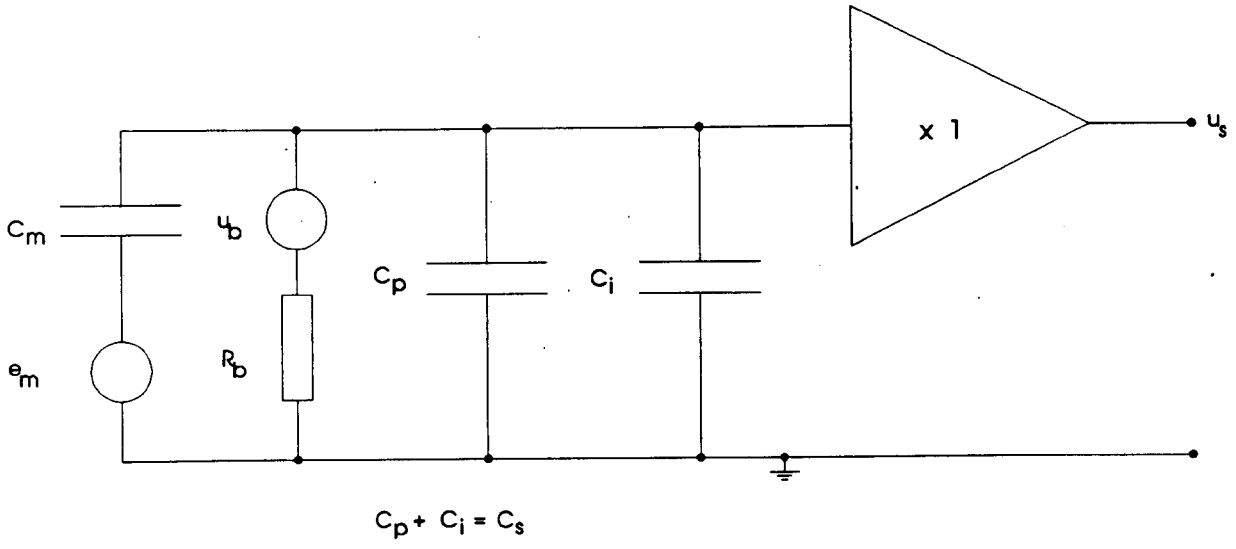

Figure 3.4(a) : The noise sources associated with a condenser microphone and its biasing.

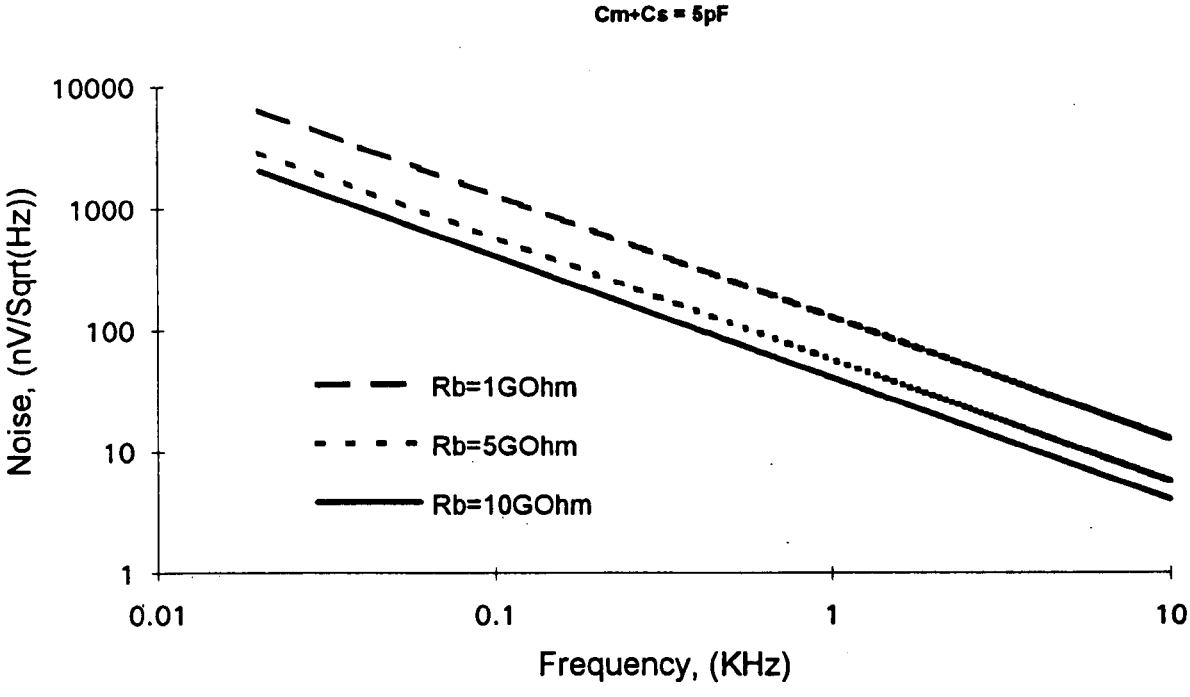

Figure 3.4(b) : Calculated noise contribution from a condenser microphone bias resistor.

3.1.4 Sensitivity of the condenser microphone

Four characteristics can be used to define the sensitivity of a microphone for the conversion of acoustic pressure to an output voltage of a source follower. The first two characteristics, the mechanical sensitivity S_m and the electrical sensitivity S_e, when multiplied with each other and the sound pressure p give the open circuit microphone signal e_m

$$e_m = S_m S_e \, p \tag{3.7}$$

If the microphone is connected to a source follower, for impedance conversion, this signal e_m is attenuated by electrical loading caused by the bias resistor Rb, the input capacitance of the amplifier C_i and parasitic capacitance C_p due to wiring and packaging. The third characteristic is thus the gain H_c attributable to this electrical loading and the final characteristic is the gain H_a of the source follower itself.

If these four characteristics are combined, the output signal v_s of the source follower is

$$v_s = S_m S_e H_c H_a \, p \tag{3.8}$$

It should be noted that the lower corner frequency of the frequency response is determined by the attenuation due to the electrical loading [34] discussed. More detailed definitions of sensitivity and models for circular plates and membranes are given in appendix A1.1.

3.1.5 Practical considerations of condenser microphones

Maximum allowable pressure

It is important to consider the maximum pressure before a diaphragm collapses in the direction of the backplate. A high sensitivity microphone subjected to a high sound pressure is more likely to collapse. Electrostatic attraction forces between parallel plates must also be considered since they will assist diaphragm collapse for a high sound pressure. A

microphone with a high sensitivity thus has a reduced maximum allowable sound pressure. Depending on the thickness h of the diaphragm and the plate separation d, the fracture pressure p_f should be considered and is given by the following expression [40]

$$p_f \propto \frac{\sigma_f^2 h}{Ed} \tag{3.9}$$

where σ_f is the fracture stress of silicon (3.10^8 Pa) and E is the Young's modulus.

Temperature sensitivity

Factors that can lead to temperature sensitivity in a condenser microphone structure are thermal mismatch between a microphone and its substrate for a two chip structure, thermal mismatch for different materials that may make up the microphone structure and/or inbuilt stress of the diaphragm. The first two problems are solved by choosing materials that have closely matched thermal expansion coefficients. For the final situation, the temperature dependence can be minimised, if the change in diaphragm stress with temperature is small in comparison to the initial diaphragm stress. The two options are thus to make the diaphragm stress as low as possible and provide good thermal matching of the materials of the microphone construction, or to make a diaphragm with sufficiently large initial stress.

Pressure doubling effect.

When the frequency of sound increases to a point where the wavelength is of the order of the diaphragm size, the diaphragm acts as a high impedance obstacle in the sound field, from which, the wave will be reflected. When this happens the pressure that is sensed is incorrectly high. This condition is known as the 'pressure doubling' effect. For subminiature microphones of millimetre dimensions this effect is not usually observed below 100kHz. [41]

3.2 Sensitivity measurements

Sensitivity S is usually measured by sweeping the frequency of a sinusoidal sound over a wide range. If a reference microphone is used, the output voltage Vout of the test microphone can be related to a known pressure level or unit pressure P(0).

$$S = \left| \frac{V_{out}}{P(0)} \right| \qquad (3.10)$$

For a flat response, device sensitivity must be almost constant over a large frequency range. For these measurements, the sound field must be perpendicular to the microphones. The pressure response for other angles must be compensated for.

3.3 Computer modelling

It was not possible to derive and simulate a complete model for the p^+ microphone structure because effects on the frequency response and sensitivity due to the air gap and intrinsic diaphragm stress were unknown. Thus a full quantitative prediction of the electrical sensitivity and frequency response are not given.

Programs were written to support the design and development process of this work and this section gives a brief guide to their construction, results and application.

Static diaphragm deflections, for a given pressure, were calculated across the surface of square or circular diaphragms. From these deflections the capacitance was calculated by integration of small areas corresponding to each deflection. The following formula expresses the capacitance C_T for the case of the square diaphragm

$$C_T(P)=\frac{\epsilon}{d}\int_0^a\int_0^b \frac{\delta x \delta y}{1-\frac{w(x,y)}{d}} \tag{3.11}$$

where w(x,y) represents the deflection at an x,y point on the diaphragm, a is the diaphragm length, b the width, d the thickness and ϵ the permittivity of the air gap. (For a square diaphragm b=a.) The percentage change in capacitance is given by

$$\%C=\frac{C_T-C_o}{C_T} \tag{3.12}$$

where C_o is the capacitance with no deflection

$$Co=\frac{\epsilon ab}{d} \tag{3.13}$$

The deflection w(x,y), which is a function of a, b, h and pressure q, can be obtained from Timoshenko's formulae [35] for clamped diaphragms.

Similar numerical calculations were carried out for circular diaphragms (Appendix A1.1 and A3.1), where the deflection of the diaphragm was divided into annular rings with different deflections, the capacitances for each annular ring were calculated and then summed to give C_T. The zero deflection capacitance for a diaphragm with radius R is given by

$$C_o=\frac{\epsilon \pi R^2}{d} \tag{3.14}$$

Evaluation of the deflection and capacitance models for a 1mm diameter x 1 μm thick diaphragm with a 1 μm air gap are shown in figures 3.5(a) and (b) for a static pressure range of 0 to 16 Pa. This range is appropriate for an acoustic microphone since it would represent a maximum SPL of 118 dB (Note : Human hearing range is from 2 x 10^{-5} Pa to 20 Pa or 0

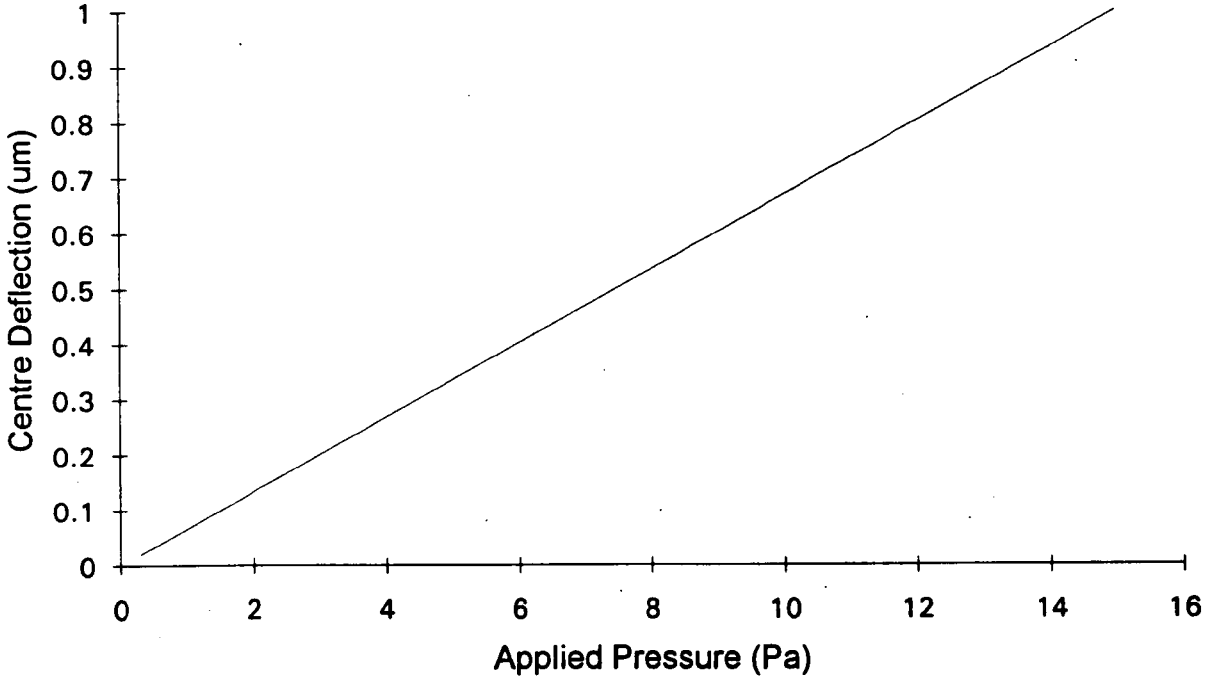

Figure 3.5(a) : Deflection of a 1 mm diameter x 1 um thick p^+ silicon diaphragm for different static pressures.

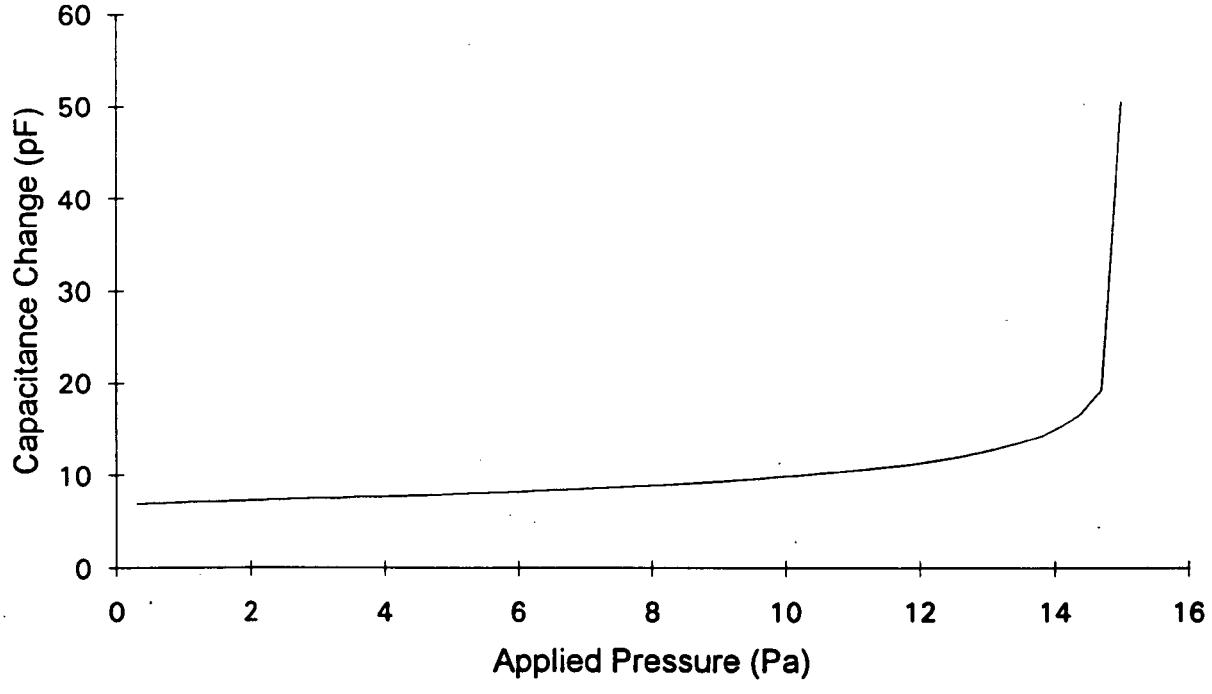

Figure 3.5(b) : Change in capacitance for a 1 mm diameter x 1 um thick p+ silicon diaphragm for different static pressures and a 1 um air gap.

to 120 dB SPL, damage to the ears can occur in excess of 120 dB SPL). The first figure shows the centre deflection of the diaphragm, with no applied bias, for a statically applied pressure and it can be seen that the air gap is reduced to zero at the centre of the diaphragm for 15 Pa. This indicates that the choice of a 1 μm thick diaphragm is appropriate for the desired SPL range. The next figure 3.5(b) shows the change in capacitance for this applied pressure, and it can be seen that as the pressure is increased, corresponding to a narrowing of the air gap at the centre of the diaphragm, the capacitance rises rapidly. The final figure 3.5(c) indicates the percentage change in capacitance with respect to the original parallel plate value and for a pressure of 10 Pa the percentage change is about 50 %. This value would seem to indicate that the values chosen for diaphragm/back electrode area and air gap thickness will yield significant and measurable capacitance changes in the pressure range of interest.

Effects of variation of diaphragm and air gap thickness

For a stress free circular or square diaphragm that is 1um thick and has an air gap of 1um it was found from simulation that a variation of +/-10% in the diaphragm thickness caused a maximum change in mechanical sensitivity of 37% and a similar variation for the percentage change in capacitance. The impedance at 50 Hz only shows a 1% variation. For a +/- 10% variation in the air gap for the 1um thick diaphragm the percentage change in capacitance shows a maximum variation of 12 % for a mechanical sensitivity of 0.067 um/Pa and the impedance at 50 Hz varies by a maximum of 10%. These results show that the thickness of the p^+ diaphragm represents an important parameter if the mechanical sensitivity is to be controlled. Both the diaphragm thickness and the air gap depth must be fabricated with thickness variations that are much less than +/- 10% if the microphone mechanical and

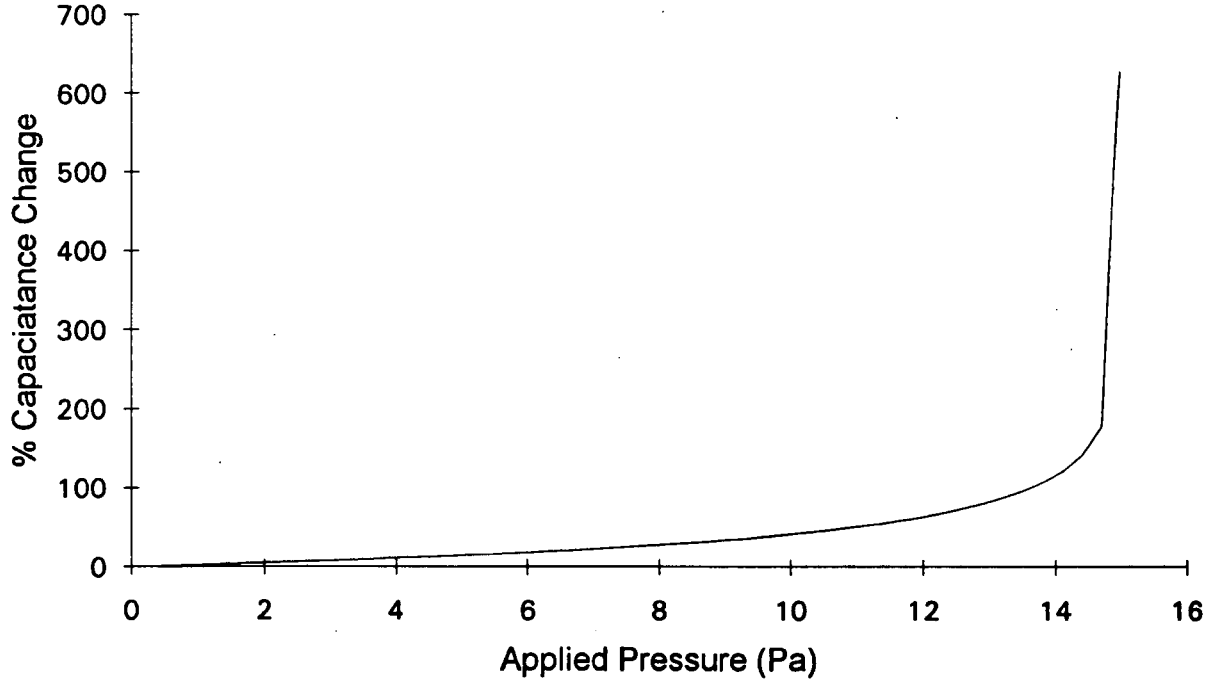

Figure 3.5(c) : Percentage change in capacitance for a 1 mm diameter x 1 um thick p+ silicon diaphragm for different static pressures and a 1 um air gap.

electrical sensitivity are to be controlled. (For simplicity, air damping effects have been neglected for mechanical sensitivity calculations.) For a variation in diaphragm thickness of +/-1% a 3% maximum variation of mechanical sensitivity is calculated and a 4% variation of change in capacitance. It should be possible to control the diaphragm fabrication parameters such that the thickness does not exceed +/-5% of the designed target thickness.

Electrostatic Calculations

The magnitude of the applied bias voltage across the parallel plates determines the level of electrostatic forces acting on the diaphragm and thus affects the working point, sensitivity and the initial capacitance of the microphone. It is important to determine the optimum bias voltage from suitable models for the miniature silicon microphone.

The electrostatic force per unit area P_r acting on the diaphragm should be less than the normal reaction force per unit area P_e in order to prevent the diaphragm from collapsing for a given bias voltage or pressure. If the bias voltage is increased, or the air gap is narrowed due to impinging sound waves, P_e becomes much larger and can exceed P_r, when this happens the diaphragm will collapse into the back chamber. The magnitude of P_r is also affected by the residual stress of the diaphragm, requiring different bias conditions from that of the stress free case. The models in appendix A1.1 for electrostatic attraction of a circular diaphragm have been calculated for the microphone defined earlier in this section. For a stress free diaphragm and a 0.7 V bias fig. 3.6(a) shows the effects on the diaphragm forces, expressed per unit area, as the centre deflection of the diaphragm is varied. A point is reached, for a deflection of 0.2 μm where P_r and P_e cross each other, at this point P_e-P_r equals zero and microphone operation is stable because of the negative gradient of P_e-P_r. The

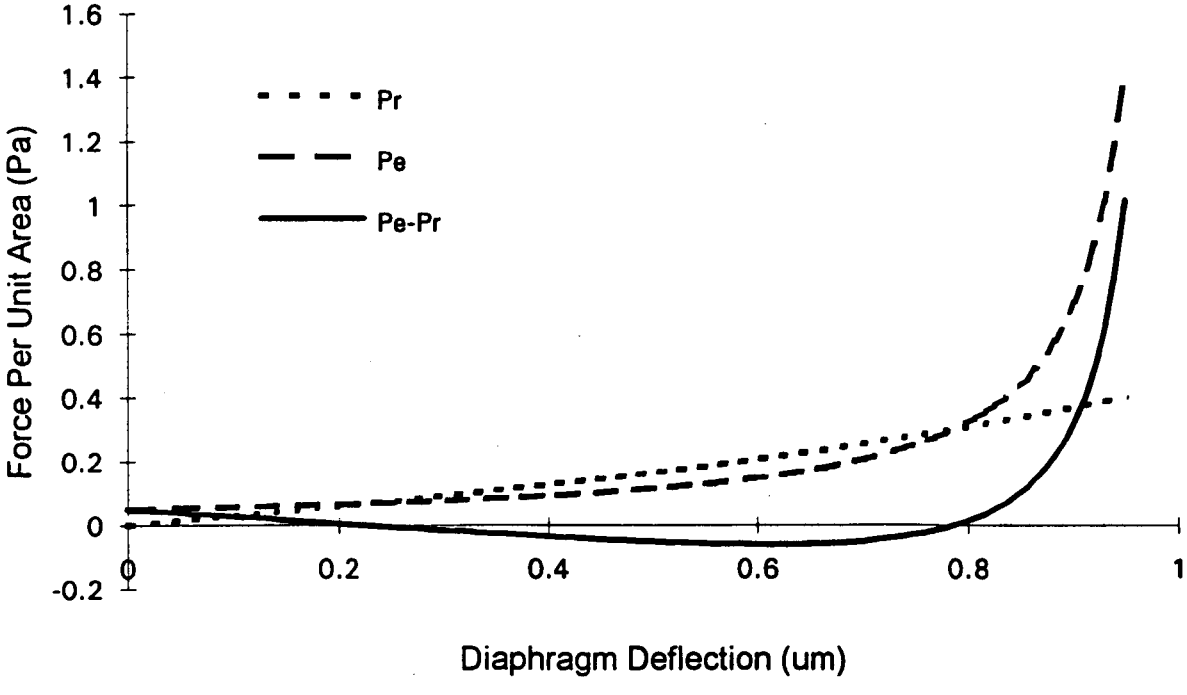

Figure 3.6(a) : Forces acting on a 1mm diameter x 1 um thick p^+ silicon diaphragm, stress free, for different deflections within a 1um air gap and a 0.7 V bias voltage.

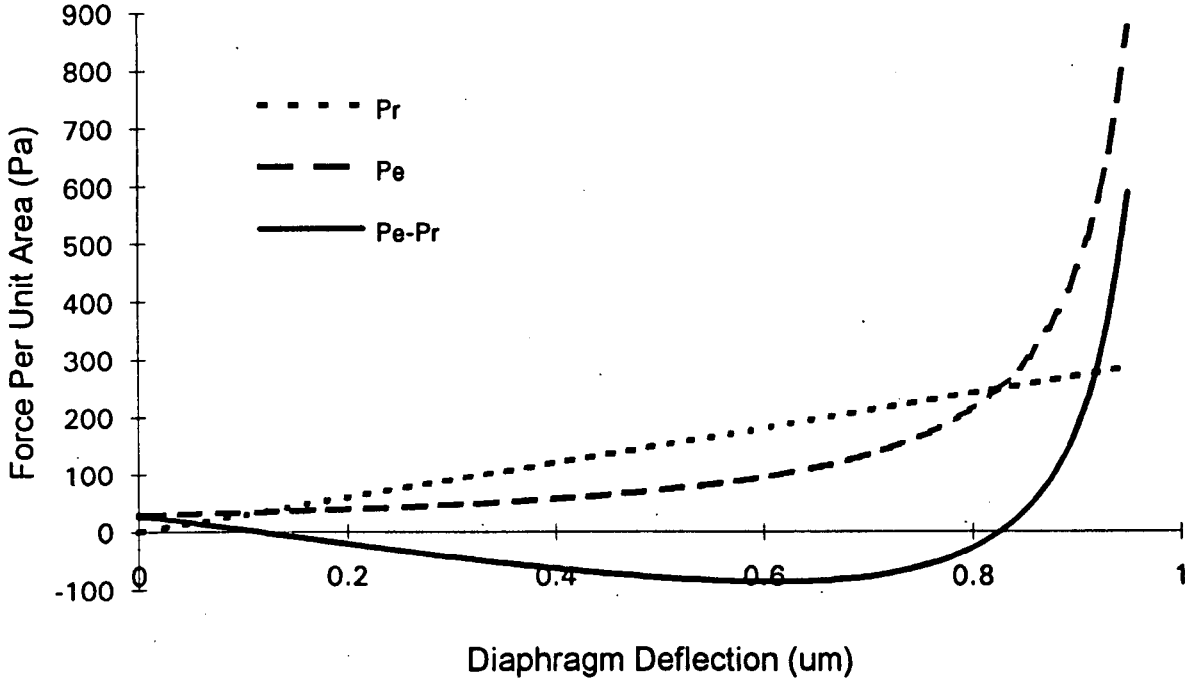

Figure 3.6(b) : Calculated forces acting on a 1mm diameter x 1 um thick p^+ silicon diaphragm, with 100MPa residual stress, for different deflections within a 1um air gap and a 7 V bias voltage. (Graph obtained from numerical evaluation of models in appendix 3.)

second point where P_e-P_r is zero is unstable, because beyond this point, P_e exceeds P_r and the P_e-P_r gradient is positive causing the diaphragm to collapse due to the magnitude of P_e. Fig. 3.6(b) shows the same situation for a diaphragm with a 100MPa residual stress causing the forces involved to be 1000 times greater than for the stress free diaphragm. A bias voltage of 7V has been used to reflect this, since the larger P_r requires a much larger P_e to deflect the diaphragm. It should be noted for both curves, that as the bias voltage is increased from zero, the P_e curve rises in the y direction until it is above the P_r curve and there are no longer two points of intersection, at this point the diaphragm has no stable working point and will collapse. It is instructive to plot the bias voltage against the first stable working point for the diaphragm geometry given to find the maximum bias voltage that can be applied to the structure. Fig[1]. 3.7(a) shows that the maximum bias voltage that can be applied to the stress free diaphragm is 0.8V and fig. 3.7(b) shows the value to be nearly 9 V for a 100MPa residual stress. Both structures have a maximum operating point of about 0.4 μm. For 1 μm p^+ diaphragms the residual stress can be up to 100 MPa or more, so it is clear from this work that for miniature circular microphone structures, a low bias voltage of up to 9 V may be necessary depending on the stress value. Such a low voltage means that an electret microphone structure is unnecessary for microphones with very narrow air gaps.

Microphone Impedance

Very small microphones can have a very high impedance which means that obtaining a measurable signal can be extremely difficult. The impedance for the microphone defined in this section is shown in fig. 3.8 for three different air gap sizes. It is apparent that as frequency decreases the impedance increases according to the $1/(2\pi fC_m)$ relationship. For a smaller air gap the impedance decreases as the microphone capacitance increases. This would

[1] The steps in fig 3.7(a) and (b) are caused by computer numerical approximation and evaluation of the models used.

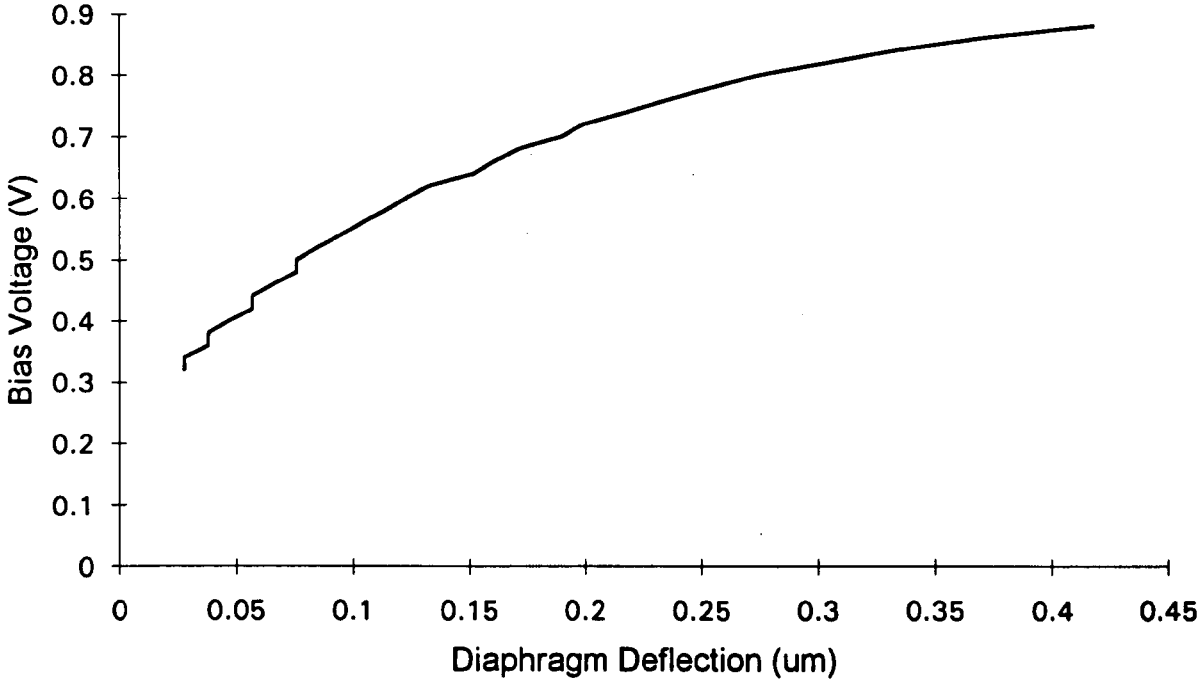

Figure 3.7(a) : Calculated deflection of a 1mm diameter x 1 um thick p^+ silicon diaphragm, stress free, within a 1 um air gap due to electrostatic attraction for different applied bias voltages. (Graph obtained from numerical evaluation of models in appendix 3.)

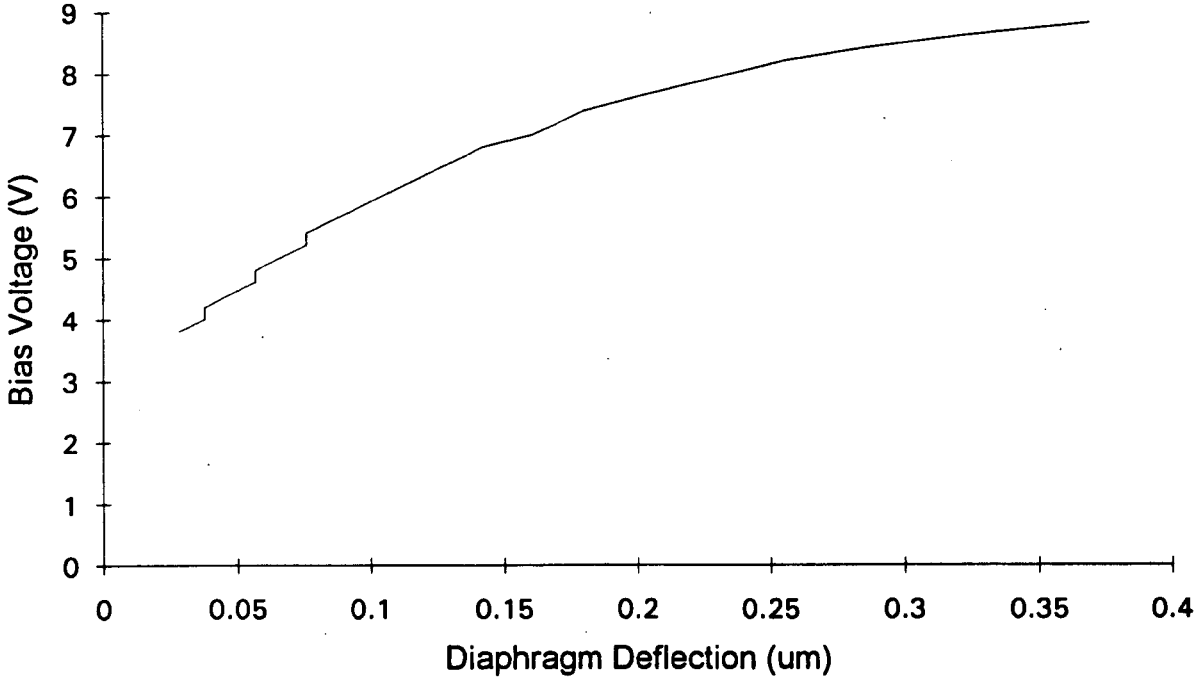

Figure 3.7(b) : Deflection of a 1mm diameter x 1 um thick p^+ silicon diaphragm, with 100MPa residual stress, within a 1 um air gap due to electrostatic attraction for different applied bias voltages. (Graph obtained from numerical evaluation of models in appendix 3.)

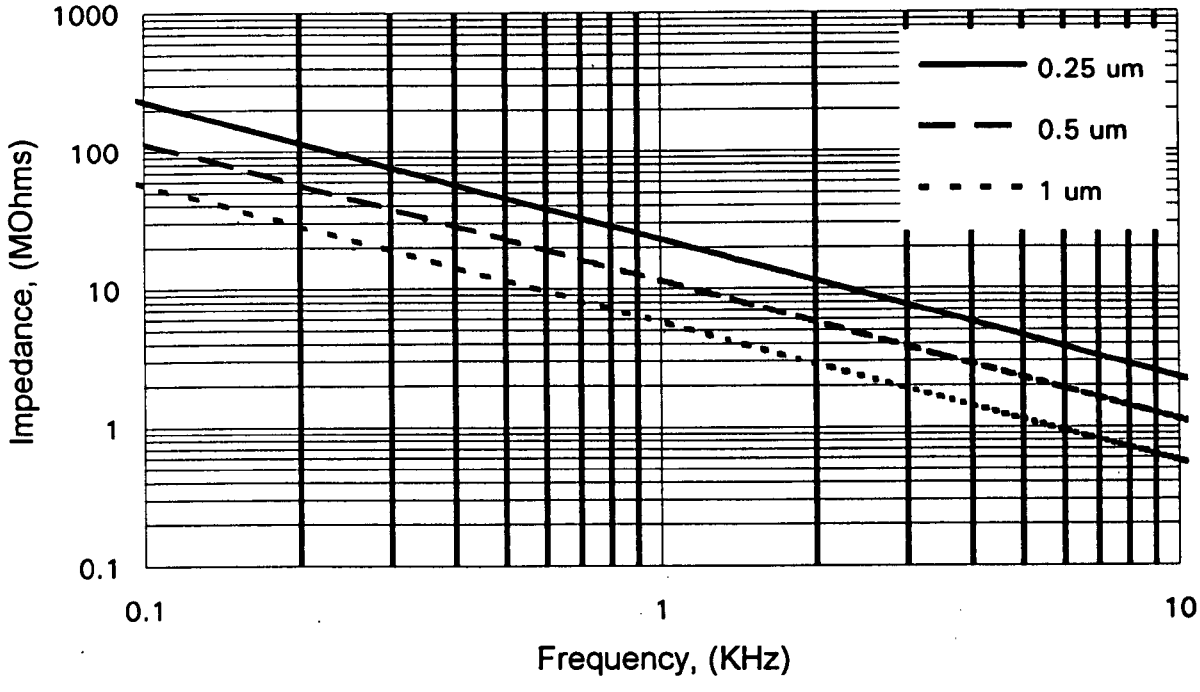

Figure 3.8 : Calculated impedance at different frequencies of a 1 mm diameter condenser microphone for different air gap thicknesses.

indicate that the applied bias voltage could be used to control the microphone impedance to some extent. The bias resistor used for the microphone forms a potential divider with the microphone impedance for small signal output, so it is important that the bias resistor chosen is as large as possible in order to maintain a low cut off frequency. ($F_c = 1/2\pi C_m R_b$). For example, if the reactance of the microphone with a 1 μm air gap is 200 MΩ at 100 Hz then the bias resistor should be at least 10 times larger. This will result in a 10% reduction of the open circuit microphone signal at this frequency but will require a 2 GΩ resistor. Resistors of such high values are available in thick film surface mount form up to values of 10 GΩ and can be used for biasing miniature microphones. It is also important that the input of the amplifier used for impedance conversion has a correspondingly high input impedance. (It should be much larger than the bias resistor) Modern FET input operational amplifiers can achieve input impedances of 1.5 TΩ (1 Tera Ohm = $1x10^{12}\Omega$) or more and so would not load the microphone significantly. Since impedances are very high for the microphone 'front end', it is important to keep interconnections as short as possible between the microphone and the amplifier input stage and probably even screen the microphone to prevent unwanted stray capacitance and parasitic noise problems from occurring.

Finite element analysis

Finite element analysis was carried out using the Algor package to determine the resonant frequency of the proposed 1 mm^2 x 1 μm edge clamped square diaphragm structure, assuming a uniformly heavily doped (p^+) structure (See Ch. 4) with a Young's modulus of $3.12x10^{11}$ MPa. A value of about 22kHz was determined for the first resonant mode and agreed well with formulae calculations shown in appendix A1.2. The elementary model is shown in fig. 3.9.

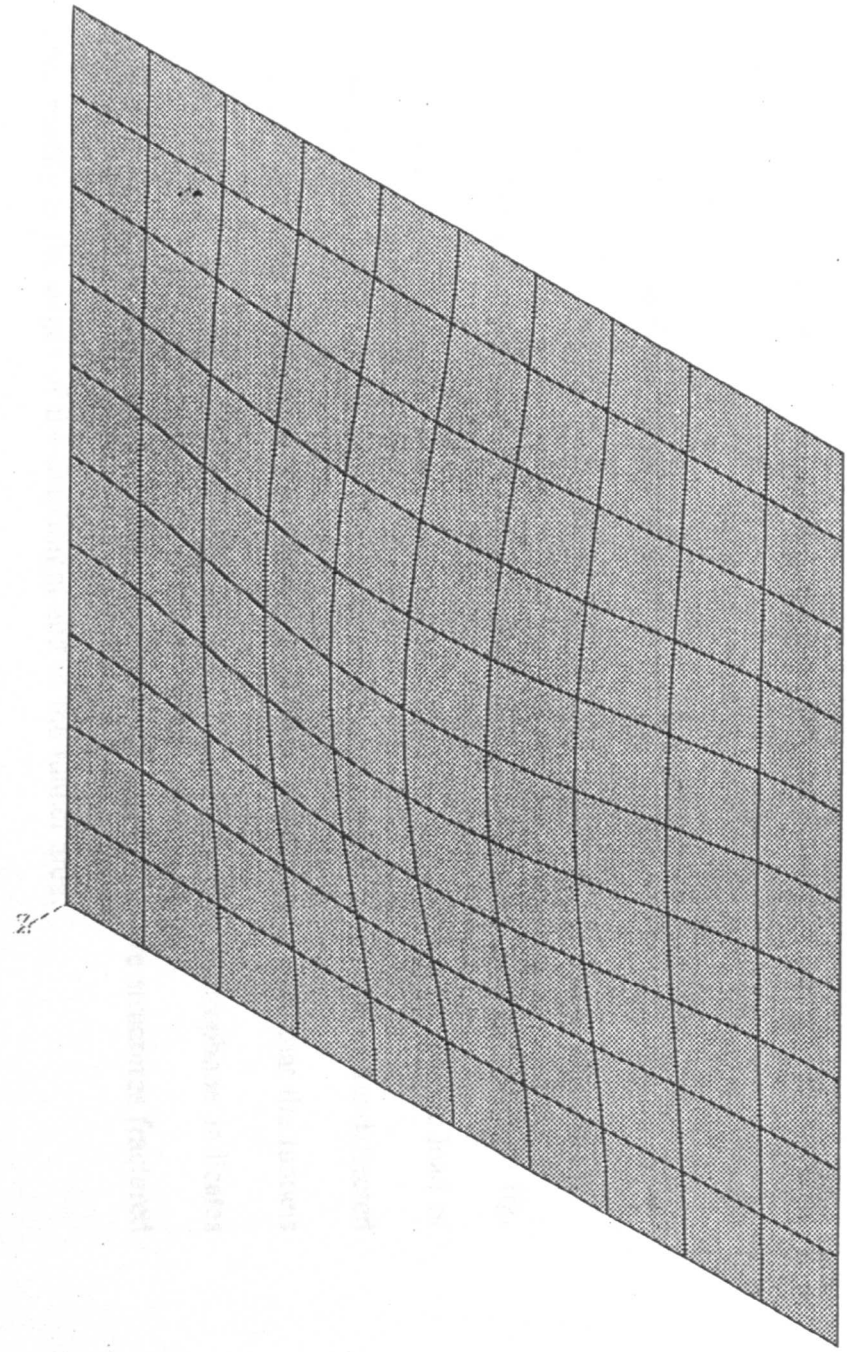

ANSYS 4.4A
AUG 11 1993
9:20:17
PLOT NO. 1
POST1 DISPL.
STEP=1
ITER=1
FREQ=20111
DMX =51120

DSCA=0.132E-08
XV =1
YV =1
ZV =1
DIST=0.674E-03
XF =0.500E-03
YF =0.500E-03

Figure 3.9: Finite element model of a 1mm^2 square diaphragm with clamped edges for determination of the first resonant frequency.

To carry out finite element analysis, models composed of suitable elements were constructed for the fabricated devices, the model for the square microphone is shown in fig. 3.10. The red triangles indicate elements that have been prevented from moving and symbolise the point where the p^+ silicon is electrostatically bonded to the glass substrate. The model represents a plane through the structure with all the mass concentrated in that plane and does not take into account any effects that may be caused by the three dimensional geometry of the actual structures. For the circular microphone model shown in fig. 3.11 there are more elements in the diaphragm area for the sake of modelling displacements and stresses more clearly. The model does not take into account residual diaphragm stress or stress changes that could be caused by different thermal expansion coefficients of the diaphragm and glass backplate. Both of these effects could also be temperature dependent. Further assumptions are that the material is isotropic and has linear elastic behaviour.

The Von Mises stress (See glossary) or 'equivalent stress (MPa)' profiles are shown in fig. 3.12 and fig. 3.13 for the square and circular microphones respectively, for a static load of 1Pa on the structure. It can be seen that the stresses are highest at the centre of the deflected diaphragm and near the clamped areas at the edge. It is interesting to note that the tunnels for the circular microphone exhibit minimal stress, but the square microphone indicates increasing stress toward the centres. This could indicate why the square structures fractured more readily at the edges of the diaphragm and in the tunnel area.

For the same load the displacement plot for one quarter of the square microphone diaphragm is shown in fig. 3.14, where it can be seen that the deflection is greatest at the centre of the microphone and zero at the clamped edges. The equivalent plot is shown for the whole of

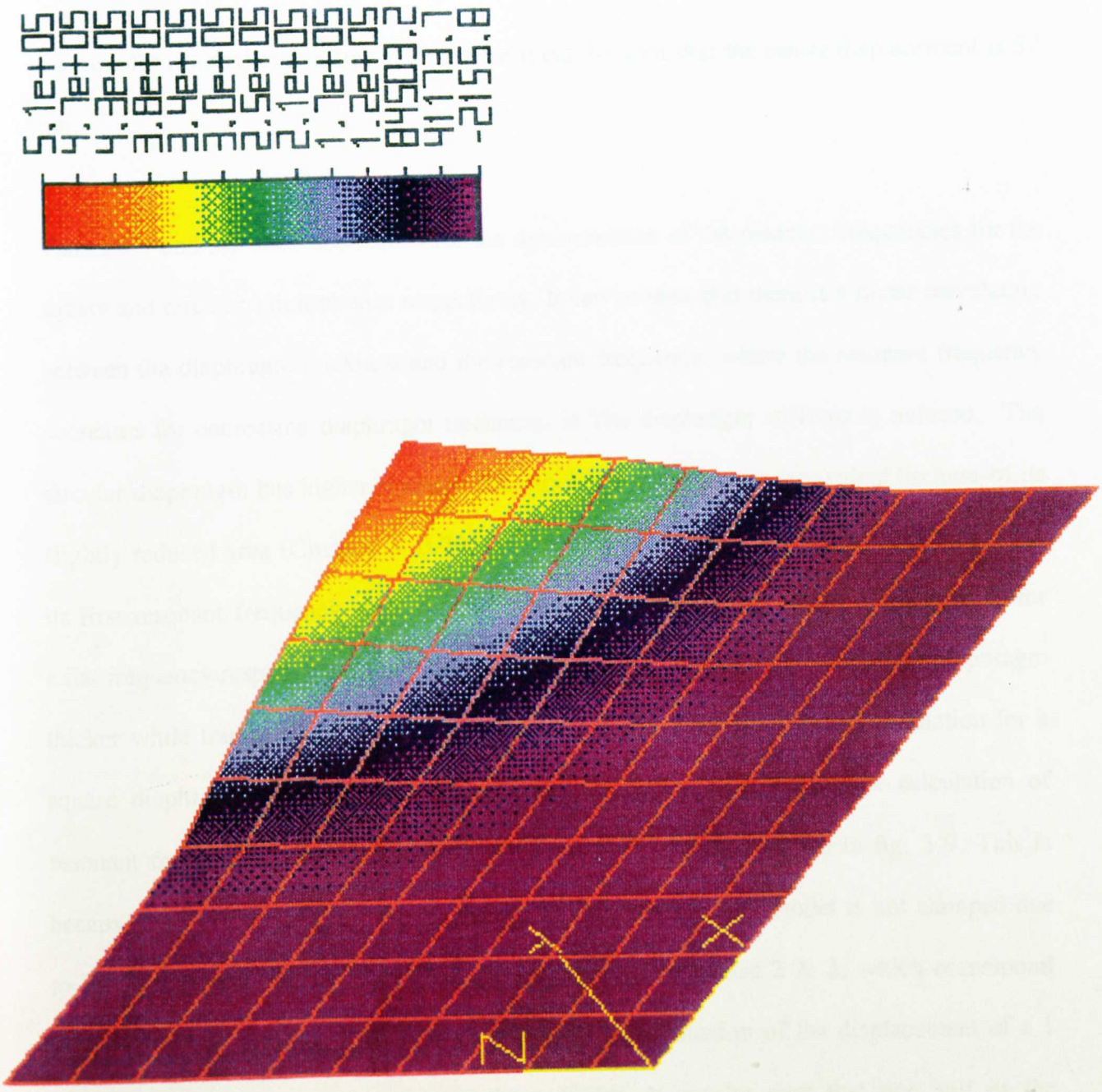

Figure 3.14 : Displacement profile of a 1mm^2 diaphragm subjected to a static load of 1Pa.

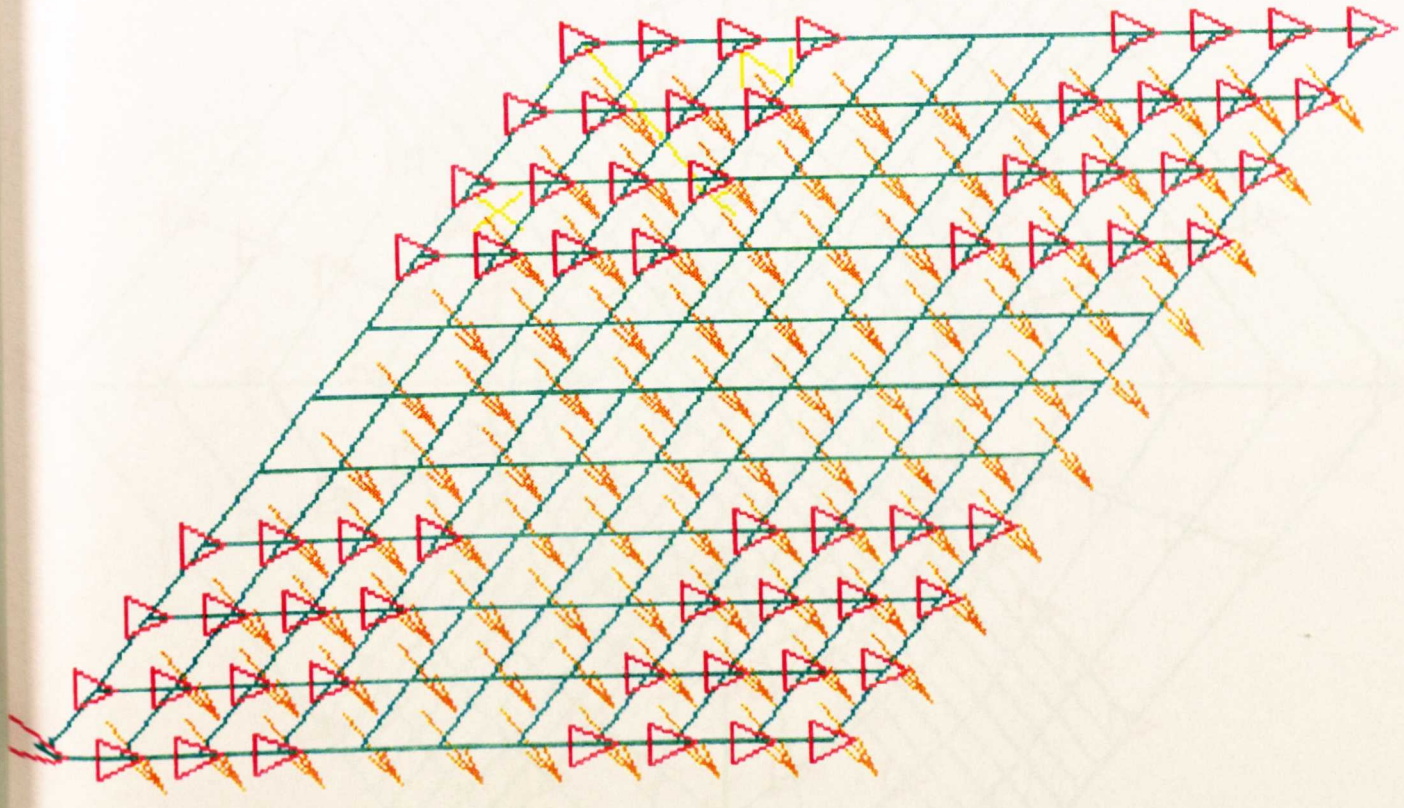

Figure 3.10 : Advanced finite element model of 1mm^2 square silicon microphone design where the red triangles represent where the p^+ silicon structure is bonded to a glass substrate or clamped.

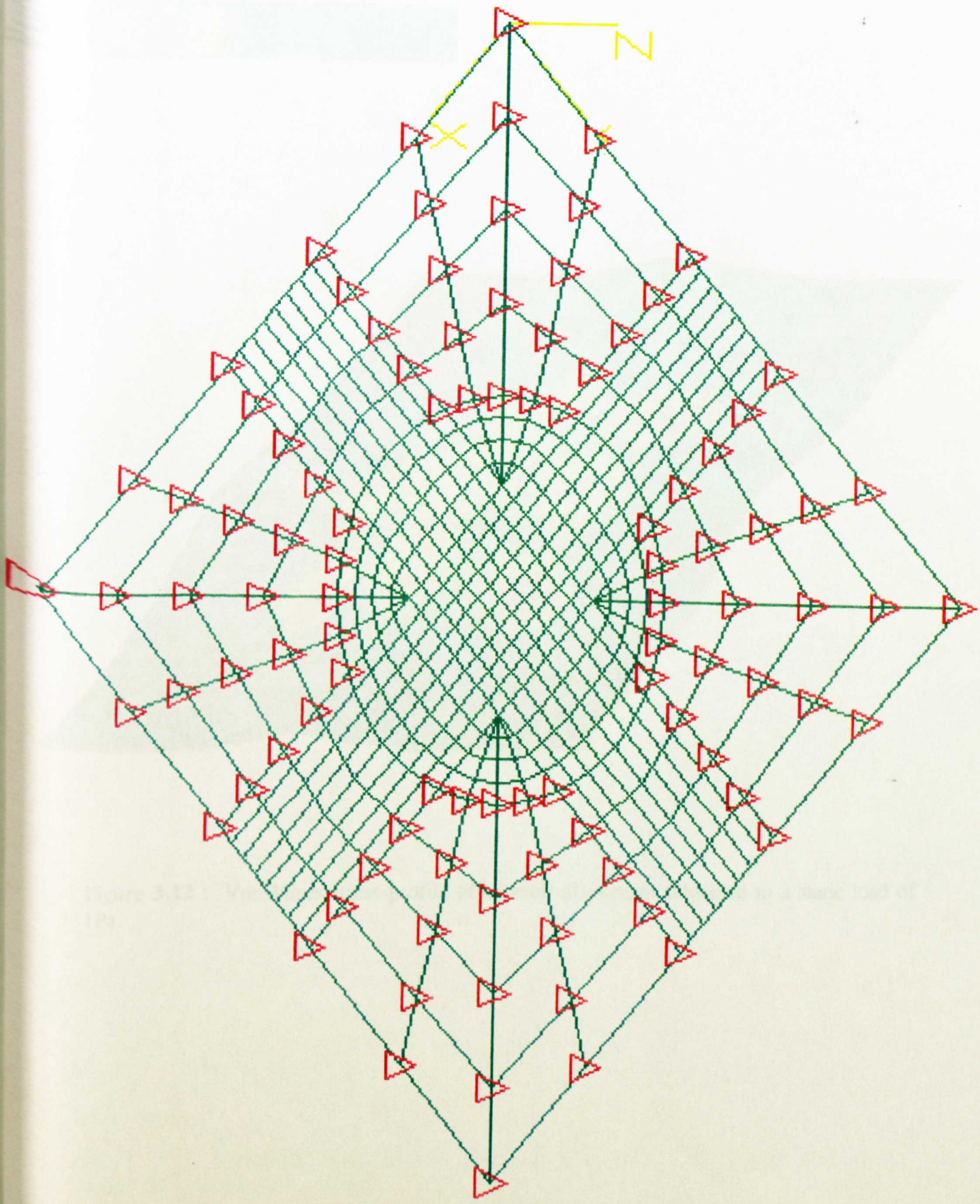

Figure 3.11 : Advanced finite element model of a 1mm diameter circular silicon microphone. where the red triangles represent clamped areas of the structure.

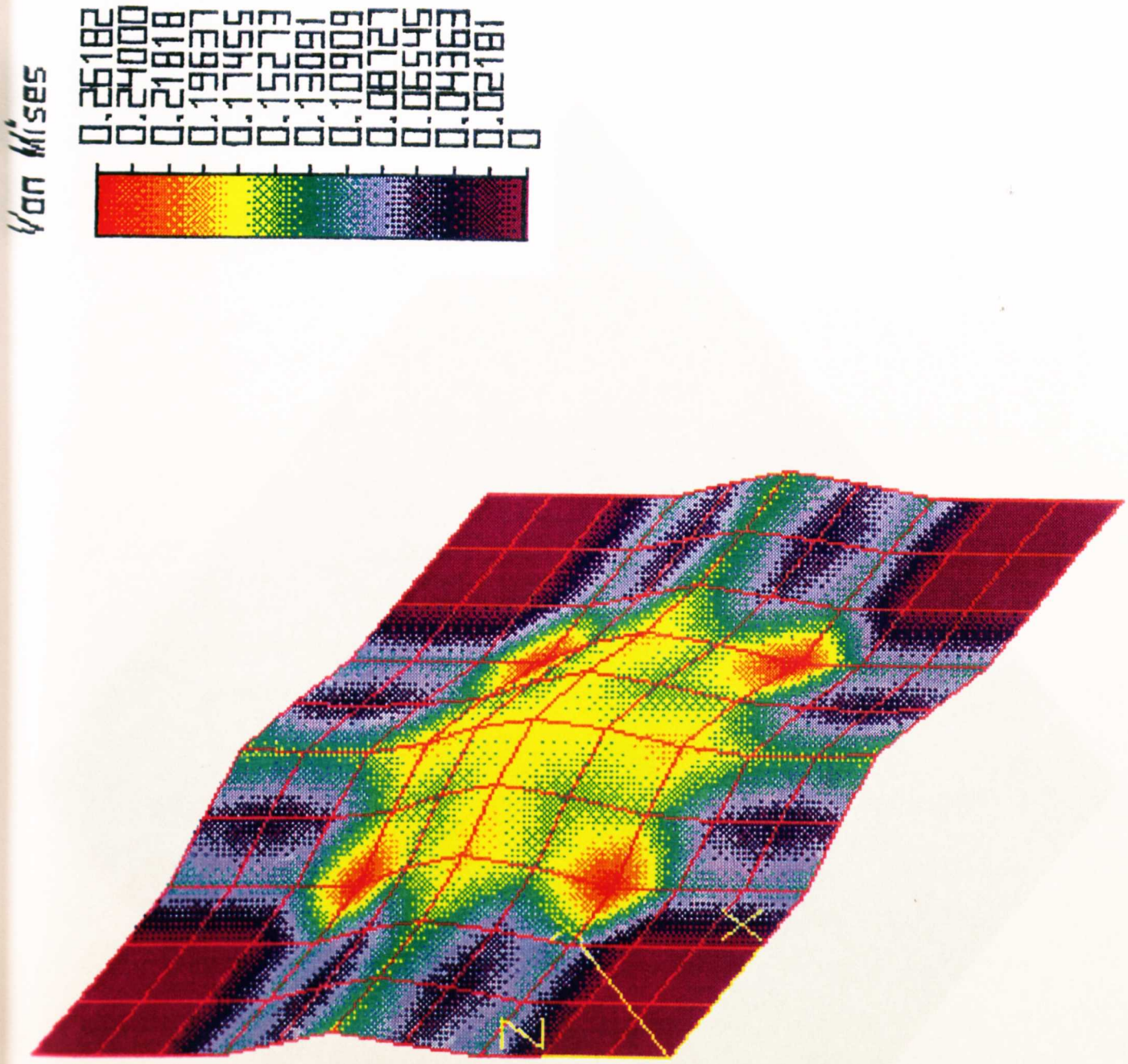

Figure 3.12 : Von Mises stress profile of a 1mm^2 diaphragm subjected to a static load of 1Pa.

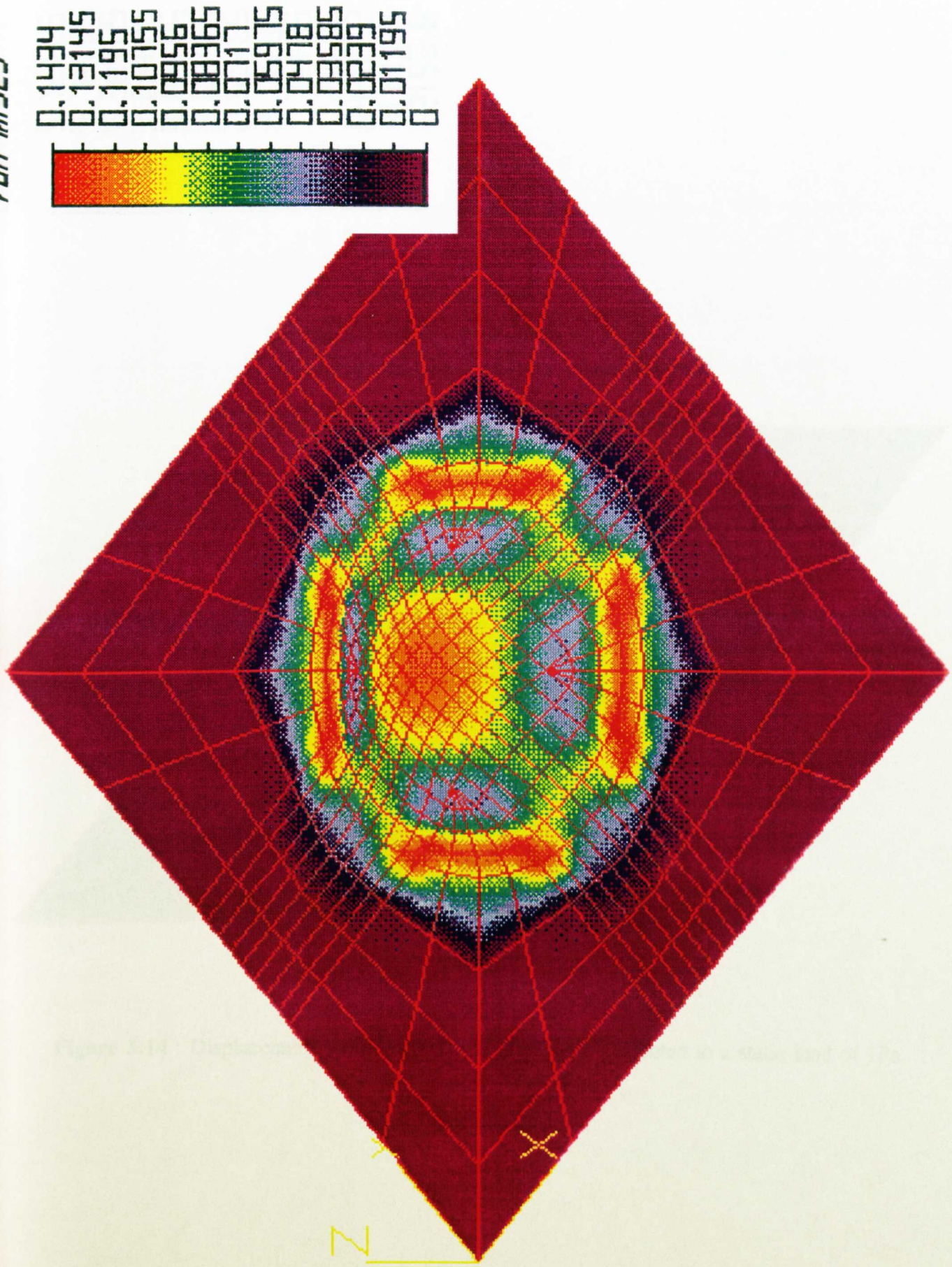

Figure 3.13 : Von Mises stress profile of a 1mm diameter circular silicon microphone subjected to a static load of 1Pa.

the circular microphone in fig. 3.15, where it can be seen that the centre displacement is 57 nm.

Tables 3.1 and 3.2 show the results for the determination of the resonant frequencies for the square and circular microphones respectively. It can be seen that there is a linear correlation between the diaphragm thickness and the resonant frequency, where the resonant frequency decreases for decreasing diaphragm thickness. ie The diaphragm stiffness is reduced. The circular diaphragm has higher resonant frequencies than the square equivalent because of its slightly reduced area (Circular = 0.79 mm^2, Square = 1 mm^2). The square diaphragm has its first resonant frequency well within the audio frequency range which is undesirable for a flat frequency response, however this frequency can be increased by making the diaphragm thicker while trading sensitivity. It is also apparent that the finite element simulation for a square diaphragm gives a lower first resonant frequency than the simple calculation of resonant frequency shown in appendix A1.2 and the simulation shown in fig. 3.9. This is because 50 % of the edge of the diaphragm in the finite element model is not clamped due to the four lateral tunnels. Table 3.2 shows the resonant modes 2 & 3, which correspond with each other, and fig. 3.16 shows a graphical representation of the displacement of a 1 μm circular diaphragm resonating in these modes. It can be seen that one half of the diaphragm is 180° out of phase with the other half.

Finite element analysis was a useful tool in predicting the static mechanical characteristics of the microphones, and was used in conjunction with fabrication results to improve understanding and design of the new microphone structures.

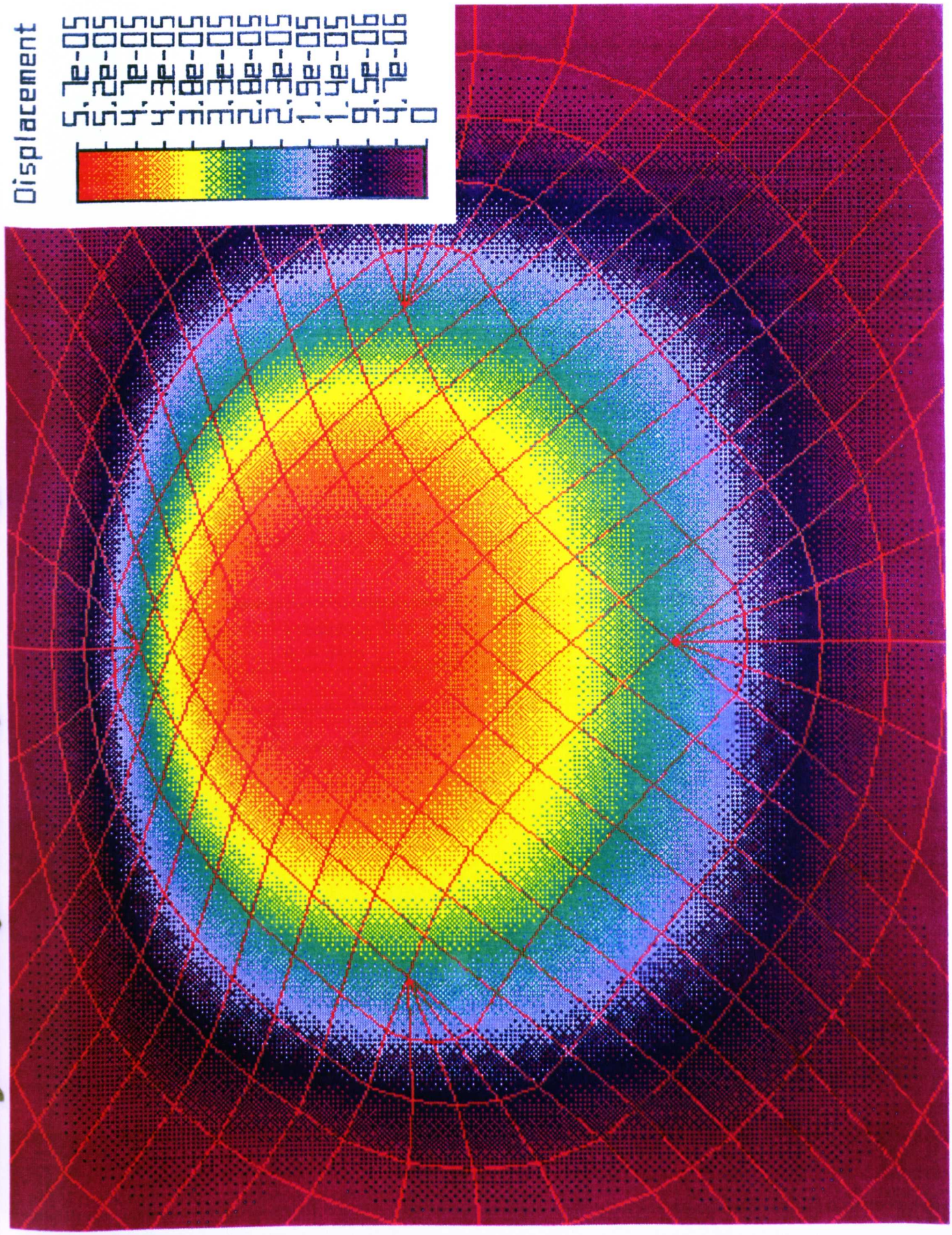

Figure 3.15 : Displacement profile of a 1mm diameter circular silicon microphone subjected to a static load of 1Pa.

Table 3.1 : Computer FEA simulation results for modal analysis of a square diaphragm with the following dimensions:-
Overall size : 2 mm^2
Diaphragm :1mm^2 x 1um
Tunnel :500 um x 500 um x 1 um
Boundary Conditions :All corners fixed, mass distribution as in actual structure.

Resonant Mode	Frequency /Hz For the following diaphragm thicknesses d = 1um	d = 0.5um	d = 0.1 um
1	11000	5500	1100
2 & 3	15000	7500	1500

Table 3.2 : Computer FEA simulation results for modal analysis of a square diaphragm with the following dimensions:-
Overall size : 2 mm^2
Diaphragm :1mm dia. x 1um thick
Tunnel :400 um x 400 um x 1 um
Boundary Conditions :All corners fixed, mass distribution as in actual structure.

Resonant Mode	Frequency /Hz For the following diaphragm thicknesses d = 1um	d = 0.5um	d = 0.1 um
1	17500	8750	1750
2 & 3	36000	18000	3600

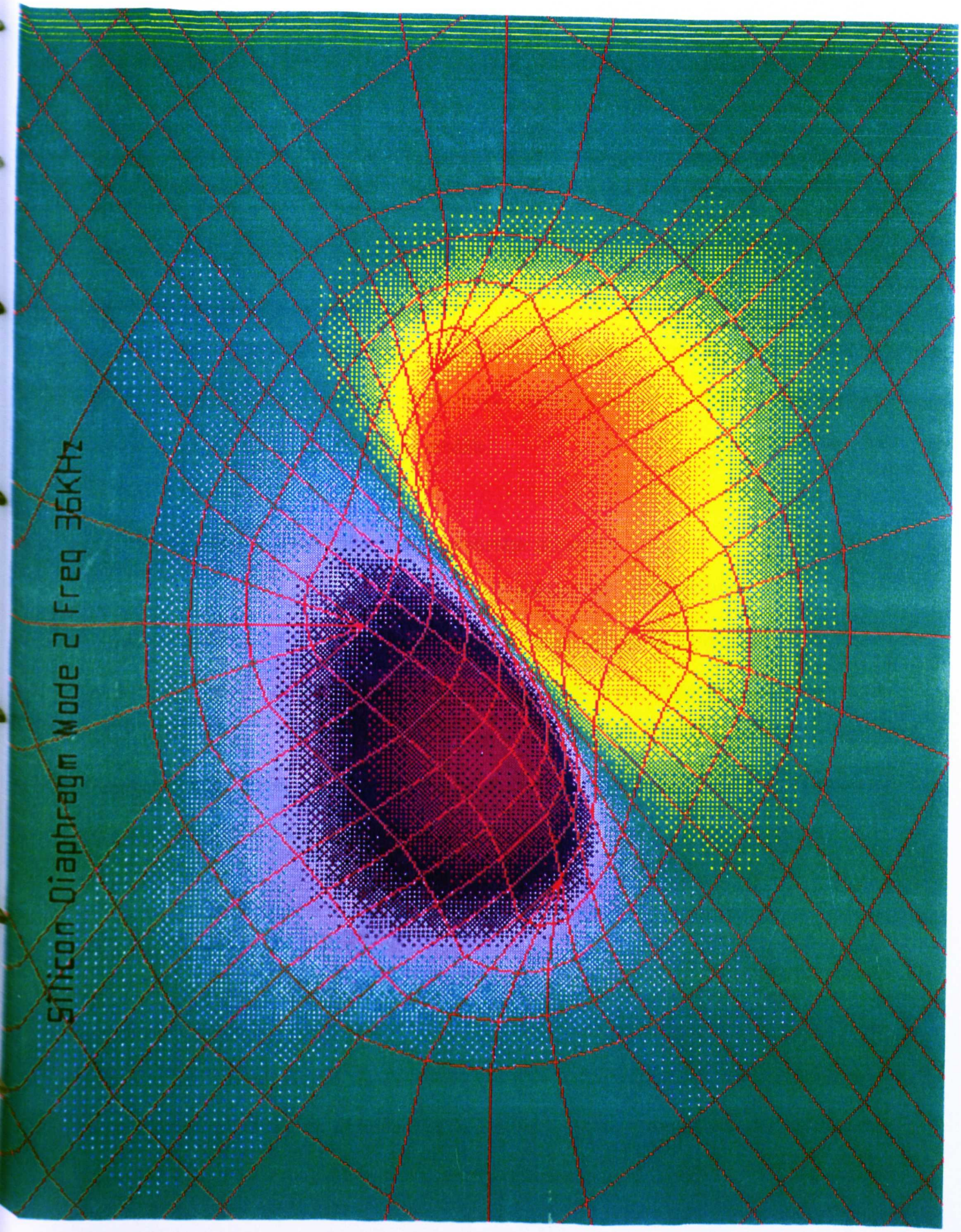

Figure 3.16 : Circular 1mm diameter silicon diaphragm resonating in mode two at 36kHz, where one half of the diaphragm is 180° out of phase with the other half.

4.0 SILICON MICROPHONE FABRICATION THEORY AND TECHNIQUES

The first section of this chapter outlines the microphone structure and technology. Further sections give details of the theory, modelling and techniques required to understand the fabrication processes that were used and developed for this project. Process modelling including diffusion, oxidation and etching were carried out using devised computer programs, (Some of the computer programs are listed in appendix 4) in order to produce the graphs shown in this chapter and appendix 2, thus providing essential reference material for setting process fabrication parameters required in the experimental work. References are given where necessary for all the described models.

4.1 Proposed fabrication technology and device structure

Most of the microphones described in chapter 2 required the use of technologies such as ion implantation, chemical vapour deposition (CVD) and/or plasma enhanced CVD [42] as well as some dry etching techniques for one or more stages of their fabrication. Since these very advanced and expensive facilities were not available for this project, more modest micro fabrication equipment (See appendix A3.3) was used, or adapted, in order to fabricate a heavily p-type (or p^+) silicon microphone on glass by utilising etch stop principles.

All of the areas of expertise and techniques used for this project had to be developed by the author from scratch, based on study of the literature, since no provision was made for device fabrication within an experienced micro engineering facility. The techniques that had to be characterised and developed for this work included mask fabrication, photo lithography, silicon oxidation, diffusion of impurities in to silicon, silicon etching/etch stop techniques, thin film deposition of metals on glass, electrostatic bonding, gold ball bonding and device

packaging. Many of these processes could not be fully characterised because sophisticated measurement equipment and expertise was unavailable in house. It was not possible to send samples to commercial clean rooms due to high cost and the risk of contamination of their clean room facility.

Fabrication overview

The devised fabrication scheme for this project can be divided into three main phases. The first phase consists of the wafer processing, the second is the glass processing and the final phase is bonding the glass substrate to the silicon wafer for silicon dissolution. The complete fabrication cycle requires four masks for its implementation and each mask is used to define the following device features :-

Silicon Wafer Processing

Mask 1 : Back chamber

Mask 2 : p^+ rim

Mask 3 : p^+ diaphragm

Glass wafer processing

Mask 4: Metallisation for fixed electrode and contacts

Simulation work based on the design considerations discussed in the last chapter were carried out in order to specify the device geometry and hence the mask dimensions. The structure that was fabricated is detailed in this chapter along with the theory to support the experimental work in the next chapter.

Device structure

The microphone structure that was proposed is shown in fig 4.1(a). It is made of single crystal n-type silicon heavily doped with boron in order to form a p^+ structure and is bonded to a glass substrate. This p^+ silicon structure has a thick p^+ supporting rim for a very thin p^+ diaphragm which forms the moveable electrode required in a condenser microphone. The backchamber underneath the diaphragm, outlined in fig 4.1(b) is connected to the exterior of the structure via four tunnels, one in each side of the rim, to allow pressure equalisation and possibly reduce viscous damping.

The metallisation fabricated on the glass substrate (refer to fig 4.1) forms the two contacts for the structure and the fixed back electrode. One of the contacts connects to the p^+ structure itself, the other connects to the backplate through one of the tunnels. The fixed and the moveable electrode are thus electrically isolated from each other, but form a capacitive structure.

Overall dimensions of a single square microphone M1 structure (fig. 4.1) are 2mm x 2mm, the diaphragm is 1mm x 1mm and depending on fabrication, has a thickness that can be varied from 1 μm to 5 μm. The top of the rim is 500 μm wide, has a height of up to 12 μm and has a tunnel in the centre of each face that is 400 μm wide. The tunnels are an extension of the backchamber and both are controlled in height from between 0.5 and 2 μm. This height determines the air gap of the microphone and can be fabricated very accurately by an oxidation technique that has been developed. The backplate electrode is 0.8 x 0.8 mm and the contact pads are 250 x 250 μm with 100 μm wide connecting traces.

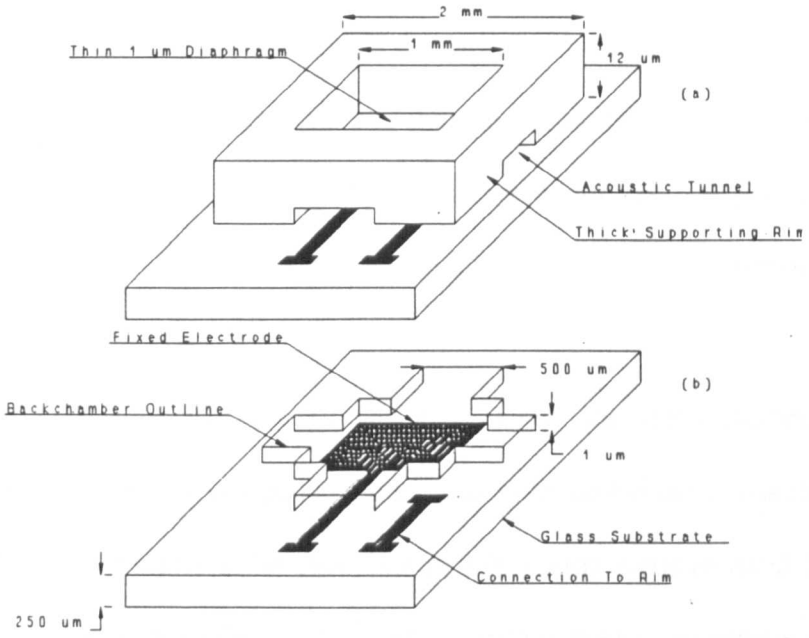

Figure 4.1 : Geometry of a square (a) p^+ doped microphone structure, (b) Back chamber.

Improvements were made to microphone M1 for subsequent fabrication of microphone M2, which has slight dimensional modifications incorporating a 1mm diameter circular diaphragm and a 0.8 mm diameter back electrode. These alterations provided fabrication improvements over the square diaphragm geometry and are indicated in subsequent chapters. These M2 details are shown in fig. 4.2(a) which indicate the three dimensional geometry, and fig. 4.2(b) which shows a plan view of the top and the underside of the structure.

The optical photographs of plates 6.12 and 6.13 show the microphones M1 and M2 respectively which have been developed using the processes described in chapter 5. The flow diagram of fig 4.2(c) summarises the overview of fabrication steps devised for this project and includes references to the relevant sections regarding theory, experimental and results described in this thesis Each stage is also cross referenced to the pictorial process guide shown in fig. 5.1. (Chapter 5).

4.2 Lithography

Positive resist was used for this work for electrode fabrication and negative resist was used for wafer processing. Lithography involves application of the photo resist to the substrate, a pre-bake, exposure, development and then a hard bake depending on the process. Lithography is carried out in a yellow safelight area, in ultra clean conditions using vertical laminar flow hoods to prevent particle contamination.

Negative resist

Negative resist consists of two components, a photosensitive cross linking material that gives the resist its exposure characteristics and a non photosensitive synthetic rubber compound that

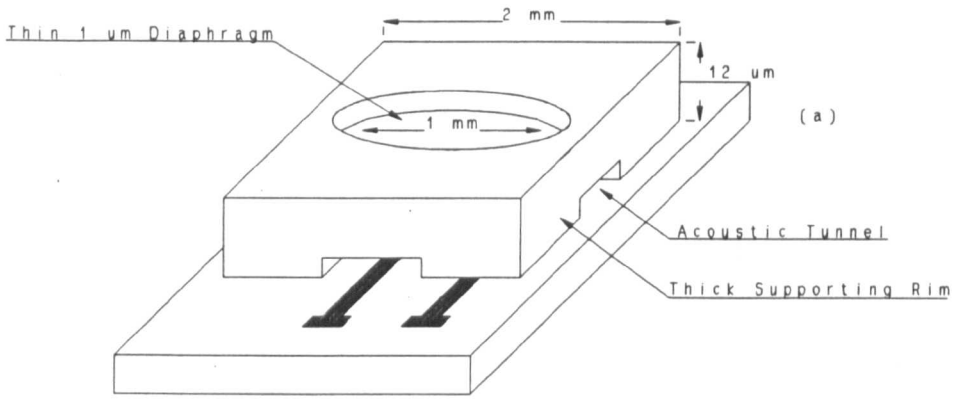

Figure 4.2(a) : Geometry of a p^+ doped circular microphone structure.

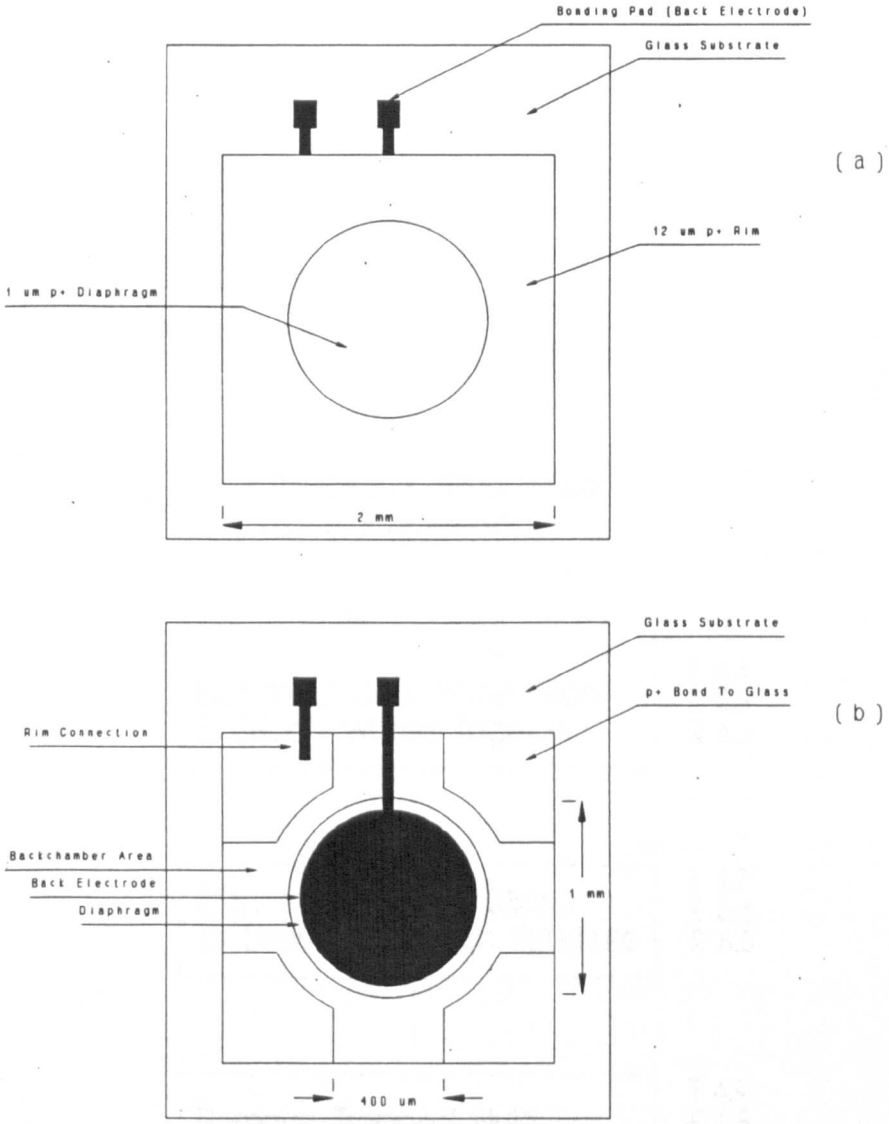

Figure 4.2(b) : Plan view of a circular microphone structure. (a) Top view, (b) Looking through the glass substrate.

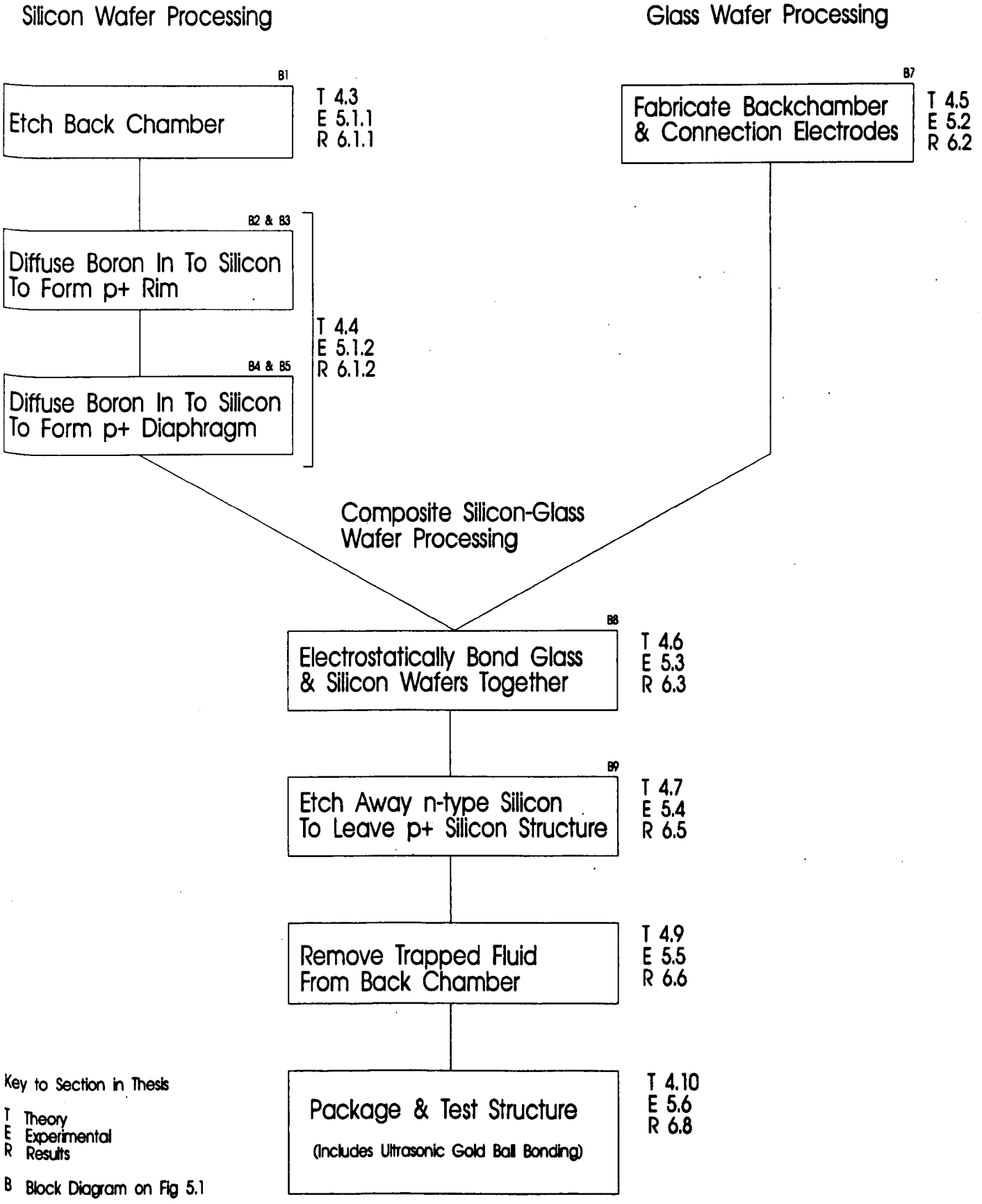

Figure 4.2(c) : Flow diagram of the main stages employed for silicon microphone fabrication. (Note : This figure indicates the key elements that make up the structure of this thesis with respect to microphone fabrication implementation - Fig 5.1 should be consulted for comparison and further reference)

provides the etch resistance, adhesion and film forming properties. Exposure cross links the rubber material and makes it insoluble in the solvent developer.

Positive resist

This resist is composed of three ingredients. A photo active compound, a resin(s) and the carrier or solvent system. The photoactive component gives the resist its developer resistance and special absorption properties. Most unexposed positive resist films are very developer resistant showing attack rates of only 1-2 nm/s. An inhibitor helps to slow the etch rate of the resin. Exposed areas are rendered highly soluble so that the dissolution rate in developer increases to 100-200 nm/sec or 100 times faster than the developer dissolution rate.

Photo resist application

Prior to resist application the wafer surface must be clean and dry to ensure good adhesion. This can be achieved by removing particulate matter with nitrogen gas and then heating the wafers at 250°C for 30 mins. and allowing to cool. The wafer is transferred to a vacuum chuck and photo resist is applied in liquid form onto the centre of the wafer. The vacuum chuck is spun at high speed, were the spin duration, viscosity of the resist and rotational speed help to determine the film thickness. From manufacturer's data, the thickness is quoted as being inversely proportional to the square root of the spin speed. Speeds of 1000 to 5000 rpm can yield 0.5 μm - 2.5μm thicknesses.

Pre baking

Pre baking is carried out to expel retained solvents and to ensure reproducible exposure times. It improves the adhesion of the coating so that the photo resist can withstand the

development step. It also hardens the film to resist damage from routine handling and developing. The soft bake time and temperature are very important and have a direct impact on the exposure parameters. Negative resists that are not completely softbaked will not completely cross-link when exposed, the developer will attack and cause scumming areas. Unexposed areas are washed away by the developer.

Positive optical resists which left only partially softbaked will not be completely reacted (sensitized) when exposed, and will appear more photosensitive because the developer will aggressively dissolve away any positive resist film that retains a relatively high solvent content. The unexposed areas will also be attacked by the developer at a much higher rate than if the coating were properly baked. The softbake has more direct affect on resist sensitivity than the hard bake time. Soft bake temperatures above 100°C will begin to degrade the sensitivity noticeably. Times for the soft bake range from 10 to 30 min in an oven or on a hot plate at 80-90 °C in air or nitrogen atmosphere depending on the manufacturers specifications and the application.

Exposure

Exposure leads to polymerisation of the polymer molecules which gives greater chemical resistance to the developer and adhesion of the photoresist. Poor exposure results in poorly adherent images that are damaged or lost during development. Lamp deterioration in the ultraviolet region can lead to poor exposures. This was found in practice and a recalibration process was carried out when a new lamp was fitted. Pattern transfer is carried out by placing a photo mask over the wafer prior to exposure. Alignment marks are introduced on each mask and transferred to the wafer for subsequent mask registration purposes. A mask

aligner is used to carry out registration and exposure.

Hard baking

This process is used to harden photoresist and improve adhesion to the substrate. A typical process involves baking the wafer in an oven for 20-30 mins at 120-180 °C.

Development

Development is specific to the resists used and depends on the application. For the resists used in this work the negative resist required five solutions for development and the positive resist required one solution. Development was carried out at room temperature with continuous agitation of wafers. (See appendix A2.1 for details) The positive resist developer consists of 3% wt. tetramethyl ammonium hydroxide and water.

Photo resist removal

Photo resist removal can use liquid resist strippers which cause resist to swell and lose adhesion to the substrate, or by resist ashing which requires dry processing in an oxygen plasma.

4.3 Oxidation theory

For this project silicon dioxide was used as the primary masking material for high temperature diffusion work and in the process of back chamber fabrication. Controlling oxide growth rates and setting oxide fabrication parameters requires study of oxidation theory.

Thermal oxidation is usually carried out between 900 - 1200 °C and occurs when oxygen or

water vapour arrives at a silicon surface and combines with the silicon to form silicon dioxide SiO_2 according to the following equations:-

$Si + O_2 ---> SiO_2$ Dry oxidation reaction

$Si + 2H_2O ---> SiO_2 + 2H_2$ Wet oxidation reaction

The high temperatures are necessary to allow the water vapour or oxygen to diffuse more readily through the growing oxide in order to reach the silicon surface for the oxidation reaction to take place. The growth rate will decreases with time, since increasing oxide thickness will limit this process. As the oxide grows, it consumes silicon in addition to expanding above the original surface, where 46% of the total oxide thickness represents consumed silicon.

A simple model for oxidation, based on Fick's first law of diffusion, assumes that oxygen diffuses through the existing oxide layer and does not accumulate in the oxide. Since the derivation is quite common [45], the result will be given and discussed.

$$X_o(t)=0.5A[[1+\frac{4B}{A^2}(t+\tau)]^{0.5}-1] \qquad (4.1)$$

where $A=2D/k_s$, $B=2DN_o/M$, and $\tau = X_i^2/B + X_i/(B/A)$.

D is the diffusion coefficient, k_s is the rate constant for the reaction at the $Si-SiO_2$ interface, N_o is the concentration of the oxidising species in the oxide, M is the number of molecules of the oxidising species, X_i is the initial thickness of oxide on the wafer and t is the oxidation time. For short times with $(t + \tau) << A^2/4B$, the oxide thickness is given by

$$X_o(t)=(\frac{B}{A})(t+\tau) \qquad (4.2)$$

where it can be seen that oxide growth is proportional to time and the rate is limited by reaction at the silicon interface. The linear growth rate constant is given by the ratio B/A.

For long times with $(t + \tau) >> A^2/4B$ and $t >> \tau$, the oxide thickness is given by

$$X_o(t)=\sqrt{(Bt)} \qquad (4.3)$$

where the oxide growth is proportional to the square root of time and rate is diffusion limited. The parabolic rate constant is given by B. This latter relationship is of interest in this work, since it can be used to predict oxides thicknesses of 1μm or more which are suitable for diffusion masking and backchamber formation. Factors which affect oxidation rate include temperature, pressure, crystal orientation and impurity doping.

The linear and parabolic rate constants are both temperature and wafer orientation dependent and can be described by an Arrhenius relationship of the following form

$$D(T)=D_o\exp^{(-\frac{E_A}{kT})} \qquad (4.4)$$

where Do is a pre-exponential coefficient, D(T) is the appropriate temperature dependent rate constant and E_A is the activation energy for wet or dry oxidation. Considering the parabolic rate constant B, and substituting data from the publication by Deal [43] for (100) silicon (Do=386 μm^2/hr and E_A=0.71 eV) in to eqn. 4.4, enables calculation of the change in B as a function of temperature for wet oxidation at 1 atm. It can be seen from fig. 4.3 that as temperature increases, so does B, and hence from eqn. 4.3 the oxide thickness is greater for a given oxidation time. The increase in oxide thickness, derived from eqn. 4.3, is shown in

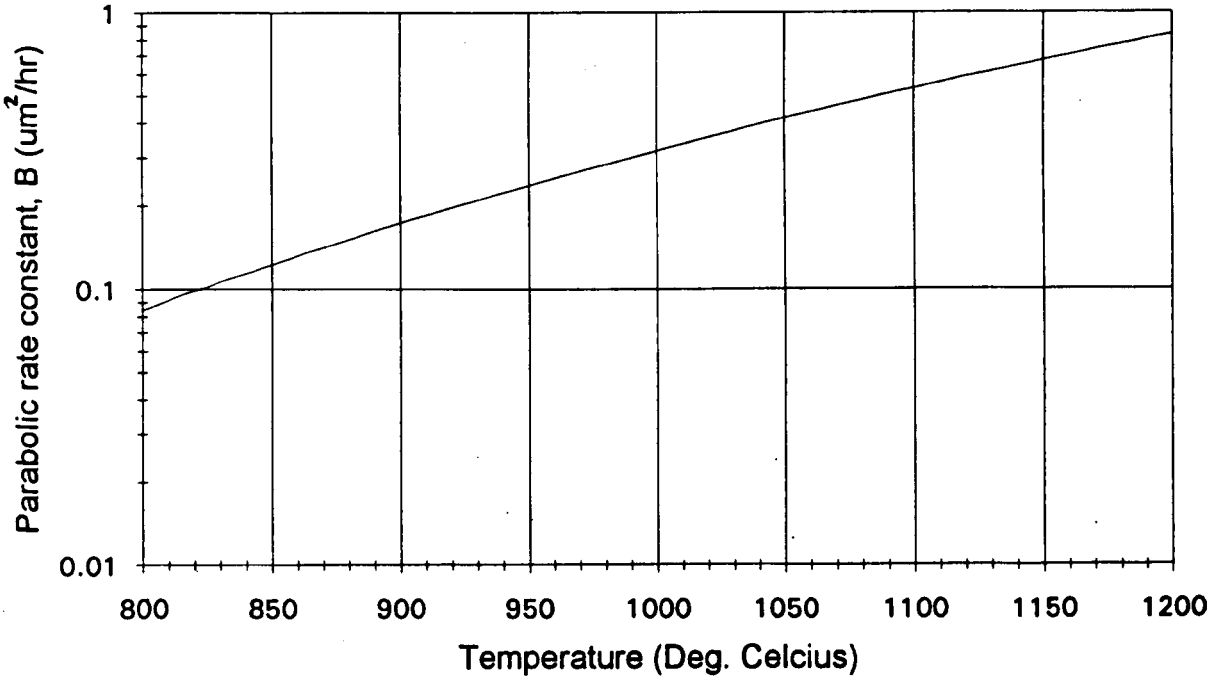

Figure 4.3 : Change in the parabolic rate constant B as a function of wet oxidation temperature. (Calculated from eqn. 4.4 for E_A = 0.71 eV , D_o=386 um^2/hr)

fig. 4.4 for different temperatures. The parabolic rate constant for dry O_2 as a function of temperature has a much lower value, because oxygen is less soluble in silicon dioxide than water. The oxide thickness resulting from the lower rate constant is shown in fig. 4.5 for comparison purposes.

Oxidation growth rate can be enhanced by high pressure since the square root of the parabolic rate constant is proportional to the partial pressure of the oxidising species. This implies that high pressure oxidation can be used for growing thicker oxides for a given temperature and time. Alternatively, a low temperature, high pressure oxidation can be used to achieve similar process times to an atmospheric high temperature oxidation. This can be useful for preventing significant dopant redistribution for oxide growths subsequent to diffusion. It is also possible to carry out low pressure oxidations to grow thin highly controlled oxides for VLSI purposes.

Oxide quality is influenced firstly by growth rate, where a slow growth rate results in a more dense high quality oxide and secondly, by orientation which influences the number of silicon bonds available at the silicon surface available for oxidation and hence the quality of the Si-SiO_2 interface.

The parabolic rate constant is independent of crystal orientation since it is a measure of the diffusion process of the oxidising species through a random network of amorphous silica, however the linear rate constant is highly orientation dependent because it depends on the surface density of silicon atoms.

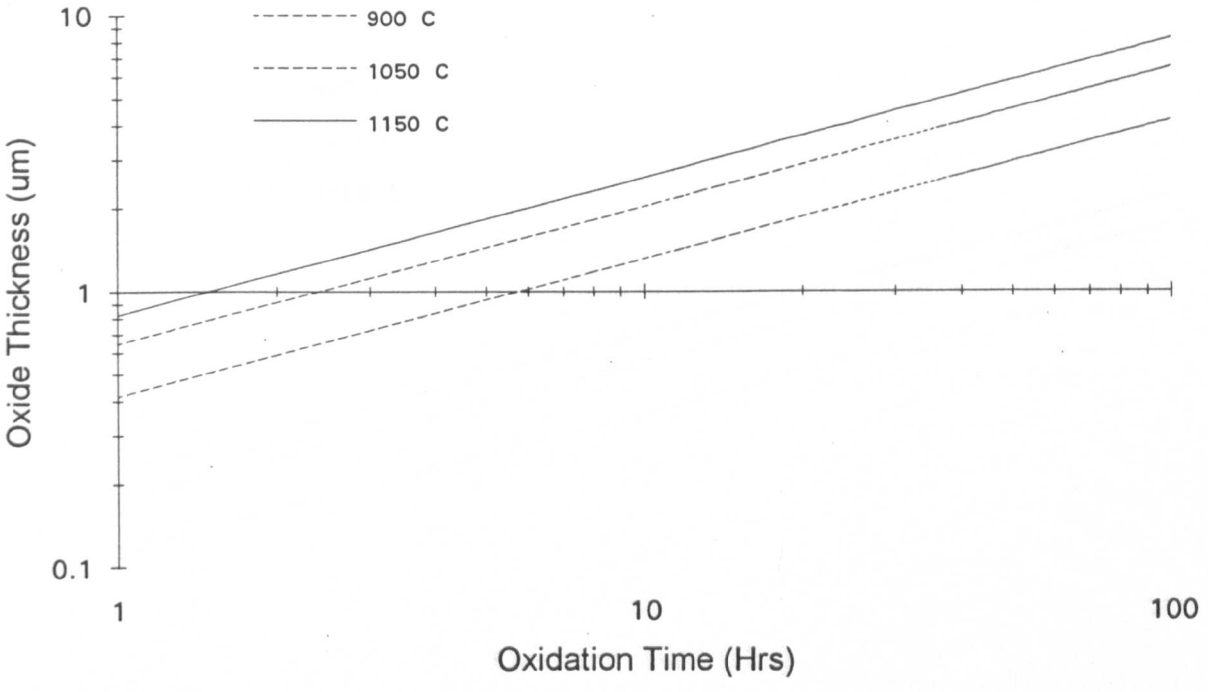

Figure 4.4 : Calculated wet oxide thickness (eqn. 4.3) as a function of oxidation time and growth temperature.

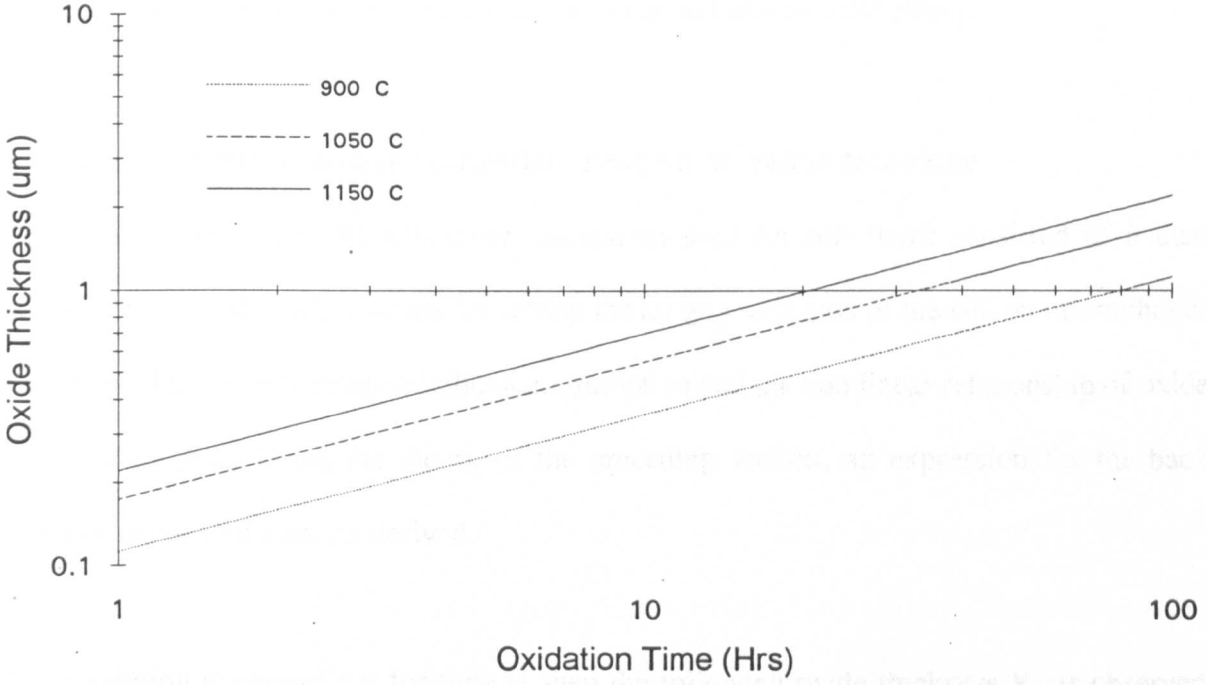

Figure 4.5 : Calculated dry oxide thickness as a function of oxidation time and growth temperature.

The linear and parabolic rate constants are sensitive to impurities either in the oxidising gas or the silicon substrate. Chlorine can be introduced into the oxidation ambient which improves oxide quality and the Si-SiO_2 interface, it also increases the linear rate constant slightly and causes a linear increase of the parabolic rate constant with concentration. Heavy doping of silicon also alters the oxidation characteristics. For example, boron will segregate into the growing oxide reducing the concentration at the surface of the silicon. The boron in the oxide will weaken the silicon dioxide bond structure, enhancing the diffusion of the oxidising species through the oxide and thus increasing the oxidation rate, which gives a larger parabolic rate constant. The linear rate constant shows little effect.

4.4 Theory for backchamber fabrication using an oxidation technique

The finalised method of backchamber fabrication used for this work consisted of a dual oxidation process that was devised for setting the air gap thickness of the silicon microphone. It consists of taking advantage of silicon consumption and the non linear relationship of oxide growth with time. Using the theory of the preceding section, an expression for the back chamber depth will now be derived.

If an oxidation is carried out for time t1 then the following oxide thickness X_{t1} is observed

$$X_{t1}=\sqrt{Bt1} \tag{4.5}$$

The oxide is patterned with a window such that the oxide in the window is all etched away, a new oxide is then grown for time t2 to give an oxide thickness X_{t2} in the window area.

$$X_{t2}=\sqrt{Bt2} \tag{4.6}$$

The oxide thickness surrounding the window is now $X_{(t1+t2)}$ which implies

$$X_{t1+t2}=\sqrt{B(t1+t2)} \tag{4.7}$$

From the original paper by Deal [45], 46 % of the oxide thickness consists of silicon consumption, so it follows that if all the oxide is removed after the second oxidation, the window area will represent a larger consumed depth X_{cd} of silicon than the surrounding area.

$$X_{cd}=0.46*((X_{t1}+X_{t2})-X_{(t1+t2)}) \tag{4.8}$$

Substituting equations 4.5 to 4.7 into 4.8 gives

$$X_{cd}=0.46\sqrt{B}((\sqrt{t1}+\sqrt{t2})-\sqrt{t1+t2}) \tag{4.9}$$

Setting t1=t2 to give the optimum X_{cd} simplifies eqn 4.9 to

$$X(t)_{cd}=0.47\sqrt{B}(2\sqrt{t}-\sqrt{2t}) \tag{4.10}$$

The parabolic rate constant is temperature dependent and can be calculated from eqn. 4.4. It should be noted that the total oxidation time to achieve a given backchamber depth X_{cd} is 2t and requires two separate oxidations of time t. A graph of backchamber depth versus oxidation time in hours for different temperatures is shown in fig. 4.6. From this graph a 1 μm deep back chamber could be fabricated using two 11 Hr. wet oxidations carried out at 1150 °C.

4.5 p^+ Diffusion theory for short and long diffusion time

The theory of diffusion of boron into silicon for short and long diffusion times will be discussed in this section since the process was required to form p^+ etch stop microphone profiles in n-type silicon.

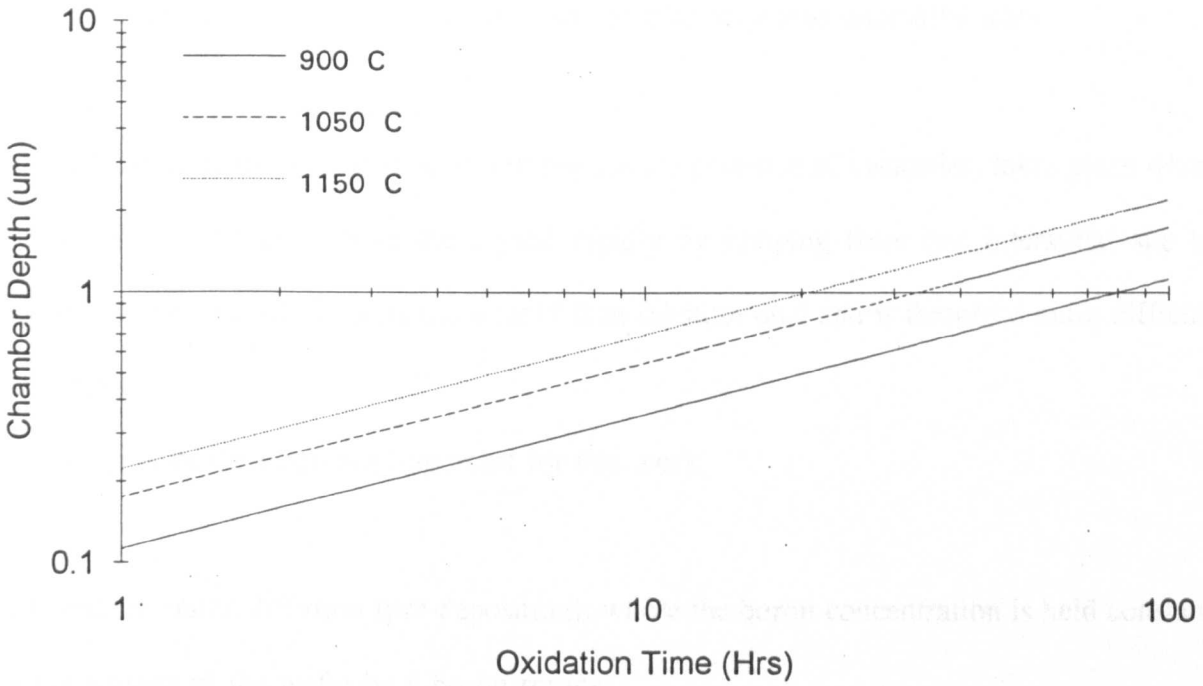

Figure 4.6 : Calculated microphone backchamber depth (See eqn. 4.10) as a function of oxidation time for three different growth temperatures.

The diffusion process is carried out at temperatures ranging from 900°C to 1200°C where the impurity, in this case boron, is introduced into a silicon surface through windows in a suitable mask. For this work, the mask used was silicon dioxide which has been discussed in detail in the last section. The following two mechanisms influence the diffusion process:-

i) **Substitutional diffusion** takes place when the boron atom substitutes for a silicon atom in the lattice and can move from one site to another. This process is dependent on the presence of vacancies in the lattice which statistically occur naturally and are also generated by high temperature, were silicon atoms can be displaced into interstitial sites.

ii) **Interstitial diffusion**, which does not require the presence of vacancies, takes place when boron atoms diffuse through the crystal rapidly by jumping from one interstitial site to another. Interstitial diffusion is more rapid than substitutional and is therefore more difficult to control.

Two types of diffusion are important for this work,

i) Constant source diffusion (pre-deposition), where the boron concentration is held constant at the surface of the wafer by a boron source.

ii) Limited source diffusion (drive-in), for when the boron source is removed and no additional dopant is supplied to the silicon.

A model can be derived for each of these cases for a one dimensional diffusion process. According to Fick's first law of diffusion the boron particle flux per unit area J is

proportional to the rate of change of boron concentration N with distance, or concentration gradient of the boron particles, and is given by

$$J=-D\frac{\delta N}{\delta x} \tag{4.11}$$

where D is the diffusion coefficient. The boron flux continuity equation states,

$$\frac{\delta N}{\delta t}=-\frac{\delta J}{\delta x}=\frac{\delta}{\delta x}[D\frac{\delta N}{\delta x}] \tag{4.12}$$

that the rate of increase of boron concentration with time equals the boron flux gradient. Assuming D to be independent of position and doping concentration, for low concentrations of boron dopant atoms, Fick's second law of diffusion is obtained by combining eqns. 4.11 and 4.12

$$\frac{\delta N}{\delta t}=D\frac{\delta^2 N}{\delta x^2} \tag{4.13}$$

The boundary conditions for solution of this partial differential equation depend on whether the diffusion is source limited or unlimited.

For a **constant source diffusion** the boundary condition is that the boron concentration is held constant at the surface of the wafer, which yields the solution:

$$N(x,t)=N_o erfc(\frac{x}{2\sqrt{Dt}}) \tag{4.14}$$

for which N_o is the impurity concentration at the wafer surface where x=0. The complementary error function describes the diffusion front concentration N(x,t) proceeding into the wafer as a function of distance from the surface x and time t, with N_o remaining constant.

From equation 4.14 the boron dose Q can be calculated which represents the total number of boron atoms per unit area delivered into the silicon for a given t. Obviously the dose will increase with time assuming the boron source delivers a continuous flow of boron atoms to the wafer surface. By summing the diffused boron concentration throughout the silicon the dose is:

$$Q=\int_0^{\infty} N(x,t)dx=2N_0\sqrt{\frac{Dt}{\pi}} \qquad (4.15)$$

The initial boundary condition for the **limited source diffusion** uses an impulse function at the silicon surface which has a magnitude equal to the dose Q. A Gaussian distribution for N(x,t) is evident in the following solution:

$$N(x,t)=\left(\frac{Q}{\sqrt{\pi Dt}}\right)\exp^{-\left(\frac{x}{2\sqrt{Dt}}\right)^2} \qquad (4.16)$$

The concentration of boron at the silicon surface decreases with time as the diffusion front with concentration N(x,t) moves into the silicon, because Q remains constant. Conditions for the profile determination can be found from the Dt product and are summarised as follows:-

Dt drive-in $>>$ Dt predeposition $=>$ Gaussian distribution.

Dt drive-in $<<$ Dt predeposition $=>$ Erfc distribution.

Like the oxidation diffusion coefficient the diffusion coefficient is exponentially related to temperature and follows the Arrhenius relationship of eqn. 4.4 in section 4.2. A plot of D for boron against temperature is shown in fig. 4.7 for Do=10.5 cm^2/sec and E_A= 3.69eV. (Do is the diffusion coefficient cm^2/s extrapolated to infinite temperature) The complementary

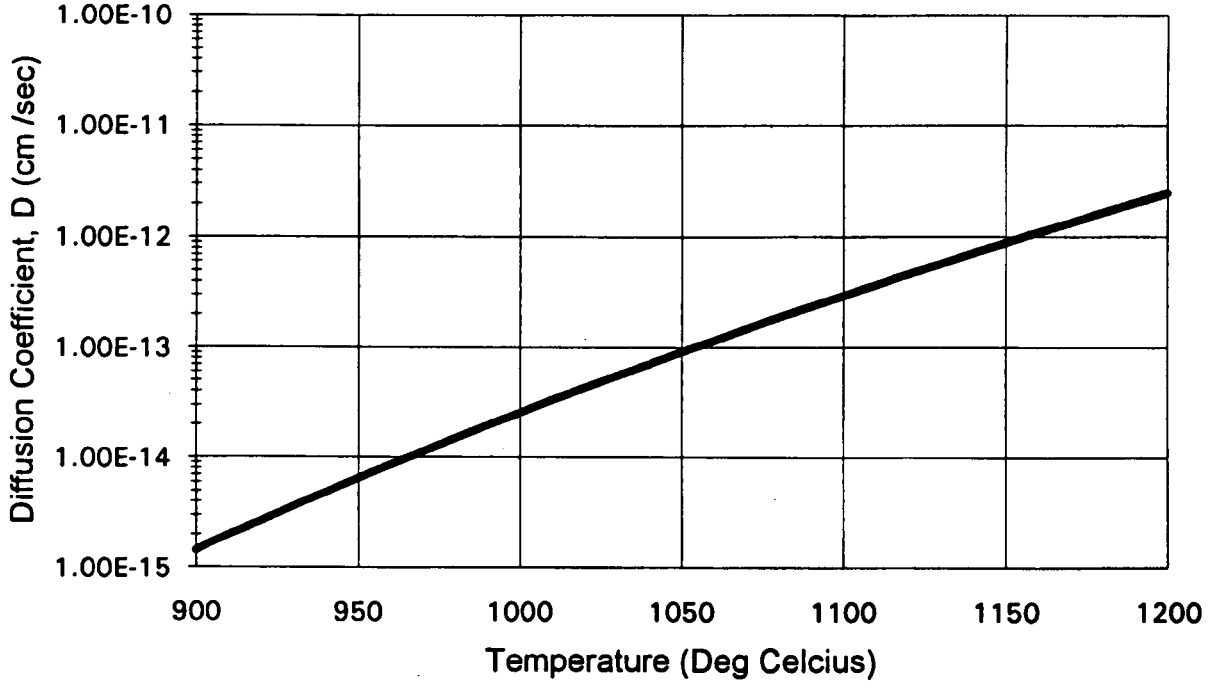

Figure 4.7 : Boron diffusion coefficient as a function of furnace temperature calculated from the Arrhenius relationship (Sect. 4.2, eqn. 4.4).

error and Gaussian functions are shown in fig. 4.8 for eqns 4.14 and 4.16 for comparison purposes and because they were used for numerical evaluation of the models in section 4.11.

Since the silicon processing for the microphone structure involves many thermal stages, it is important to know the final boron distribution after the processing is complete. This can be determined by summation of the Dt products for the high temperature cycles that may affect the final profile. The resulting Dt product is then used in conjunction with the relevant boron distribution eqns. 4.14 and 4.16 to determine the final profile.

To obtain high silicon surface concentrations of boron, which is important for obtaining a good etch stop (see section 4.6), the solid solubility limit of boron must be considered. This limit increases with increasing temperature, which means that high surface concentrations can be achieved for high predeposition temperatures. For example, the solid solubility limit of boron in silicon at 1100 °C is about 3.3×10^{20} atoms/cm^3.

Determination of junction depth is important for estimating where the etch stop will begin to take effect, in addition to predicting the rim and diaphragm thickness, for given diffusion conditions. Consider boron being diffused into a starting wafer which consists of uniformly doped n-type material with a background concentration N_B. Where the boron profile intersects N_B the net impurity concentration is zero, this point represents the metallurgical junction depth x_j. If N(x) is made equal to N_B at $x=x_j$ for the constant source and limited source equations in eqn. 4.14 and 4.16, the following two expressions for x_j are obtained:

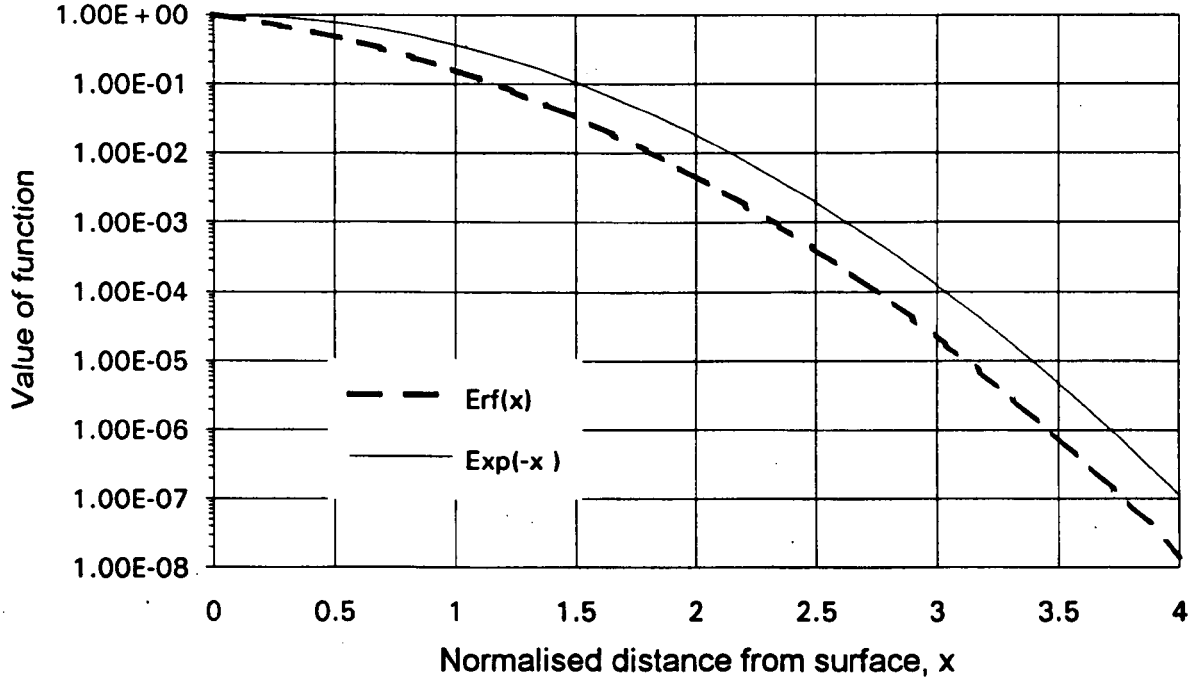

Figure 4.8 : The calculated Gaussian and Complementary error function profiles used for diffusion model calculations.

For the complementary error function:

$$x_j=2\sqrt{Dt}erfc^{-1}(\frac{N_B}{N_o}) \tag{4.17}$$

For the Gaussian distribution:

$$x_j=2\sqrt{Dtln(\frac{N_o}{N_B})} \tag{4.18}$$

The diffusion coefficient will become concentration dependent when the boron concentration exceeds the silicon's intrinsic carrier concentration n_i [44], which means that the discussed theory will not adequately describe the doping behaviour. The diffusion equation has to be solved for linear, parabolic and cubic dependencies of the diffusion coefficient on concentration [95] in order to predict the correct profile which is more abrupt than for the constant diffusion coefficient. Boron diffusion is best modelled by a first order dependence[45] of the diffusion coefficient, which can be derived from eqn. 4.12.

4.6 Evaporation and sputtering of thin metal films on glass

Evaporation and sputtering, which are forms of physical vapour deposition (PVD), were investigated and used for thin film deposition on a patterned glass substrate for this work. This section will outline the PVD techniques used and some supporting theory.

A vacuum is required for PVD which is obtained by pumping a vacuum chamber from atmosphere to a pressure of about 13.3 Pa with a roughing rotary pump. This is followed by further evacuation to 6.7×10^{-3} Pa using a diffusion pump backed by the rotary pump.[46] To minimise outgassing, and reduce the pump down period, the system and substrate should

be very clean and free from contaminants. For sputter coating a pressure of about 1 Pa of argon gas is required in the chamber. This can be achieved by introducing a small quantity of argon into the chamber through a needle valve.

Pressure and temperature changes cause variation in the film deposition parameter called the mean free path λ, which is the average distance the molecule travels before it collides with another molecule.

$$\lambda = \frac{kT}{\sqrt{2}\pi P d^2} \tag{4.19}$$

in which d is the diameter of a gas molecule (0.2-0.5 nm). For a background pressure P of 1 x 10^{-4} Pa, a 0.4 nm air molecule has a λ of 60 m which means that, for example, evaporated gold atoms would not interact with the background air molecules and should travel in a straight lines from source to target. For sputtering, using argon gas at a pressure of 100Pa, λ is only 60 μm which means that the evaporant is scattered with the argon atoms and arrives from random directions at the target.

Film thickness is monitored using a piezoelectric quartz crystal in oscillation. The resonant frequency of the crystal is changed by added weight as a thin film is deposited on its surface. This change in mass can be determined electrically by measurement of the frequency shift. A detailed acoustic analysis is given by Sauerbrey for a loaded crystal which is treated as a one dimensional composite resonator of quartz and film material [47]. The result is given by

$$T_f = \left(\frac{D_q}{D_f}\right).\left(\frac{N_q T Z_f}{(3.14 Z_q)}.\tan^{-1}\left(\frac{Z_q}{Z_f}.\tan\left(3.14\left(1-\frac{T_q}{T}\right)\right)\right)\right) \tag{4.20}$$

the following expression for film thickness T_f,

T = Period of loaded crystal

T_q = Period of unloaded crystal

Z_f = Acoustic impedance of the film material

Z_q = Acoustic impedance of quartz

This expression is valid for heavily loaded crystals and was used for film thickness calculation in this work.

For evaporation, the metal source to be deposited is heated in a vacuum to the point of vaporisation and then evaporates to form a thin film that will cover a substrate, or glass wafer, placed in front of the source. Two types of evaporation were employed using this technique :

i) Filament Evaporation

The source, in the form of a short length of wire, is placed in a tungsten filament. The filament temperature can then be increased electrically until the metal evaporates. This method can result in high impurities in the surface film from the filament. It is also difficult to control for evaporation of composite materials because the lowest melting point material evaporates first resulting in a film that does not have the same composition as the source material.

ii) Electron Beam Evaporation

A high intensity beam (up to 15kV) is focused on the source target which can consist of a water cooled crucible filled with the metal to be evaporated. The beam causes material to

evaporate from the centre of the crucible which can reduce the chance of impurity evaporation. X-rays are generated for voltages >5-10 keV and substrates can suffer radiation damage from the x-rays and electrons. Evaporation from a small area onto a plane receiver, which is analogous to the equipment used, will now be considered. The growth rate G of a deposit at points corresponding to the area dS_2 for a surface source is given by [48]

$$G=\frac{m}{\pi\rho}\frac{\cos\phi.\cos\theta}{r^2} \tag{4.21}$$

where, for the material being deposited, m is the mass evaporation rate (g/sec), ρ is the density. The angle ϕ is measured from the normal to the plane of the source and θ is the angle of the substrate relative to the particle stream. (See fig. 4.9a)

Let the total mass M_t equal the product of m with time and the total thickness t be the product of G and time. From eqn. 4.21 and fig. 4.9(b) the thickness of the deposit from R is

$$t=\frac{m_t}{\pi\rho}\frac{\cos^2\theta}{r^2}=\frac{m_t h^2}{\pi\rho r^4}=\frac{m_t h^2}{\pi\rho(h^2+\delta^2)^2} \tag{4.22}$$

The thickness of the deposit just below the source, at O is

$$t_o=\frac{m_t}{\pi\rho h^2} \tag{4.23}$$

so combining 4.22 and 4.23 gives a variation in thickness of

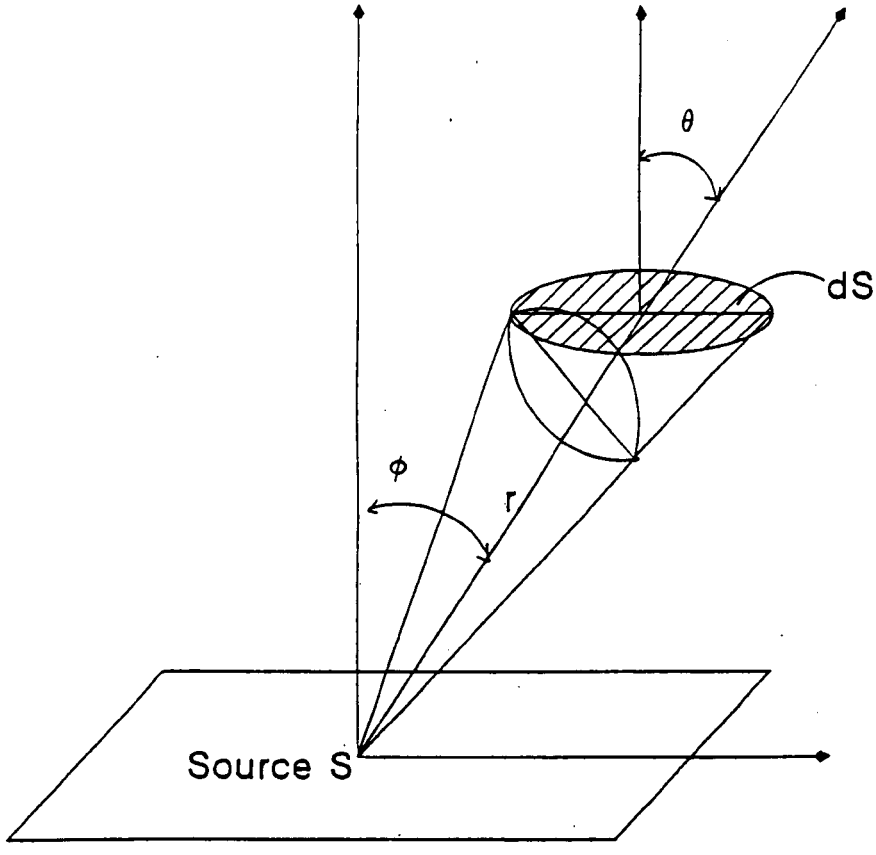

Figure 4.9(a) : Theoretical geometrical layout for evaporation from a point source onto a parallel plane surface with area dS.

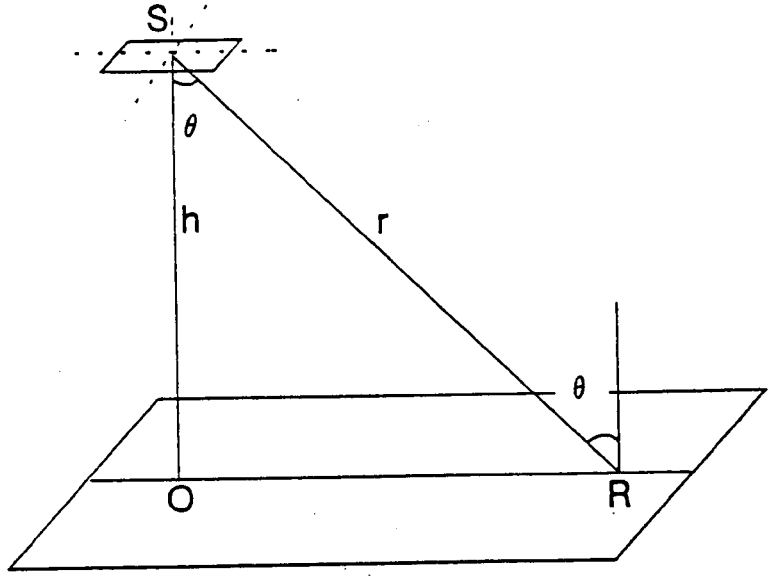

Figure 4.9(b) : Evaporation from an area S onto a parallel plane surface.

$$\frac{t}{t_o} = \frac{s^4}{(h^2+\delta^2)^2} = \frac{1}{(1+(\frac{\delta}{h})^2)^2} \qquad (4.24)$$

A graph of t/to against δ/h for this equation is shown in fig. 4.10. This figure shows that the film is not uniform across the substrate for the evaporation arrangement used. A similar derivation and result can be obtained for a circular target, which was used for sputtering, by considering the target as a ring of point sources.[49]

Magnetron sputtering involves the bombardment of a target to be evaporated with energetic ions (usually Ar^+), causing atoms to be ejected and deposited onto a substrate placed in front of the target. Both DC and RF discharges can be used to create a plasma from which useful ions are extracted and accelerated to a target which is vacuum compatible. Deposition rate depends on the source to substrate distance and can be as high as 1μm/min for aluminium and its alloys.

A disadvantage of circular magnetron sputtering is that deposition rate is not uniform across the region where the substrates are placed. This can be overcome by mechanical motion of the substrate table so that the substrate is exposed to the average evaporated particle flux. The following two types of sputtering were used :

i)RF Sputtering

Radio frequency (5-30 MHz) is used to supply energy to argon atoms.

ii)DC Sputtering

The target acts as cathode in diode system using DC power source.

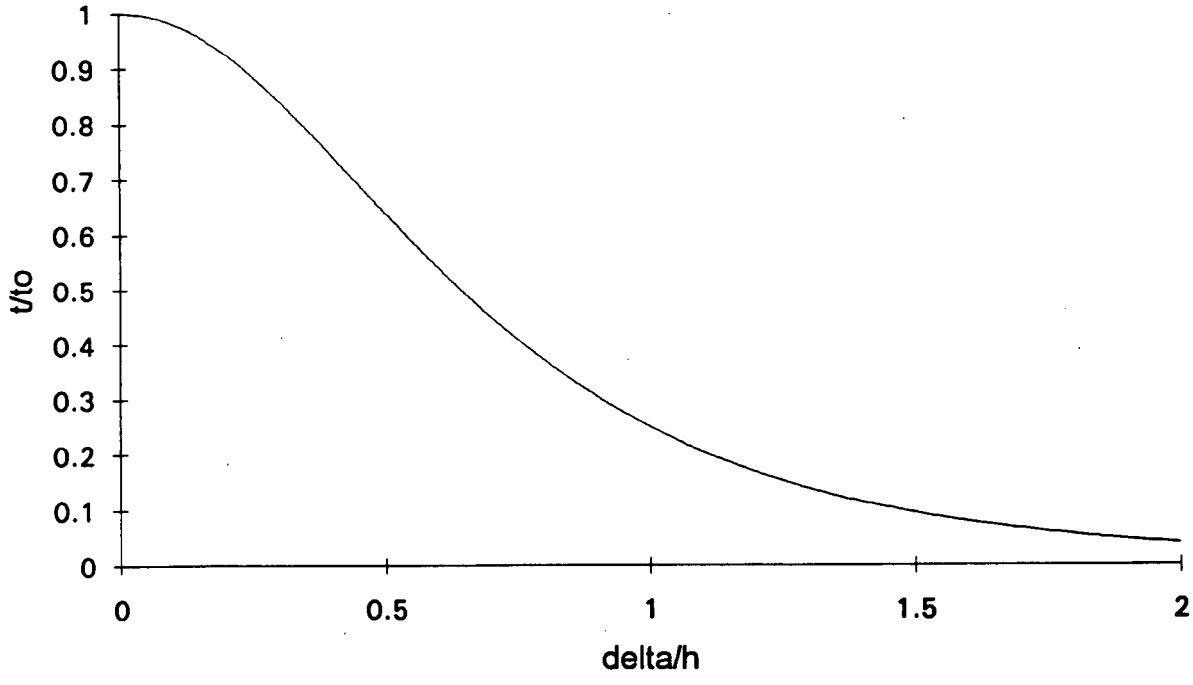

Figure 4.10 : Theoretical distribution of a deposit on a plane surface for evaporation from a small directed surface source. (Calculated from eqn. 4.24)

Work on the sputter mechanism has been carried out by Wehner and Fetz [50,51]which explains the energy exchange mechanism between bombarding ions and cathode atoms. The number of atoms N per unit area per second leaving the target is given by

$$N=\frac{J_+}{gq}S(E,M1,M2) \qquad (4.25)$$

where J_+ is the current density of the bombarding ions, q the electronic charge, g the number of charges per ion and S the sputter yield in atoms per incident ion which is a function of the ion energy E, the mass of the ion species M1 and the mass of the target material M2. The sputter yield characteristic fig. 4.11 as a function of ion energy is important for practical purposes for setting up the sputter process for a given target. The yield increases rapidly from the threshold energy and the threshold energy decreases with increasing atomic number of the evaporant. Above a few hundred volts, there is a change over region where the sputter yield increases more slowly, the value of changeover depends on the ion species and target used. In the tens of kilovolts region, the yield can be in the range of 0.1 to 20 atoms per ion and beyond this, the sputter yield reaches a maximum and then gradually decreases as incident ions are implanted in the target. For practical sputtering, in order to minimise the energy required to eject a target atom, an ion energy suitable for a sputter yield of one atom per ion such as 1000 V is used. (Control range usually between 0.5 and 3 kV)

Thin film properties [52], which have to be considered in this work for metallisation, can be very different from bulk samples of the same material. From electron microscopy research, film growth by condensation from a vapour source has been observed in the range of the first hundred to few thousand angstroms of apparent thickness and is dependent on the evaporant, the substrate and temperature. The initial growth proceeds in the following stages:

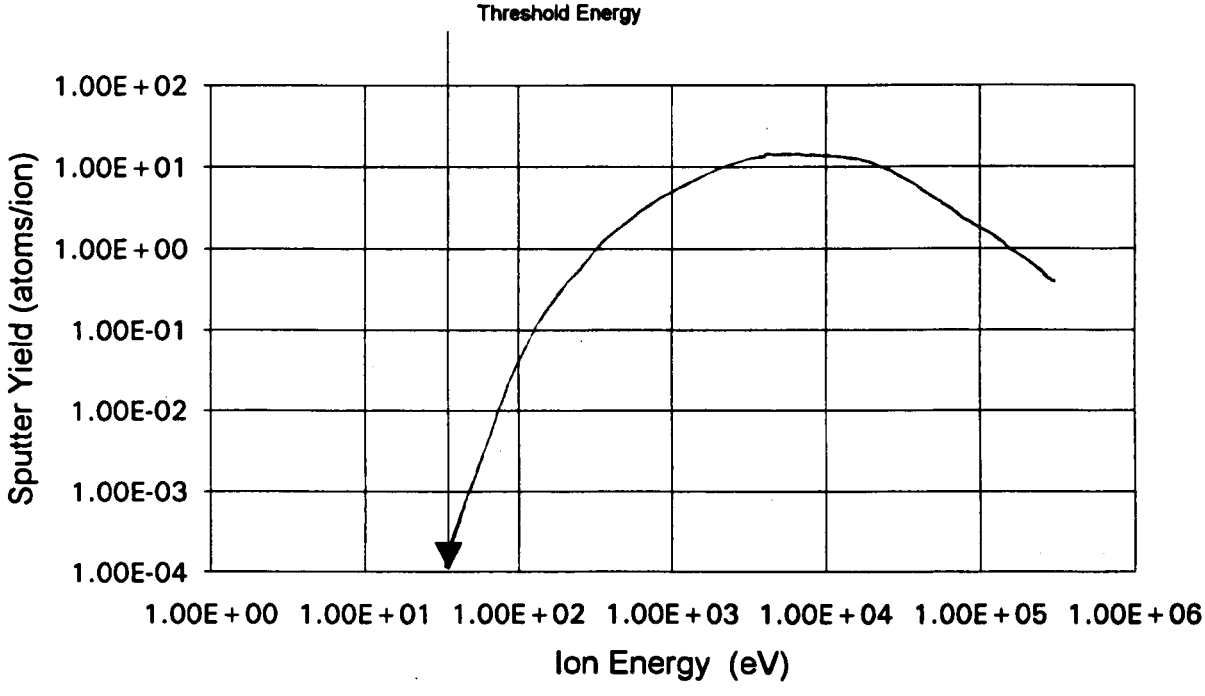

Figure 4.11 : Indication of a typical sputter yield as a function of ion energy for RF magnetron sputtering.

i) Nucleation occurs, where small nuclei (Order of 0.5 nm) appear and are statistically distributed over the substrate surface.

ii) The nuclei grow into larger three dimensional islands.

iii) The islands coalesce and the interconnected islands form a network containing empty channels.

iv) The channels are filled.

The first three stages will give a film with differences in physical properties such as electrical conductivity and film density in comparison to bulk samples of the same material. Beyond the last stage and depending on the conditions of growth the film can become amorphous, randomly or uniaxially (direction of growth) oriented polycrystalline, amorphous or identically oriented. (epitaxial)

4.7 Principles of electrostatic bonding

Electrostatic bonding was used to form a strong chemical bond between a silicon wafer containing fabricated p^+ devices and a borosilicate glass (A form of pyrex glass) wafer with fabricated back electrodes. The technique requires the application of a large voltage between 250-1500 V in the respective temperature range of 600 - 200 °C to be applied between the two materials placed in intimate contact. The glass used must become slightly conductive at the temperatures involved for the bonding to be effective. It is also very important that both surfaces are free from dust or contamination and have a surface roughness that is smaller than $1\mu m$ +/- $0.1\mu m$, due to the limited deformation sustainable by the two bonding materials. In order to prevent the materials from cracking during cooling and to limit undesirable stresses at the bonding interface the materials should have closely matched thermal expansion coefficients.

The proposed mechanism for electrostatic bonding [53] is that positive sodium ions in the glass become more mobile at elevated temperatures. Under the influence of a given applied potential they migrate towards the cathode where neutralisation can occur. A space charge layer is developed in the glass adjacent to the silicon surface due to net negative ions. A parallel plate capacitor is then established between the two surfaces to be bonded with most of the applied potential dropped across the sub micron air gap. A large electrostatic field is established which exerts a force sufficient to attract the silicon and glass into intimate contact for establishing a hermetic seal. The applied potential is then across the space charge layer in the glass which results in a strong field that is capable of transporting oxygen from the glass to the silicon surface in order to form a SiO_2 chemical bond interlayer. The growth of this SiO_2 on the silicon surface into the glass network has to be at least 20 nm thick to form a good glass-silicon bond with a bond strength above the fracture stress of silicon.

Parameters for the bonding process vary widely depending on the materials used, the apparatus and the application. The main parameters include applied voltage, resulting current density, temperature, bonding time and bonding atmosphere [53]. The voltage required for bonding will depend on temperature, glass type and thickness. For example, a 0.5 - 5 mm thick piece of glass at 300°C will require a bonding voltage of at least 1000V. The bonding time will depend on the applied voltage, temperature and the area to be bonded and for the example given will take about 20 mins for an area of 1 cm^2. The response curve of fig. 4.12 shows an exponentially related decay of current with time which, for the example given, initially peaks at about 0.25 mA/cm^2 and decays to about 0.02 mA/cm^2 after 5 minutes. (The experimental values of fig. 4.12 were obtained from laboratory work and are shown for comparison purposes) Lower bonding temperatures give rise to lower mobility of ions in the

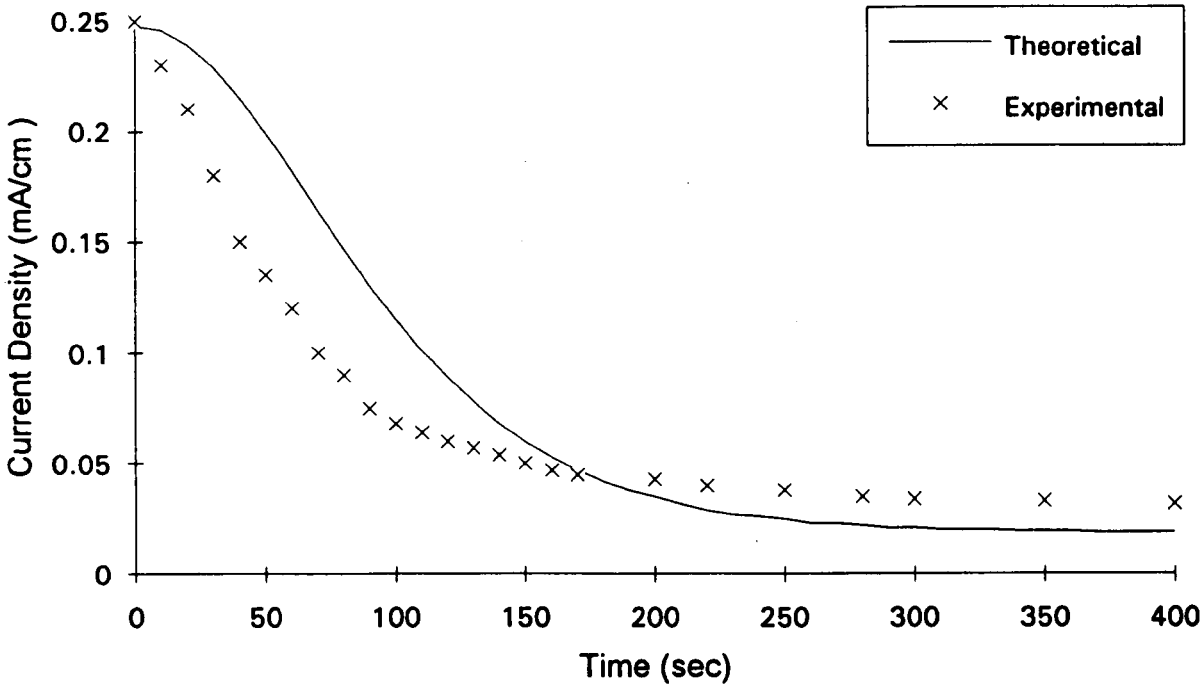

Figure 4.12 : Typical current response for a 1 cm^2 silicon to borosilicate glass electrostatic bond, with an anode voltage of 1000 V and a bonding temperature of 300 °C.

glass and hence longer bonding times.

Ambient conditions that have been used to give successful bonds include air, nitrogen, argon and helium. The ambient air atmosphere is the most convenient and may even assist the bonding process due to the presence of free oxygen. Additionally, some externally applied pressure on top of the glass-silicon to be bonded can promote better contact between the two bonding surfaces, which in turn may cause the reduction of the maximum applied potential required and improve conditions for a strong chemical bond to occur.

4.8 Anisotropic etch rates and selectivity

Selective etching was used to realise the p^+ microphone structures from their respective doped etch stop profiles in silicon. This section reviews the selective etchants investigated for suitability for this work and details elementary models used for etch rate and selectivity prediction.

Etch rate and surface finish [54] are dependent on temperature, pressure, concentration, additives and byproducts that build up during the etching process. Etch selectivity [55] can be dependent on these factors and the properties of the materials to be selectively etched. Electrochemical etching methods allow selectivity to be controlled to an even greater degree than a simple chemical etch. [56] Unfortunately, electro-chemical methods are not used for this project due to incompatibility with the fabrication procedure.

This section details anisotropic silicon etchants that exhibit strong dependence of etch rate on crystal direction and dopant concentration in addition to temperature, pressure and

solution concentration. The different aqueous alkaline solutions that can be used fall into the two categories of organic and inorganic chemicals. Hydrazine N_2H_4 and water (1962) was the first organic etchant used [57] where pyrocatechol $C_6H_4(OH)_2$ or iso-2-propyl alcohol (IPA) could be added as a moderator. Since hydrazine is extremely dangerous and unstable, ethylenediamine [58] (EDP) $NH_2(CH_2)2NH_2$ was found to be a suitable alternative. Inorganic solutions consist of aqueous solutions containing hydroxides of alkali metals [59] where IPA can be added as a moderator. These include KOH, NaOH, LiOH, CsOH where the first of these is the most commonly used. Ammonium hydroxide NH_4OH, proposed by M. Asano[60] in 1976, can also be used and even more complicated derivatives including quaternary ammonium hydroxide, tetra methyl ammonium hydroxide TMAH ($N(CH_3)_4OH$) and tetraethyl ammoniumhydroxide (TEAH) $(C_2H_5)_4NOH$). The main etchants investigated for this work included EDP, TMAH , KOH and will be discussed further.

EDP

Non aqueous ethylene diamine shows no etching of silicon and a water molar ratio of 1:2 shows maximal etching indicating that water is a necessary component. This rate can be increased by up to a factor of three by the addition of pyrocatechol. Pyrazine can also enhance etch rates. Abu-Zeid et al. [61] has shown that stirring can increase etch rates, indicating that a diffusion process influences dissolution rates. An undesirable phenomenon of EDP is that exposure to oxygen causes 1,4-benzoquinone and other products to be formed which gives a darkening of the solution and an increased etch rate. This can be reduced and even eliminated by continuously purging apparatus with nitrogen, or any inert gas, to prevent solution contact with air[58].

Four recipes for EDP solutions have been developed by Finne and Klein[58], Reisman et al.[62] and Bassous[63] for different requirements.

Type	Qty	S	F	B	T
Water	ml	133	320	320	470
Ethylene Diamine	ll	1.0	1.0	1.0	1.0
Pyrocatechol	g	160	320	160	176
Pyrazine	g	6	6		

The main recipes used are F for its high etch rate and S for its slower etch rate and/or lower temperatures. These two types also show an anisotropy etch rate ratio for (100)/(111) silicon of 19 with pyrazine and 13.5 without. Silicon dioxide residues can appear on the silicon surface if the etchant solution is saturated with silicon and if the water content is too high. For types F and B, 10g of silicon can be etched at 100 °C before residues appear on the silicon surface.

TMAH

This more recent etchant features compatibility with silicon chip manufacture and is used as a positive resist developing solution. This is because it is free from mobile metal ions such as potassium or sodium which cause undesirable breakdown in electrical characteristics of gate oxides and semiconductor junctions respectively. Etch rates of TMAH have been investigated by Tabata[64] and are comparable with those of EDP but much lower than KOH. The etch rate of the (100) and (111) crystal planes increases with temperature and

decreases with concentration from 45 wt.% down to 5 wt.%. The etch ratio between the (100) and (111) planes decreases with increasing temperature and concentration and can vary from 10-35 for the conditions of etching studied by Tabata. For example, at a temperature of 90°C and 5 wt. % concentration the etch rate of the (100) plane is 84 μm/hr and 2.4 μm/hr for the (111) plane with an etch ratio ((100)/(111)) of 35, but for a 45 wt.% at the same temperature, the etch rate of the (100) plane is 24 μm/hr and 1.2 μm/hr for the (111) plane with an etch ratio of 20. Below concentrations of about 15 wt.%, Tabata found that etched (100) planes were covered with pyramidal shaped hillocks bounded by (111) planes, but for concentrations exceeding 22 wt. % , smooth surfaces were obtained. This means that etch rates of less than 60 μm/hr have to be used to obtain a smooth (100) plane for concentrations greater than 22 wt.% and temperatures below 90 °C. (At 22 wt.% the (100) etch rate is 60 μm/hr at 90°C and 32μm/hr at 70°C)

For a thermal silicon dioxide masking layer, the etch rate increased for increasing temperature and reducing concentration. For example, at a temperature of 90°C and 5 wt. % the etch rate is between 15-18 nm/hr and for 45 wt.% at the same temperature the rate is between 9-12 nm/hr. The lower the temperature, the higher the (100) silicon/silicon dioxide etch ratio, the average etch rate of silicon dioxide is about $5.3x10^3$ lower than the (100) silicon plane for pure TMAHW and $34.7x10^3$ for a doped(13.5g/l) 5 wt.% solution at 80 °C. Silicon nitride can be considered a perfect masking material since it shows no measurable etch rate. Generally, selectivity of etching dielectric materials increases with doping of the etchant solution.

It is possible to use aluminium with TMAH, which is very desirable for low cost electrode

fabrication. Passivated aluminium shows resistance to etching by TMAH solutions when the solution is doped with silicon. The silicon doping content required increases nearly linearly with concentration according to Schnakenberg [65], for example, a 10wt.% TMAH solution requires 30 g/l of silicon and a 25 wt.% solution requires 120 g/l at 80 °C. Schnakenberg found that the increased silicon doping of the solution causes the pH value to be reduced, the viscosity to increase and a reduction in the quality of the silicon etch surface finish in the form of increased hillock formation. No significant change was observed for silicon etch rates and ratios though.

KOH

Inorganic potassium hydroxide, water and isopropyl alcohol was first studied by Price [66] in 1973 and he showed a maximal etch rate for this solution with a 30% KOH concentration. He found that the addition of IPA leads to a decrease in etch rate and stirring has no effect. His results indicated etch ratios of 35:1 for (100)/(111) crystal planes. The overall gross reaction for etching of silicon was suggested by Palik et. al. [67] and indicates that added alcohol has no chemical role in the reaction, it does however dissolve in KOH solution in an increasing quantity with reducing KOH concentration and improve the etched surface finish. The reaction also evolves hydrogen gas.

$$Si + 2H_2O + 2OH^- \text{---}> Si(OH)2O_2^{-} + 2H_2$$

Further details regarding the chemical interactions of KOH and the different silicon planes are given by Price [68].

Seidel suggests a best fit equation for the etch rate R, for which high concentrations of KOH greater than 15 %, show a proportionality to the fourth power of the molar water

concentration. ie.

$$R \sim [H_2O]^4[KOH]^{\frac{1}{4}} \tag{4.26}$$

By using the Arrhenius law

$$R = R_o e^{-\frac{E_a}{kT}} \tag{4.27}$$

where E_a is the activation energy and R_o the pre-exponential factor, he incorporates the temperature dependence of the etch rate into the following empirical formula

$$R = k_o[H_2O]^4[KOH]^{\frac{1}{4}} e^{-\frac{E_a}{kT}} \tag{4.28}$$

and has found the curve fitting parameters to be E_a = 0.595 eV and k_o = 2480 μm/h.(mol/litre)$^{-4.25}$ for a (100) surface for KOH concentrations ranging from 10-60 %. This allows etch rates to be calculated for different concentrations and etch temperatures. Seidel also describes an electrochemical model for the reaction mechanism of anisotropic silicon etching [54]. It should be noted that the addition of 250 ml of isopropyl alcohol per litre of water will cause about a 20 % reduction of etching of the (100) plane.

The reaction for etching silicon dioxide has been proposed by Seidel et. al.[69] and is described as follows

$$SiO_2 + 2OH^- \text{---} > SiO_2(OH)_2^-$$

where a linear correlation has been found between SiO_2 etch rates and the hydroxide concentration. The etch rate of SiO_2 rises linearly with concentration to a maximum for a 35 % KOH solution and decreases in proportion to the square of the molar water concentration for higher percentages, which can be used as a basis for predicting etch rates

of silicon dioxide, when coupled with the Arrhenius law, which takes into account temperature dependence.

The SiO_2/Si etch ratio is an important measure for determining the suitability of SiO_2 as a masking material during etching and is quite dependent on the etchant composition and its temperature. Seidel has found it to be two orders of magnitude larger for EDP solutions than for KOH. The higher the temperature and the higher the etchant concentration, the lower the etch ratio. For example, with a thermally grown oxide, a 50 % KOH solution at 110 °C exhibits an etch ratio of only 70, but a 10 % KOH solution at 30 °C has a ratio of about 3000. If the full thickness of a wafer is to be etched, then the latter ratio is the most suitable for using SiO_2 as an etch mask, however the penalty for a high ratio is a slow etch rate and in this example it is about 3 μm/hr for the 10 % solution, which would require over 5 days to etch a 380 μm thick standard wafer. Etch ratios can also be determined theoretically from discussed calculated etch rate data for Si and SiO_2.

A limitation of the KOH solution is its incompatibility with standard IC processing due to the high mobility of potassium ions in silicon and silicon dioxide. This leads to poor gate oxides and undesirable behaviour of semiconductor junctions. Solutions of TMAH and water (TMAHW)[70] do not give this problem, but have similar etching properties to KOH and are a preferred etchant for IC process compatible work. Additionally, silicon doped TMAHW does not attack aluminium with a native oxide, but KOH does, making TMAHW even more desirable for use with devices utilising aluminium electrodes. The (100) silicon etch rates can be higher than EDP or hydrazine solutions, but not as high as KOH solutions where (111):(100) etch ratios are comparable (Order of 35 at 95 °C) and rise with increasing

temperature. The maximum etch rate for (100) occurs for 5% TMAH and 20% for TEAH. The pH value and silicon doping content have quite significant effects on the etching characteristics of TMAHW solutions [71]. When doping is increased, the pH decreases, resulting in increased hillock formation. They also form on a (100) surface below 15 % TMAH. Selectivities for silicon dioxide layers are higher than KOH and similar to the other etchants and increase with silicon doping. LPCVD silicon nitride is not etched by any of the mentioned etchants and can serve as the best masking material. Higher concentrations above 20 % are preferable for smoother surfaces, however etch ratios and rates are lower. The etch rate is constant over a long period of time since TMAH does not decompose below 130 °C.

Selectivity

For this work, the influence of dopants on the etch rate is an important consideration. The rest of this section will detail the etch behaviour of highly boron doped silicon, for aqueous solutions of KOH and EDP. It is well known that as the boron concentration in doped silicon exceeds 7.10^{19} cm^{-3} (atoms/cm^3) [72] the etch rate is drastically reduced for EDP solutions and at higher concentrations, the rate is reduced further. For KOH solutions, large etch rate reductions were observed by Price[73] for concentrations greater than 5.10^{18} cm^{-3}. Other dopants such as phosphorus and germanium influence the silicon dissolution rate, but at much higher concentrations where phosphorus must be greater than 5.10^{20} cm^{-3} and germanium greater than $2.5.10^{21}$ cm^{-3}. For germanium, Seidel has shown that for a concentration of $5.10^{21}cm^{-3}$ the etch rate is reduced by only a factor of two. However, germanium can be codoped with boron to compensate lattice strain caused by high boron concentrations. Seidel indicates that for a 1.10^{20} cm^{-3} boron etch stop, a 1.10^{21} cm^{-3} germanium concentration will yield stress free and dislocation free layers. Furthermore, he

detects no difference in etching properties when compared with only boron doped layers. For phosphorus, Seidel reports a reduction in the etch rate by a factor of four for a concentration of 5.10^{20} cm^{-3}. An approximate comparison for the silicon etch rates as a function of the three mentioned dopants is given in fig 4.13 and clearly shows boron acts as the best etch stop. For this reason, the boron dopant is chosen as the most viable etch stop for this work.

Seidel has presented an etch model based on the work of Raley et al. [74] which relates the dependence of the etch rate R as a function of temperature T on the boron concentration C_B for the two crystal orientations (100) and (110).

$$R(T)=\frac{R_i(T)}{[1+[\frac{C_B}{(C_o(T)}]^a]^{\frac{4}{a}}} \tag{4.29}$$

Where

$$R_i(T)=R_o e^{-\frac{E_1}{kT}} \tag{4.30}$$

$$C_o(T)=C_o^* e^{-\frac{E_2}{kT}} \tag{4.31}$$

This expression, a suitable curve fit for experimental data, is derived from the fact that the experimental etch curves can be divided into two regions. One of constant etch rate and the other of a sharply decreasing etch rate. If asymptotes are drawn from these regions until they intersect, the critical boron concentration C_o is defined. Thus below C_o the etch rate R(T) is independent of boron concentration and equal to $R_i(T)$ and above C_o the etch rate becomes inversely proportional to the fourth power of the boron concentration. The parameter a is a positive integer that determines the smoothness of the transition region around C_o. An overall

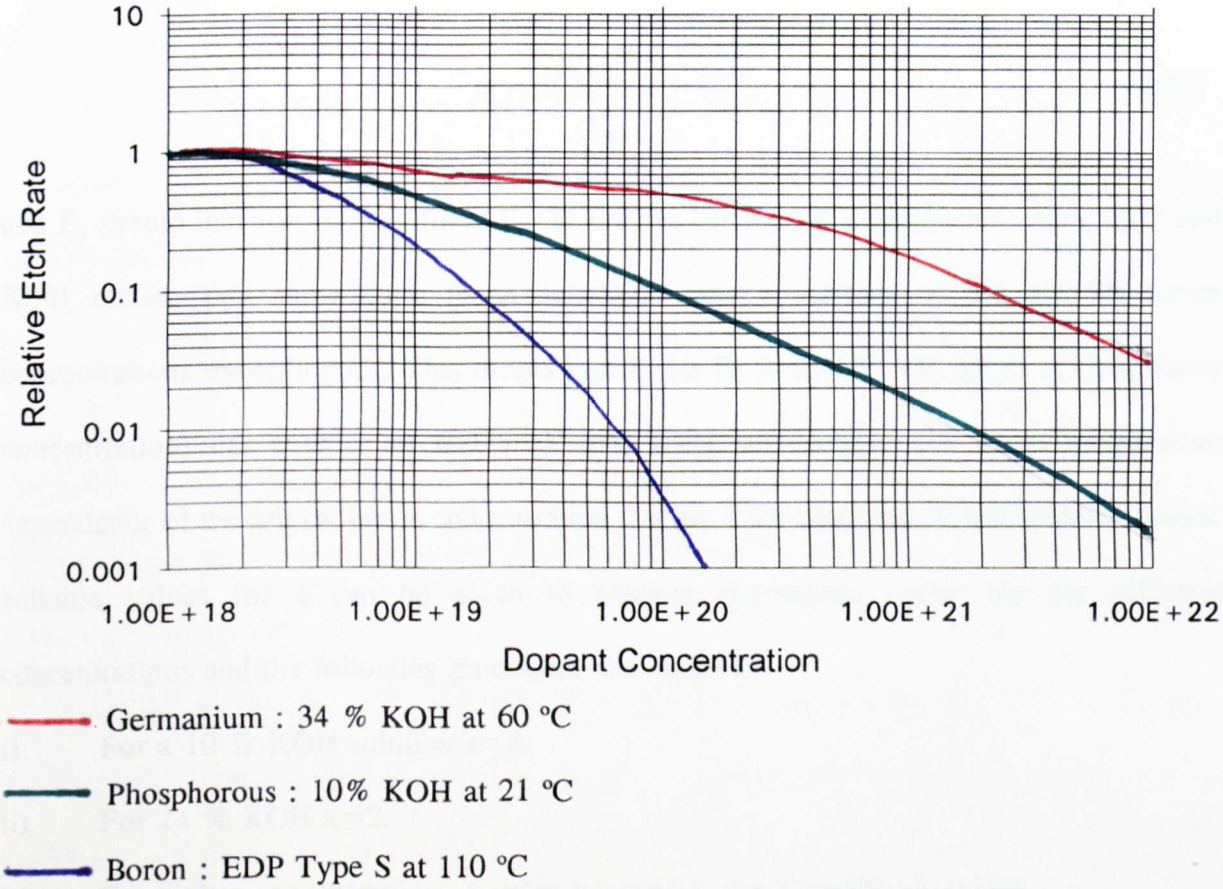

Figure 4.13 : Seidel's [74] comparison of the relative etch rates of germanium, phosphorous and boron doped silicon as a function of dopant concentration.

change in etch rate is caused if temperature T changes, which for an increase, results in a vertical shift of the curve. This is accounted for by the substitution of eqns. 4.30 and 4.31 which obey an Arrhenius law and account for the temperature dependence of R_i with activation energy E_1, and C_o with activation energy E_2.

For very large boron concentrations where $C_B >> C_o$ eqn. 4.29 is simplified to

$$R(T) = \frac{R_o C_o^{*4}}{C_B^4} e^{\frac{-(E_1+4E_2)}{kT}} \qquad (4.32)$$

and E_1 should increase by four times E_2. Seidel has carried out experiments, using EDP and KOH etches, that show there is an activation energy increase of 0.1 eV for boron concentrations exceeding C_o. This means that E_2 (ie E_2 Activation energy of critical boron concentration) has a value of 0.025 eV and takes into account the slight temperature dependence of the critical boron concentration that has been observed. From Seidel's results, suitable values for a can be given to achieve appropriate curve fits for different concentrations and the following guidelines can be given.

i) For a 10 % KOH solution a=4.

ii) For 24 % KOH a=2.

iii) For higher concentrations, a value between 1 and 2 should be chosen.

iv) For KOH concentrations that exceed 40 %, the inverse fourth power dependence was not observed within the range of boron concentrations used for Seidel's experiments.

The etch stop effect is dependent on the etchant composition. For example, for low KOH concentrations, sharp etch stop behaviour is observed, but for high concentrations the transition region becomes more smooth. The boron etch stop for highly doped silicon is less effective for increased KOH concentration. Thus, for a high boron concentration, the etch

rate increases with increasing etchant concentration. But for lightly doped silicon, with a low boron concentration, the etch rate decreases with increasing etchant concentration.

For KOH solutions with a concentration below 15 %, a white residue can be formed on the silicon surface due to increased water concentration effects[54], however the addition of IPA allows the benefits of improved etch stop selectivity and prevention of this residue, by reducing the KOH concentration. For this work a 17% KOH + IPA solution was used at low temperatures to achieve the best etch stop while avoiding residues caused by lower concentrations. Fig. 4.14 shows the calculated etch rate for different boron concentrations at three different temperatures using a 1l KOH + 250ml IPA solution, where the reduction in etch rate can clearly be seen beyond concentrations of $2x10^{19}$ boron atoms/cm^3.

Etch Rate Characterisation

Appendix 2 gives details on the experimental techniques of etch rate characterisation which were devised for this work and provides results from evaluation of the numerical models given in this section for 17% and 40% KOH solutions respectively, since these solutions were used in the final processing schedule. Experimental data points are given for comparison with the theoretical.

4.9 Isotropic Etchants

Isotropic etchants were used for etching silicon dioxide masked with photo resist and for silicon etching, their characteristics are examined in this section.

Isotropic etchants show no preferential etching and etch at a uniform rate in all directions

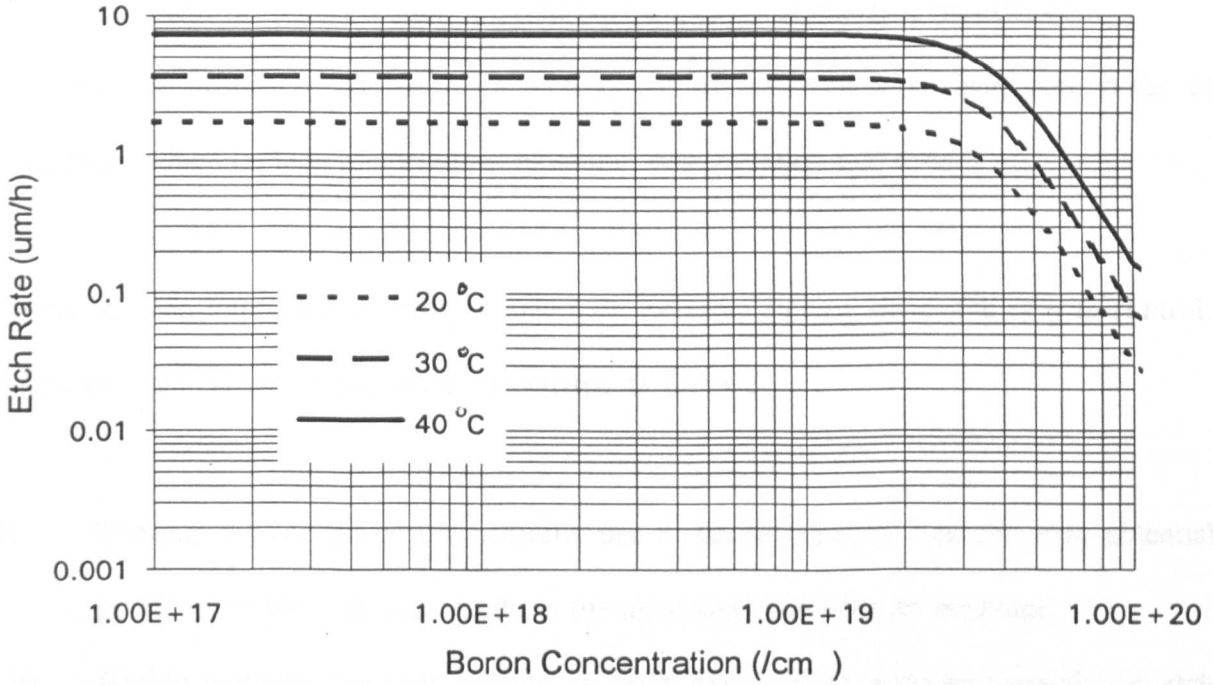

Figure 4.14 : Calculated etch rate of silicon as a function of boron dopant concentration and temperature in a 17% KOH etch solution. (Calculations based on eqn. 4.32)

from the original exposed surface. However, as the etchant undercuts the mask, gaseous and liquid byproducts from the reaction are trapped slowing the etching and altering the idealised uniformity as they randomly escape, or are flushed away. Turbulence in the etched cavity will influence the vertical cross section and also affect the uniformity. Over etching will increase lateral etching which can have significant implication on geometry tolerance.

The physical etchant mechanism is:-

i) The reactants are transported to the reacting surface, for example by diffusion.

ii) Chemical reaction occurs at the surface

iii) Products from the reaction are transported away, for example by diffusion

This will be influenced by the main etching control parameters in decreasing order of sensitivity which include temperature, agitation, concentration and time.

Agitation is an important control parameter for isotropic etching since it is easy to control. The five main types of agitation are discussed as follows

i) Thermal convection occurs naturally due to the temperature and chemical potential gradients in the bath and results in the most lateral etching or undercut.

ii) Bubble agitation involves passing an inert gas such as nitrogen through the etch solution to provide movement. A 20% increase in etch rate can be achieved but uniformity is not as good as other techniques.

iii) Mechanical (usually wafer or stirrer) agitation can increase the etch rate by 25% and reduce undercut.

iv) Ultrasonic agitation can more than double etch rates but causes protective masking materials such as photo resist to lift off.

v) Spray etching involves spraying the surface continuously with the etchant and gives the highest etch rates and lowest lateral undercut of all the above techniques. It is also the most expensive and difficult technique to implement for dangerous etchants.

Fig. 4.15 shows a comparison between convection etching and the ultrasonic agitation method on the etched depth over time. It can be seen that the agitation gives significant improvements in the etch rate. Convection etching was used for this work since it was the easiest to implement, given the hazardous nature of the etchants involved. (Plate 5.1 shows the etching facilities that were used)

The commercially available isotropic etches used for this work were a silicon, silicon dioxide and contact etch and are detailed as follows.

Silicon Etch

The silicon etchant consists of an oxidising agent and a complexing agent. The overall oxidising reaction is

$$2HNO_3 + 2Si \text{ ---> } 2SiO_2 + 2NO + H_2$$

where the nitric acid oxidises the silicon surface. The oxidising rate is a function of the atomic density in the exposed silicon surface which means this reaction is anisotropic. For example the (111) plane has the highest atomic density and oxidises more rapidly. The complexing agent etches away the silicon dioxide to expose a fresh silicon surface for the oxidising reaction to continue. A suitable silicon dioxide etchant is hydrofluoric acid and completes the silicon etchant reaction as follows

$$SiO_2 + 6HF \text{ ---> } H_2SiF_6 + 2H_2O$$

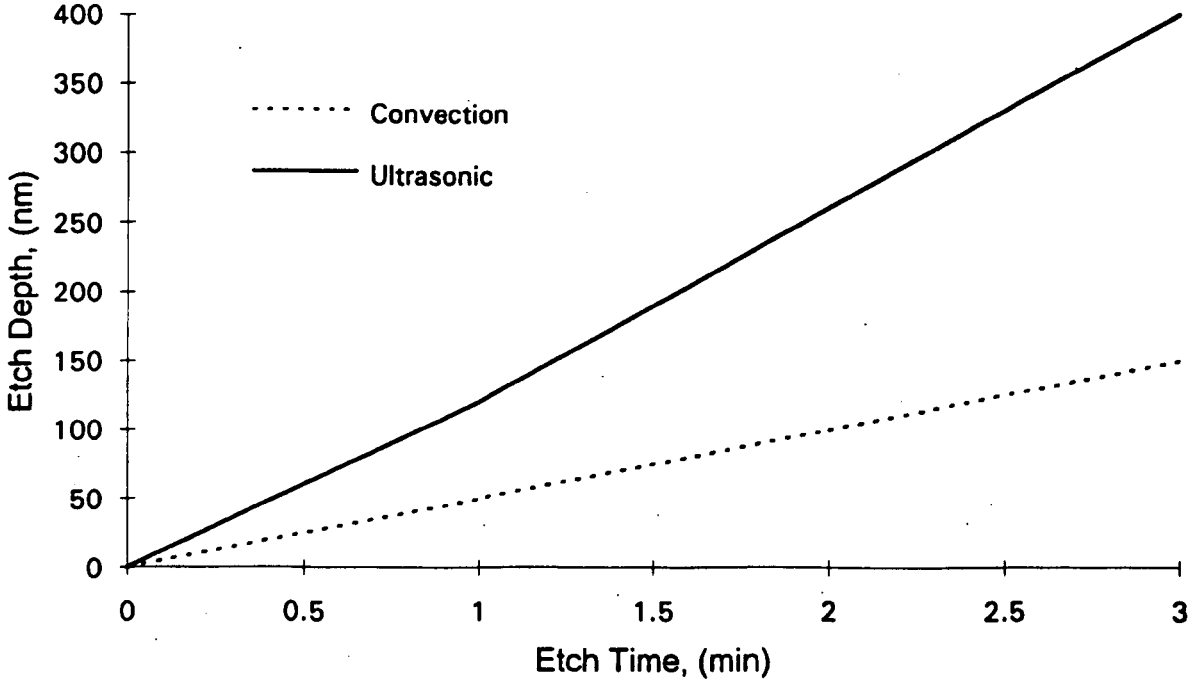

Figure 4.15 : Graph to show the effects of etchant agitation on etch depth for given etch times in an isotropic etch. (Reproduced from manufacturer's data)

The strength of the two agents and mixture proportions determines the overall anisotropy of the etchant. Moderators such as water or acetic acid (CH_3COOH) can be added to the etchant to stabilise the etch rate, increase the rate and improve the surface finish. These variations in etchant composition serve to modify the degree of anisotropy in the etching action and can be used to control the sidewall and backchamber geometry as well as surface smoothness. A high hydrofluoric acid concentration and low nitric acid concentration means that the reaction rate is controlled by the nitric acid and independent of the hydrofluoric acid since the excess hydrofluoric acid is able to dissolve the silicon dioxide formed during the reaction. However, low hydrofluoric and high nitric acid concentrations mean that the rate is controlled by the ability of the hydrofluoric acid to remove silicon dioxide as it is formed. This situation is isotropic and not sensitive to crystallographic orientation which is why it is suitable for polishing action.

The commercial colourless silicon etch used in this work consists of a volume ratio of glacial acetic acid as the moderator, 70% nitric acid and hydrofluoric acid in the corresponding ratio 5:2:2. The etch rate is typically 5μm/min at room temperature, but because the removal of silicon is an exothermic reaction, the etch rate exhibits a non linear increase with time. In the longer term the etch rate decreases non linearly as the solution becomes saturated with silicon.

The silicon etch was used to thin silicon wafers and etch backchambers. For all techniques using near isotropic etchants, some degree of corner roundness and non planarity of the backchambers can occur. This effect was neglected for this work due to relatively large geometries for back chambers.

Silicon dioxide etch

The silicon dioxide etch consists of hydrofluoric acid which etches silicon dioxide according to the second reaction above and is completely isotropic. The etch rate of silicon dioxide is influenced by its density, porosity, stress, structure and purity and the higher the crystallinity the lower the etch rate. It is relevant to note for this work, since thermal oxides are grown on doped silicon, that boron doping of silicon dioxide decreases the etch rate as a function of increasing boron concentration for a given temperature and etchant composition. This is illustrated in figure 4.16, where the etch rate of boron doped and undoped silicon dioxide is shown for different temperatures.

The commercial colourless silicon dioxide etch used in this project consists of a volume ratio of 40% ammonium fluoride (NH_4F) as the moderator (buffer) and 40% hydrofluoric acid in the corresponding ratio NH_4F:1 (ratio NH_4F:HF with HF=1) where the lower ratios of buffer to HF give the highest etch rates. For example, a 4:1 solution etches thermally grown silicon dioxide at about 100nm/min, the uniformity of this etch rate with depth is shown in fig. 4.17, where the experimental points fall in a straight line yielding a constant etch rate, this would not be the case for a varying oxide density. By changing the composition of the buffer solution, by adding water, it is possible to control the etch profile produced on etching.

A commercial 10:1 etch or contact etch was used to remove thin films of silicon dioxide in a mask window prior to diffusion or metallisation and consists of deionized reverse osmosis water and 48% hydrofluoric acid. Fig. 4.18 shows the etch depth versus time for a contact etch (From manufacturers data), indicating a constant etch rate of about 38 nm/min .

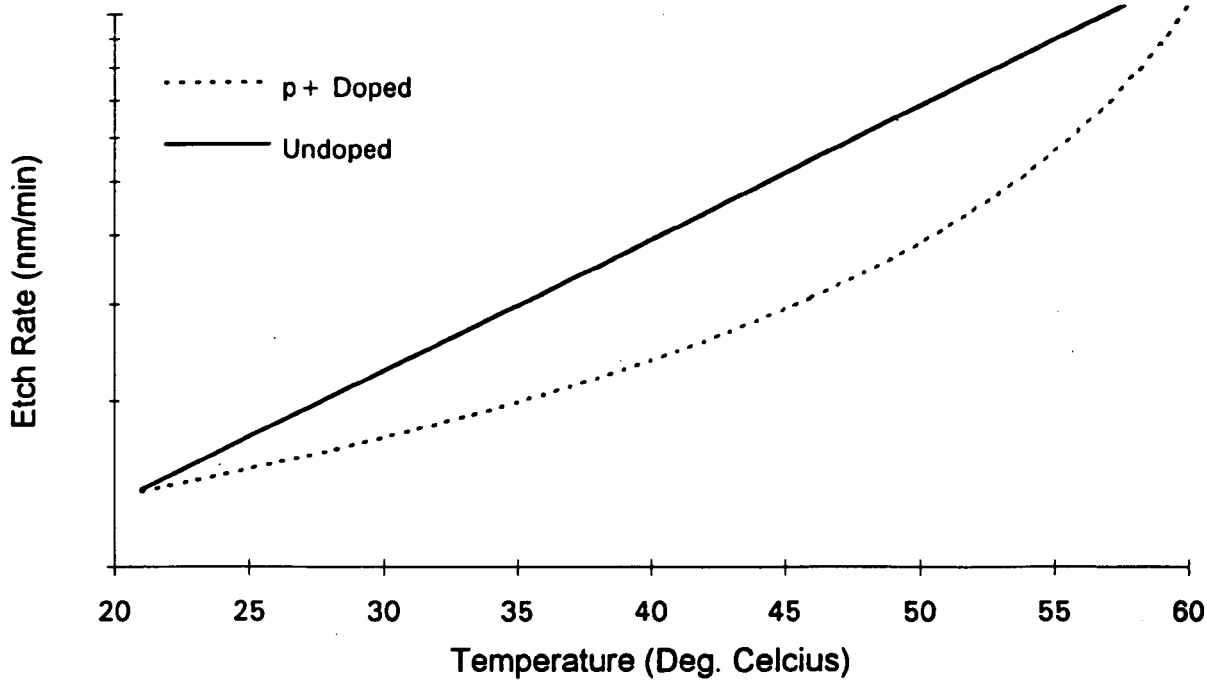

Figure 4.16 : Comparison of the etch rate of undoped and boron doped silicon dioxide for different temperatures in an isotropic silicon dioxide etch. (Reproduced from manufacturer's data)

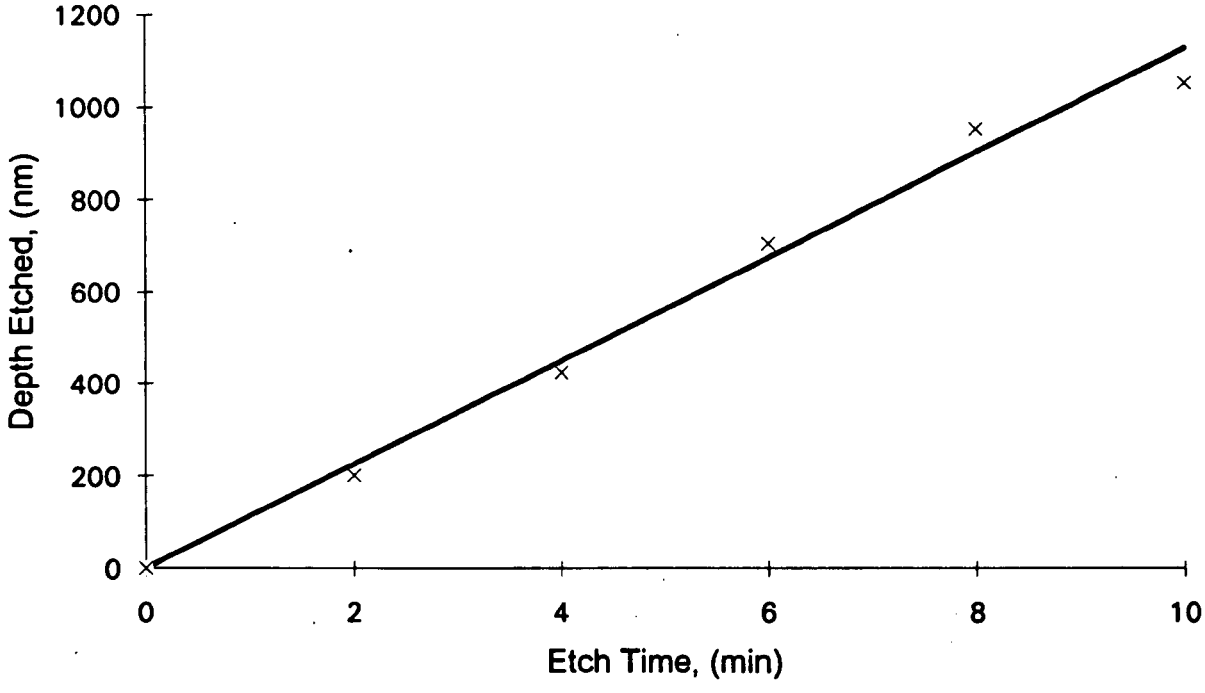

Figure 4.17 : Experimental results that show etch depth versus etch time for a commercial isotropic silicon dioxide etch maintained at 22°C. A constant etch rate of 100 nm/min can be deduced from the gradient of the line. (Note : Crosses indicate experimental data.)

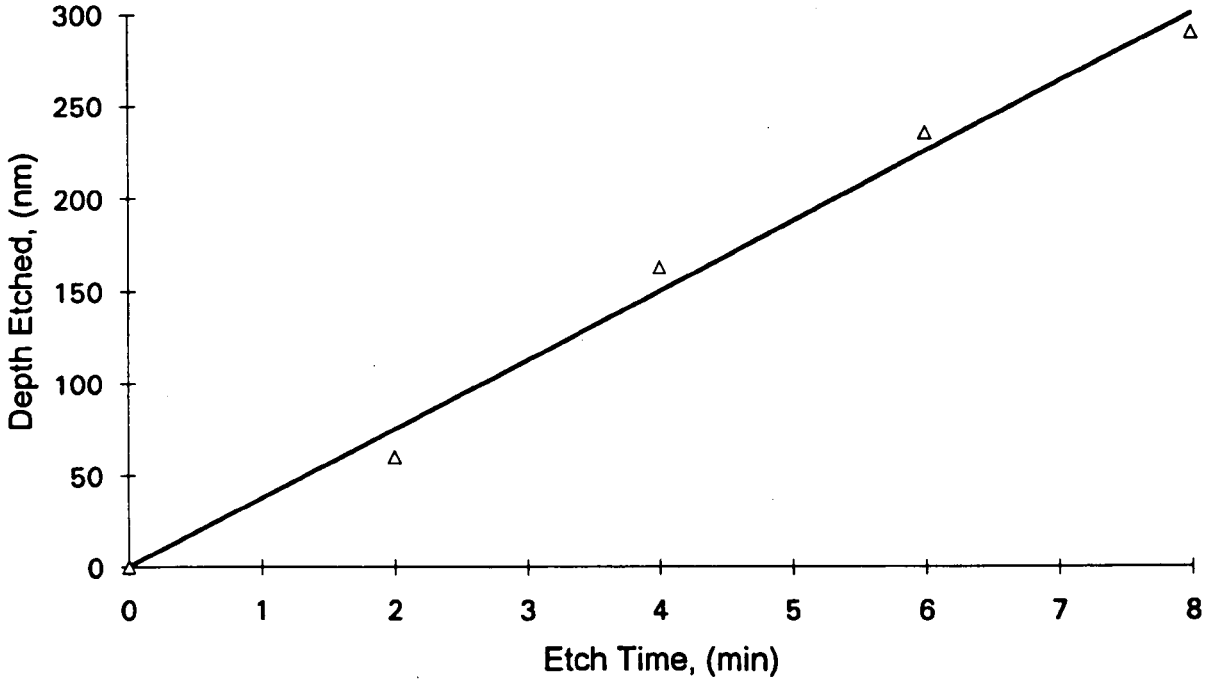

Figure 4.18 : Experimental results that show etch depth versus etch time for a commercial isotropic silicon dioxide contact etch maintained at 22°C. A constant etch rate of 33 nm/min can be deduced from the gradient of the best fit line. (Note : Triangles indicate experimental data.)

4.10 Surface tension effects for thin parallel plates

For thin air gaps of less than a micron, between two smooth 1mm^2 parallel plates, stiction can be a problem if the plates are allowed to touch fig. 5.4. For a silicon microphone with a 1 μm thick diaphragm that has undergone wet chemical processing, followed by subsequent rinsing, stiction can occur as the water dries due to surface tension pulling of the diaphragm onto the substrate. The mechanical force required to overcome the stiction to free the diaphragm can be sufficient to fracture the microphone structure. To avoid stiction, the surface tension of the final rinse phase must be reduced so that the force on the diaphragm is decreased as the rinse fluid evaporates. (Methods that were devised to reduce stiction are discussed in section 5.5 and 6.6)

4.11 Packaging considerations

Testing the microphone structures requires some form of packaging such that they can be integrated with conventional electronics. It has already been explained that the capacitance microphone has a very high impedance and therefore requires impedance conversion circuitry in close proximity to the device in order to reduce parasitic capacitance. This has to be taken into account when specifying a suitable package.

Connection to the microphone is via small bonding pads. These have been designed such that they are suitable for a wire bonding technique called ultrasonic gold ball bonding, which will now be discussed.

Ultrasonic bonding

This is a technique where two similar or dissimilar metals are joined by the introduction of

high frequency vibrational energy in the area to be joined. A tip with a small capillary wire fed through it is forced against the bonding pad and caused to vibrate, by application of ultrasonic energy, in a plane parallel to the bond interface. The combined static and vibratory forces introduce stresses in the wire and the bonding pad which cause plastic deformation to occur in the bond zone. As a consequence of this plastic flow, intervening layers of oxide are shattered and a solid phase bond is generated. This technique introduces little or no contamination into the surrounding substrate area and can provide a bond that remains stable electrically and mechanically during subsequent processing and exposure of the package to the service environment. More specifically, for the gold ball bonding technique employed for this work, the substrate is held on a vacuum chuck and kept at about 150°C. A 25μm wire is threaded through a capillary and severed with an electrical arc to form a gold ball which is larger than the wire. The capillary is lowered onto the bonding pad on the substrate and the ball is forced against the pad with a suitable force and ultrasonic energy for a pre-determined short duration to form a gold ball bond. The capillary is then raised and the substrate is moved, the wire is pulled out of the capillary until the next bonding pad location has been located and is directly under the capillary. The capillary is lowered so that the side of the capillary forces the wire against the pad. Again a suitable force and ultrasonic energy is applied for a pre-determined time until a fish tail is formed and the capillary wire is detached. The capillary is raised and an electrical arc is applied to the tip of the wire emerging from the capillary to form the gold ball ready for the next bond.

The quality of the bonding process can be made by inspection of the gold ball and the fish tail formation. A more quantitative measure of bond strength can be gained for either the wire bond pull test or the shear test [75], the latter being the most suitable for testing the gold ball bond. The destructive wire bond pull test consists of measuring the force necessary

to pull a bond off the substrate and the shear test records the force required to laterally push a gold ball off a pad or substrate.

Gold ball bonding requires that the substrate is heated up to and maintained at a minimum of 100°C, that the surface to be bonded to is flat and clean and that the bonding pad is thicker than 100nm. The gold wire used can be bonded to gold or aluminium pads with suitable adjustments to the bonding parameters. The length of connections should not exceed 5mm since the gold wire may sag and touch the substrate.

A suitable IC header or TO-series package can be used to mount miniature components with the microphone, in addition to providing a lead out for connection to external circuitry. Connection between bonding pads can be implemented with a gold ball bonder.

5.0 EXPERIMENTAL

The following sections give details of the evolution of fabrication steps, shown simplified in fig. 5.1, that were developed for implementation of the microphone structures. The figure is explained as follows :-

Silicon Processing

1) Etch backchamber into n-type silicon to a target depth of 1μm.

2) Grow 1 μm of silicon dioxide on the wafer and pattern oxide using rim mask.

3) Diffuse boron into exposed areas of silicon to a depth greater than 8 μm to define rim structure.

4) Grow 1 μm of silicon dioxide on the wafer and pattern oxide using diaphragm mask.

5) Diffuse boron into exposed areas of silicon to a target depth of 1 μm to define diaphragm structure.

6) Remove all silicon dioxide

Glass Processing

7) Pattern glass with metal contacts which form back chamber electrode and connection to microphone structure.

8) Align and electrostatically bond the glass wafer to the silicon wafer such that the appropriate metallisation is in contact with the desired p^+ areas of the silicon wafer. (See fig. 4.2(b) for indication)

Silicon dissolution of the wafer

9) Remove all the unwanted n-type silicon using etchant (Such as KOH, EDP or

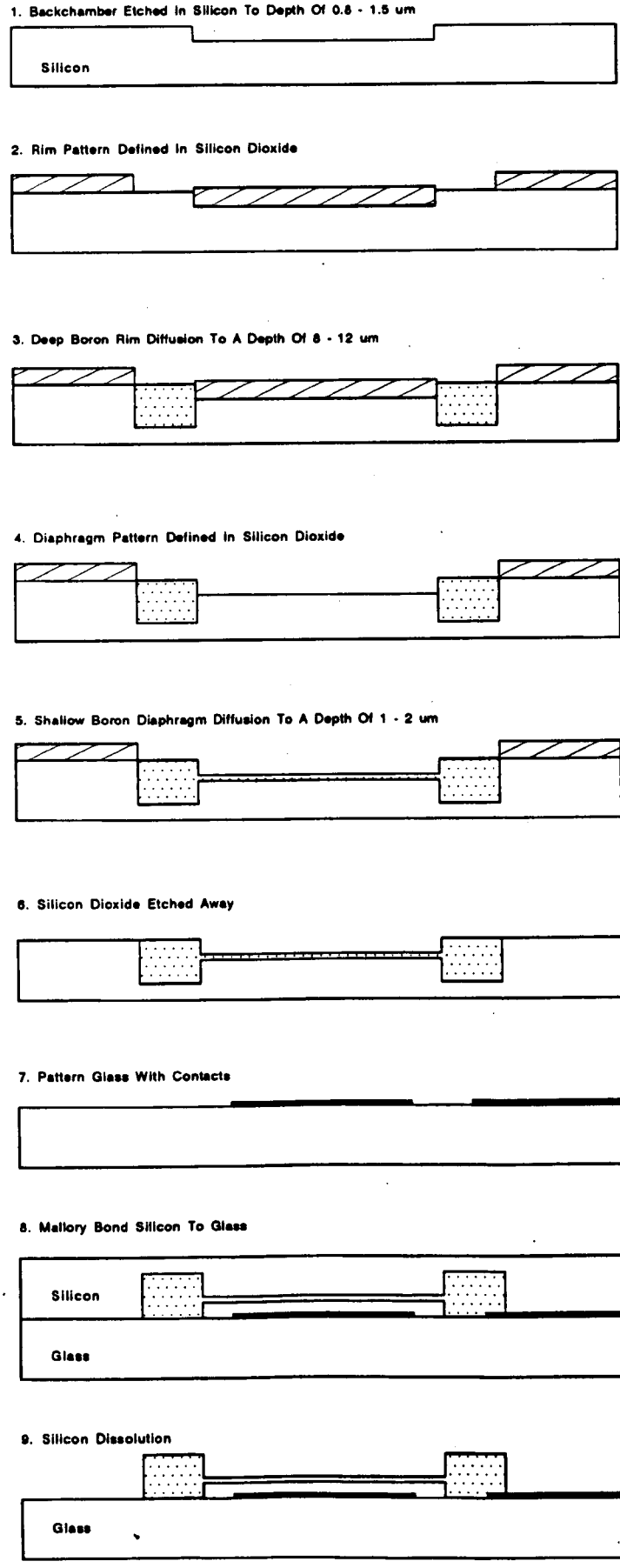

Figure 5.1 : Fabrication sequence for the manufacture of a p^+ silicon microphone on glass.

TMAHW) to produce p^+ silicon microphone structure. Remove all fluid from behind the backchamber to yield the rim suspended diaphragm structure.

More precise detail of the finalised implementation of these processing steps and the exact recipes are given in the processing schedule of A3.1. Due to the long duration of experiments for development work for this thesis the schedule described in appendix 3 took three years to evolve and finalise. A timescale for one complete batch fabrication run of this schedule is given in A3.2. Furthermore, the experimental development of suitable masks for the required miniature geometries is described in appendix 2.

5.1 Wafer processing

For this work 3" dia. x 380 μm thick n-type (100) wafers of moderate doping (10^{16}-10^{17}) with one polished face were used. Silicon dioxide was grown on these wafers, using a 1000 °C wet oxidation process, for primary masking material for the silicon wafer. For example, a standard 4 hour wet oxidation process was used to grow approximately 1 μm thick masking oxides. Optical photo lithography was used to transfer patterns onto the silicon dioxide using positive, or negative, photo resists that respond to ultra violet light. [76]

Three masks were used to carry out the silicon processing and their use in the different steps will now be explained.

Overview

The backchamber cavities were either etched, or formed by a double oxidation technique [77] that was developed (Sect. 4.2), to a controlled depth of between 0.5 and 2 μm using mask

one. A wet oxide was grown and the second mask was used to pattern the oxide with windows defining the rim of the structure. A deep predeposition of boron was carried out at 1050°C for 16 hrs. to provide a highly concentrated $\sim 5\mu m$ p^+ type diffusion profile (Fig. 5.2 (a)) for a rim etch stop. The third mask was used in a similar way to define the diaphragm area, where a much shorter pre-deposition diffusion time of 1 hr. was required to fabricate a $\sim 1\mu m$ diaphragm profile (fig. 5.2 (b)). All the remaining oxide was removed and the wafer was ready after cleaning for the process described in section 5.3.

5.2 Glass processing

This process used the fourth mask to define the electrode patterns on a 3" borosilicate glass wafer that was 0.5 mm thick. Metallisation was deposited using either electron beam evaporation, thermal evaporation or RF/DC sputtering. (Sect. 4.6) For investigation of multi layer metallisation a combination of these techniques was employed.

Patterning of the glass was achieved, using a UV mask aligner, by either of the following two lithographic techniques, dependent on which was the most appropriate for the metallisation scheme in use.

i) Positive resist lift off process

A lift off process was developed which is detailed in the process schedule of appendix A3.1 for metallisation up to 100 nm thick. The borosilicate glass wafer was applied with a thick layer of positive photo resist which was patterned with a negative mask of the electrode configuration. The metal layer (< 100 nm) was deposited and then acetone was used to lift off the unwanted metal resulting in a metal pattern on the glass.

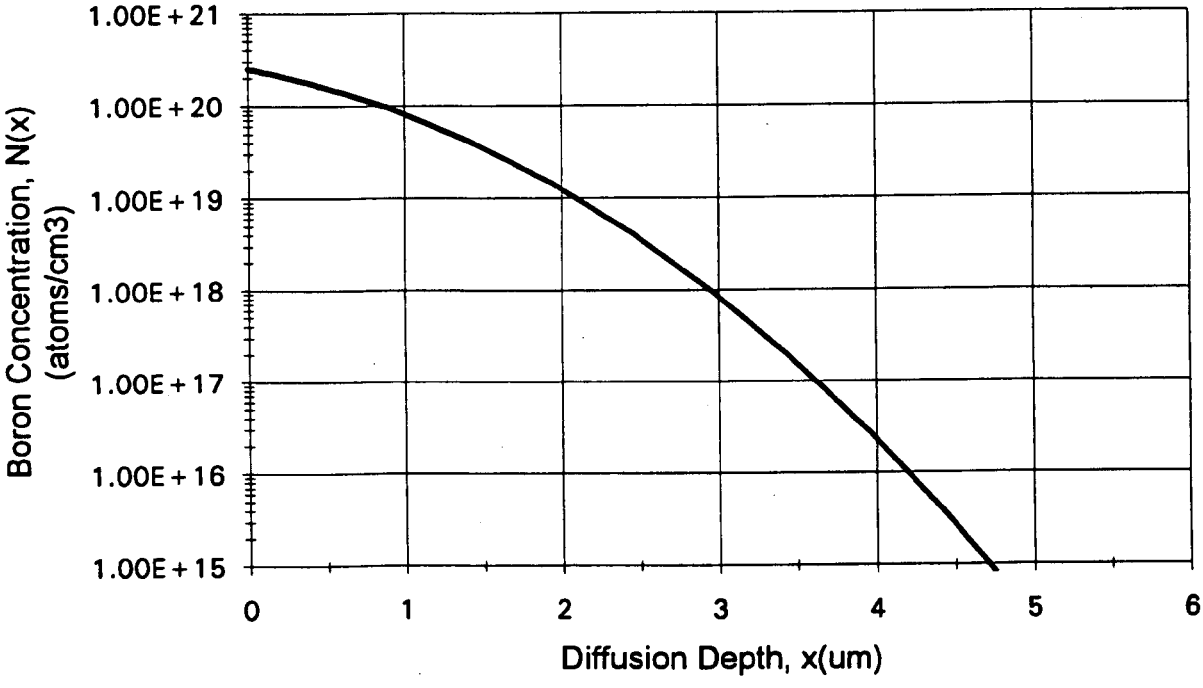

Figure 5.2(a) : Calculated diffusion profile for a 16 hr. pre-deposition used to define the microphone rim, carried out at a temperature of 1050 °C. (See section 4.4)

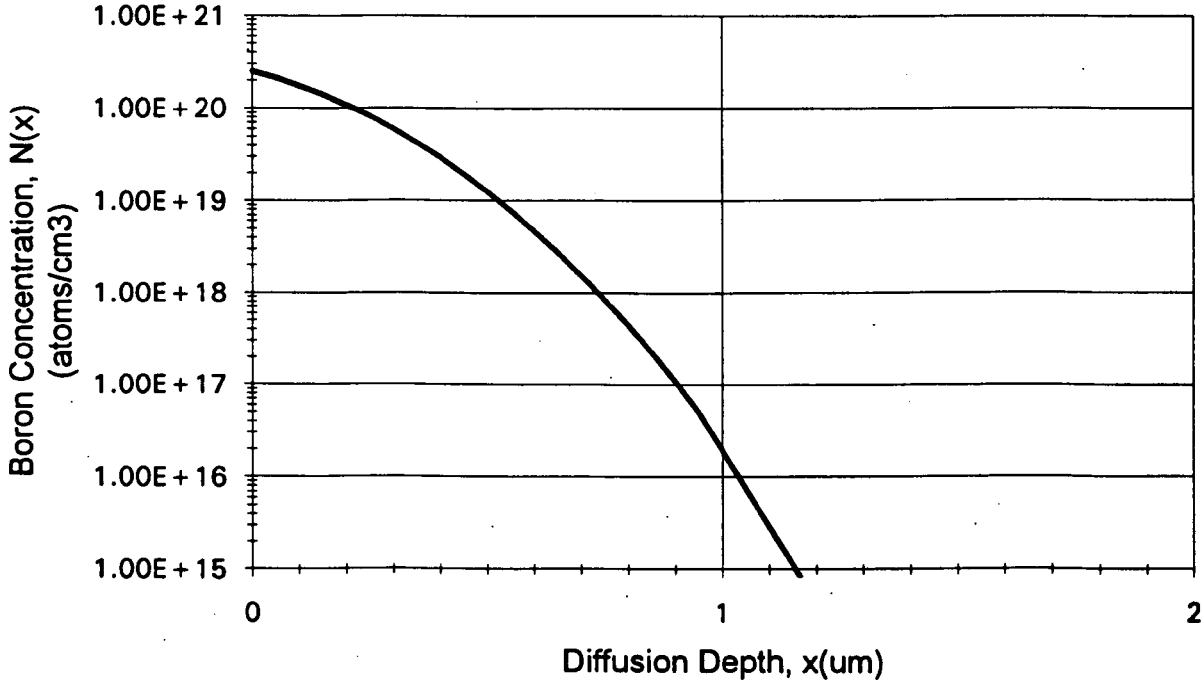

Figure 5.2(b) : Calculated diffusion profile for a 1 hr. pre-deposition used to define the microphone diaphragm, carried out at a temperature of 1050 °C. (See section 4.4)

ii) Negative resist lithography

The metallisation was deposited on the glass wafer and then coated with negative photo resist, standard negative resist lithography was used to transfer the electrode pattern from a negative mask onto the wafer. An etchant suitable for removal of the unwanted metallisation was used. The photo resist remaining on the required metallisation was stripped by plasma etching.

5.3 Electrostatic (Mallory) anodic bonding

The glass and silicon wafers were registered with each other and anodic bonding [78] of the glass to the silicon was carried out (Sect. 4.7), using the apparatus shown in fig. 5.3, to form a permanent bond between the two wafers. The single composite wafer was then diced into individual dies ready for silicon dissolution.

The parameters of voltage, current, temperature and time for the electrostatic bonding process varied depending on the area to be bonded and the type of silicon, glass and apparatus used. This required characterisation of the process each time any of the latter variables were changed. It was found that for ease of handling and high device yields, a 3" x 0.5mm borosilicate glass wafer and a 1cm diameter aluminium electrode were most suitable for use with the devised anodic bonding apparatus.

The progress of the bond was monitored by studying the current waveform during the bond formation. From the initial peak current, an exponential decay was observed with time. The bonding voltage was terminated when this current decayed to one quarter of the peak value, which gave strong unbreakable bonds for this work. This method was used since the current

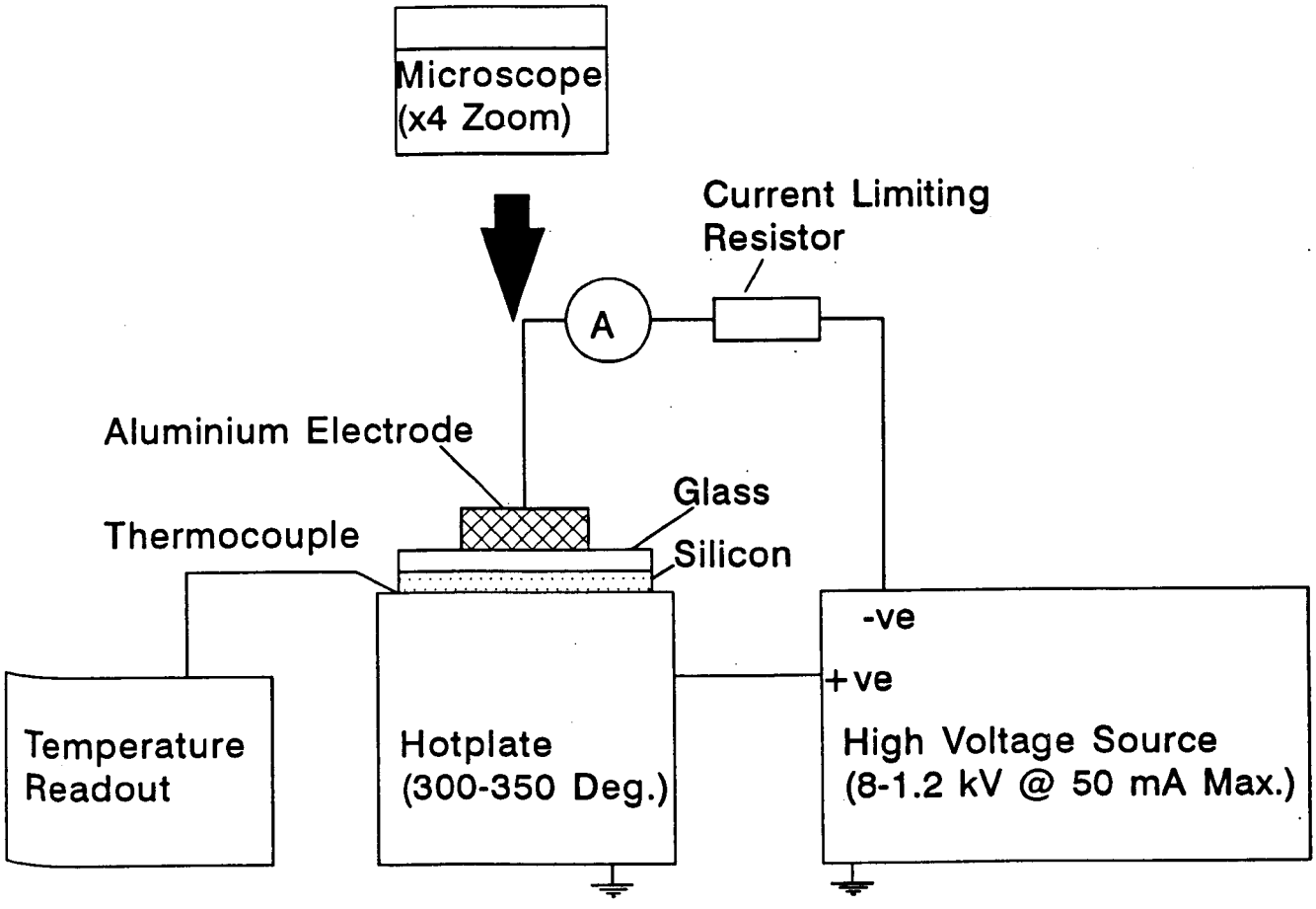

Figure 5.3 : Apparatus used for electrostatic (anodic) bonding of silicon to glass.

never decayed completely to zero and bond strength and quality appeared to be dependent on bonding time and the minimum decayed current. There was a sharp transition between the occurrence of bonding for a fixed voltage and a change in temperature. For example, if the voltage was fixed at 800 V, the bond would not occur at 300°C, but would at 320 °C. For further increases in temperature, the bonding time was reduced and the exponential current decay was more rapid until at 500 °C, the bonding was near instant for the area under the electrode. At these higher temperatures, glass softened and started to show signs of viscous flow causing damage to electrodes on the glass and undesirable bonding characteristics. It was advantageous to keep bonding voltages and temperatures as low as possible for this work while maintaining acceptable bonding times of less than 10 mins. per bond.

5.4 Silicon dissolution

Each individual composite die (See section 5.3) was etched with a two stage etching process to yield the structure. The first etch was designed to remove the bulk of the n type silicon quickly, and the second was very selective between the p^+ and n type silicon, such that the p^+ silicon remained when the etch was completed. The trade off for high selectivity was an extremely slow etch rate, hence the need for the first etch. When the etch was completed, the structure was rinsed with millipore water (See Glossary) to remove any traces of etchant. (Note sect. 4.8 & 4.9 descibes etching theory)

The etching apparatus shown in plate 5.1 was designed for long term unsupervised use and consisted of two 1l chemical reaction vessels immersed in a temperature controlled agitated 10l water bath. A double surface water condenser was used for each of the reaction vessels to re-condense vapours from the etchant, so that its composition could be maintained.

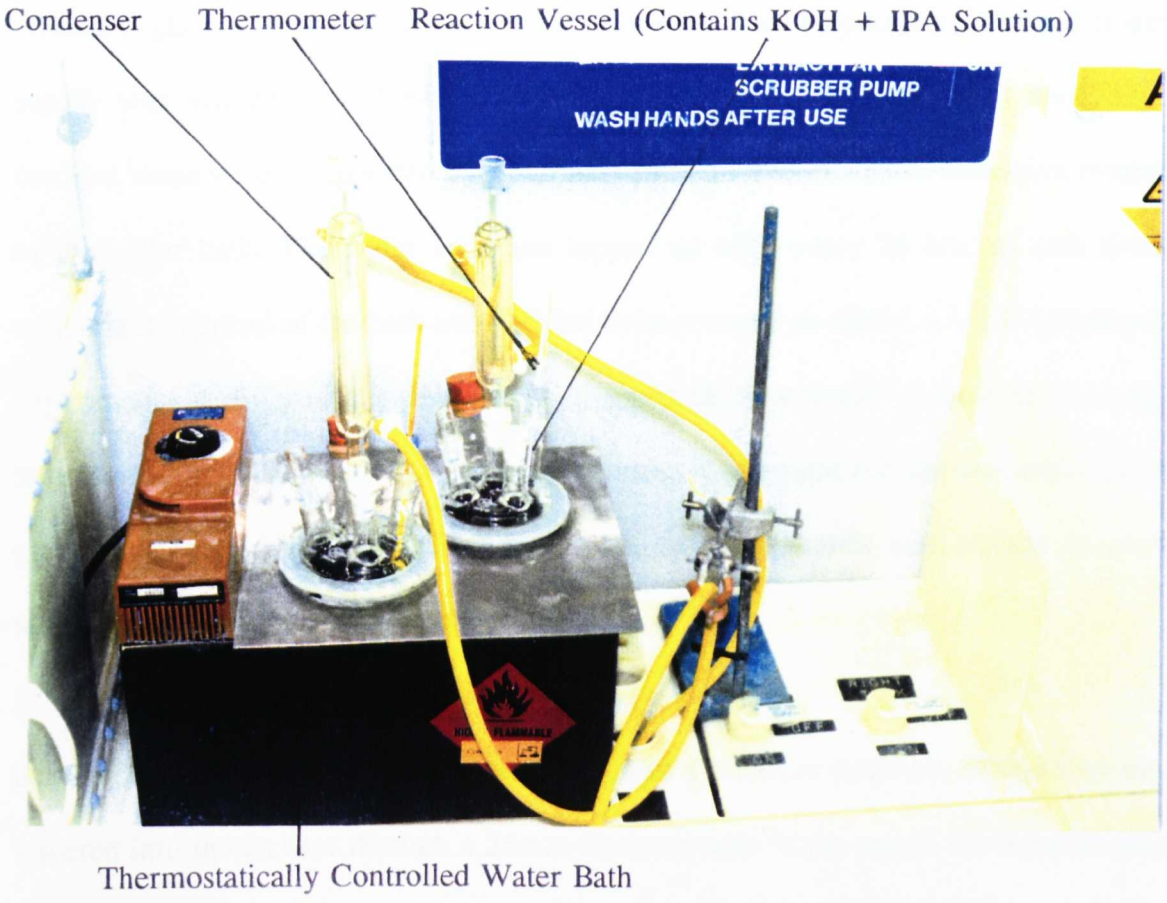

Plate 5.1 : Silicon dissolution apparatus.

Ordinary glass thermometers were used to monitor the temperature, and a nitrogen gas supply was available for bubble agitation of the etchant solution when necessary. The reaction vessels were supported by a stainless steel lid that prevented excessive evaporation of the water bath. The water bath was topped up after every 24 hrs. of etch time. The temperature control of the bath was verified to be accurate to within +/- 1°C by carrying out experiments at different temperatures with a pen chart recorder to monitor the long term temperature stability over 48 hr. etching periods. A platinum iridium thermocouple with a glass envelope was placed inside one of the reaction vessels and etchant to sense the temperature variation for these experiments.

Samples were mounted on a PTFE platform, with a stainless steel rod, so that they could be lowered into the etchant through a 25mm dia bung hole in the top of the reaction vessel. A rubber bung was used in the bung hole to support the rod in place, with the samples being submersed in the solution. The main etchant used for this work was analytical grade potassium hydroxide which was weighed out and added to reverse osmosis deionised (or millipore) water to make 1l of the required solution concentration, 250ml of electronic grade isopropyl alcohol was added to this solution when etching silicon structures. Mixing KOH with the millipore water resulted in an exothermic reaction that evolved heat. It was therefore important to allow the solution to clear and cool to room temperature before carrying out etching experiments. Fresh solutions were prepared after approximately 1.5 g of silicon was dissolved in the solution.

5.5 Back chamber fluid removal

Due to the wet chemical etching stage and subsequent rinse, water was present in the back

chamber. If the structure was allowed to dry naturally, the surface tension of the water pulled the diaphragm into contact with the backplate as it evaporated, fig. 5.4. The diaphragm then became permanently bonded [79] to the back plate rendering the structure useless. To avoid this problem, clean t-Butyl alcohol was used, because it has a lower surface tension and the ability to sublime from a solid to a gas under given conditions of temperature and pressure. The structure was rinsed with this liquid and then frozen [81] so that a solid was formed in the backchamber. The structure was then put under vacuum and at about 13 Pa the solid in the back chamber sublimed to a gas and the diaphragm was released [80, 81].

An alternative less aggressive method was devised. This involved immersing the structure in electronic grade isopropyl alcohol (IPA) for two hours, so that the water from the backchamber was removed. The structure was then transferred to a clean uncontaminated chloroform solution for two hours and subsequently placed on a clean liniment free absorbent fabric, such that all the chloroform evaporated. The structure was examined with an optical microscope to establish that the back chamber was clear of fluid.

Heating structures in an oven for 12 hr. periods at 250°C after they had been immersed in isopropyl alcohol was investigated. This technique was abandoned after a few attempts with several devices, since none of the diaphragms showing stiction could be released. It was also undesirable to have additional device heat treatments with uncharacterised consequences on the different elements of the microphone structures

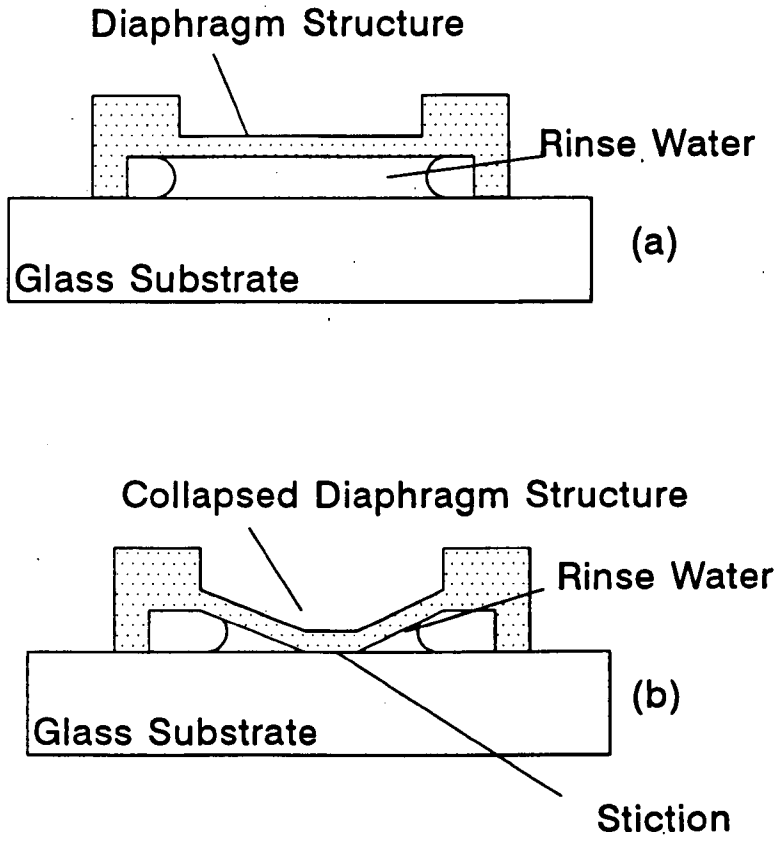

Figure 5.4(a) : Trapped liquid under a silicon microphone diaphragm. (b) Diaphragm collapses as structure dries out.

5.6 Packaging

The glass die with the completed structure was glued with epoxy onto a suitable package with gold pads, and 25 μm gold wires were gold ball bonded from the microphone electrode pads to the package pins where possible.[79,Ch 8] Electrical tests were then carried out to determine device properties. It was important to determine whether the device continuity between the diaphragm and the back electrode was open circuit, short circuit or resistive before further tests could be carried out. A special low voltage continuity tester that subjected a maximum of 100 mV to the devices was used in order to try and prevent the test instrumentation voltage from collapsing the diaphragm. The electrode geometry was fabricated such that there were two connections to the rim and two to the back electrode. This enabled the continuity/resistance of the back electrode to be measured and also the electrode-rim-electrode path. If either of these was found to be open circuit, it was assumed that the back electrode or the electrode-boron connection was faulty respectively. Conversely, they both had to be of sufficiently low resistance ($<$ 10Ohms) to merit further device testing.

6.0 FABRICATION RESULTS AND CONCLUSIONS

The following chapter details the most important difficulties encountered in the processing techniques, problems and results obtained for each of the fabrication steps given in the last chapter. A complete processing schedule for the silicon microphone M2 is given in appendix A3.1 based on the work of this thesis.

6.1 Silicon processing

Many of the silicon processing steps were well defined and were quite reproducible such as standard masking oxidations, lithography and etching of SiO_2 to obtain a pattern.

Test wafers were used for process control at every step to ensure that the fabrication stages met design specifications. Standard techniques such as measurement of sheet resistance with a four point probe, capacitance-voltage measurements for testing oxide quality and ellipsometry for checking oxide thickness were used to help with process control. The following subsections detail areas that required some special process development.

6.1.1 Backchambers

This section summarises results from various backchamber etching experiments and compares the wet etching and oxidation techniques with each other.

6.1.1.1 Wet etching

A silicon dioxide mask was used for separate wet etching experiments of silicon using anisotropic KOH, TMAHW and an isotropic commercial silicon etch.

KOH & TMAH

The graphs of fig. A2.4 were used to determine etch times for KOH where more detail is given on these etchants in section 4.6 of this thesis. For all experiments, a 1l solution in a pyrex beaker was maintained at 22 °C with continuous stirring. TMAH was an expensive etch with a slow etch rate and gave a very poor surface finish with a white residue. This etchant was found to be unsuitable for use for back chamber fabrication. Both anisotropic etchants gave inclined edges which reduced the effective area of the back chamber and could cause problems with subsequent masking and diffusion if not taken in to consideration.

Silicon etch

The silicon etch was isotropic and resulted in near vertical walls for the back chamber. The commercial etch was composed of 47 % HF + 53 % HNO_3 + CH_3CO_2H and had a specified etch rate of 5μm/min @ 22°C. A 500 ml solution was used in a polythene vessel (Plate 6.1) and gave an average etch rate of 3.0 μm/min for the n-type wafers used. A 1000 °C wet oxide was etched at a rate of 0.24 μm/min which meant that a 1μm oxide remained for 4 mins in the etch. This gave a maximum allowable back chamber etch depth of 12 μm. A 20 second etch was used to try and achieve a 1 μm deep back chamber. It was important that a fresh solution was used for characterisation etching (see section 4.10) and then used for back chamber etching before being discarded, to avoid etch rate changes. It was difficult to maintain an exact temperature of the etchant during the characterisation process, since for weight loss and thickness measurements the test wafers had to be thoroughly washed and dried resulting in undesirable sample temperature changes. The etch required special safety and handling precautions and could not be used in conjunction with electrical temperature control equipment.

Plate 6.1 : Wet chemical etch station with a cascaded weir for washing wafers in millipore water.

From tallisurf measurements, wet etching methods could be used to obtain depths from between 1 μm to 3 μm at room temperature. The back chamber finish showed a minimum surface roughness of about 0.2 μm +/-0.05μm for the silicon etch at room temperature. If the back chambers were over etched, it was possible that they could be deeper than the diffused rim of the diaphragm in subsequent processing. The final result was diaphragms that fractured easily, because the diaphragm was higher than the supporting rim in the completed microphone.

6.1.1.2 Oxidation

The backchamber oxidation process involved two 6 hr. wet oxidations at 1100 °C to obtain calculated back chamber depths of 0.75 μm. This depth was verified to within 10% from tallisurf measurements (See appendix 2) and a smooth (< +/- 0.1 μm) backchamber surface profile was also measured. If deeper back chambers were required by the oxidation method, more oxidations and further lithography had to be carried out, which extended the process duration further. This required alignment of the mask more than once, which inevitably gave rise to mask misalignment problems. This technique could be circumvented by using high pressure oxidation which allows silicon dioxide to be grown at much faster rates.

The oxidation process subjected wafers to additional thermal cycles, especially for multiple oxidations, which occasionally caused unwanted stresses and wafer surface problems.

A general comparison of the two backchamber fabrication techniques raised the following points:-

1) The wet etchants had to be characterised (Appendix 2) for determination of etch rate, which required lengthy experiments before the backchambers were etched.

2) It was very difficult to control a wet etch to obtain precise etch depths in the one micron range. Oxidation was used to obtain accurate sub micron depths, with an accuracy of better than +/-0.1 μm.

3) The oxidation process gave much smoother backchambers and hence rear side of diaphragm than wet chemical methods.

4) The wet chemical method took a day to complete the back chambers, but the oxidation process took three days and was more expensive.

It was concluded from experiments that accurate, reproducible depth control of back chambers was achieved by using the oxidation method with one masking step and two long oxidations. Additionally, the back chamber surface profile was much smoother than for wet etching, which would yield a higher quality finished diaphragm, due to a more even diffusion profile in subsequent processing.

6.1.2 Doping

Initially a 16 hr pre-deposition followed by a 16 hr drive in was used to define the rims, however this gave a boron concentration that would not provide an adequate etch stop. The pre-deposition at 1050°C on its own when coupled with a 4 hour drive in, needed for the subsequent oxidation stage, did provide a good etch stop. Rim depths of greater than 5 μm were measured from this process.

It was important to profile the furnace and check operating temperatures as often as possible, because the masking properties of a wet oxide were not very good at 1175°C for very long pre-deposition times. This was discovered when an incorrectly inserted thermocouple in the

furnace caused it to operate at this temperature. The result was that wafers were heavily p type regardless of masking.

There were three problems that emerged from the doping process that required solution.

i) Pitting of the wafer surface

ii) Oxide spots

iii) Excessive borosilicate silicate glass (BSG) build up and consequential silicon consumption.

The first of these problems was solved by introducing a small amount of oxygen into the furnace during the pre-deposition such that pitting was prevented. It was essential that too much oxygen was not introduced because the BSG build up could be too rapid and cause interference with the constant source diffusion process [79, Ch 4], resulting in unexpectedly low doping levels.

The second problem was caused by moisture on the wafers undergoing rapid oxidation and was solved by altering the furnace loading/unloading temperature and ensuring wafers were thoroughly dry before loading into the furnace.

The final problem was more serious and was partially resolved. The length of the pre-deposition resulted in a substantial thickness of BSG which caused silicon to be consumed as in normal oxidation. This glass was extremely difficult to remove and necessitated experimentation with the following techniques for removal.

i) Boiling the wafers in nitric acid for many hours.

ii) A short wet oxidation of 1-2 hrs. followed by a contact etch.

iii) A 30 min. dry oxidation followed by a 3-4 hr. HF etch.

The first method did not work very well and was hazardous, the second method was successful, but caused undesirable silicon consumption that led to subsequent problems in the electrostatic bonding process. The final method was the one chosen since it gave the least silicon consumption and was the easiest to perform.

The silicon consumption caused during the pre-deposition process was highly undesirable and difficult to control. The rate of growth of the BSG was related to the small quantity of oxygen that was introduced into the furnace during pre-deposition. This level was set to prevent pitting and stop excessive glass build up and could not be varied significantly. The modelling of the rate of growth of BSG requires a more sophisticated model than the standard oxidation model because the growth rate is affected by the doping process as well as temperature and oxygen levels. Practically, the unwanted silicon consumption resulted in rims that were recessed from the wafer surface when the BSG and SiO_2 mask were removed, leading to poor electrostatic bonding of the rim later in the fabrication process. It was estimated from experimental results, for the pre-deposition conditions given, that the silicon consumption could be as large as 0.2 μm. Adjustment of diffusion time, temperature and oxygen level could substantially reduce this worst case figure. This problem was of no consequence for the short diaphragm diffusion because BSG build up was minimal and easy to remove.

6.2 Glass processing and metallisation

A layer of metallisation, no thicker than 100 nm, had to be deposited on the glass for use as electrodes. It was important that the deposited metal was very conductive, able to withstand temperatures up to 400 °C and unaffected by the wafer dissolution etch process. It had to have good adhesion to the BSG substrate, form a good ohmic contact with the p^+ structure and be suitable for wire bonding. Various possibilities were found in the literature [82,83] which used either Ti or Cr as an adhesion layer and gold and/or platinum as the main conductive material. A summary of the metals investigated and their properties is given in table 6.1.

There are two processes that were used for transferring the metallisation pattern to the glass wafer.

i) A negative photo resist mask with suitable metal etchant.

ii) The lift off process using positive photo resist and an acetone solvent.

The first method required a specific metal etchant for each metal deposited. For the number of metals investigated, this was not a practical solution. Chromium and aluminium etches were available, so these two metals were patterned with the first technique. The second method was a good process for single and multi-layer metallisation, providing the temperature of the substrate did not exceed more than 125 °C. If this happened, the positive photo resist was hard baked and could not be removed with acetone.

Single layer metallisation deposited by evaporation

Initial experimental work consisted of patterning the different metals, that could be suitable

Metal	Melting Point /K	Resistivity /10^{-8} Ω m	Density /gcm^{-3}	Acoustic Impedance g $cm^{-2}s^{-1}$
Aluminium	933	2.45	2.7	8.17
Chromium	2130	12.7	7.2	28.94
Platinum	2045	9.8	21.4	36.06
Titanium	1933	43.1	4.5	14.05
Gold	1337	2.04	19.3	23.17

Table 6.1 : Mechanical and physical properties of the pure metals investigated for metallisation.

for metallisation, onto a highly polished borosilicate glass substrate and subjecting them to an aggressive 17 % KOH etch bath at 80°C in order to determine the etch stability of the thin films. Many of the metals used such as titanium, which have a high melting point, caused the photo resist to be hard baked. This problem can be alleviated by using a cooled substrate holder, however when a hot metal is deposited on a cooled substrate, severe compressive stresses can be formed in the film which can cause adhesion to be poor. Temperature controlled substrate cooling facilities were not available for this project, which meant that deposition times and rates had to be carefully controlled to prevent excessive peak temperatures. Much of the development work for a suitable metallisation scheme required a trial and error approach which was extremely time consuming.

Chromium would not adhere to the glass, so a heated substrate (300 °C) had to be built which solved the problem. A disadvantage of this system was that the vacuum plant required two hours to bring up to temperature and 24 hours to cool before the sample could be brought up to air and removed. The rate of deposition of the metal was found to affect the film adhesion and quality as well as the method of deposition. In general, the faster the rate, the poorer the adhesion and the larger the in built stress. The main metals investigated included aluminium, titanium, platinum, gold and chromium since thin films of silver and copper were found to visibly restructure and show instability at temperatures between 300-400 °C. Aluminium, which is the metallisation preferred for chip manufacture because of its alloying properties with silicon [79, Ch 7], showed good adhesion to glass and was easy to evaporate, but was attacked by alkaline KOH with etch rates that were much higher than those of lightly doped silicon, making it unsuitable. Aluminium can be used with one of the more expensive and dangerous etchants (EDP) described in section 5.5 and exhibits etch rates

that are up to a hundred times lower than n-type silicon. To achieve these low etch rates requires that the solution is doped with silicon, this was deemed inconvenient for this work.

Most of the metals dissolved away from the substrate for longer time exposure to 17 % or greater concentrations of KOH, with the exception of chromium, which survived 17 % KOH etch at 80°C for up to 4 hours. The conductivity was poor and the metallisation was prone to break up into small islands. It was found from etch rate experiments on the glass substrate that 17 % KOH solution at 80 °C attacked the substrate glass at a rate of 5-10 nm per hour. This indicated why metallisation with poor adhesion did not survive the etch process for long periods of time, because after a couple of hours of etching, the electrode metallisation could be undermined. This problem was found for all metallisation except chromium. This metal had the best adhesion and acted as a good barrier or mask to the etchant attack until the surface started to break up. A special process was developed to try and improve metal adhesion. This involved a lengthy cleaning procedure of the glass wafer and a short silicon dioxide etch to roughen the glass wafer, prior to lithography.

Further metallisation experiments with the different metals showed that titanium and chromium exhibited the best adhesion properties, since they showed no sign of deterioration in the KOH etch for the maximum investigated etch period of 48 hrs. In this time, the surrounding glass etched by about 0.2-0.5 μm, which was much greater than the metallisation thickness. This would indicate that the metallisation was acting as a perfect mask, which concludes that chromium and titanium were the most suitable candidates for the metallisation. However, both metals have a relatively high resistivity and would result in electrodes with an undesirably high series resistance of 25 ohms or more. Since the deposition of titanium

did not require the complexities of a heated substrate, it was used as the basis for continued investigation into a simple multilayer metallisation, where the second metal would improve electrode conductivity.

Multilayer metallisation

The positive lift off process was used to pattern wafers for multilayer metallisation work because it did not require the use of two metal etchants. The silicon dioxide etch of the glass wafer was carried out after patterning of the positive resist to cause roughening of the deposition areas only and protection of the polished glass. (Required for full process schedule where the polished glass must remain protected for electrostatic bonding) For this etch it was important that the photo resist was sufficiently baked to prevent it being damaged in the silicon dioxide etch, but not baked to the point where the lift off process failed, due to inability to dissolve the resist in acetone. The photograph (plate 6.2) shows the results of this process where a 65 nm titanium electrode has been fabricated on the roughened glass. The roughened glass area that is still visible at the edge of the electrode is due to the silicon dioxide etch being isotropic and etching laterally under the photoresist mask. This lateral etch will also be enhanced because the positive resist has not been fully hard baked and may 'lift' at the edges.

Titanium was used as a key layer between the glass and the second metallisation and ideally had to be fabricated so that it was much thinner than the second low conductivity layer. Platinum and gold were investigated for use as the second layer because of their lower conductivity than titanium and resistance to alkali etching. A 25nm titanium layer was thermally evaporated from a sheet of titanium and the other metals were evaporated by the

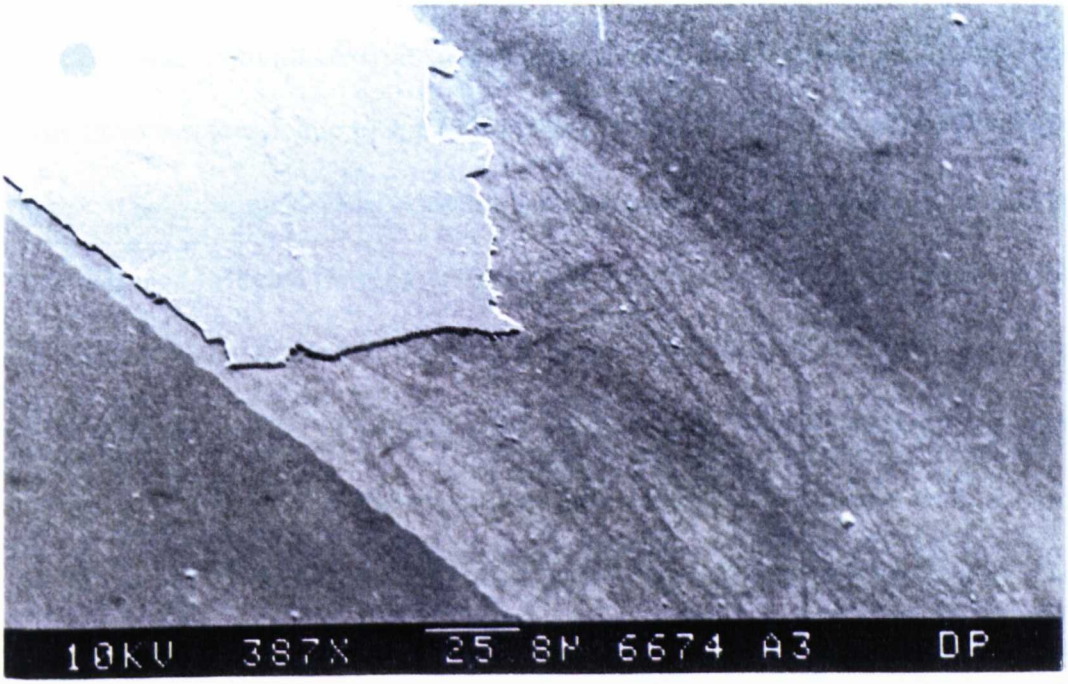

Plate 6.2 : Channel etched in polished glass substrate for adhesion of the metallisation electrodes.

electron beam method.

i) Platinum on titanium

Platinum was evaporated from a carbon boat to a thickness of 50nm and was extremely difficult to evaporate due to its high melting point of 1772°C. It was not possible to fill the carbon boat with sufficient platinum melt to prevent carbon carbon contamination during evaporation. The beam current was such that holes could be burnt in the boat which indicated that carbon was evaporated. Films that were produced rubbed off the titanium layer very easily after deposition. This was most likely due to carbon contamination present at the interface of the two metallisation, or poor adhesion qualities of platinum to titanium. Thermal evaporation of titanium was also inconvenient since excessive temperatures were generated which caused the positive photo resist to be hard baked. To overcome this, the titanium layer was deposited using RF magnetron sputtering from a 2" cylindrical target.

ii) Gold on titanium

Gold, which has a lower melting point (1064°C) and resistivity than titanium or platinum, was thermally evaporated from a tungsten boat to a thickness of 50 nm. If the ultrasonic bath was used to help with the lift off process in acetone, the gold lifted away from the titanium layer implying that the there was poor adhesion between the two layers. The titanium layer could not be removed with any amount of ultrasonic agitation. It was thought that this poor adhesion of the gold was due to a layer of oxide forming on the titanium between the two depositions. This possibility was investigated by modifying the sputter vacuum system so that it could also be used for thermal evaporation of gold without venting the system to air between depositions. Gold was evaporated immediately after sputtering the titanium, while

trying not to generate any excess heat from the evaporation that might hard bake the photo resist, by careful placement of the source. The gold film was found to have excellent adhesion to the titanium layer and ultrasonic agitation over a 30 min. period did not damage the film in any visible way. A 48 hr. etch in 17% KOH at 80 °C was carried out and the film showed no signs of damage. It was concluded that the prevention of the titanium oxide had caused the gold film adhesion improvements.

It was concluded, from the described metallisation schemes that were investigated, that the gold on titanium multilayer metallisation was the most suitable for use as microphone electrodes because of the etch resistance, adhesion qualities and low conductivity. Furthermore, the gold film was also compatible with gold ball bond adhesion, where purely titanium or chromium electrodes would not be suitable.

6.2.1 Lithography

The positive resist lithography processing is summarised in this subsection. The glass wafers were given a preparatory cleaning process before any lithography was carried out. The lithography process developed for the lift off step was a modified version of that used for silicon wafers. Lower spin speeds were used to give thicker films of positive photo resist and adhesion promoter was used to help the resist adhere to the glass. In addition, once the pattern was transferred to the photoresist and developed, the wafer was given a ten minute etch in the silicon dioxide etch. It was found that this gave significant improvements in increasing the adhesion of the key layer metallisation to the glass.

6.3 Electrostatic bonding

An experimental rig was devised and built (Plate 6.3a) to carry out the electrostatic bonding. A wafer clamping jig was designed (Plate 6.3b) to help with the glass wafer alignment process. Techniques were developed that improved the reliability and yield of the bonding process. If care was not taken with the process, it was very easy to ruin both the silicon and glass wafers and hence all the fabricated devices.

6.3.1 Electrode material and size

The electrode material and size were important for the given apparatus. Brass, stainless steel and aluminium were experimented with in various configurations. The aluminium proved to be the best electrode since it provided the best bonding performance. Sodium deposits and aluminium oxide were formed on the electrode after each bond, which interfered with the electrode/BSG contact and affected bonding parameters. The electrode surface had to be machined regularly to prevent these effects contributing to poor bonding. The machining also served as a good means of keeping the electrode surface as smooth as possible in order to maintain a good contact.

6.3.2 Quality of bonding

The most effective method of obtaining high yields with the equipment available was to bond each diffused structure individually. The main bonding parameters were voltage, temperature and area to be bonded. To prevent the 1 μm back chambers from bending and bonding to the BSG, while maintaining a good bond between the rims and the BSG, required careful settings of these parameters. Plate 6.4(a) shows a good electrostatic bond, where the blue green areas are caused by light interference from the optical microscope in the narrow back

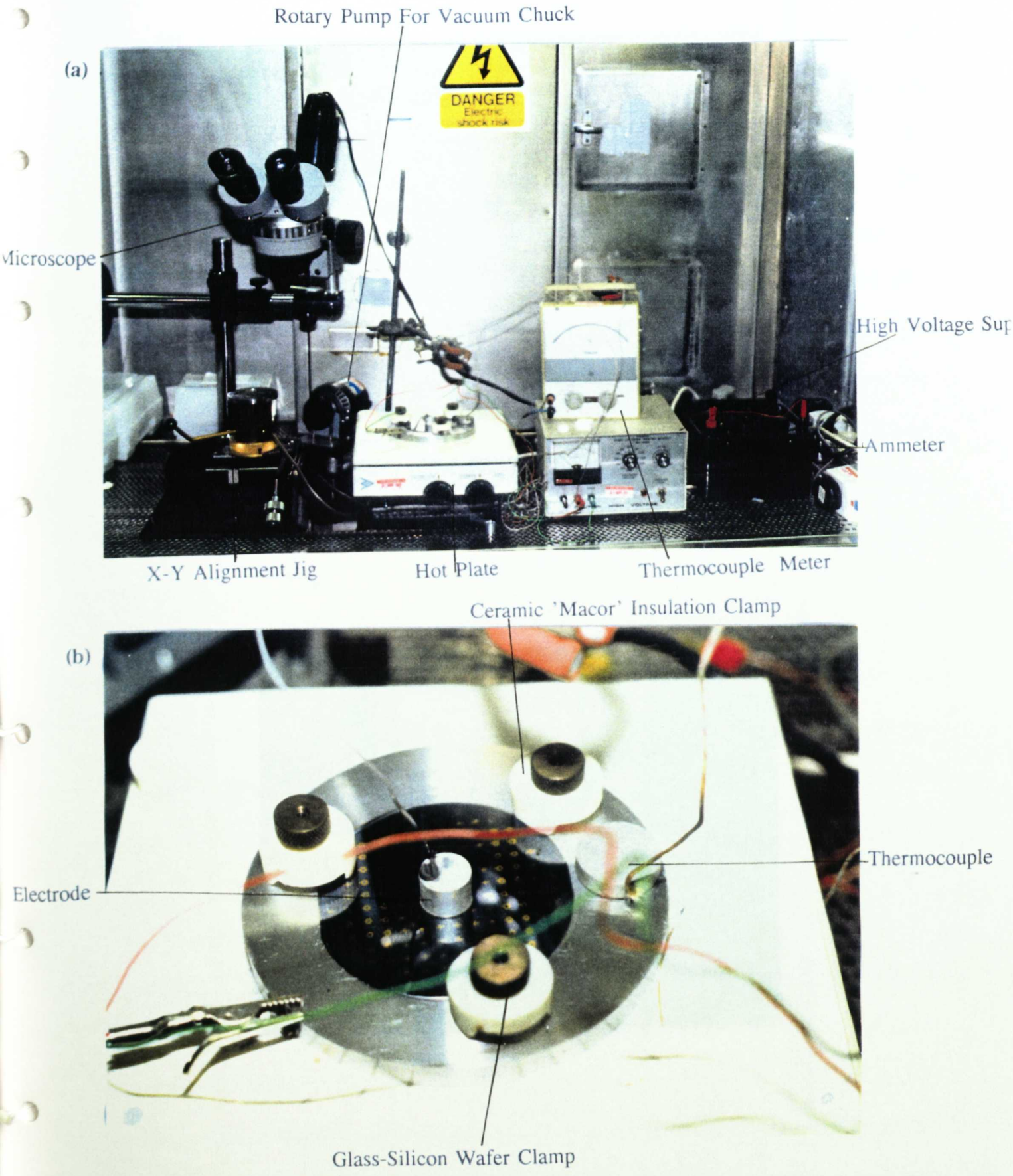

Plate 6.3(a) : Electrostatic bonding apparatus for bonding glass to silicon. (b) Electrostatic bonding of 3" wafers in progress.

(a)

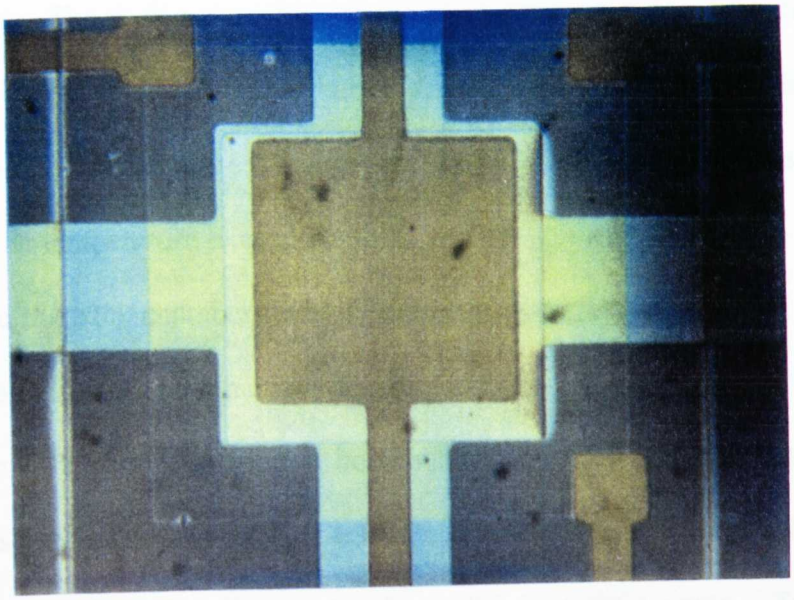

(b)

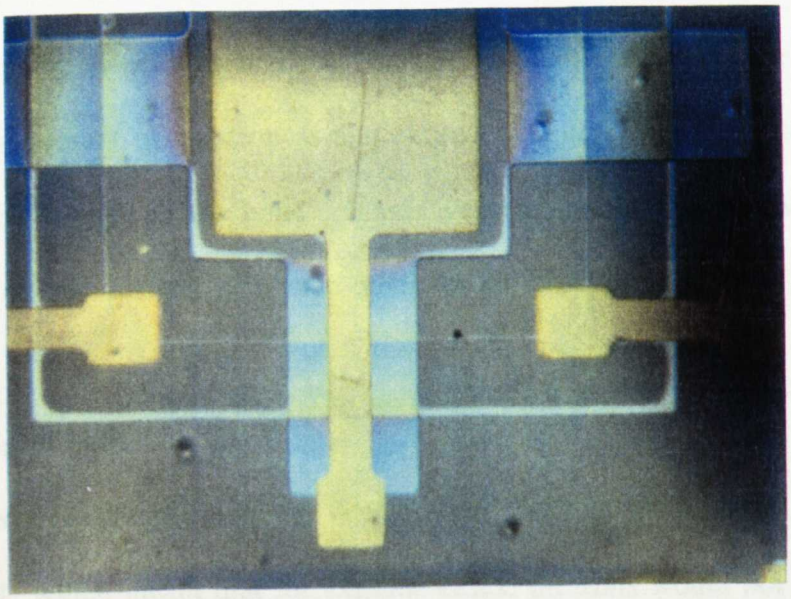

Plate 6.4(a) : Good electrostatic bond. **(b)** Poor electrostatic bond. The grey areas show the electrostatic bond. The air bubble around the edge of the rim structure indicates an unwanted recess of the rim.

chamber air gap. The dark grey areas are the electrostatic bond and the random black dots are from the exposed glass substrate where electrode damage of the glass has occurred. This damage is not significant since it is on the opposite side of the glass substrate to the structure. If the temperature exceeded 400°C and the applied voltage was greater than 1000 V, not only did the back chambers stick to the glass, the glass was melted. It is thought that this was due to extremely high current densities causing heating at the glass/wafer interface. Plate 6.4b shows a poor electrostatic bond where the back chamber diaphragm area has collapsed and sealed itself around the electrode. If the temperature was below 300°C and the voltage less than 800 V, bonding was only partial in certain areas. To obtain optimum bonding required consideration of backchamber area and depth in addition to the limits of the bonding process discussed above. Wafer warpage may also need to be considered depending on the wafer specification.

Prior wafer preparation working in a dust free environment was critical for obtaining a good bond. Any dust present or unevenness that exceeded heights of 100 nm caused air pockets or bubbles to be formed in the bond. It was very important that the two surfaces were maintained in intimate contact with each other for the bonding process.

6.3.3 Recessing of rims

Excessive silicon consumption of the rims caused them to be recessed from the silicon surface fig. 6.1, which meant that for extreme cases, the rims would not bond to the glass as shown in plate 6.5. This effect was resolved by etching the wafers in 1l of agitated 17% KOH + IPA solution for a short period to remove a micron of the surrounding silicon before electrostatic bonding was carried out. This resulted in rims that always bonded to the glass,

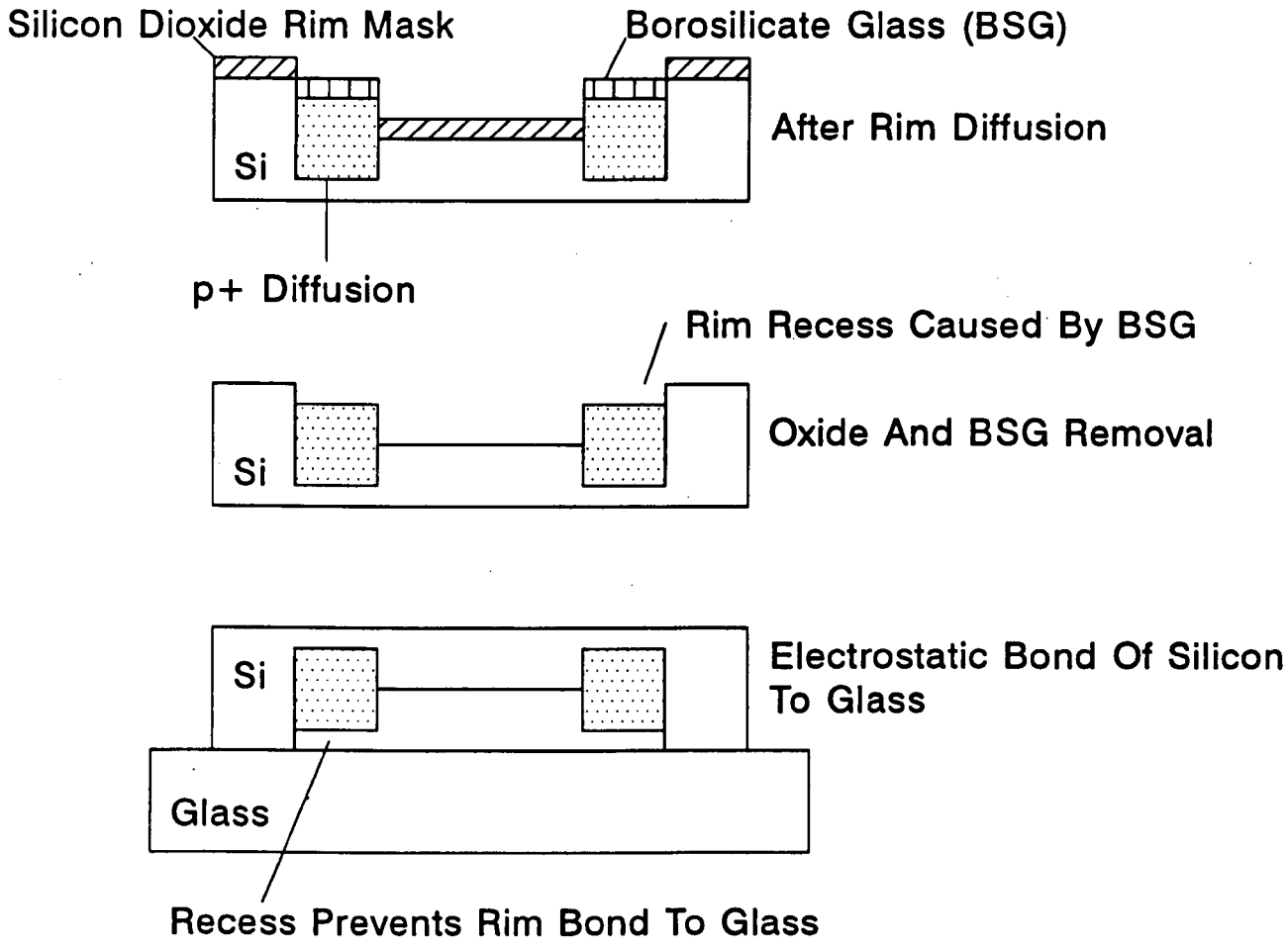

Figure 6.1 : The fabrication steps that give rise to unwanted silicon consumption and recessed rims.

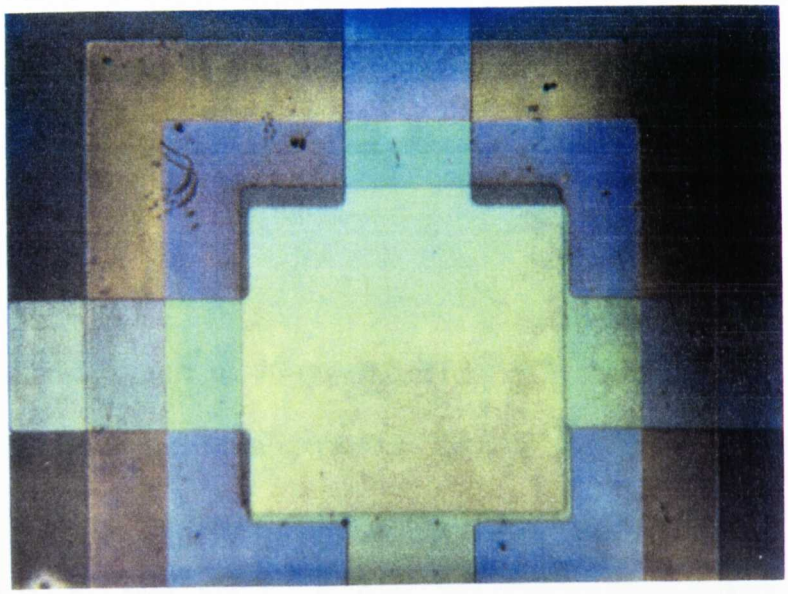

Plate 6.5 : Poor bonding of silicon to glass due to recessed rims caused by unwanted silicon consumption.

since due to etch stop behaviour, they protruded from the silicon surface slightly. Care had to be taken not to etch too much n-type silicon away because this could result in the silicon surrounding the rim area not electrostatically bonding. If a silicon hermetic seal did not surround the rims, then the silicon dissolution process attacked the structure side of the wafer immediately.

Plate 6.4(a) also indicates one of the reasons why the M2 structure was developed as a successor to the M1 structure. Misalignment of the back chamber with the rim has caused the diaphragm diffusion to be carried out on a non recessed part of the silicon which should in fact have been the rim area. Fig. 6.2 indicates this problem more clearly, where it can be seen that this misalignment has caused the diaphragm to be bonded to the glass and resulted in a sharp fragile 1μm edge. In the areas where this misalignment has occurred, the diaphragm is not supported by the rim and would probably cause fracture in a completed structure. The M2 structure overcomes this problem because the rim intrudes into the back chamber area to support the diaphragm fig. 6.3. This intrusion is sufficient to eliminate the unwanted electrostatic bonding shown in plate 6.4(a), since it allows for a large mask misalignment of the rim and the backchamber. This modification was also designed to offer better structural support for the diaphragm to minimise fracturing caused by diaphragm intrinsic stress. Furthermore, the diaphragm diffusion overlaps the rim so that the diaphragm mask mis alignment does not cause an unwanted hole in the diaphragm.

6.3.4 Narrowing of gap between glass and silicon

It was observed during bonding for some of the devices, that a bond was formed in the backchamber and tunnel areas (Plate 6.4b), rendering the devices unusable. This occurred

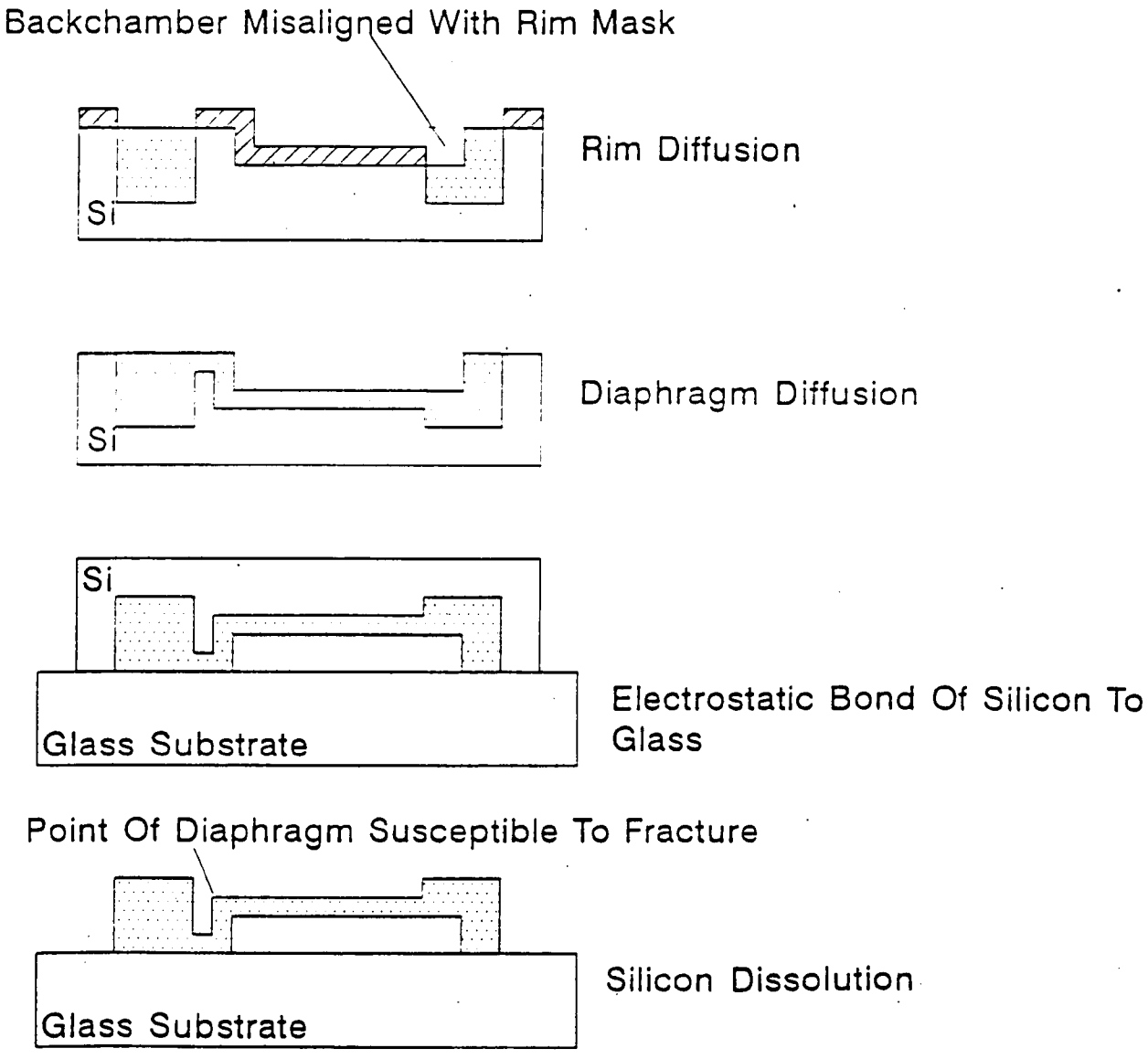

Figure 6.2 : Mask misalignment in the fabrication process leading to structure faults.

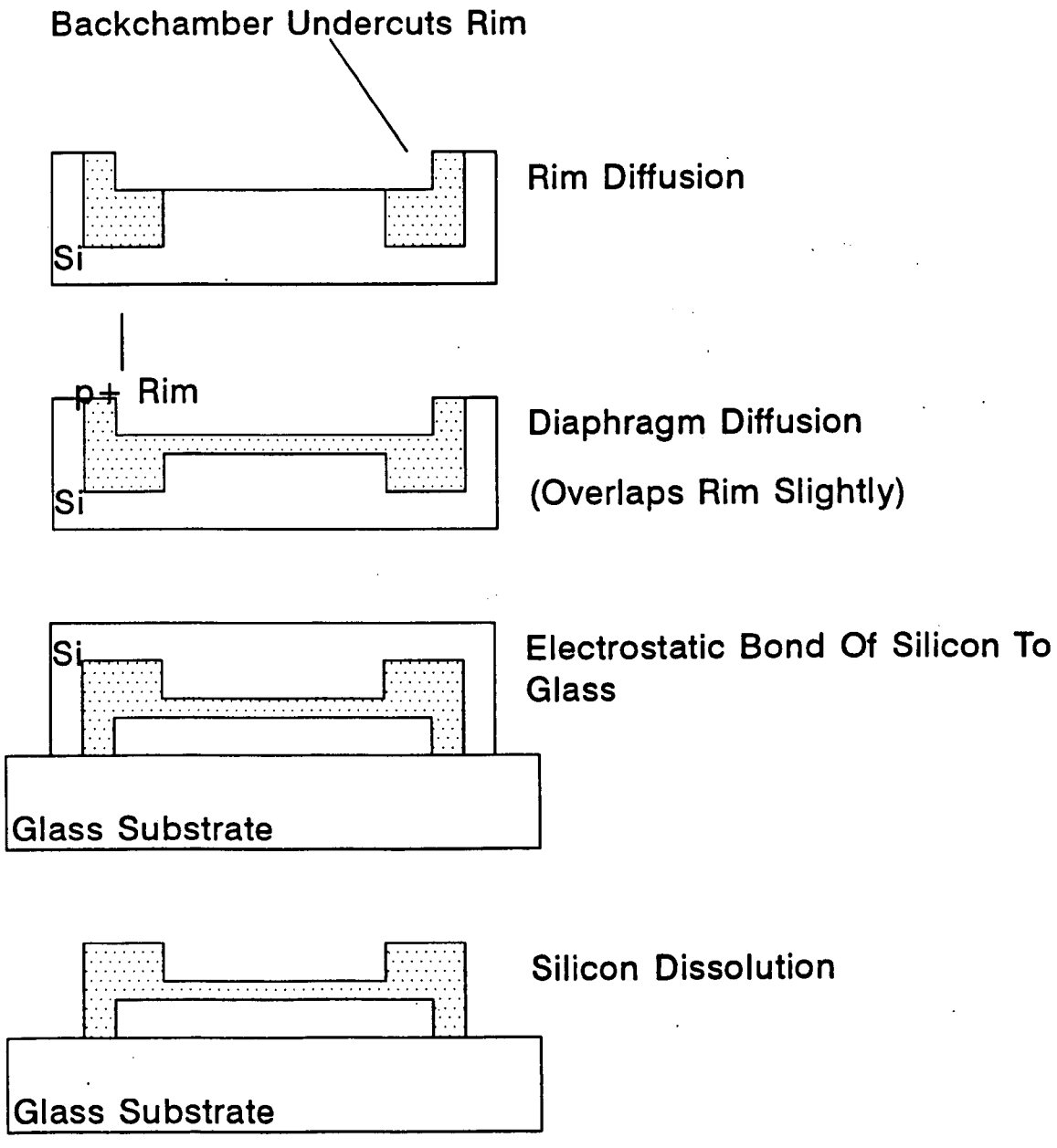

Figure 6.3 : Structure design that is tolerant of small (< 100um) mask misalignments

because the gap was less than a micron and the bonding parameters were incorrect. There are many reasons why the gap may have been smaller than expected, but it is thought that the main contributor was silicon consumption of the rims reducing the effective gap depth.

Summarising, reproducible bonding conditions were very difficult to obtain, since the parameters used were dependent on the apparatus used and previous fabrication variables of the silicon and glass wafers. (For example, nonuniform silicon consumption of diaphragm rims) Estimation of bond quality was carried out visually and was thus qualitative, which meant that actual bond strengths were unknown. Plate 6.6(a) shows an M2 doped structure in the silicon before electrostatic bonding and plate 6.6(b) shows the same stucture after bonding to the glass substrate with gold-titanium electrodes. The bonding parameters are given in the process schedule of appendix A2.1.

6.4 Die separation

For separation of individual dies, a diamond scribe was used to scribe the silicon side of the wafer using scribing borders as a guide [79,Ch 8] , these were perpendicular and parallel to the wafer flat. These scribed lines were along the natural cleavage planes of the wafer and encouraged the wafer to fracture along these axes. Due to the glass-silicon composite, fracture was difficult and some damage with loss of yield was a problem. A diamond saw would be a preferred method of dicing. It should be noted that the glass-silicon composite would not cleave from the glass side. If air pockets, due to poor bonding around areas of dust etc., were under a scribed line to be cleaved, the complete wafer could shatter because the glass-air-silicon layers interfered with the normal cleaving mechanism.

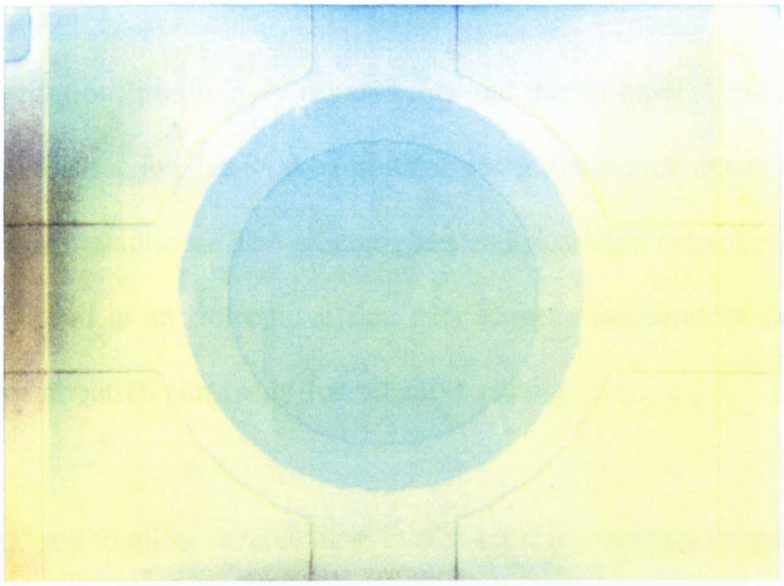

Plate 6.6(a) : Silicon wafer with M2 microphone structure before electrostatic bonding.

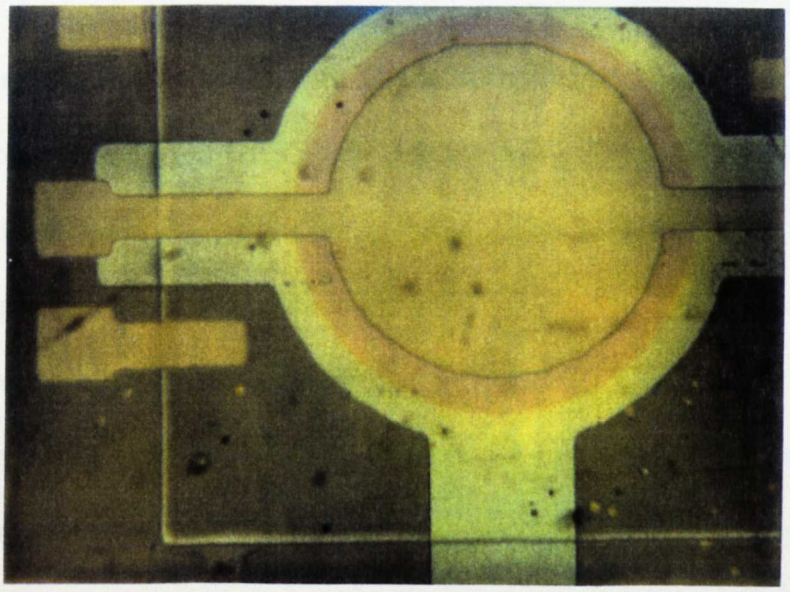

Plate 6.6(b) : Silicon wafer with M2 microphone structure after electrostatic bonding to glass with metallisation.

6.5 Wafer dissolution

Etch rate characterisation, preliminary experiments and theory have already been discussed in chapter 4 and so this section details the results of wafer dissolution experiments to achieve microphone etch stop structures. The silicon-glass samples used were between $5mm^2$ and $7mm^2$ and were etched in an isotropic silicon etch at room temperature (section 4.8) to a silicon thickness of about 80 μm ready for selective etching.

Apparatus was devised to allow safe etching in two separate reaction vessels (Section 5.4). Initially, the apparatus could only be used for etching an individual die and not a whole wafer. A holder was constructed that allowed ten or more devices to be etched simultaneously for 1 l of etchant solution. Three alkaline anisotropic etchants were investigated including TMAH [84], EDP [54] and KOH [54].

TMAH

Aluminium electrodes with a thickness of 50 nm were fabricated on a 0.5 mm thick glass electrode and etched in a 1l TMAH 5 wt.% solution at 80°C, which was doped with 15 g of silicon (3.5 wafers for a 3" x 380 μm 4 g wafer). The aluminium was found to etch at approximately 8nm/min since the electrodes were completely dissolved in just over six minutes, assuming an accurate film thickness. The n-type (100) silicon etch rate was found to be 30 μm / hr, which indicated a silicon to aluminium etch ratio of about 63. The same solution was used to try and obtain some etch stop structures, but only very damaged rims were obtained. In view of the expense of TMAH, the inconvenience of doping with silicon, the unlikely use of thin electrodes (less than 100nm) due to the low silicon to aluminium etch ratio and no characterisation of its non- electrochemical etch stop behaviour in the literature,

it was decided that this etch was not convenient for this work.

EDP

The EDP type "S" solution was used at 70 °C with continuous nitrogen purging for silicon dissolution and found to etch silicon very slowly (<9 μm/hr.). The etch appeared to be quite selective, yielding high quality etch stop structures. Unfortunately, brown residues and crystals formed under the diaphragm when the etch was complete. These crystals were seen to distort diaphragms badly and a method was not found to prevent their occurrence. In view of this, and the dangers of working with EDP, further use of this etch for silicon dissolution was not carried out.

KOH

Samples were etched in a 1l, 17 % KOH + IPA solution at 40 °C with an etch rate of 5.5 μm/hr for about 11 hrs to remove 60 μm of the remaining silicon. This temperature was chosen since it maintained a compromise between a smooth etch finish on the n-type silicon and reasonable selectivity, giving a margin of error for incorrect etch rates if the structure appeared. When the structure was visible, or the etch time interval was complete, the temperature was ramped down to 20 °C to optimise etch selectivity at the expense of etch rate and allow etching to complete. At this temperature, the etch rate was just over 1μm/hr. which meant that structures could take between 15 and 30 hrs. to complete depending on the accuracy of the previous etch stages. Excessive etching beyond these times could cause the diaphragm to be etched away depending on the diaphragm doping profile. For some samples, small nodules of silicon (< 10 μm dia) remained on the structure and the glass substrate. Trying to etch these away could thin the diaphragm to such an extent that it became

unnecessarily fragile. If previous etching was non-uniform, a corresponding non uniform etch stop structure was obtained from one side of the structure to the other due the low etch rates of the doped areas. Over etching could cause the structures to lift off the glass substrate due to attack of the glass substrate and the electrostatic bond by the etchant. Any amount of over etching did not appear to damage the gold on titanium electrode scheme.

In conclusion, the silicon dissolution stage was not optimal and gave results that were largely dependent on processing parameters from other stages such as dopant profiles, or electrostatic bond quality. Furthermore, the KOH etching system was found to be the most convenient, low cost and easy to use method of silicon dissolution of the three investigated for this work.

6.6 Trapped fluid removal

For the sublimation method for removing fluid from the back chambers, it was found that ice expansion from frozen t-butyl alcohol could cause serious fracturing of structures. The processes of sublimation of the ice to gas, under vacuum, appeared to be quite aggressive causing visible deformations in diaphragms, which could have contributed sufficient forces to cause weakening and fracture of the diaphragms and tunnel areas. Completion of this process resulted in a reduced visual surface quality of structures, where the t-butyl alcohol left behind an undesirable residue shown in plate 6.7. This residue could be removed by rinsing in IPA, with the disadvantage that backchambers re-filled with fluid and regained stiction problems. Another disadvantage of this process was that for the apparatus available, it was difficult to reduce the vacuum to less than 1.3 kPa for sublimation to occur before the solid t-butyl reverted to a liquid (Required pump down in less than 2 mins.). The resultant transition from a liquid to a gas was found to cause increased stiction effects. This problem

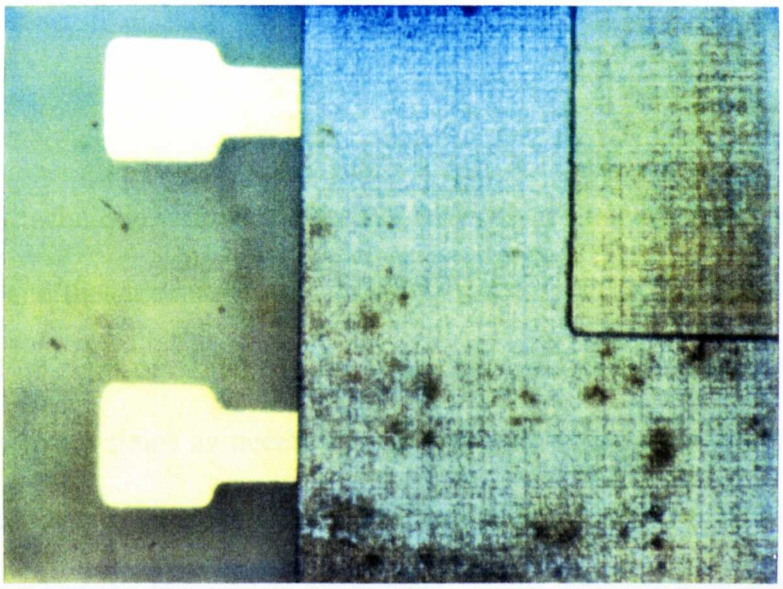

Plate 6.7 : Unwanted residue from freeze dry process.

could be solved by using a cooled holder in the vacuum system and a more rapid evacuation time. The method used was found to be about 40 % effective due to insufficient control of the melting ice.

The chloroform technique was very effective provided the backchamber was free from any traces of water and the chloroform was completely free from particulate contamination. The method showed no signs of damage to the structures and if it was unsuccessful, could be re-implemented as many times as necessary. It was important to conduct the process under laminar flow conditions, since any traces of dust on the chloroform surface were deposited on the structure when the chloroform evaporated. These deposits were found to reduce gold ball bonding success.

For dry diaphragms that collapsed at a later stage due to application of a bias voltage, it was possible in some cases to reverse the collapse by putting the structures in a dry cold atmosphere of 0°C for 1 hr. It was thought that contraction of the diaphragms increased their tension to an extent that they overcame the forces attracting them to the substrate. This technique did not work for diaphragms with stiction caused by residual liquid in the back chamber and was thus only applicable to dehydrated backchambers.

6.7 Completed structures

This section gives details of the completed structures and is supported by photographic results. These photographs should help clarify issues raised in other sections of this thesis regarding structure fabrication.

Plate 6.8 shows one of the first square diaphragm structures that was fabricated. The p^+ structure can be seen on the glass substrate without any electrodes. The diaphragm has collapsed and is held to the glass by stiction and the structure has been scratched. The glass surface appears to be much smoother than the structure rim where the rim shows evidence of boron pitting. For this early structure the diaphragm diffusion was the same size as the rim diffusion mask. Mask misalignment can be seen which has resulted in the step seen on the right hand side of the picture.

Plate 6.9 shows an early fabrication attempt at making an array of four diaphragm structures. The crosses were for glass and silicon wafer registration at the electrostatic bonding stage. One of the diaphragms was observed to be flat and intact, but the other three were fractured. The electrodes consisted of a 65nm titanium layer and could not be gold ball bonded. The occasional crystalline clusters seen in the bottom right hand corner of the photograph were undissolved n-type silicon. Due to the observed fracturing and damage to the structure it was decided that working on array fabrication was too complex and subsequently, only single microphone structures were developed.

Plate 6.10 shows the M1 microphone structure with titanium electrodes. The diaphragm was completely flat and the etch surface was free from boron pitting. Only very small quantities of undissolved silicon remain. Plate 6.11 shows an identical structure from the same batch that has fractured and buckled. The tensile stress in the diaphragm, due to boron doping, has caused the diaphragm to show positive curvature or a negative bending moment which can be accounted for in the discussion of section 8.0. The picture inset of plate 6.11 shows the start of the fracture and it would appear that the ragged edges of the rim mask diffusion

Scanning Electron Microscope (SEM) Photographs

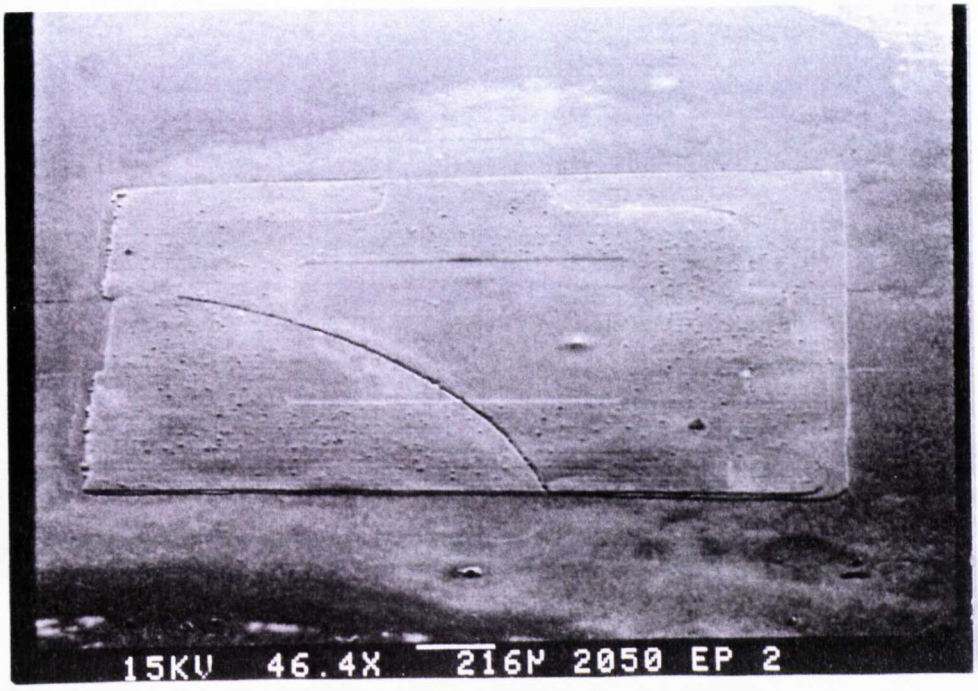

Plate 6.8 : Initial fabrication results for silicon p+ microstructure on glass. (No electrodes)

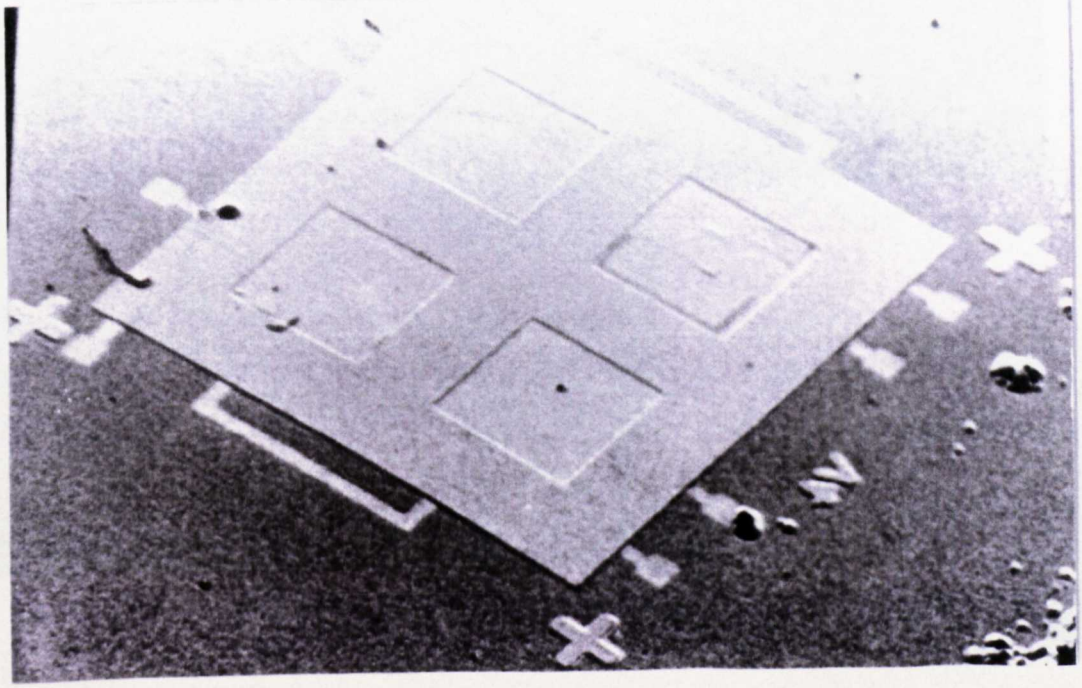

Plate 6.9 : Initial fabrication results for 2 x 2 silicon microphone array prototype with titanium electrodes.

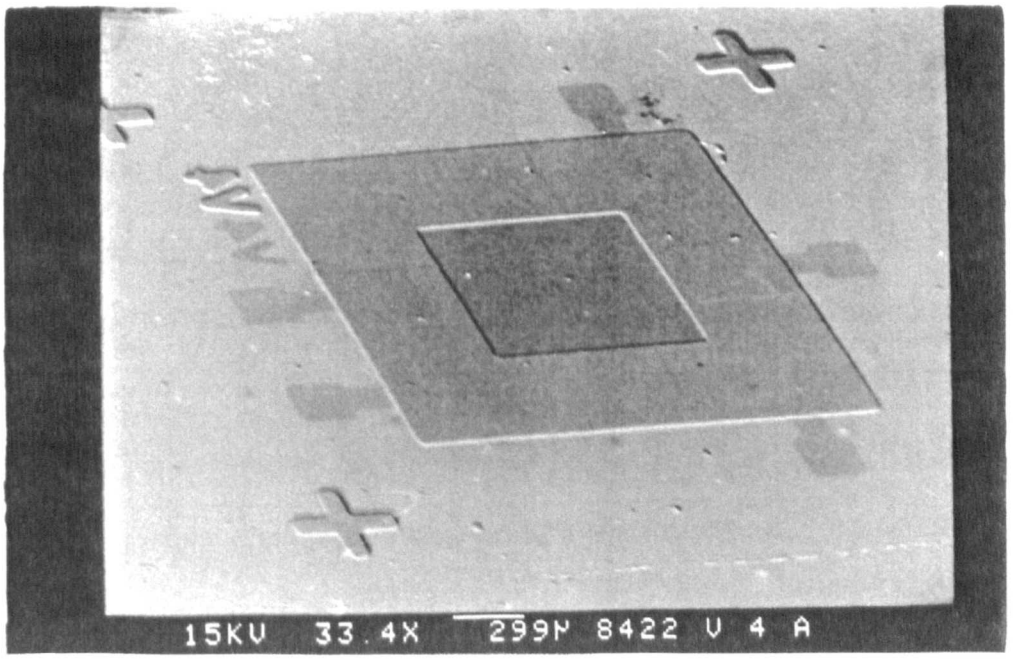

Plate 6.10 : Silicon p+ microphone (M1) on glass (2 x 2 mm^2)

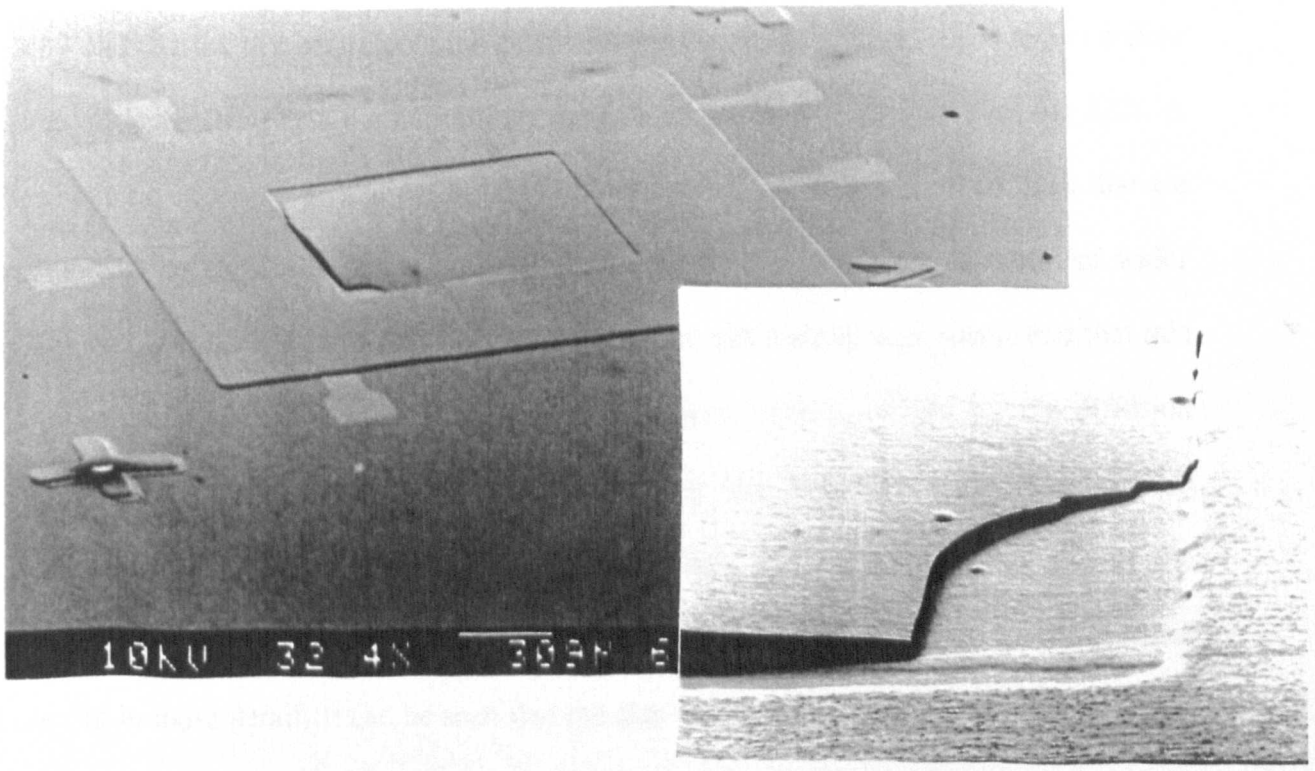

Plate 6.11 : Silicon p+ microphone with a fractured diaphragm.
(Note : The intrinsic tensile stress is causing a downward curvature of the diaphragm)

could have been responsible for initiating the fracture due to stress concentration effects. This problem could have been reduced by using high quality chrome masks.

Plates 6.12 and 6.13 show the M1 and M2 structures respectively for comparison purposes. However, the M2 structure has been dehydrated and the M1 structure is shown in IPA, which is evident from observation of the air bubble trapped underneath the M1 diaphragm. Both structures were made using the processing schedule of appendix A2.1 and therefore have gold on titanium electrodes that are suitable for gold ball bonding. It can be seen from the two photographs that the etch stop process control was such that very few clusters of undissolved silicon remain and the devices appear to be uniform when viewed optically. The outline of the tunnel and backchamber areas underneath the p^+ rim can be seen for both structures, since the tunnel area of the rim diffusion is raised above the remainder of the rim area, due to the depth of the back chamber. The darker shadowed area, which is square for M1 and circular for M2, represents the extents of the diaphragm diffusion and shows a clear overlap with the rim (This overlap allows for 200 μm of mask mis-alignment for M2). A pattern can be observed on the p^+ structure which consists of a fine mesh of lines that are perpendicular to each other. The lines fall perpendicular and parallel to the original wafer flat, indicating that they are related to crystallographic orientation. It is speculated that this pattern is the result of edge dislocations in the silicon crystal, caused by the diffusion process, that have been exposed and highlighted by the etching process. (Section 8.0 discusses the literature available on this phenomena) Plate 6.14a shows one of the electrodes entering the tunnel into the back chamber and plate 6.14b shows the etch surface of the rim in more detail. It can be seen that the etch pattern has a high density of these lines and that they are perhaps only a micron or so in width and hundreds of microns in length.

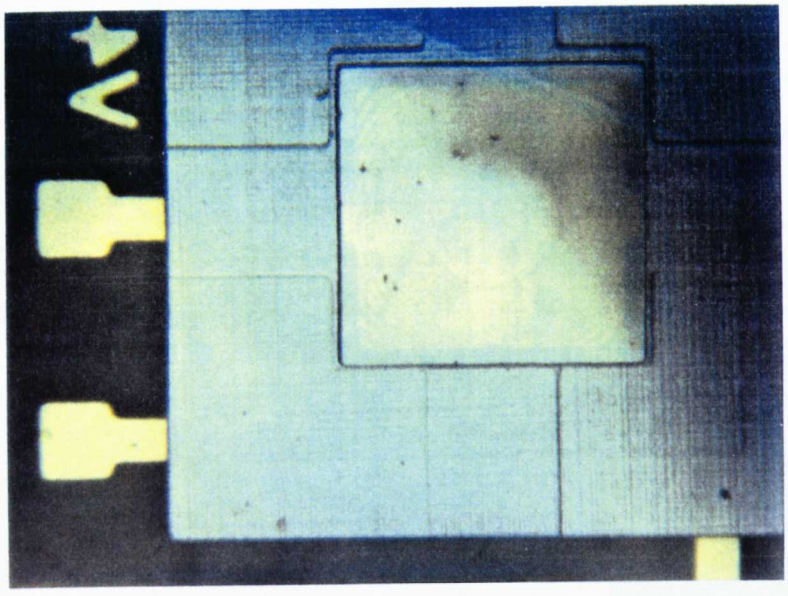

Plate 6.12 : M1 p^+ Microphone structure on glass with gold electrode bonding pads.

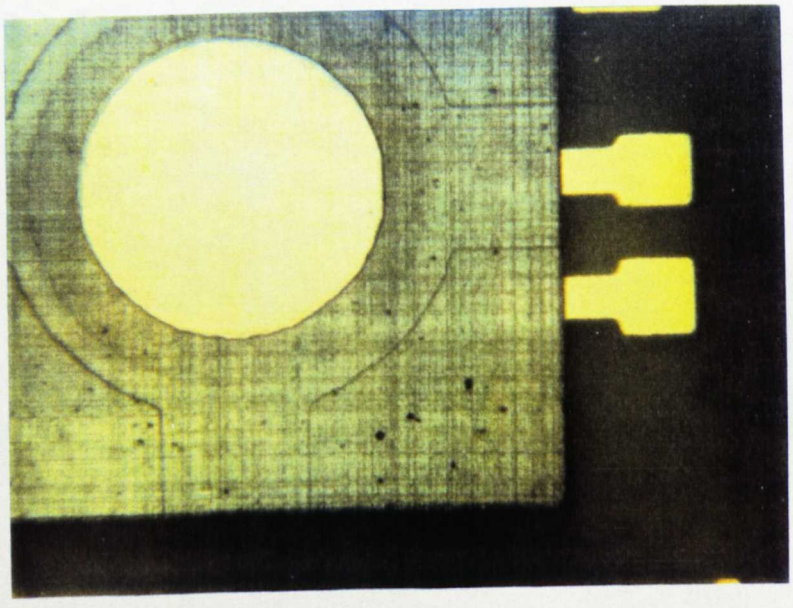

Plate 6.13 : M2 p^+ Microphone structure on glass with gold electrode bonding pads.

(a)

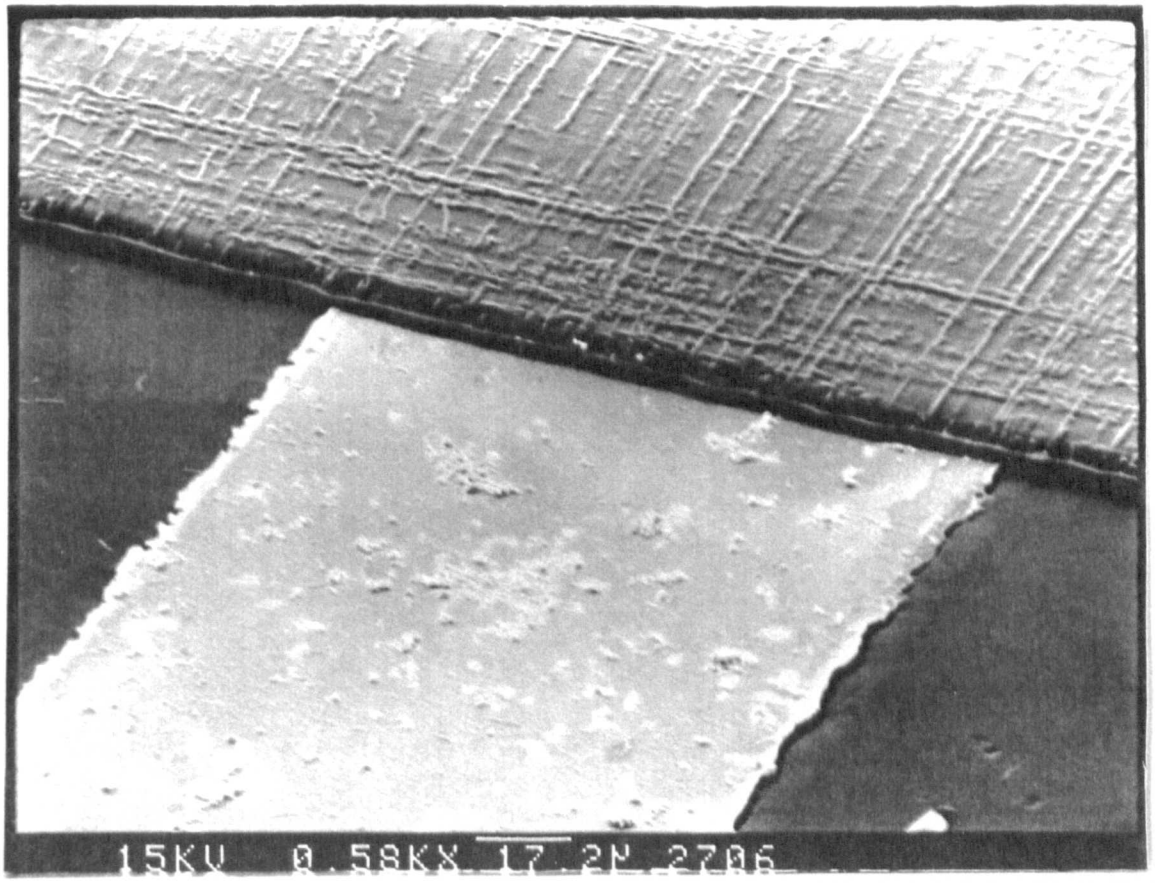

(b)

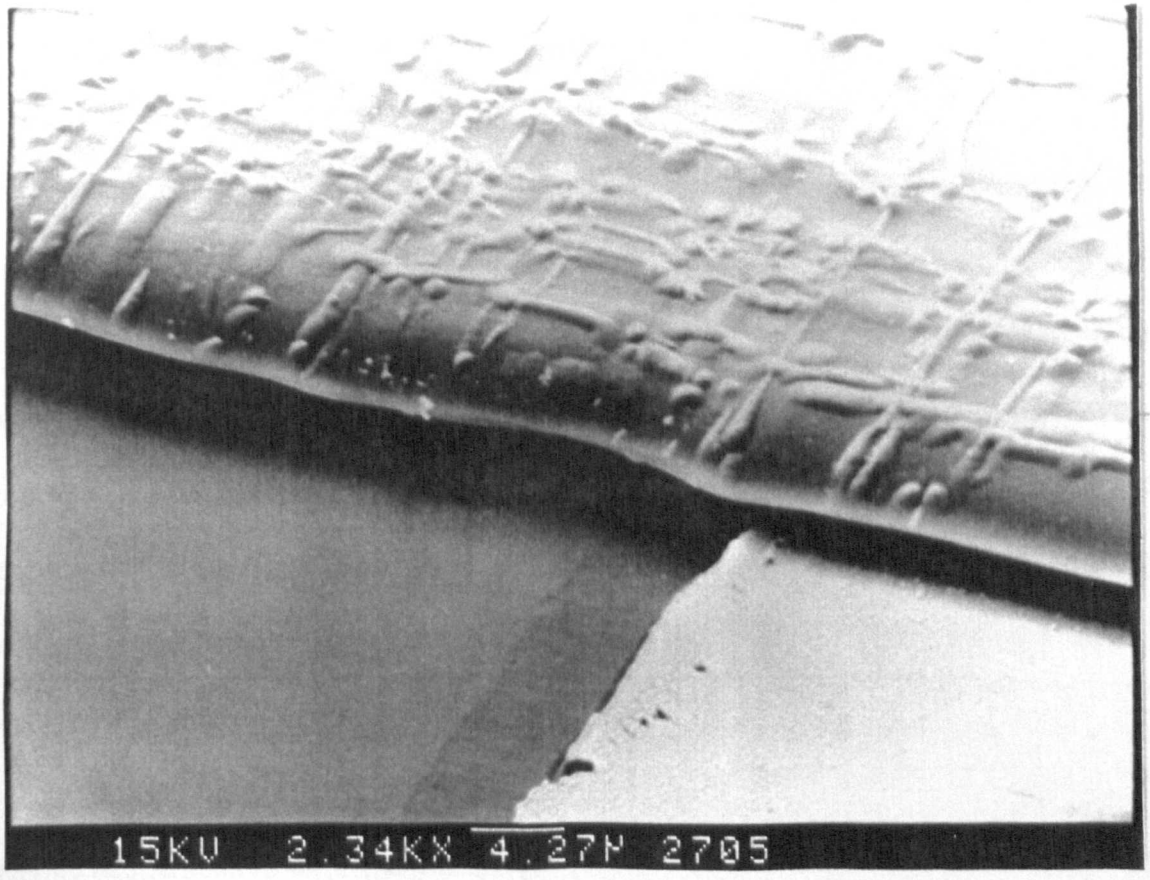

Plate 6.14(a), (b) : Electrode entering the acoustic tunnel of a p^+ silicon microphone on a glass substrate.

Atomic force microscopy (AFM) has indicated that they protrude from the rim surface. If these lines are due to thousands of edge dislocations, the diffused boron may have increased concentration in these areas, resulting in a better localised etch stop and hence the observed features. These features were not found on the polished surface of a p^+ doped wafer until it was etched in KOH for a significant period. (Dislocations are also pushed further into the diffusion profile)

Other factors influencing the surface roughness of the structures, but not the cause of the mentioned regular patterns, are

i) The roughness of the n-type surface during etching, which is proportional to the original roughness of the back of the wafer.

ii) The overall roughness of the etched surface, which is proportional to the original roughness of the polished surface diffused into.

An additional surface feature, that was observed, is shown in plate 6.15(a) and (b). Here conical protrusions with a hole in the centre are seen in a diaphragm. This feature is the result of a pit caused in the polished side of the wafer during the diaphragm diffusion. This unwanted feature was eliminated by introducing a small quantity of oxygen (ml/min) into the furnace during the boron pre-deposition stage. (See section 6.1.2) It would appear from the photograph that these pits have punched their way through the diaphragm diffusion and possibly plastically deformed or damaged/eroded the p^+ silicon. These features could be investigated as microstructures in their own right.

Many etched structures were fractured, especially in the diaphragm area (Plate 6.11). This

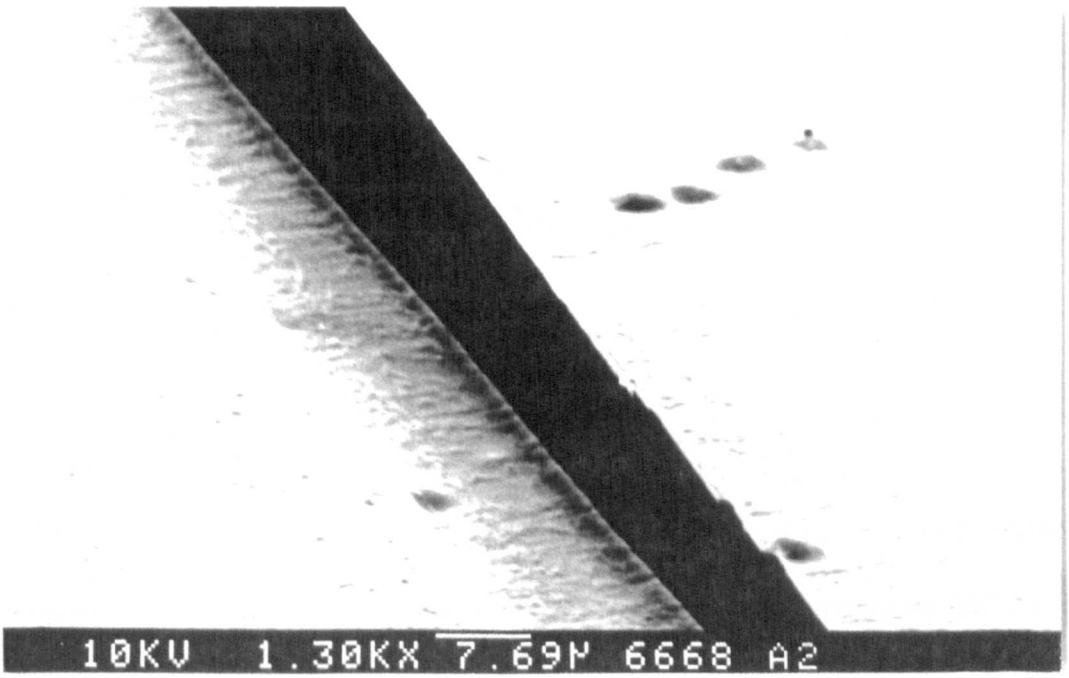

Plate 6.15(a) : M1 microphone that has fractured near the diffused rim. (Pitting effects that can be caused during diffusion are clearly visible)

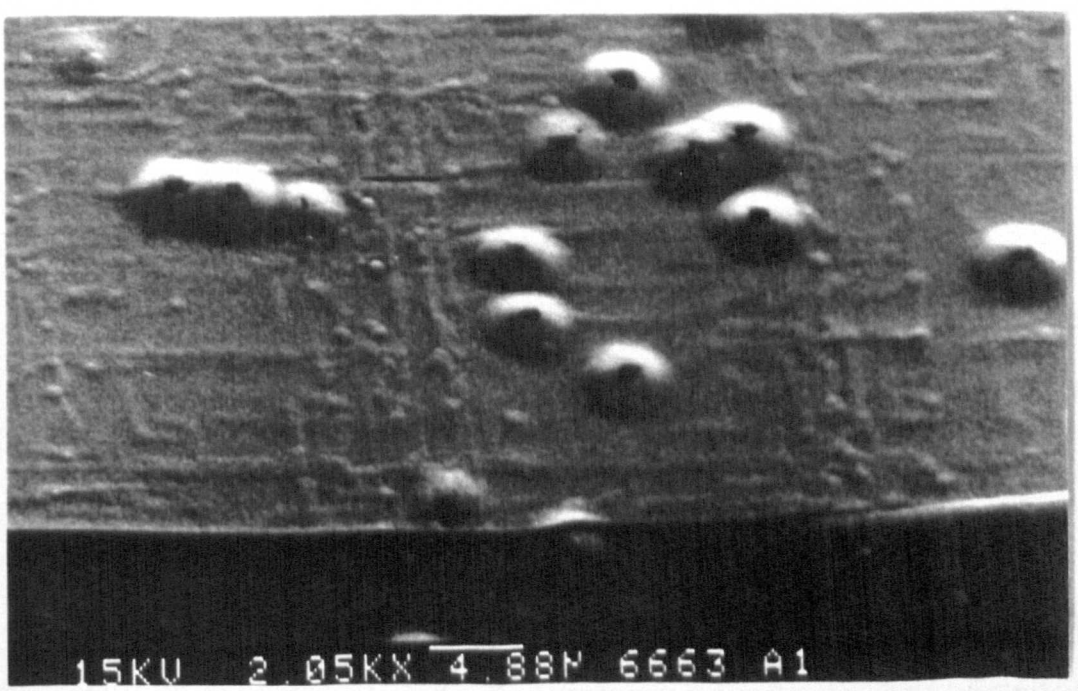

Plate 6.15(b) : Higher magnification of pitting effects from the top of the silicon diaphragm where n-type silicon has been dissolved away in KOH.

was attributed to unavoidable poor handling, trapped air, turbulent effects in the etching process or inbuilt stress in the structures, caused by the diffusion of a high concentration of boron atoms into the silicon lattice. It is known that oxidation of a diffused layer can cause stress build up due to segregation effects in the SiO_2-p^+ interface [85].

6.7.1 Fracturing

For the first square structures that were fabricated (Plate 6.8), fracturing could occur and was attributed to the following causes:-

i) Poor masking or mask damage

ii) The corners of the square backchambers and diaphragms concentrated stresses. It is thought that in some cases, this concentrated stress could have exceeded the fracture stress of silicon.

iii) Tensile stress as a result of the diffusion profile (See section 8.0) could cause the diaphragms to buckle and in some cases fracture. This stress contributes to (ii)

iv) Some fractures were seen to extend along the tunnel edges indicating a point of stress build up. It is thought that the stress in the rim diffusion is higher than the diaphragm. Most of the rim is bonded to the glass substrate, but the tunnel regions are not, which allows deflection of the rim section in this area.

v) During silicon dissolution, trapped air in the backchamber trying to escape put pressure on the thin p^+ diaphragm and caused a positive curvature above the rim. In extreme cases the diaphragm was observed deflecting which caused diaphragms to fracture.

vi) For the square diaphragm mask design, misalignment of the backchamber and rim could cause a situation where the diaphragm was bonded to the glass substrate fig 6.2

and a very thin p^+ corner was exposed. This represented a very weak point and structures with this defect were all fractured.

vii) Dehydration using t-butyl alcohol (see section 5.5)

The problems of i) and vi) were eliminated for the circular microphones M2 by careful mask design. The backchamber was recessed under the rim to make the diaphragm more tapered. ie. A thick rim supporting a thinner rim [86]. Since the diaphragm mask overlapped the rim and the backchamber was recessed, no unwanted gaps appeared in the diaphragm and no bonding of the diaphragm to the glass substrate occurred, due to small mask misalignment errors. The diaphragm suspension stability was also improved by this technique.

6.7.2 Under etching

It was found for some structures, after investigation with an optical microscope, that the rim bond was undermined by the KOH + IPA etch. This could be attributable to the silicon dioxide interlayer of the bond being etched in addition to the glass substrate. It appeared that once the bond was damaged, the interface was etched away in a few hours. In extreme cases the structure came away from the glass substrate.

It is thought that the rate of this under etching depends on

i) The type of glass used for the substrate and its etch rate in the silicon dissolution stage.

ii) The strength of the electrostatic bond, which can be controlled with the bonding parameters.

iii) The composition and type of selective etchant used for the wafer dissolution process.

Plate 6.16 (a) shows a completed M1 microphone structure and (b) shows the underside of the same structure. The etchant attack can be clearly seen in the areas where the rim should be bonded to the glass. Only islands of bonding remain, which would cause the stress distribution throughout the whole structure to be non uniform and unpredictable, with a direct influence on the sensitivity of the device. It was also apparent from study of this problem that small ($< 1\mu$m width) linear air gaps remaining in the rim after electrostatic bonding acted as channels for the etchant to undermine the bond. These channels were caused by the 100nm step in the electrode (ie Surrounding the electrodes in the rim area) and the step at the edge of the diaphragm diffusion, caused by a small amount of silicon consumption. This latter case was resolved in the M2 design by reducing the diaphragm diffusion boundary and implementing a rim over hang to support the diaphragm. The former problem could only be minimised by reducing the thickness of the metallisation.

6.7.3 Electrode quality

Plate 6.17 shows the results, which were only apparent after silicon dissolution, of poor adhesion between the gold and the titanium layer. This result rendered the completed device unsuitable for electrical test. In this case, the poor adhesion could have been caused by the formation of titanium oxide. The gold film also shows stress effects, since it has curled up, which could have been caused by incorrect deposition rate or substrate temperature.

The thin film adhesion, conductivity and etch resistant properties were considered to be very important in order for the film to survive the wafer dissolution process, be suitable for wire bonding and have low unwanted series resistance. The total thickness of film could not exceed 100nm since this was found to disrupt the electrostatic bonding of the rim. For the

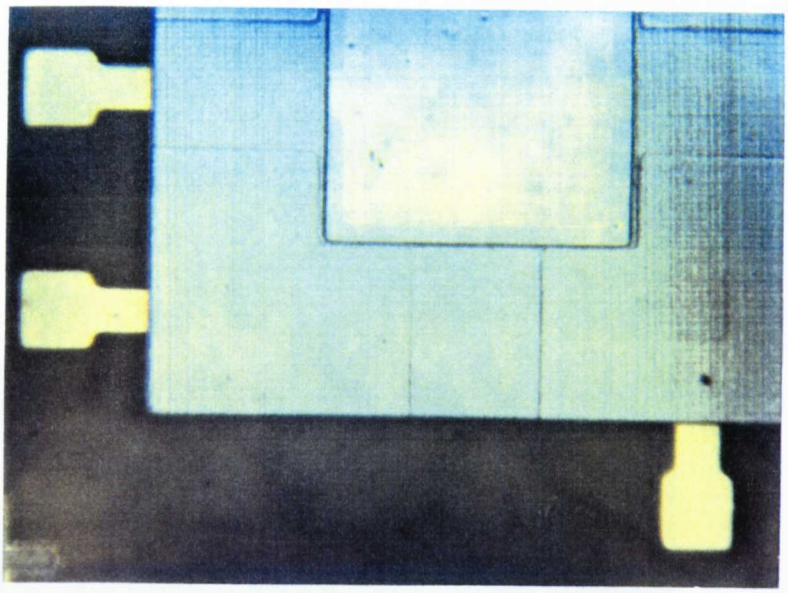

Plate 6.16(a) : Top view of a silicon microphone after KOH etch.

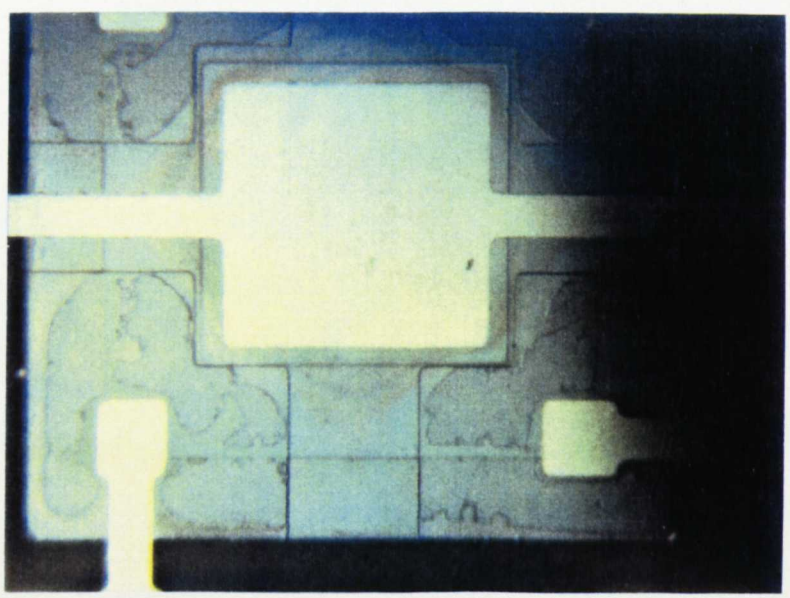

Plate 6.16(b) : View of above microphone through glass substrate showing etch damage to the electrostatic bond.

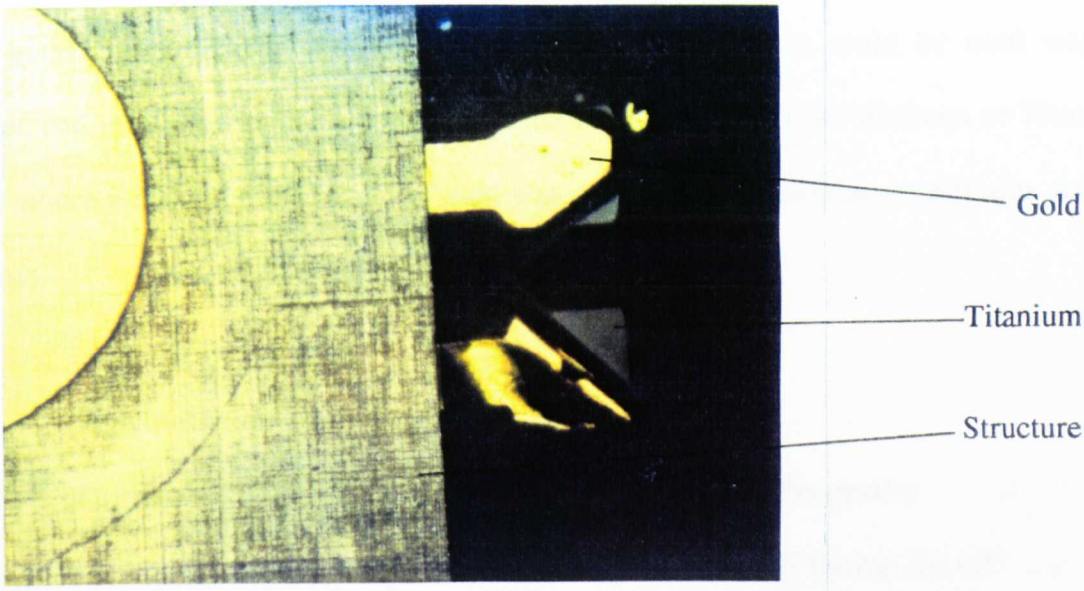

Plate 6.17 : Poor gold adhesion to the titanium layer.

two layer metallisation scheme that was chosen it was desired to maximise conductivity while retaining good adhesion. The minimum thickness of titanium that could be used was investigated and the following table summarises the results. A total film thickness of 70nm was used, where a maximum of 60 nm of gold was deposited to maximise experiments and reduce costs.

	Thickness /nm		
Sample	**Titanium**	**Gold**	**Observed Film Properties**
A	10	60	The film came off during lift off
B	15	55	65% of the film remained after lift off
C	25	45	Good adhesion was observed
D	40	30	Good adhesion was observed

Note : For this table a 10 min. HF etch of the glass in the electrode area was carried out to promote titanium adhesion.

These results indicate that a minimum titanium film thickness of about 25nm is required to provide good adhesion of the gold to the glass. Samples C and D were subjected to a 48 hr. etch in a 40% KOH solution at 50 °C to investigate the stability of the films in aggressive alkali etch conditions. No deterioration of the electrodes was observed although the glass surface was roughened. Samples of C and D, both etched and unetched were tested for suitability for gold ball bonding. The gold ball bonding was carried out at 150 °C and the following results were obtained. Where bonds were successful, the gold ball bond pull test was carried out with a pair of tweezers.

Sample	Average results for gold ball bonding
C Etched	Bond high quality, gold wire broke on pull test
C Unetched	Bond high quality, gold wire broke on pull test
D Etched	Gold ball bonding difficult, poor results
D Unetched	Bond pulled away with part of gold metallisation

From these results it was concluded that a gold film thickness of greater than 45 nm was required to provide a suitable film for gold ball bonding. This thickness is 55nm below the recommended thickness required for gold ball bonding. To determine the gold ball bond resistance, ten of each of the type C samples for the etched and unetched samples were measured. The measurement was for the combined gold ball bond and the fish tail bond, and values ranging from 0.1-0.4 ohms were measured. The resistance of the gold film, assumed to be negligible in this case, was ignored. Each bond was assumed to be about half the resistance of the reported value range. There was no measurable difference in the resistance for bonds for the etched and unetched cases. This indicated that the etching does not affect the bond resistance.

6.8 Packaging and wire bonding

Microphones were glued with epoxy onto a chip carrier with gold pads, to allow gold ball bonding from the structure. Successful packaging required a great deal of precision, since it was very easy to damage the microphone structures when positioning and glueing. Plate 6.18 shows the gold ball bonding apparatus used for wiring a microphone structure glued onto a TO5 header. The header is shown mounted in an aluminium block for substrate heating. It was found that the ultrasonic energy generated by the gold ball bonder was

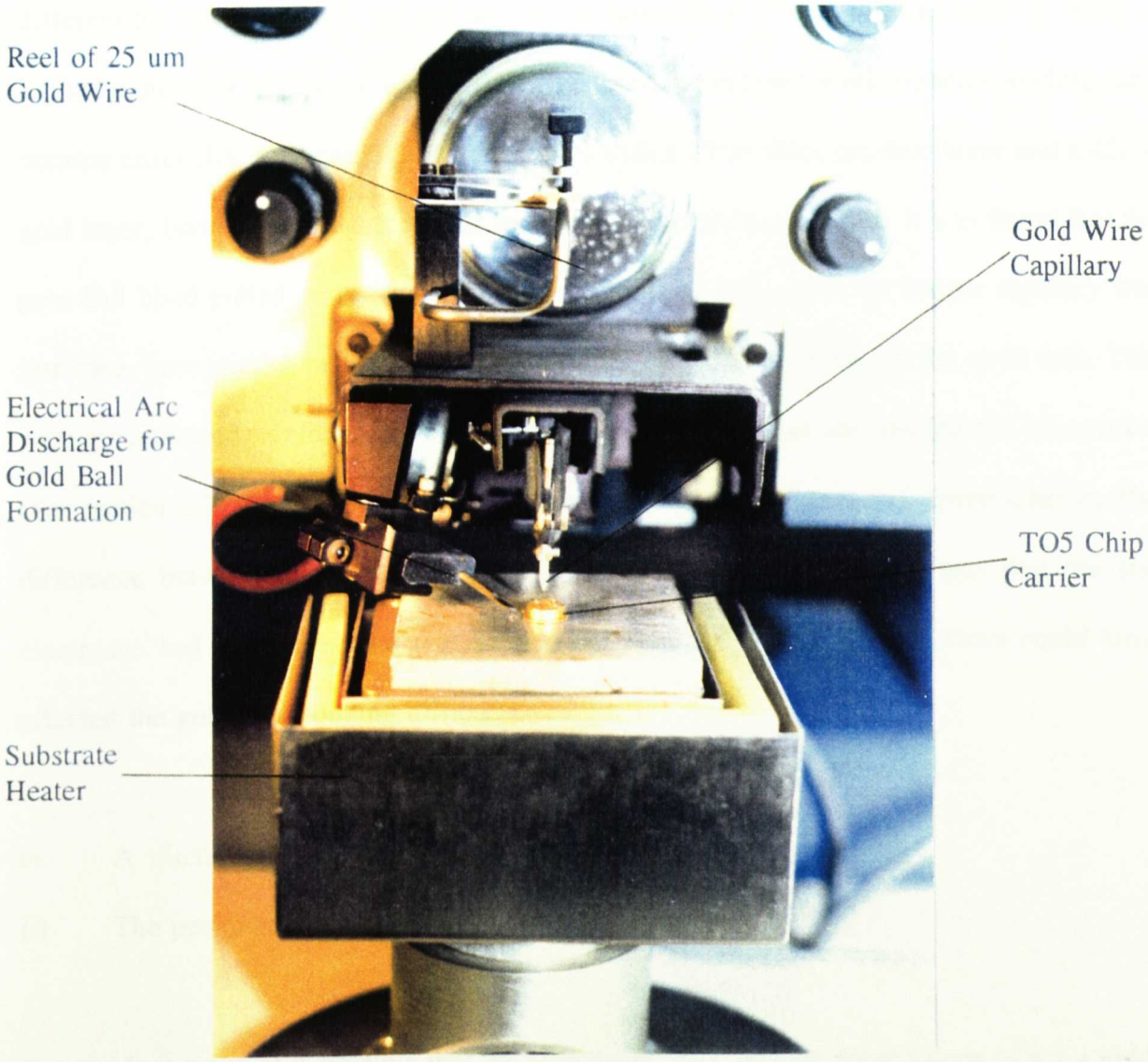

Plate 6.18 : Gold ball bonding apparatus.

sufficiently localised that it did not fracture the structures. However, making successful gold ball bonds (Plate 6.19) was complicated by the fact that the bonding parameters could be different for each structure, even though a test substrate was used prior to bonding. Only a limited number of bonding attempts could be carried out before the microphone bonding pads became unsuitable for bonding. For electrodes with a 25nm thick titanium layer and a 45nm gold layer, bonding was unsuccessful for 85 % of the devices bonded. It was found that the gold ball bond pulled away from microphone electrode pad, when the bonder capillary was retracted, removing a small circle of gold with the same diameter as the gold ball. This problem indicated a gold adhesion or morphology problem. This was unexpected, since trials (See section 6.7.3) indicated that the bond should be good for this metallisation scheme. The difference between the microphone electrodes and the test electrodes was that the test electrodes had not undergone the electrostatic bonding process. Two factors could have affected the gold ball bonding difficulty

i) A silicon gold interface formed at 350 °C

ii) The prolonged exposure to temperatures in excess of 300°C.

For the first point, it is possible that the gold layer could contain some silicon, since a gold-silicon eutectic is formed at 350 °C. This can only be avoided by careful time and temperature control of the electrostatic bonding process.

The second factor was investigated by subjecting freshly deposited films, according to the unetched sample C specification (Section 6.7.3), to temperatures of between 300°C and 350°C for three different time intervals and then trying to gold ball bond to the annealed

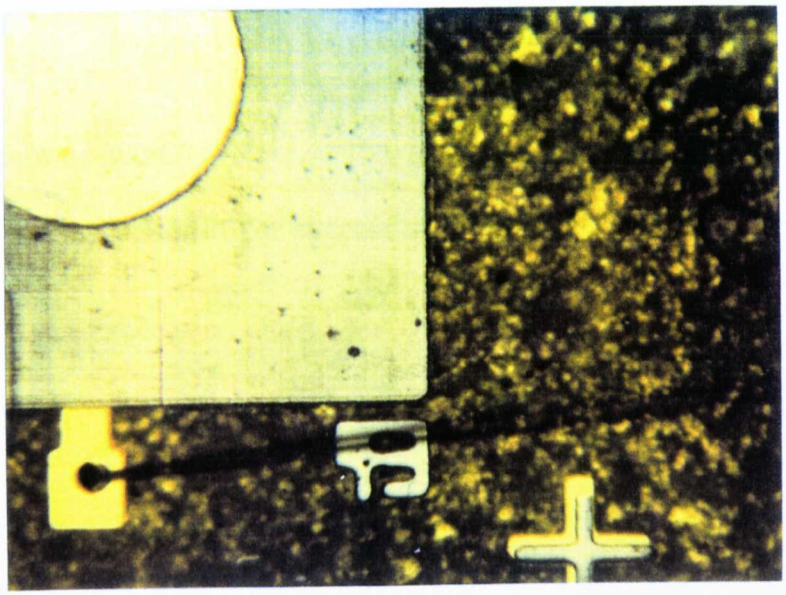

Plate 6.19 : Successful gold ball bond to the M2 structure with 25 um gold wire.

films. The results for the gold ball bonding are given as a percentage for 10 bonds on each sample.

For a temperature of 300°C

Time /mins	**% Result for success of Gold Ball Bonding**
15	10
30	7
45	1
60	0

For a temperature of 350°C

Time /mins	**% Result of Gold Ball Bonding**
15	6
30	2
45	0
60	0

These results show that annealing the films causes a change in the morphology of the gold film which in turn affects the success rate of the gold ball bond. It is also clear that the higher the temperature, the more rapid the change. It was also found by further experimentation that a 60nm thick gold film showed the same behaviour, but over longer anneal times, which suggested that a thicker gold film takes longer to be altered than a thin one. These results can be correlated with the 15% of microphone structures that could be bonded successfully, since they had a short electrostatic bonding time of less than 30 mins.

at a lower temperature of 300°C. Additionally, non-uniformity of the gold film thickness may have caused some electrodes to be thicker than others, which would also help to reduce the likelihood of the onset of gold film deterioration. For anneal times exceeding two hours at 350 °C, the electrodes changed colour from gold to blue. The resistance of these blue electrodes was measured to be several hundred ohms, which indicated a complete change in the film conductivity properties, since the initial resistance was fractions of an ohm.

Subsequent to finding that annealing a thin gold film causes changes in its properties, further research of the literature was carried out. Results of which are given in the discussion (Section 8.0) of this work. Further investigation of the gold films with scanning electron microscopy was not undertaken, since gold film morphology has been studied extensively by other researchers.

7.0 TEST & MEASUREMENTS

The following chapter details the few areas of structure characterisation and electrical measurement that were possible within the framework of the research period. Some of the characterisation experiments required the fabrication of special test structures, details of the fabrication procedures for these are briefly outlined where necessary. Due to poor yields and resource limitations it was not possible to undertake an extensive detailed electrical test program in order to verify implemented microphone characteristics with design specifications. The results from this chapter can only offer a guide to the possible characteristics of the new devices while highlighting the difficulties of testing miniature silicon electrostatic microphones.

7.1 Measurements of metallisation electrode and p^+ silicon sheet resistance

It is very important for the microphone structure and metallisation to have the highest possible conductivity in order to prevent undesirable resistances from reducing the electrical sensitivity. The ideal resistance for the metallisation and the p^+ silicon would be zero ohms respectively. For the experiments of this section it was assumed that the films to be measured could be fabricated with a high degree of uniformity.

An investigation of the resistance and sheet resistance of different track widths of p^+ silicon was made using a specially designed test structure shown in fig. 7.1(a). It comprises a symmetrical "Van der Pauw" structure [87] that can be used to determine the sheet resistance of the test structure independently of its size. The same structure, with simplified masking requirements, was used to determine the resistance and sheet resistance of the metallisation scheme on glass and is shown in fig 7.1(b). The rest of this section outlines the principle of

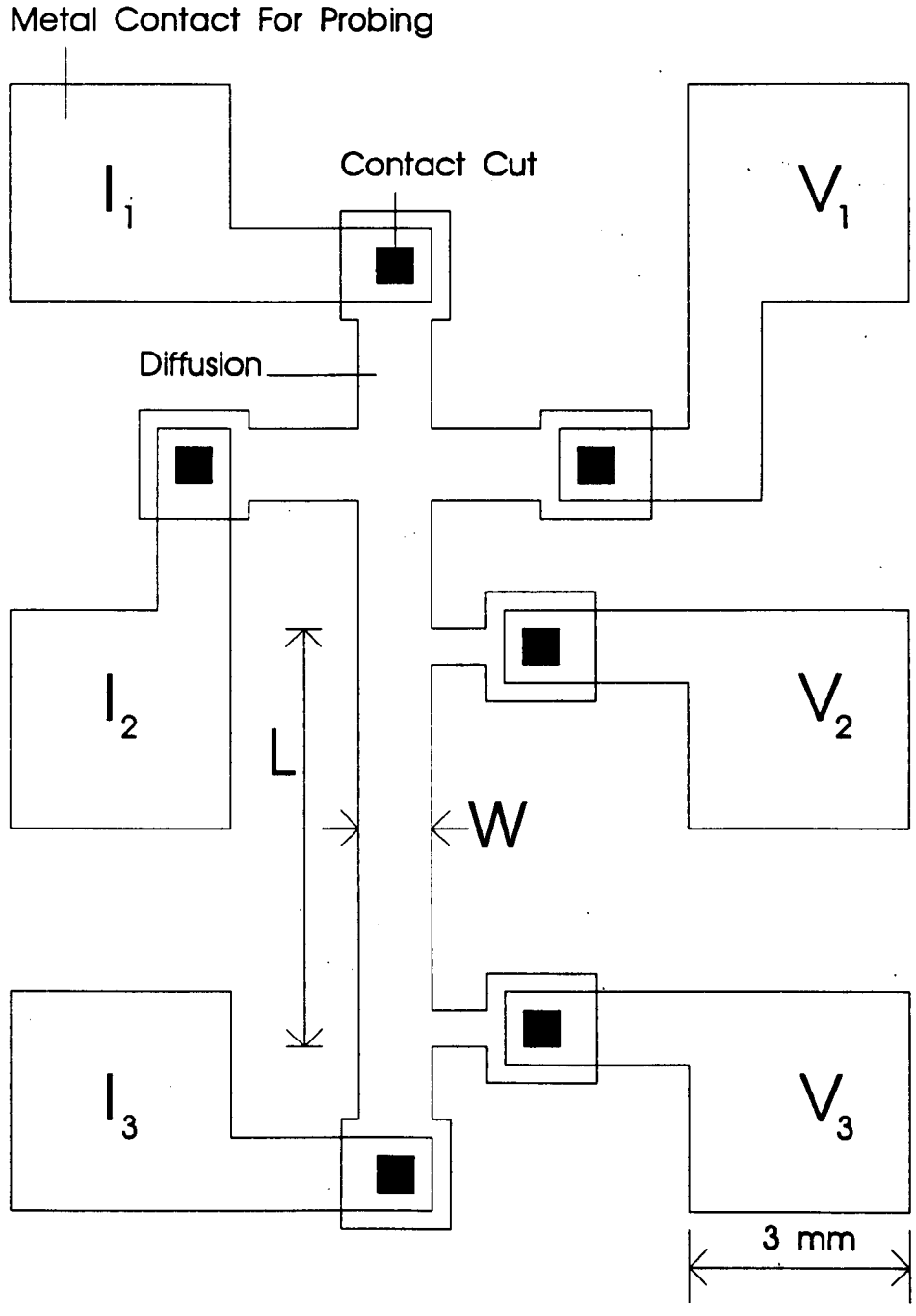

Figure 7.1(a) : Test structure for measurement of p^+ silicon sheet resistance, with built in compensation for lithography errors.

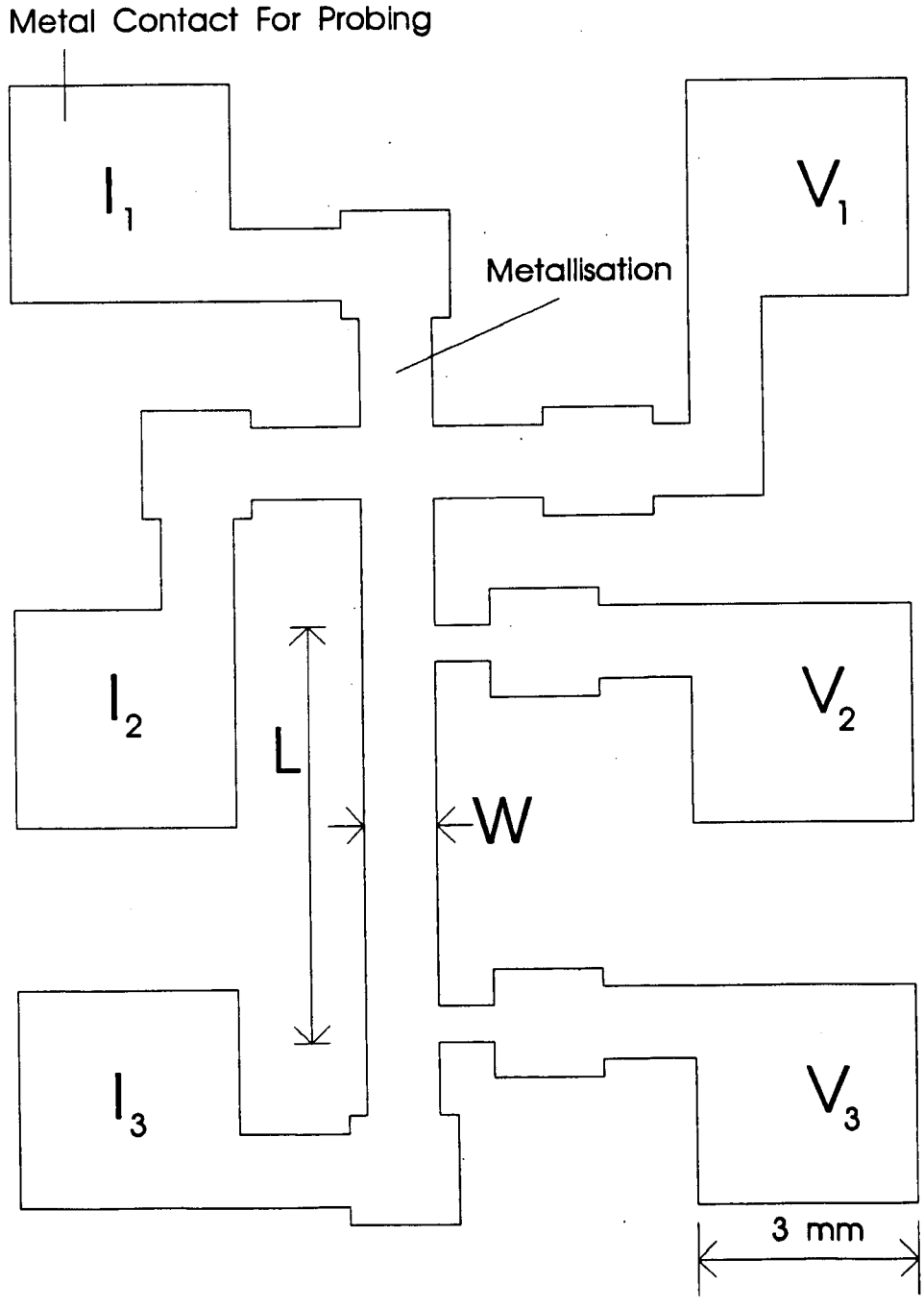

Figure 7.1(b) : Test structure for measurement of metallisation sheet resistance.

measurement for these two test structures.

A known current I_a is forced between I_1 and I_2 and the potential difference ΔV_a between V_1 and V_2 is measured, which enables the sheet resistance of the thin film under test to be evaluated from the following equation. (See ref. [89] for derivation details)

$$R_s = \frac{\pi \Delta V_a}{I_a \ln(2)} \tag{7.1}$$

Furthermore, the track width W could be determined from the test structure by forcing a known current I_b between I_2 and I_3 and measuring the potential difference ΔV_b between V_2 and V_3. The resistance R of the length L is given by

$$R = \frac{\Delta V_b}{I_b} \tag{7.2}$$

and also

$$R = \frac{R_s L}{W} \tag{7.3}$$

thus by substituting equations 7.1 and 7.2 into 7.3 and rearranging for the linewidth W the following expression is obtained

$$W = \frac{\pi L}{\ln(2)} \frac{\Delta V_a}{I_a} \frac{I_b}{\Delta V_b} \tag{7.4}$$

The length L can easily be measured with a travelling microscope and is made much larger than W so that process tolerances have minimal effect on the determination of W.

This structure was chosen because sheet resistance measurements were independent of structure size and contact pads could be large for easy probing. An additional feature was the measurement of W which allowed the lithographic process to be evaluated.

The following two sections discuss the results from preliminary investigations for the metallisation and p^+ doped silicon test structures respectively.

7.1.1 Metallisation

Measurements were carried out to determine values for the resistance of the 45 nm gold + 25 nm titanium metallisation scheme for different track widths. From the small quantity of data that was obtained in table 7.1, it would appear that the electrode sheet resistance was two or three times the calculated value, depending on the track width. The measured sheet resistance decreases with increasing track width. These higher than expected values could be due to metallisation thin film effects or the ragged edges of the lithography/lift off processes having an influence on the film resistance. For the calculations of resistance, the titanium film has been neglected since the sheet resistance of a 25nm titanium film is 38 times larger than the sheet resistance of a 45nm gold film. If it is assumed that the two films behave as resistors in parallel a 5% error for the sheet resistance of the gold only film is calculated, for a length L to width W ratio of one, compared to the composite film. This error is even lower for higher ratios as used in the experiment.

Assuming the gold film has the same resistivity value as the bulk material and metallisation thin film effects have not occurred, the measured sheet resistance can be used to calculate the gold film thickness. This is also shown in table 7.1 and gives film thicknesses ranging

Table 7.1 : Resistance data for metallisation electrodes.

Width(W) /mm	Rs Ω/□	L/W	Meas. R /Ω	Calc. R /Ω	Calc.t_{Au} /nm
0.1	1.90	28.1	53.4	12.65	11
0.2	1.99	14.05	28.0	6.32	10
0.5	1.58	5.62	8.9	2.53	13
1.0	1.21	2.81	3.4	1.26	17

For thin film thickness measurements, t_{Ti}=25nm, t_{Au}=45nm.
For ρ_{Au}=2.04e-8 Ω m , the calculated Rs_{Au}=0.45 Ω/□ .
L=2.81 mm

Notes on sheet resistance:
The resistance R of a rectangular block of uniformly doped material is

$$R=\frac{\rho L}{A}$$

where ρ is the resistivity of the material, L is the length of the material and A is the cross sectional area.
If W is the width of the material and t the thickness then the resistance is given by

$$R=\left(\frac{\rho}{t}\right)\left(\frac{L}{W}\right)=R_s\left(\frac{L}{W}\right)$$

where R_s is the sheet resistance of the material. The ratio of L/W thus determines the total resistance for a measured or calculated sheet resistance which depends on the density of the material and the film thickness.

from 11nm to 17nm. This indicates that the film deposition process was not very uniform and that the film thickness monitor value was in error. Considering the geometry of the deposition system and the positioning of the thin film crystal monitor, source and target, poor uniformity was the most likely cause of the wide spread of sheet resistance values obtained. Even the largest calculated thickness of 17nm is 37% of the required thickness. These thinner than expected gold films may have contributed to some of the problems encountered at the packaging stage, (section 6.8) depending on the sample batch.

From the presented results it is clear that narrow, thin metallisation will yield undesirably high resistance. This problem can be reduced by increasing the gold film thickness up to 75nm to reduce sheet resistivity, or by increasing the track width slightly. For the M2 design, the 400 μm tunnel width puts an upper limit on the width of the back electrode. Increasing the track width will however increase the microphone parasitic capacitance.

A detailed investigation of possible thin metal film effects for the previously mentioned metallisation scheme was not undertaken due to the discovered poor uniformity of the deposition process and the cost of gold. However, it is anticipated that for very narrow track widths ($< 100\mu$m) and thin gold layers (< 15 nm) the resistivity of the film will become exceptionally high and not practical for use as an electrode. For the measurements that were carried out, no unexpected high increases in sheet resistance were observed and discrepancies between calculated and measured values were largely attributable to poor thin film thickness control.(See theory section on film thickness)

Subsequent to this study, the sputter plant was modified to include a rotating substrate (60

rpm) holder, a titanium target shutter and a clamp for the thin film monitor crystal. Tooling factors were re-evaluated for the titanium and the gold deposition process and a veeco 4 point probe was used for sheet resistance and resistivity measurements of the thin films deposited on the 3" wafers. Uniformity was dramatically improved as was film thickness reproducibility and control. Low cost aluminium was used to investigate thin film thickness control and fig. 7.2 shows a comparison of a sputtered thin film aluminium distribution on a glass substrate before (7.2(a)) and after (7.2 (b)) the sputter plant was modified. For fig. 7.2(a) the maximum thickness variation is as much as 64% on the desired film thickness of 50 nm, but for fig. 7.2(b) the variation is only 11 % and the uniformity is clearly much better. The implemented enhancements and improved control of film uniformity and thickness for the metallisation scheme required for the microphone structure, resulted in vast improvements in yield for subsequent stages such as electrostatic bonding and gold ball bonding.

7.1.2 p^+ Doped silicon

Tests were carried out on a p^+ doped Van der Pauw structure in a silicon wafer. The diffusion was carried out with the same parameters as the rim diffusion described in the processing schedule of appendix A2.1 and the basic processing steps are shown in fig. 7.3. Calculated and measured values of resistance are shown in table 7.2 for the different track widths and agree well. The maximum deviation from the calculated sheet resistance of 3 ohms/square is only 12%. The maximum variation of measured sheet resistance, from the average value of 3.2 ohms/square, is about 10%, which indicates a much better film uniformity than for the metal films. These values are comparable to those measured on process test wafers, using a commercial four point probe, during rim fabrication.

(a)

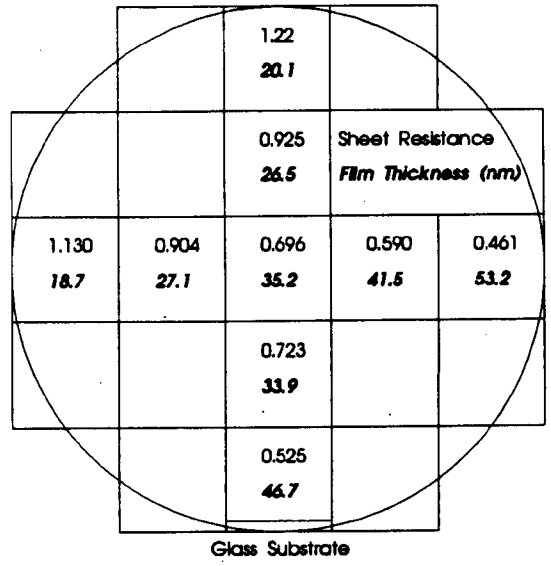

(b)

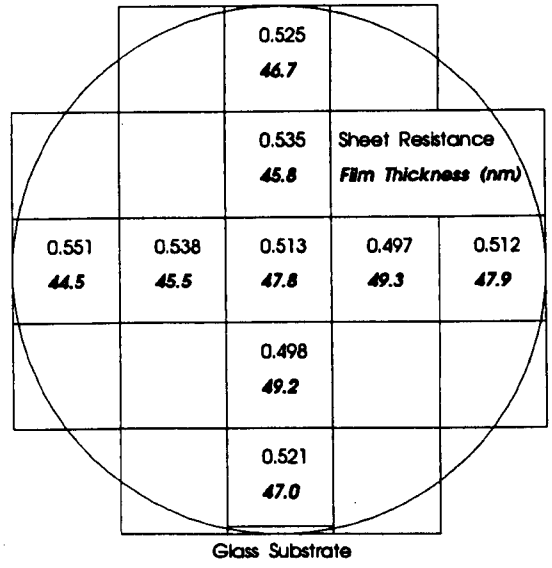

Figure 7.2 : The sheet resistance (Ohms/□) and film thickness (nm) distribution for a 50 nm thin film of sputtered aluminium deposited on a borosilicate glass substrate for **(a)** Static substrate, **(b)** Rotating (60 rpm) eccentric substrate holder.

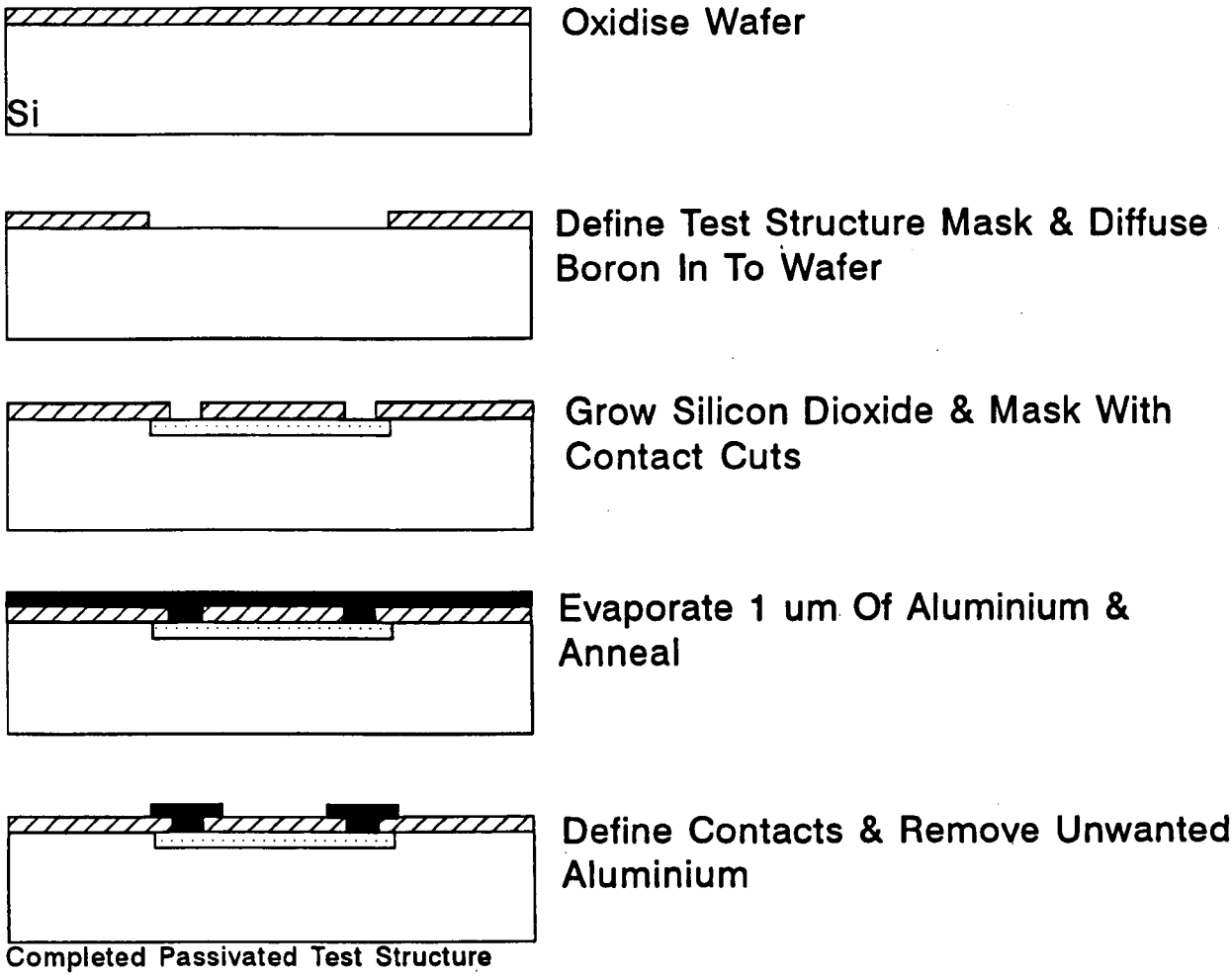

Figure 7.3 : Fabrication stages of p^+ sheet resistance test structure (Shown in fig. 7.1)

Table 7.2 : Resistance data for doped electrodes.

Width /mm	Rs Ω/□	L/W	Meas. R /Ω	Calc. R /Ω
0.1	2.87	28.1	80.6	84.3
0.2	3.13	14.05	44.6	42.2
0.5	3.35	5.62	18.8	16.8
1.0	3.31	2.81	9.3	8.43

See appendix 2 for rim deposition conditions.
The calculated sheet resistance for the doped profile = 3 Ω/□ .
L=2.81mm

For the measurements of the doped structures, it can be concluded that track widths do not significantly change the sheet resistance for widths greater than or equal to 0.1 mm for the specified doping conditions. These results do not predict the behaviour of a doped structure after silicon dissolution, but based on the described etch stop behaviour, it would be expected that the sheet resistance would increase slightly. The reason for this is that the etch stop profile would be thinner than the profile doped in silicon for the same process conditions. (Note sheet resistance calculations assume a uniformly doped material)

7.2 Measurement of diaphragm thickness optically and with atomic force microscope techniques

A novel optical interferometric technique using white light was used to examine the thickness of p^+ silicon films on glass and also investigate etch rates of these films. Atomic force microscopy was also investigated as a means of determining precise profiles of step height and hence film thickness.

Outline of fabrication of p^+ silicon test samples for thin film measurements

Test structures of $5mm^2$ x ($<1\mu m$) p^+ doped silicon were fabricated on a glass substrate using the same processing parameters given in the processing schedule for the microphone diaphragm, glass bonding and etching procedures (Appendix A2.1). The purpose of these structures was to study the microphone diaphragm diffusion profiles. Figure 7.4 outlines the main fabrication stages. Samples were etched in 1 litre of 17% KOH + IPA maintained at 22°C for different periods of time to establish an average etch rate value for that period. After thorough cleaning and drying of the samples, thickness measurements were taken.

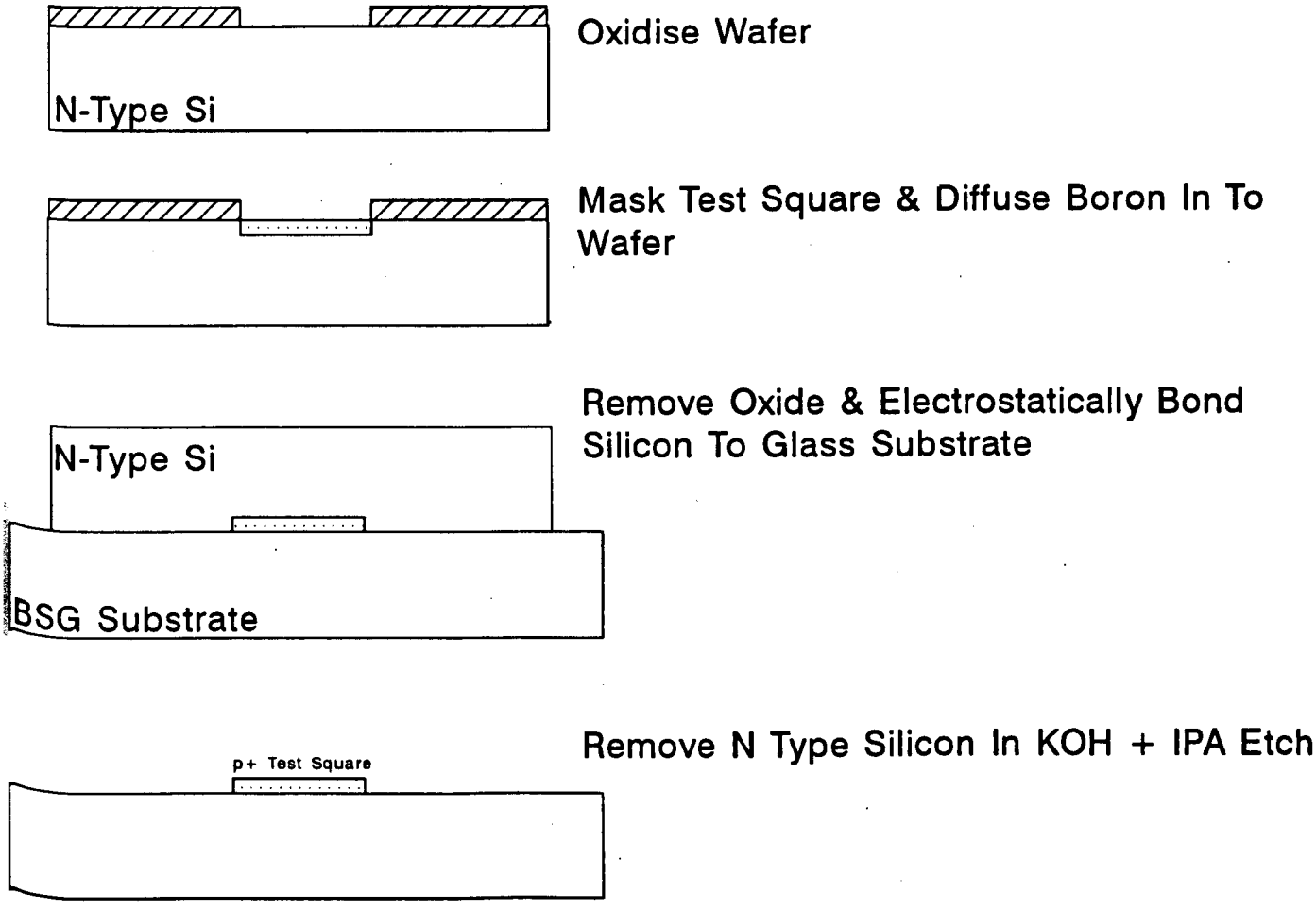

Figure 7.4 : Fabrication stages of p^+ test structure on glass for use in optical thickness measurements.

Interferometric measurement of p^+ film thickness

The interferometric set up used fig. 7.5(a) produced a graph of reflectance against wavelength for each sample tested such as that shown in fig. 7.5(b). The sinusoidal form of the plots obtained depicted minima at different wavelengths which were used in conjunction with a constructed graph shown in fig. 7.6 to determine the thickness of the doped silicon. This graph was determined from the following equation for the thickness t of the thin film

$$t=\frac{n\lambda}{2\eta} \qquad (7.5)$$

for a series of straight lines derived from n orders between the wavelength λ =400 nm to λ = 780 nm for a film of refractive index η. For intrinsic silicon the value of η was chosen to be 3.5, however it must be indicated that the refractive index increases with dopant concentration, but not significantly in the concentration ranges of interest.

Results of thickness measurements for 6 samples, using the interferometric technique, are shown in table 7.3. Three thickness measurements were taken for each sample, the initial thickness h_o, the thickness h_1 after etching the sample for time t_1 and the thickness h_2 for an etch time of t_2. The etch rates R_1 and R_2 were calculated for t_1 and (t_1+t_2) respectively. It can be seen from the table that h_o is not very consistent for the standard diffusion and etch conditions, which could raise questions relating to the validity of the experimental procedure for sample preparation, since it was difficult to keep samples clean and uniformly etched. Furthermore, the effect of surface roughness such as that shown in plate 6.14(b) could significantly influence measurement results in a way that has not been investigated. The samples used for this work were not examined using a scanning electron microscope and so their surface roughness was not determined. No visible roughness was seen with an optical

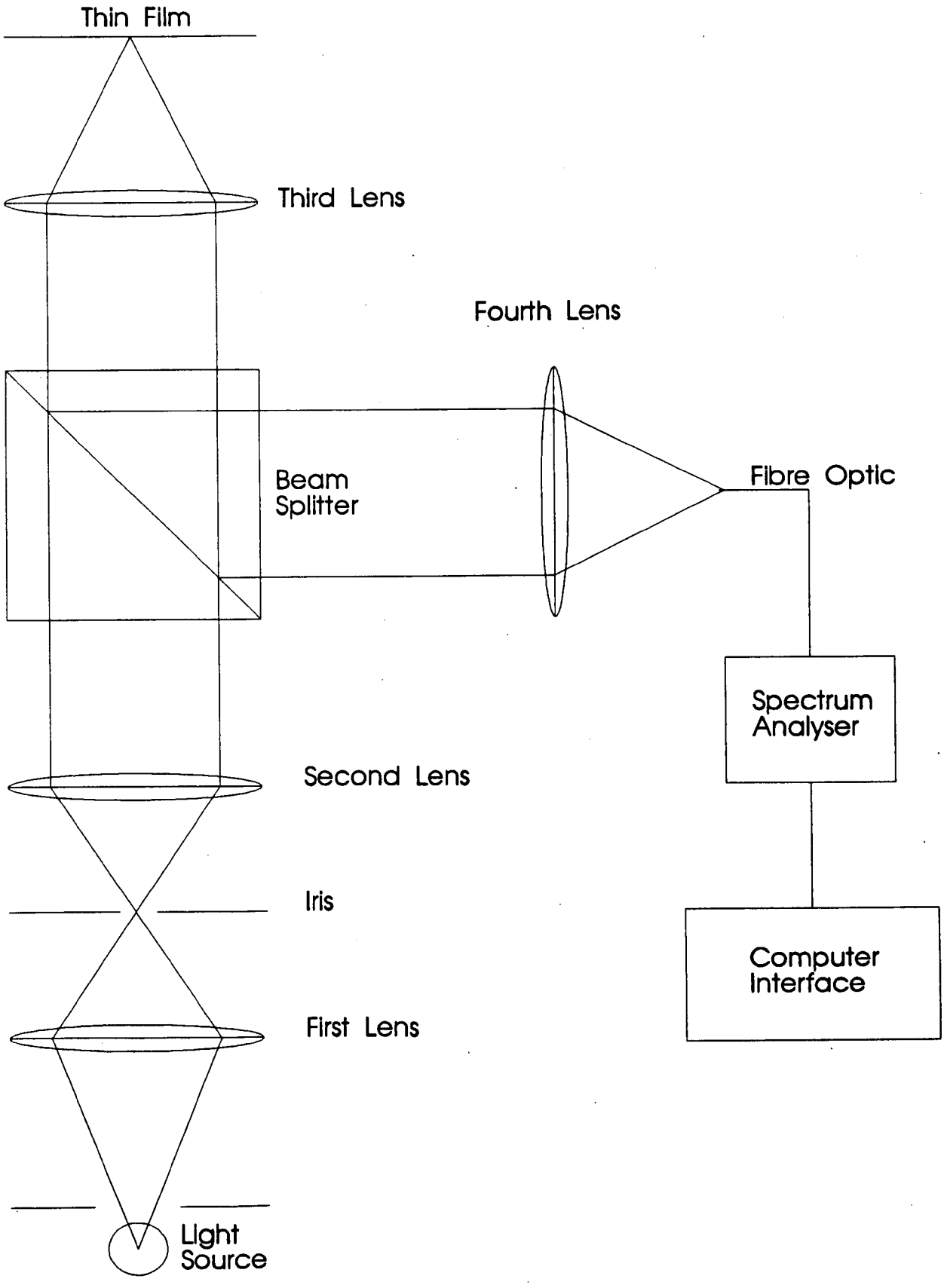

Figure 7.5 (a) : Optical interferometric apparatus used for obtaining graphs of reflectance against wavelength for thin translucent p^+ silicon films.

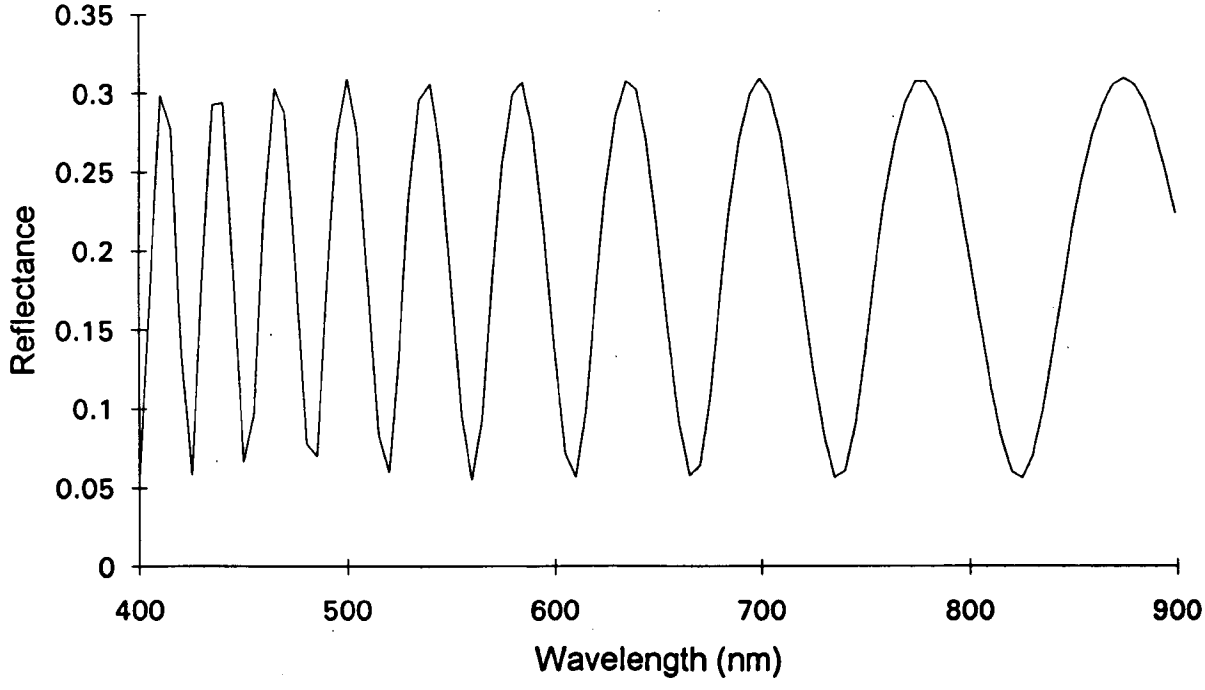

Figure 7.5 (b) : Measured reflectance as a function of wavelength for a 1 um thick p^+ test structure on a glass substrate.

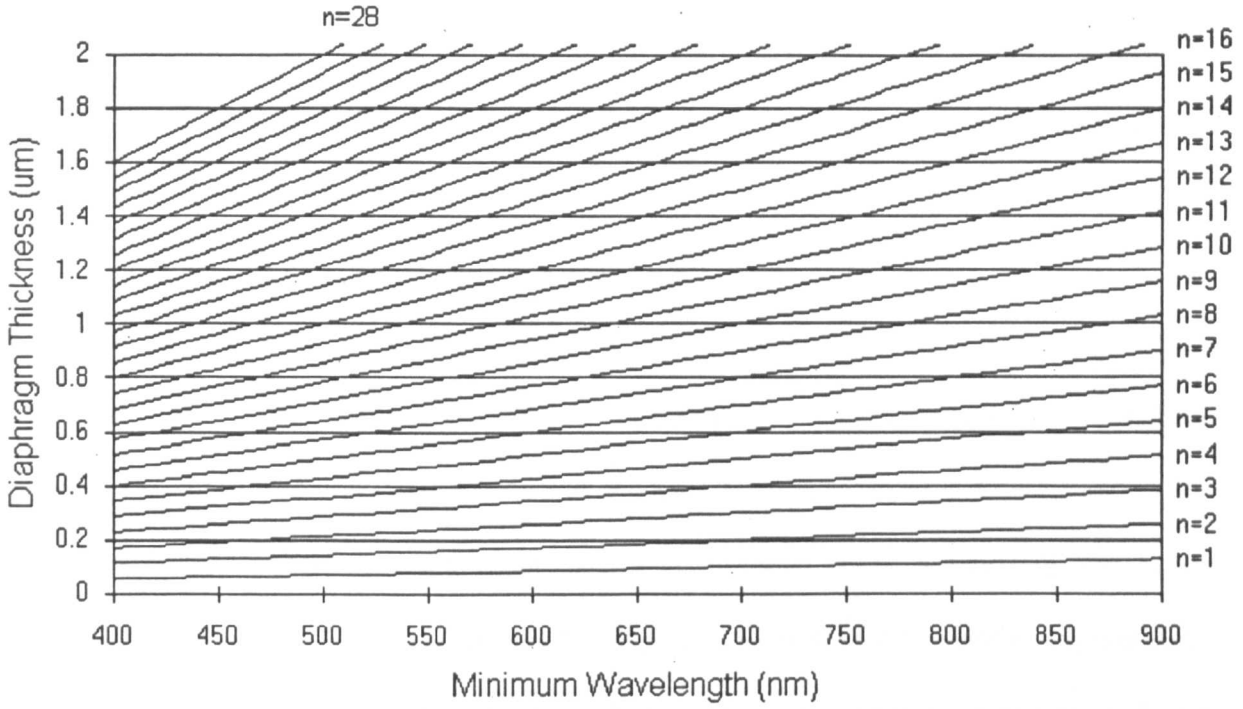

Figure 7.6 : Chart calculated from equation 7.5 for the determination of diaphragm thickness as a function of the minimum wavelength for waveforms obtained from interferometric apparatus.

microscope. Since the surface features seen in fig 6.14(b) are sub-micron, it was not appropriate to investigate the samples with the available talysurf measurement equipment discussed in section 4.11.

If the diffusion profile is assumed to conform with the models of section 4.4 and hence the calculated profile shown in fig. 5.2(b), the experimental thicknesses (Table 7.3) indicated can be related to the boron concentration at that point in the profile. It would be expected that sample 6 has a higher etch rate than sample 1 because h_o is larger and the boron concentration would be lower. This was not the case, may be due to either experimental measurement error or non uniform diffusion. However, sample 3 does show a lower etch rate than sample 1, which corresponds with the fact that sample 3 is thinner.

The smallest thickness measured was 0.45 μm, which is close to the critical boron concentration point in the diffusion profile of 3×10^{19} atoms/cm^3. At this point in the diffusion profile the etch rate would be expected to reduce and saturate, as the etch stop property becomes more significant. Samples 5 and 6 showed this limiting thickness which could not be reduced by further etching according to the measurement technique used in the experiment.

It is clear from the results of these thickness measurements that further work is required to obtain more statistically conclusive results. This would involve using more samples and the development of an improved preparation procedure. This was not carried out in this thesis due to fabrication and time constraints.

Sample Number	h_o /um	t_1 /Hrs	h_1 /um	R_1 nm/Hr	t_2 /Hrs	h_2 /um	R_2 nm/Hr
1	0.9	7	0.62	40	5	0.52	32
2	0.53	-	-	-	-	-	-
3	0.49	5	0.45	8	-	-	-
4	1.72	-	-	-	-	-	-
5	0.45	-	-	-	-	-	-
6	1.72	17	1.24	28	5	1.23	22

h_o - Initial thickness measurement
t_1 - First etch time
h_1 - Thickness after etch time t_1
R_1 - Etch rate for t_1
t_2 - Second etch time
h_2 - Thickness after etch time t_2
R_2 - Etch rate for $t_1 + t_2$

Table 7.3 : Measurements of p^+ test structure thickness.

It should be noted that the interferometric technique used can only provide an average thickness representation of the film because the light can only be focused to a spot which is comparable to the size of the silicon diaphragms measured. The apparatus used was able to yield wavelength values in 5 nm steps which could allow for accurate determination of average thickness measurements over a 1 mm^2 area. The technique could certainly be very useful for average etch rate characterisation.

One of the samples was investigated using an atomic force microscope [88], where one result can be seen in fig. 7.7. The silicon represents the raised section in the background and the glass substrate is the lower section in the foreground. The step height of one cross section is shown to be about 1μm. The two features emerging from the silicon film could be dirt on the surface. The vertical resolution of the AFM instrument used was about 5nm which meant that different cross sections gave different height values. It was found that the interferometric optical technique was more convenient and more suitable for obtaining average values of film thickness for this work, in the time available.

7.3 Electrical measurements of silicon microphone structure

The block diagram of fig. 7.8 shows the test configuration that was used for electrically testing the mounted microphone structures. This system was used to excite the microphone from a wide bandwidth speaker with a sinusoidal signal of known frequency and sound pressure level. A dBA meter which incorporates a calibrated reference microphone was used to determine the sound pressure level adjacent to the test microphone. The purpose of this arrangement was to investigate the sensitivity of the test microphone at different frequencies and hence the frequency response. An anechoic chamber was not available for this work and

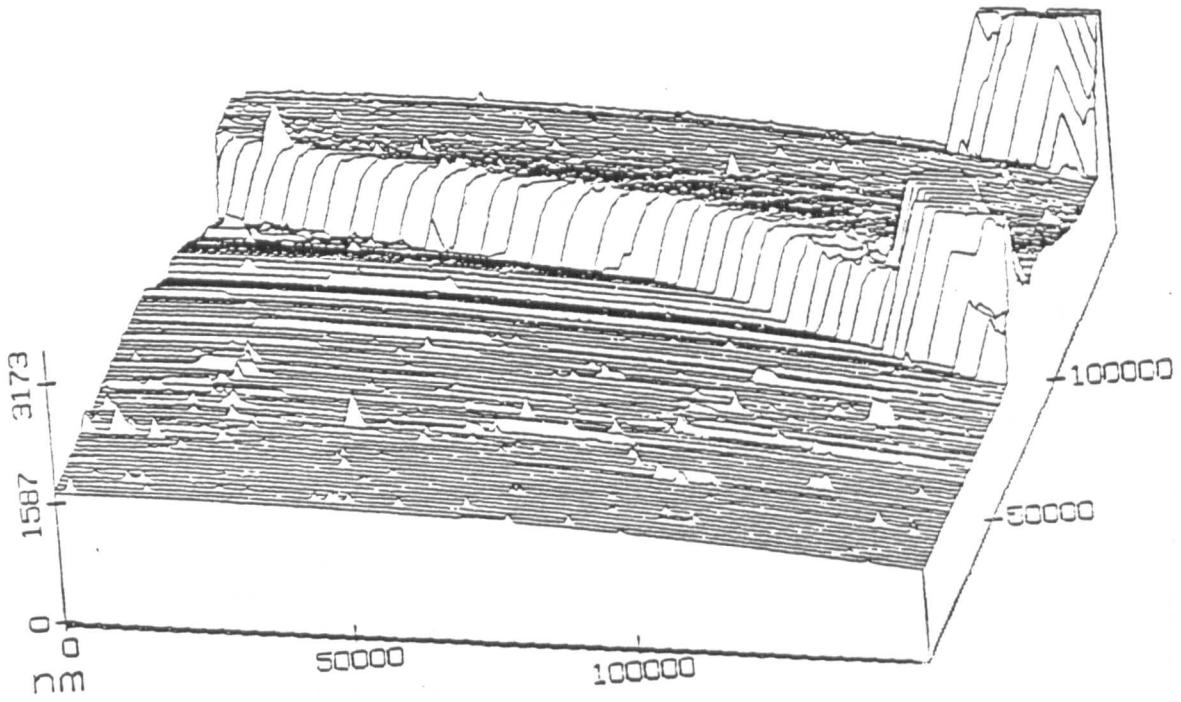

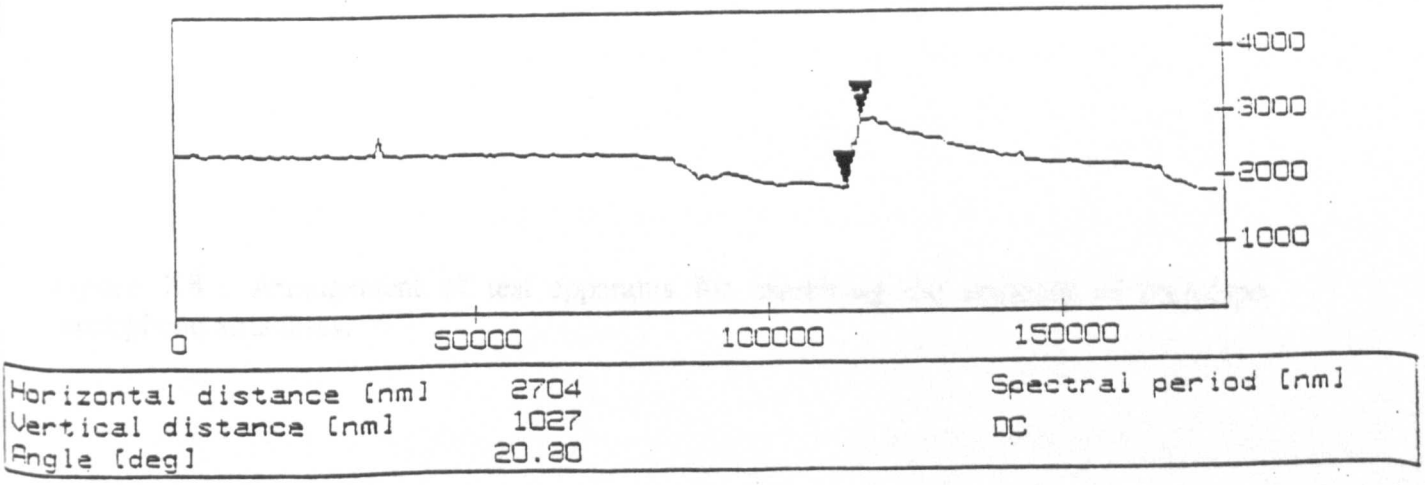

Figure 7.7 : Atomic force microscope (AFM) profile of a 1um p^+ test structure on a glass substrate.

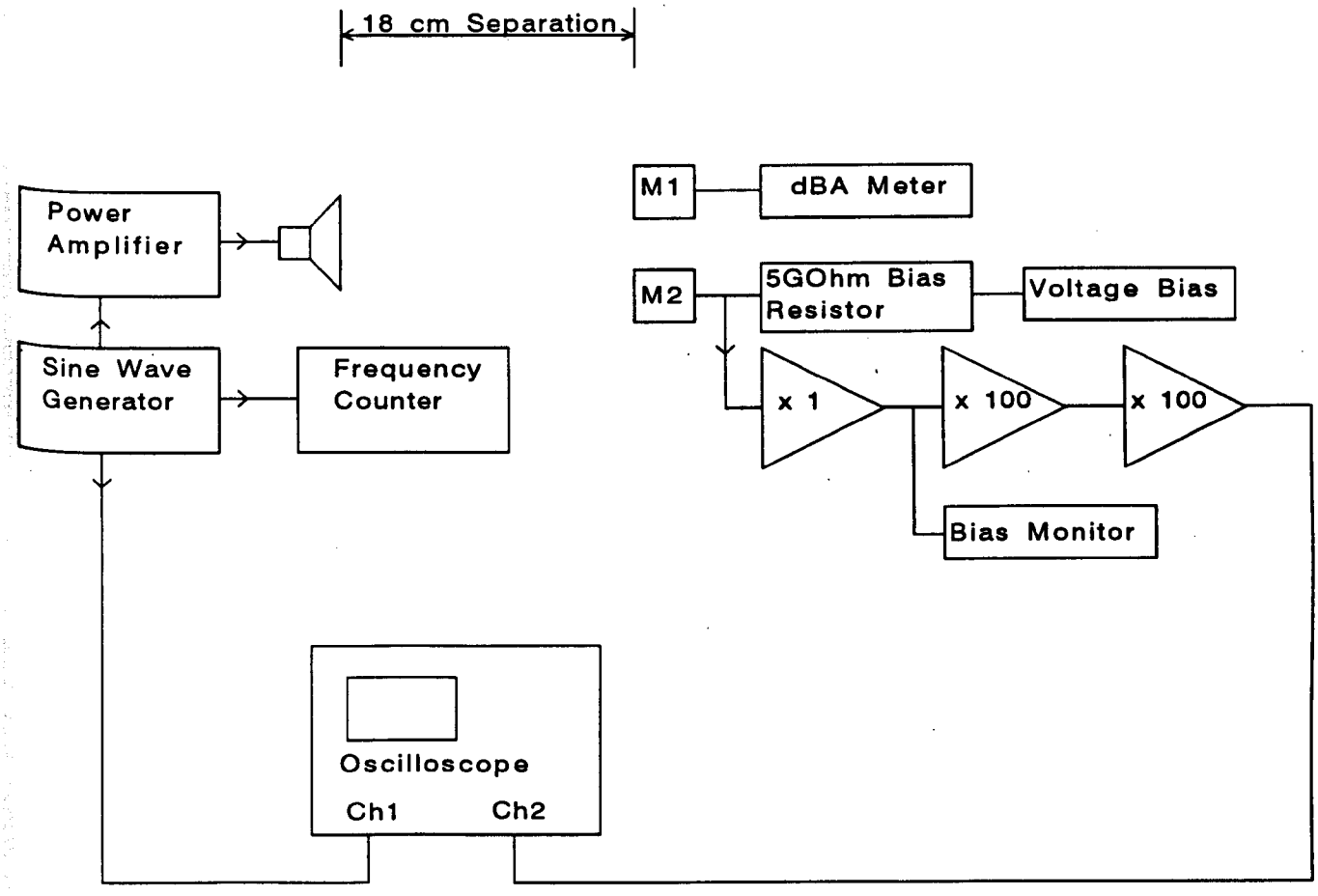

Figure 7.8 : Arrangement of test apparatus for examining the response of prototype microphone structures.

the speaker transfer function was not determined. These factors could have masked the true frequency dependent characteristics of the test microphone. The results obtained from this test scheme were used for determining, from the limited samples available, the existence of an output from the test microphone to an applied sinusoidal sound pressure level, and as a guide to the frequency response characteristics. More detailed and accurate analysis would have required further fabrication of new structures and specialised acoustic test facilities

Since the impedance of a miniature microphone capsule is very high at low frequencies and the air gap may cause significant damping, it is very important to have a large valued bias resistor and FET input stage for impedance conversion. These components must be as close as possible to the microphone capsule. A custom 5 GΩ resistor was used to bias the microphone structure from a battery supply that could be varied with a 100 turn potential divider circuit from 0 to 9 V. An OPA606 non-inverting unity gain dielectrically-isolated wide bandwidth FET buffer amplifier was used for impedance conversion because of its very high input impedance of up to 10 TΩ (1 tera ohm = 10^{12} Ohms), small input capacitance of 1pF and its low noise specification of 13 nv/ Hz at 1kHz rising to 30 nv/ Hz at 10 Hz. The output of this stage was fed through two audio amplifiers each with a fixed voltage gain of 40 dB and hence a total overall gain of 80 dB. Since the signals from the test microphones were expected to be less than 1mV, the maximum output from this amplifier was less than 10V, which is well within the supply limitations of +/-15V and the maximum output voltage swing of +/- 12V. The output of this microphone amplifier was observed on a dual trace oscilloscope and compared with a reference signal from the sine wave signal generator.

7.3.1 Procedure for the preparation of test structures and initial measurements taken

Unmounted structures (Fluid removed from back chamber) were selected from a devised storage dish (Plate 7.1) using an optical microscope. The structures were examined for selection of a device that was free from the following defects:-

i) Fractures

ii) Collapsed diaphragms

iii) Unwanted residues or crystal deposits

iv) Metallisation damage

v) Poor electrostatic bonding

The selected structure was glued on a suitable chip carrier with a 5 GΩ resistor and then gold wire bonded to the pin outs for external connection to the microphone as shown in Fig. 7.9. The Plate 7.2(b) shows a 40 pin DIL package with mounted microphone and bias resistor, the package was held in an aluminium block for the gold ball bonding process. This type of package was found to be too large and bulky for obtaining useful test results. The smaller DIL packages shown in plate 7.2(a) were found to be the most suitable for connection to the impedance conversion amplifier and were readily available. The packaged microphones were inspected, using an optical microscope, for any signs of damage that may have resulted from the packaging process prior to selection for electrical test.

Some of the first microphone samples obtained were tested with a standard ohmmeter to check for shorts between the back electrode and the diaphragm. The resistance was observed falling from a high value of 10 MΩ to a low value of less than 100 Ω over a time period of

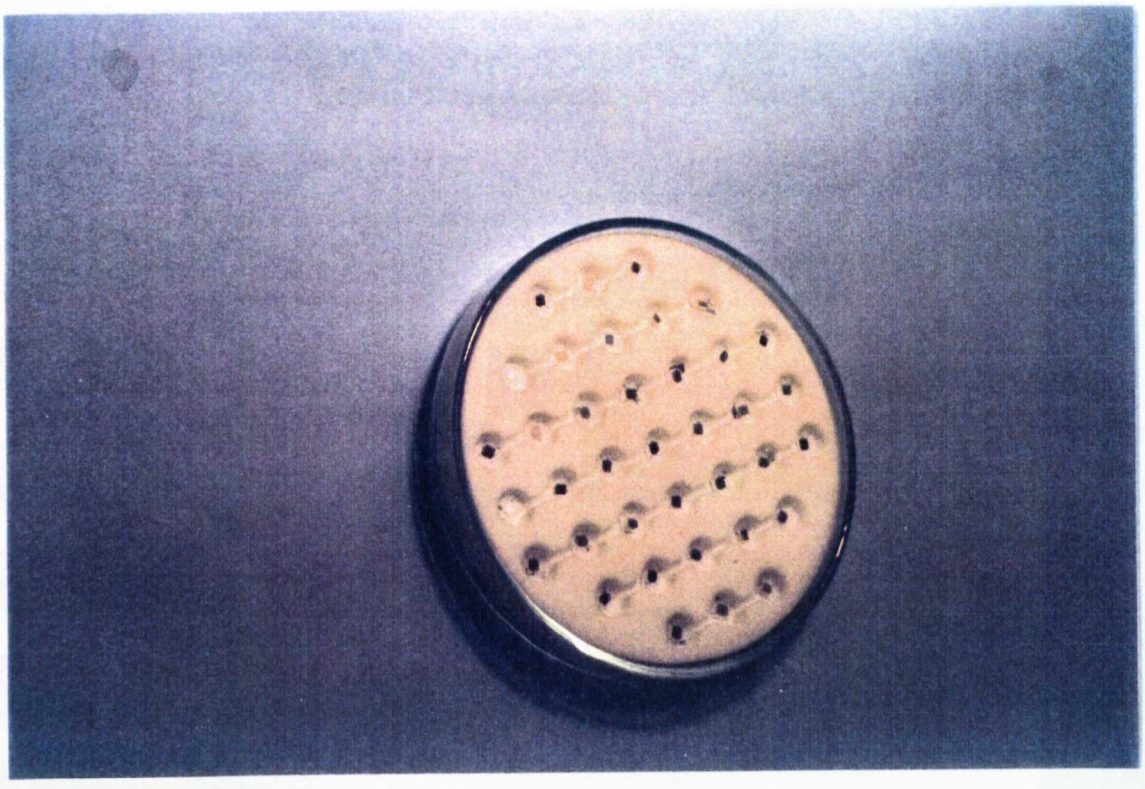

Plate 7.1 : Microphones stored for inspection and subsequent mounting.

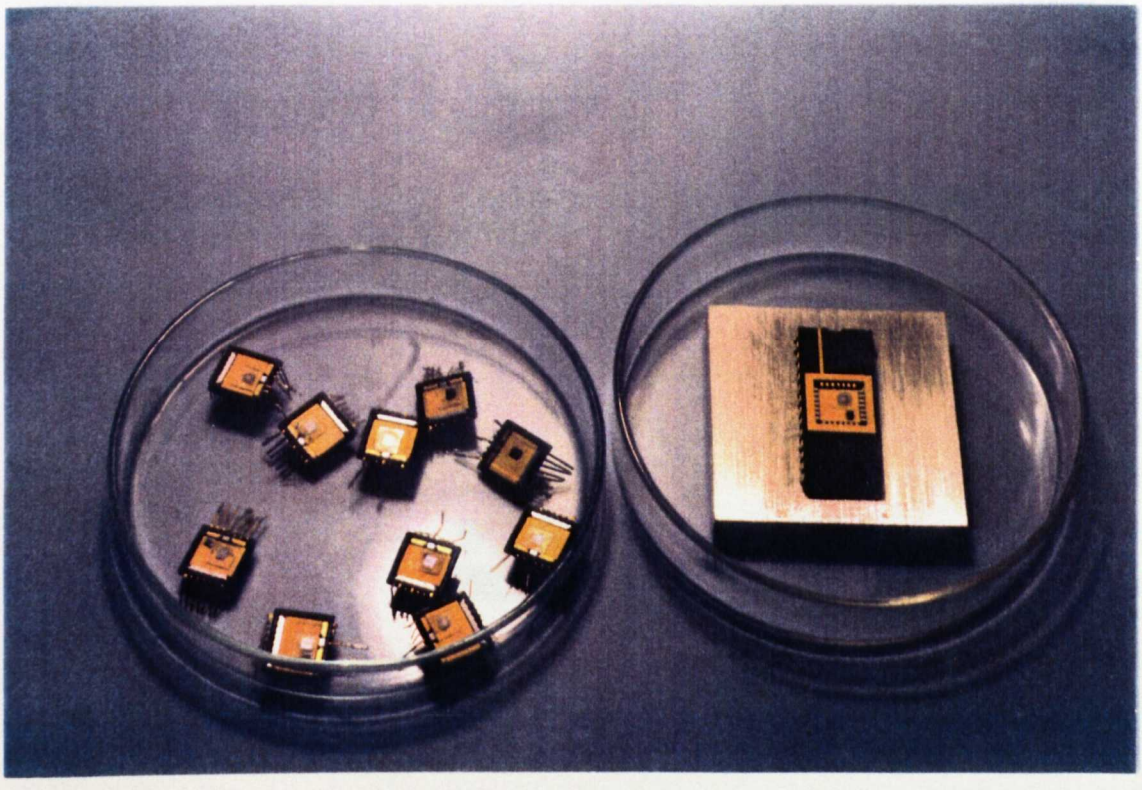

Plate 7.2 : Two types of package used for microphone testing. **(a)** 14 Pin. **(b)** 28 Pin ceramic DIL.

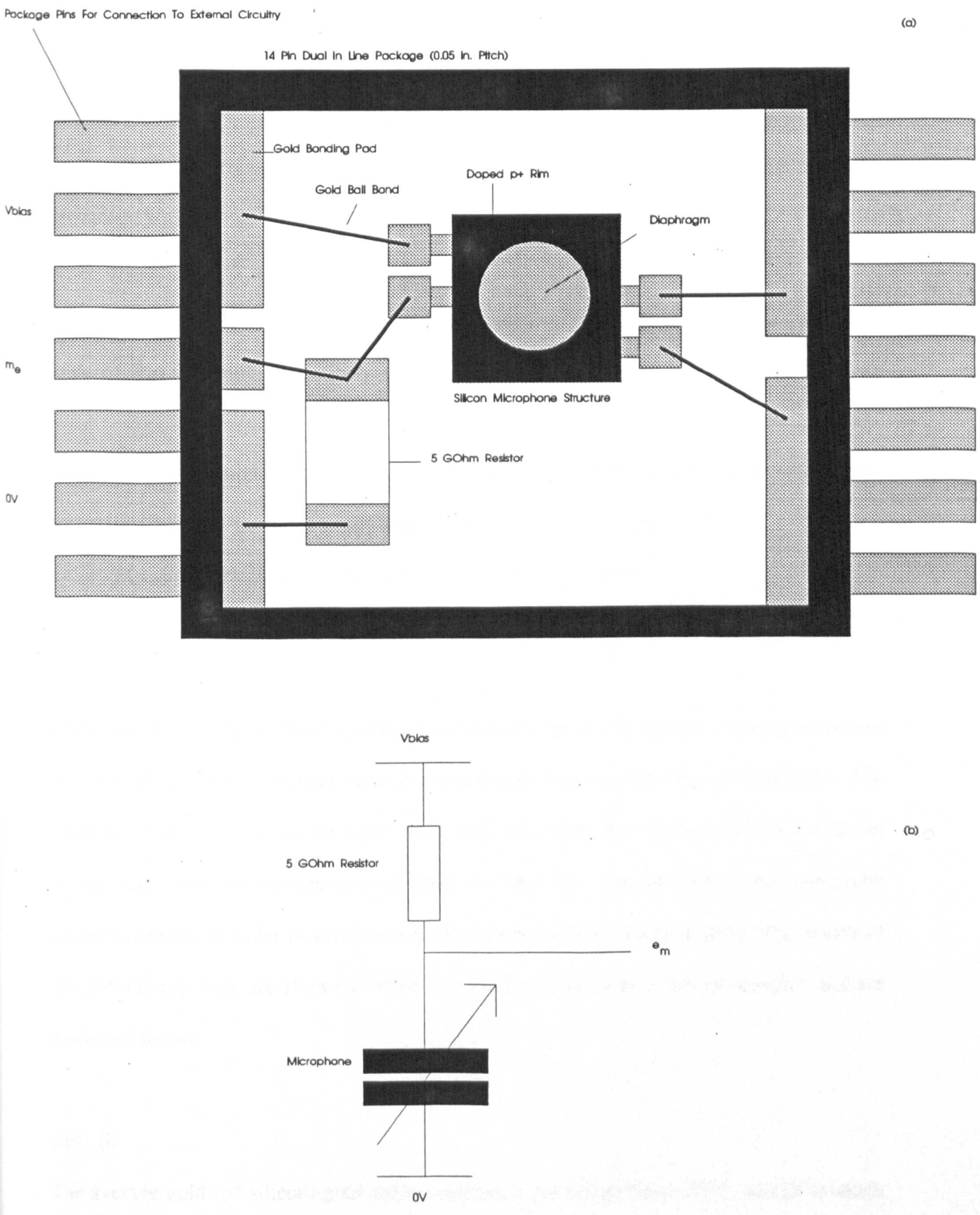

Figure 7.9 : Circuit configuration of a packaged silicon microphone with 5 GOhm bias resistor. (a) Package with mounted microphone and resistor. (b) Equivalent circuit diagram.

less than 30 seconds. The low resistance value achieved remained stable and could not be reversed, rendering the structure unusable. It was assumed that the relatively high test voltage applied to the microphone by the ohmmeter caused the diaphragm to collapse and have permanent stiction.

The following preliminary electrical tests were carried out before microphone packages were soldered into the amplifier circuitry.

i) Test conduction path from one rim electrode to another to check the p^+ silicon/gold interface for good continuity and low resistance. Fig 7.10(a)

ii) Measure through resistance of back electrode. Fig 7.10(b)

iii) Test for short circuit of p^+ structure to backchamber metallisation. Fig 7.10(c)

These tests were carried out using a special resistance meter that applied a test signal of less than 100mV in order to prevent excessive electrostatic forces collapsing the diaphragm. The meter was capable of measuring a maximum resistance of 10 MΩ. The test circuits are shown in fig. 7.10. Two measurements were taken for each test, one with the instrument probe polarity reversed in order to verify ohmic characteristics of the measurement. The results of the preliminary tests are shown in table 7.4 for 20 mounted microphone samples and are discussed below.

Test (i)

The average gold-(p^+ silicon)-gold contact resistance for values below 50 Ω was 28 Ω which means that each gold - (p^+ silicon) junction had an average value of approximately 14 Ω. The

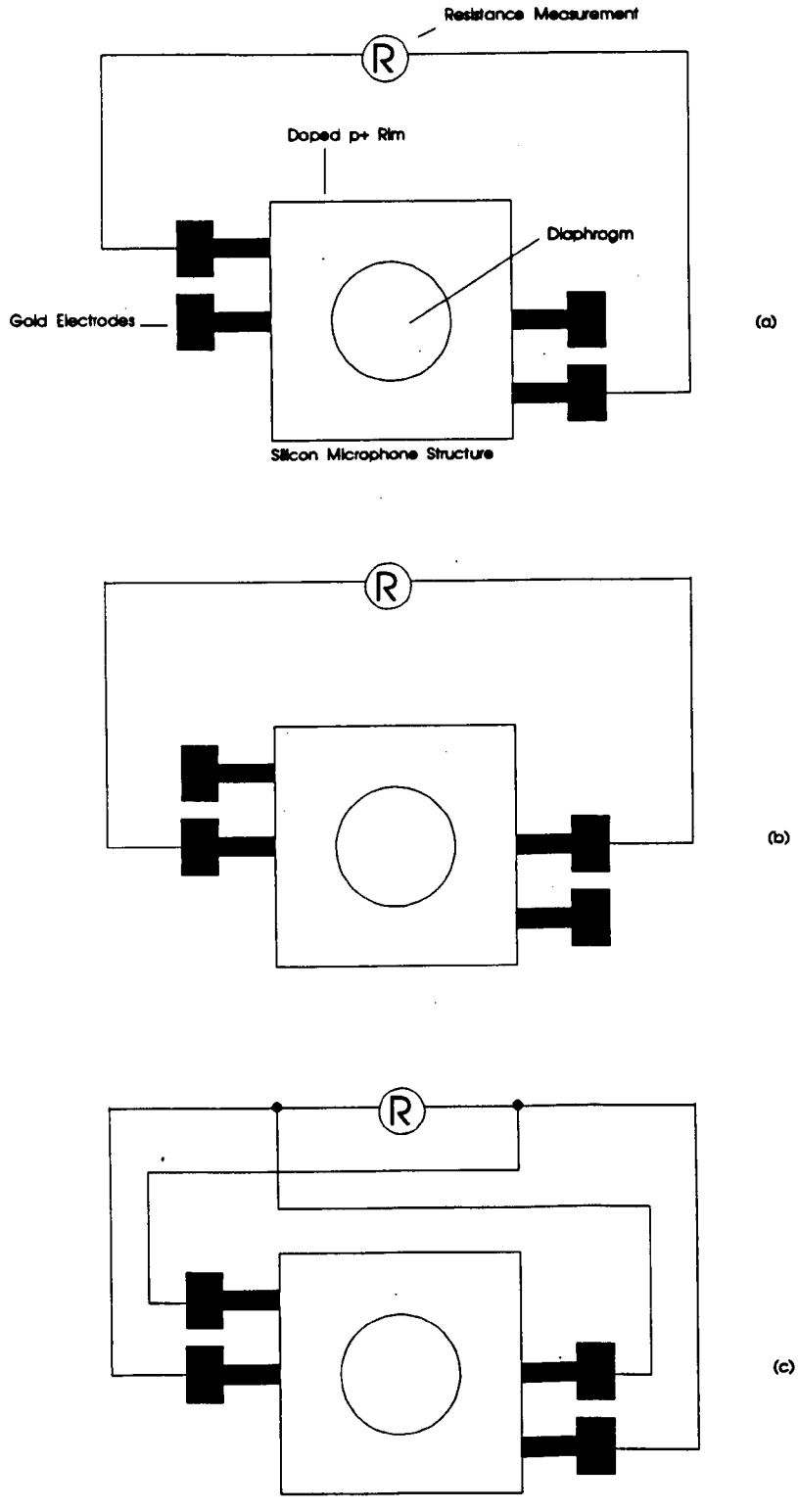

Figure 7.10 : Continuity test circuits for packaged structures.
(a) Test electrode - rim - electrode conduction path
(b) Test through continuity of back electrode.
(c) Test for diaphragm to back electrode short circuit.

Sample Number	Contact Resistance m-p^+-m /Ohms	Through Resistance /Ohms	Short Circuit Test /KOhms	Output From Frequency Tests	Estimated Capacitance /pF
1	25	0.3	0.7	No	-
2	35	0.4	0.35	No	-
3	33	0.5	O/C	Yes	7
4	20	0.3	5	No	-
5	22	0.3	300	No	-
6	21	0.3	750	No	-
7	27	O/C	O/C	No	-
8	40	0.3		No	-
9	31	0.5	390	No	-
10	28	0.5	0.2	No	-
11	300	0.7	55	No	-
12	30	O/C	600	No	-
13	29	0.5	1.2	No	-
14	O/C	0.3	O/C	No	-
15	O/C	0.3	O/C	No	-
16	29	0.5	2K2	No	-
17	27	0.4	O/C	No	6
18	27	0.3	205	No	-
19	O/C	0.7	O/C	No	-
20	5K	0.4	122	No	-

Table 7.4 : Results of tests on 20 microphone structures.

average value for the through resistance of the backchamber electrode was 0.4 Ω, which implies the average resistance to the centre of the back chamber was 0.2 Ω due to the device symmetry. Most of the values obtained are less than 50 Ω which indicates good connections to the microphone structure and a resistance that has negligible contribution to the microphone impedance at audio frequencies. The gold-(p^+ silicon) connection has a higher resistance than the backchamber through connection (See test ii) due to the gold-(p^+silicon) interface and the lower conductivity of p^+ silicon in comparison to the gold film. Further work would need to be carried out to optimise this connection for minimum resistance.

Test (ii)

All of the samples except no. 7 show a through resistance below 0.7 Ω. It is likely that no. 7 had a break in the back electrode resulting in the measured open circuit. Excluding sample No. 7, the average through resistance is 0.4 Ω. Most of this resistance is attributable to the gold ball bond contact resistance, which implies that the through connection has an extremely low resistance. A low resistance connection to the back electrode is most desirable for the same reasons as a good connection to the microphone structure (See test (i)) so that electrical sensitivity is not impaired.

Test (iii)

The short circuit test indicated that 90% of all microphones tested had a resistance below 2.2 kΩ. This indicated an undesirable low resistance path from the p^+ structure to the metallisation and hence a possible problem with the microphone air gap. For this test an open circuit result was desirable since it would indicate that the air gap was not bridged. However,

an open circuit result could also be caused by an open circuit connection to the p^+ structure or backchamber (E.g break in metallisation). This latter point was determined from the results of test (i) and (ii) and it can be seen from table 7.4 that only samples 3 and 17 indicated good rim connections, low through resistance and a DC open circuit across the air gap.

7.3.2 Frequency response investigation

Following the above tests, if the microphone showed low resistance connections to the rim, back electrode through continuity and a high diaphragm to back chamber impedance, it was then tested with an applied bias and signal amplification. A packaged test microphone is shown in plate 7.3 soldered as close as possible to the input circuitry in order to reduce stray input capacitance, which would otherwise degrade high audio frequency response.

It was found that the amplifier circuitry was very susceptible to mains interference due to its very high input impedance. This problem was reduced significantly by careful screening and guarding of the amplifier, especially close to the input. A possible way of eliminating mains interference of the microphone would be to have an integrated circuit impedance conversion stage within a few microns of the miniature microphone structure. This was beyond the scope of this project.

The bias voltage applied to the microphone was accurately monitored after the impedance conversion stage with a high impedance voltmeter. This measurement was further used to determine if the diaphragm was collapsed, since a short circuit between the diaphragm and the back electrode connects the bias voltage to OV via the 5 GΩ resistor, effectively

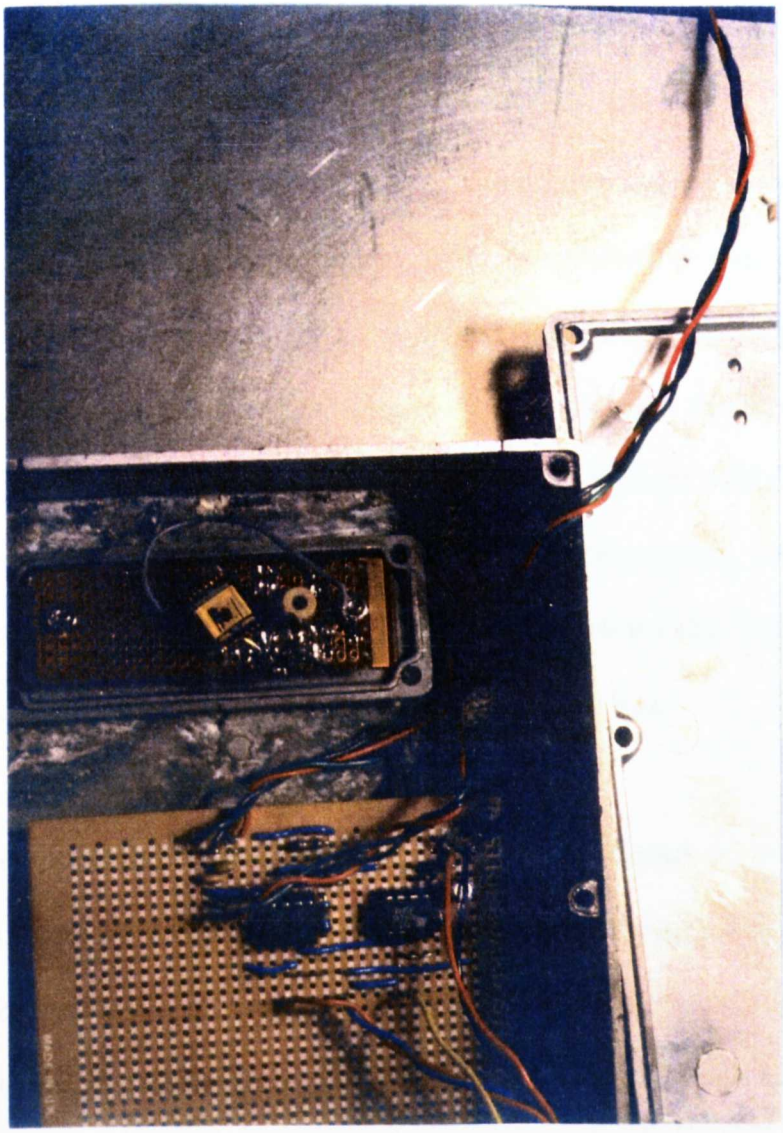

Plate 7.3 : Packaged microphone mounted on the back of an AD OPA606 pre-amplifier for impedance conversion. The circuitry is mounted in an earthed metal box for screening purposes.

grounding the amplifier input and hence the output.

Initially, the bias was set to zero for the microphone on test and then steadily increased in 100 mV increments. Between each increment, a 94 dBA sine wave was broadcast from the loud speaker and slowly swept from 10 Hz to 18kHz while the oscilloscope was monitored for the presence of a signal. The noise displayed on the scope after the 80 dB gain stage was between 1-3 V pk-pk (0.1-0.3 mV) and modulated by a 0.5V pk-pk 50Hz sine wave, which made the observation of a microphone signal difficult. The photograph, plate 7.4, shows the test apparatus detailed in fig. 7.8 and depicts the detection of a 1kHz sine wave (Shown on the oscilloscope) from the microphone housed in a screened box.

From the 20 microphones selected for test, only two exhibited output from the swept frequency acoustic excitation tests. Both microphones showed output at discrete frequencies that was very characteristic of resonant behaviour and the level of this output increased as the bias voltage was increased. Unfortunately, one of the microphones ceased output when the bias voltage was in excess of 2V and could not be recovered for further investigation. The remaining microphone was biased at 1V and the approximate frequency response was sketched as shown in fig. 7.11. It is clear from this figure that the microphone does not have the desired ideal frequency response shown in fig. 3.3 (Chapter 3) and that an explanation for the behaviour is necessary.

Before this structure was mounted, it was observed that the rim bonding was poor and may not have been fully successful in each corner of the microphone. It was thought that this may explain the unexpectedly low resonant frequencies observed. Further finite element analysis

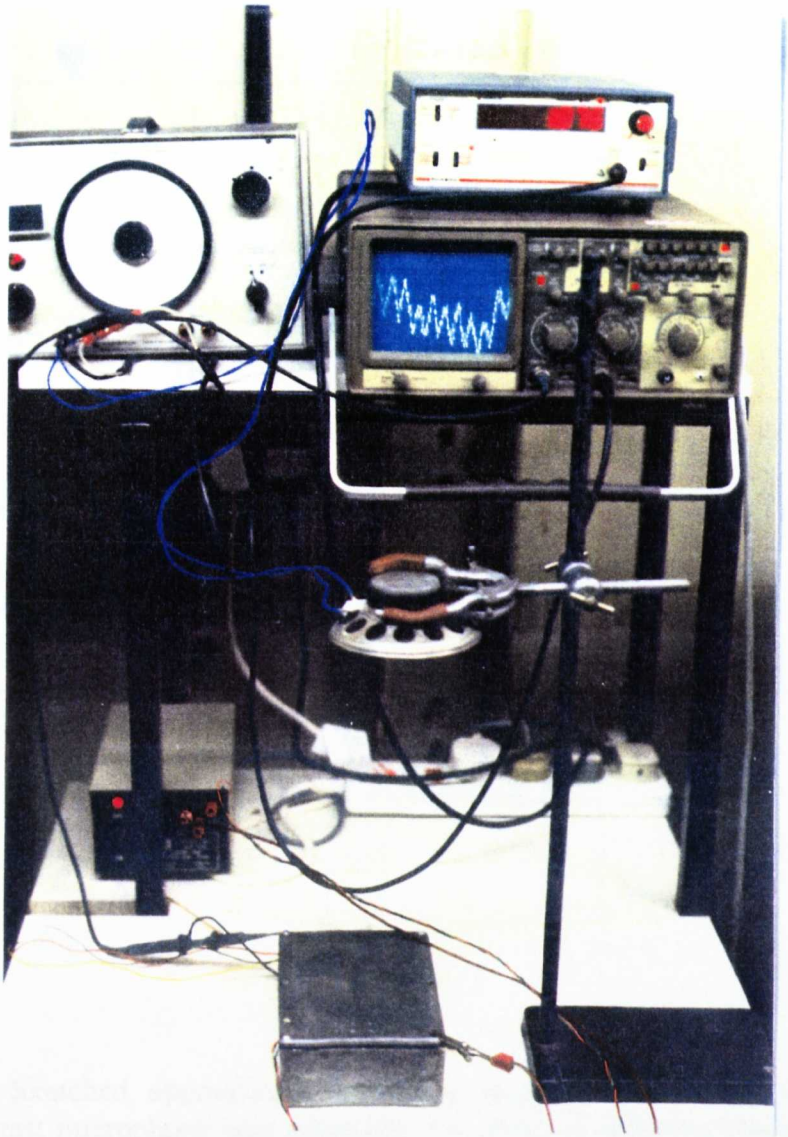

Plate 7.4 : Output from a 1mm diameter circular diaphragm silicon microphone. (Output approx. 0.2mv pk-pk for a 1kHz sinewave excitation signal with a SPL of 96 dBA.)

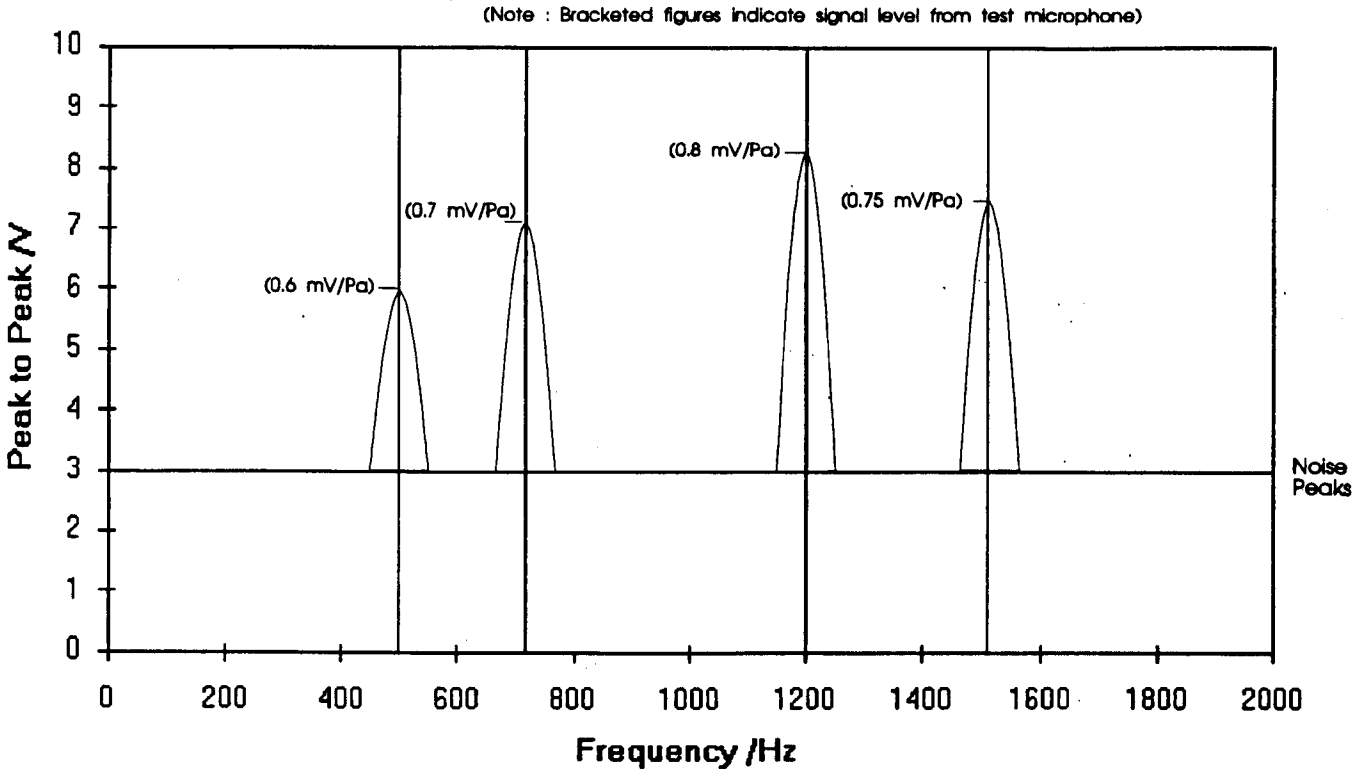

Figure 7.11 : Sketched approximate frequency response from a circular microphone structure. (The test microphone was subjected to a series of different frequency sine waves with a sound pressure level of 94 dBA at the test microphone site. The SPL measurement was taken with a calibrated commercial dBA meter)

was carried out to determine the resonant frequency of a circular microphone model with unbonded corners to yield some explanation for the experimental results of fig. 7.11.

The results of the different simulations carried out are shown in table 7.5 where it can be seen that three conditions have been simulated for a circular microphone with a 1μm thick diaphragm. Simulation A approximated the microphone structure in order to determine if the resonant frequency was lowered for one unbonded corner of the microphone structure. Clearly, from the results, the modes of resonance are substantially lowered into the audio band. Simulation B models this more accurately by making the silicon mass distribution as in the actual structure. This results in higher resonant frequencies that still lie in the audio band. It was anticipated that if more corners were free to move, the resonant frequencies would be further lowered. Simulation C shows the results for a structure fixed in one corner and results in four modes of resonance below 3kHz. Comparing the simulation results with the device frequency response measurements (See fig. 7.11) and observations of poor structure bonding to glass, it would appear that the output observed from the structure was characteristic of resonant behaviour and furthermore, characteristic of a structure that was poorly bonded to the glass substrate. (This conclusion could also indicate why this structure produced an output where others failed, since due to the poor bonding, the air gap was probably larger and p^+ silicon to backchamber shorting was less likely.)

7.3.3 Capacitance measurement

For a perfect circular microphone structure with exact designed dimensions (See fig. 4.2) and a 1μm air gap, the theoretical unloaded active capacitance is 6.95 pF and the stray tunnel to electrode capacitance is 0.89 pF, which gives a total device capacitance of 7.84 pF. The

Table 7.5 : Computer FEA simulation results for structures that are not fully bonded to the glass substrate in all four corners.

A : Structure fixed in three corners, mass concentrated in free corner
B : Structure fixed in three corners, mass distribution as in actual structure
C : Structure fixed in 1 corner, mass concentrated in opposite free corner

Resonant Mode	Freq /Hz - Sim A	Freq /Hz - Sim B	Freq /Hz - Sim C
1	442	674	73
2	1590	3490	372
3	2240	-	1136
4	4514	-	2484

time constant for this capacitance with a 5 GΩ resistor is about 40 milliseconds.

Accurate capacitance measurements could not be made with a standard AC wheatstone bridge circuit because of the applied voltage modulating the diaphragm and unwanted stray capacitance caused by the size of standard components and circuit construction techniques. A custom chip or specialist pica probe solution could be required for such measurements. An attempt was made to estimate the capacitance by using the microphone as a timing component in an NE555 astable oscillator circuit. The frequency of the square wave output F_o was used to determine the capacitance of the microphone structure C_{TM} from the following equation

$$C_{TM}=\frac{1.44}{(R_A+2R_B)F_o} \qquad (7.6)$$

where the following values were chosen, R_A=47 kΩ and R_B=470 kΩ for the timing components. The output frequency of the circuit F_o was measured using a frequency counter and then used in conjunction with measured resistor values in eqn. 7.6 to determine the overall capacitance connected to the circuitry input. Two results were obtained and are shown in table 7.4. (See section 7.3.1) and indicate the correct order of magnitude compared to the calculated value of 7.8 pF.

7.3.4 Qualitative investigation of diaphragm movement

Some microphone test structures were examined under a top lit microscope while a bias in the range of 0-8V was applied gradually in order to observe any diaphragm movement. Light interference between the air gap could be observed through the translucent diaphragms resulting in a specific colour. Initially the interference was red/pink in colour changing to

blue/green as the bias increased and the air gap became thinner. This shift of wavelength of the observed light would be expected for a reduction of a 1 μm thin air gap film bounded by two surfaces. Between 1V and 3V the microphones unrecoverably collapsed and in some cases visibly fractured. This limited experiment demonstrated the movement of the diaphragm for an increasing applied voltage up to a maximum destructive pull in voltage. Measurement of diaphragm deflection using laser techniques was not possible due to poor reflectivity of the diaphragms, surface roughness and small diaphragm size.

7.4 Measurement summary and suggestions for further characterisation

Measurements of sheet resistance showed the p^+ diffusion to be quite uniform but measurements of metallisation sheet resistance indicated poor uniformity, which was addressed by improvements to the sputter plant apparatus.

Optical measurements of p^+ silicon film thickness and etch rates were investigated and showed potential for accurate characterisation of the thin silicon films subsequent to further investigation of the technique and test structure fabrication.

From the tests and observations carried out it was clear that the miniature diaphragms deflect when subjected to an applied bias. If the bias voltage exceeded 2V, the diaphragm collapsed resulting in permanent stiction or even fracture. Many of the devices were impaired by a low resistance between the diaphragm and the backchamber which could have been caused by debris, residues or stress induced diaphragm collapse. Improved dehydration and handling methods could help reduce the influence of these factors and result in higher yields of open circuit testable devices.

The frequency response obtained was unexpected and probably not a complete representation of device behaviour due to the test environment and signal measurement limitations. It was likely that the measurements taken only indicated the resonant behaviour of the device and that signal output between resonant frequencies was masked by poor signal to noise ratio. For more detailed measurement of frequency response, the microphone should be directly gold ball bonded to a custom low noise impedance conversion and bias control chip, which would help reduce unwanted stray capacitance and noise susceptibility. A miniature screen surrounding the package would also reduce the presence of 50 Hz mains interference.

8.0 DISCUSSION

This thesis has demonstrated the difficulties of developing a silicon microstructure from scratch with limited available resources for fabrication, characterisation and test. In spite of these limitations, it was possible to solve technical problems to the extent that microstructures could be fabricated reliably by using the evolved processing schedule described in appendix 2. From the previous results chapter, it is evident that the structures did not have the desired characteristics in terms of frequency response and sensitivity, described in chapter 3, for use as condenser microphones. Hence, due to low device yields, it would not be safe to assume that the characteristics depicted in fig. 7.11 are typical for the implemented structures.

It was not possible in the time available to determine experimentally exactly why the microphone characteristics were poor and due to the lack of statistical data it is not appropriate to draw firm detailed conclusions on the outcome of electrical testing. However, from examination of the microphone references given in chapter 2 and comparison with the main fabrication problems encountered, it is possible to gain an insight into areas that should be focused on, with respect to the microphone implementation of this project, for the purpose of directing future research. These areas required survey of appropriate literature and are described in this chapter with a view to providing relevant signposts for future extension of this work.

This chapter concludes with details of a more advanced p^+ microphone that should overcome the assumed limitations of the structure employed for this work. This structure requires the use of double sided mask alignment equipment for its fabrication, a facility that was unavailable for this work.

Main areas for further research and development

The following areas have important implications for the future successful design and development of the proposed microphone structure and are listed as follows

i) Stress distribution in doped layers.

Due to the varying concentration of p^+ diffusion profiles the microphone diaphragm will have residual stress. This stress will affect the sensitivity of the microphone (See eqn A1.11) and should be controllable, predictable and measurable.

ii) Thin film properties of a gold/titanium multi layer on glass.

It was found that the metallisation scheme was more difficult to implement than anticipated and required precise control of thin film properties. It is very important to fabricate high conductivity, stable and easy to gold ball bond microphone electrodes with a precise thickness (Thickness must not deviate by more than +/- 3 nm)

iii) Thin air gap damping.

It is extremely likely that the thin air gap of 1um with no vertical back chamber ventilation holes caused damping of the silicon p^+ diaphragm, resulting in the most likely explanation for the poor frequency response that was observed experimentally. Damping was not taken into consideration at the outset because a structure could not be fabricated with holes in the back chamber using the resources available. Furthermore, satisfactory models were

not available at the design phase to predict the effects of the given backchamber design on the sensitivity and frequency response of the implemented structure. Specialised sophisticated fluid dynamics models need to be devised to provide insight into this problem.

The next three sections describe these areas in more detail and outline simple models from the literature, that have been evaluated in some cases, to give a greater insight into the complex design issues that have emerged as a result of carrying out this work. Each area represents a specialised research area in its own right and would require the design and development of highly involved fabrication and characterisation techniques beyond the scope of this project.

8.1 Stress regime resulting from boron diffusion

The structure fabricated for this work relies on the boron etch stop where the silicon must be heavily doped in excess of $5 .10^{19}$ to achieve a good stop. The boron atom, with an atomic radius of 0.88 angstroms, is smaller than that of silicon atom, which is 1.17 angstroms, so when boron enters the silicon lattice substitutionally the lattice contracts and results in a tensile stress with a negative intrinsic bending moment. This stress is non uniform through the thickness of the diffusion layer because the boron distribution is non uniform. It has been speculated that the substitutional nature may saturate at high doping levels and boron is forced to occupy interstitial sites which may eventually lead to compressive stress. The extreme results for this non uniform stress are shown for an M1 device in plate 8.1, where the diaphragm is highly buckled, and stresses in the rim have caused it to fracture in different places. Clearly a greater understanding of the stress profile is necessary in order to prevent this.

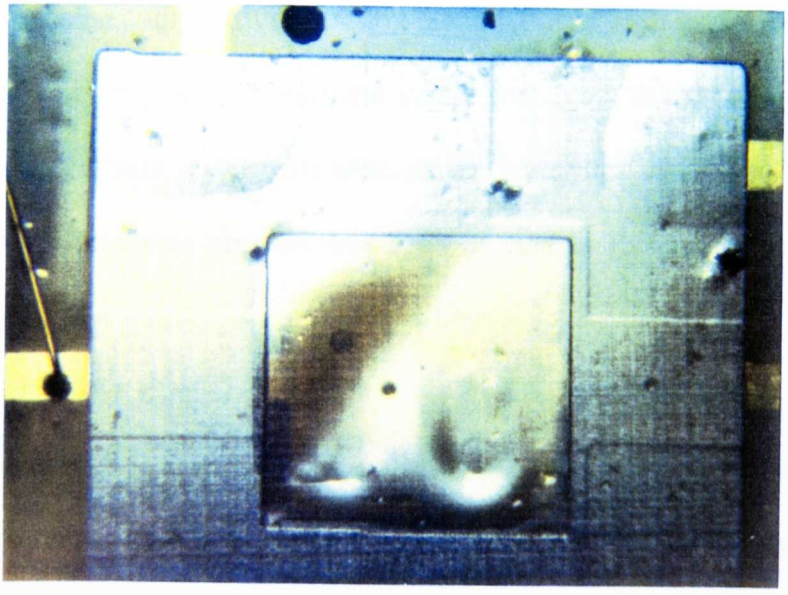

Plate 8.1 : Buckled diaphragm. Unwanted stresses in p^+ diffusions can cause a silicon diaphragm to buckle and its supporting rim to fracture.

This stress profile can be influenced by further thermal steps subsequent to diffusion and in some cases can become compressive. For thin diaphragms, a built in stress can manifest itself in the form of buckling and in extreme cases will lead to fracture. For microphone implementation an in built stress will alter device sensitivity considerably from that of a stress free plate. This stress problem has been studied in the literature and will now be reviewed.

Faroborz and Senturia[89] proposed, from suitable experiments, that the use of an oxide etch mask during membrane fabrication can alter the stress state from tensile to compressive with a positive bending moment. They indicated that plastic deformation of the p^+ silicon layer below the compressively stressed oxide was the cause. They showed that buckled membranes when etched in KOH regained their flat shape when the thin layer at the p^+ surface was removed, indicating a return to a tensile stress dominated state. The stress in the oxide layer is attributed to the thermal mismatch between the oxide and the silicon. During the cooling of the oxidised wafer, the large stresses developed at the interface provide a local permanent set in the p^+ silicon adjacent to the oxide-silicon interface. By doping electrically active boron impurities in the silicon the activation energy of dislocation motion will be reduced and plastic flow will be enhanced.

Annealing was used by Ding et. al. [90] to reduce non-uniform tensile stress in boron doped p^+ Si cantilever beams and for his experiments he found the optimum annealing time to be 1100 °C, for about an hour in a nitrogen ambient, for 1μm to 4μm thick beams. It was found that annealing could be performed before the silicon etch (ie before beams released) in either oxygen or nitrogen. Further work on stress strain curves of cantilever beams showed that

boron doped p^+ silicon films had linear elastic brittle behaviour at room temperature in the same way as bulk silicon does. He found the Young's modulus in the (110) direction to be about 124+-2.1 GPa from tensile and resonant frequency tests which is up to 28 % less than the published value for low doped bulk silicon. The high temperature annealing, either before or after the silicon etch, had no influence on the Young's modulus of the p^+ silicon films indicating that the Young's modulus is independent of the non uniform built in tensile stress. It was not determined whether the Young's modulus reduction was due to the small thickness of the films or the doping profile, however it would be expected that the Young's modulus for a thin p^+ silicon film would differ from that of the bulk silicon.

Another paper by Ding [91] suggests that residual stress in the diaphragm becomes compressive because the intrinsic tensile stress in the p^+ layer is greatly reduced by the drive in process. Experiments showed that all diaphragms etched from wafers with boron diffusion as the last high temperature process were flat, but those with drive in as the last process were buckled. There was no oxide created during the drive-in process so he concluded that the buckling was not due to stress caused by plastic deformation in the region adjacent to the silicon oxide interface. For his experiments, with etch stop diaphragms in a silicon wafer, he indicated that the drive in process greatly reduces the tensile stress in the p^+ layer due to the reduction of the maximum boron concentration and stress relief due to dislocation movement. When the diaphragm is formed by a cavity etch, local compressive stresses are generated due to adjustments of the internal stresses and the bending moments around the edges (Mechanical discontinuities) of the cavity. The net stress is composed of intrinsic tensile stress and local compressive stress and when it becomes compressive and larger than a critical value, the diaphragm buckles. The diaphragms with diffusion as the last process

remain flat because the residual stress is still tensile.

For drive-in, in an oxygen ambient, the boron atoms diffuse further into the silicon and also out diffuse into the oxide layer due to segregation effects. These two processes reduce the surface concentration of the diffusion profile near the silicon-silicon dioxide interface. The surface layer with the highest concentration is removed by the HF etch because of silicon consumption during oxidation. As a result of these processes, for thin diaphragms, the boron distribution can be nearly symmetrical about the middle plane of the diaphragm. (Ding showed this for a simulated 1125 °C two hour boron diffusion) The drive in causes the dislocations generated in the boron process to be diffused into the interior of the silicon for more uniform distribution in the p^+ layer. This can be tested for realised diaphragms, that have had an oxygen ambient drive-in, by releasing them from the edges and checking for flatness. Ding released several buckled diaphragms from the clamped edges and found them to be flat thus reinforcing his simulation results.

Further study, by Chu and Mehregany [92], investigates the effect of thermal oxidation on the residual stress distribution through the thickness of heavily boron doped p^+ silicon films by experiments with cantilever beams. A positive curvature, or negative bending moment, is shown for cantilevers of as-diffused p^+ films by upward bending of the beams. Prior to beam fabrication, by anisotropic etching, the residual stresses in the near surface region of the p^+ films are modified by thermal oxidation, which can lead to a negative curvature when the oxide is removed. The remainder of the beam has been shown to have a residual stress distribution resulting in positive curvature. To verify that the high temperature oxidation process, and not the silicon etch (where partly etched cantilevers are deformed under the

oxide mask which has compressive residual stress) cause the change in stress distribution in the near surface region, a sputtered gold/chrome etch mask was used instead of an oxide mask. The cantilever deflections were within 10 % of those that were etched with an oxide mask, indicating that the thermal oxidation step is the primary cause of residual stress distribution through the film thickness.

Cross sectional studies using transmission electron microscopy (TEM) of the microstructure of heavily boron doped silicon have been carried out by Ning et al. [93] They compared a borosilicate glass BSG - boron doped silicon interface with a thermally oxidised - boron doped silicon interface and investigated the high density of stress relieving dislocations that are generated for heavy boron doping. These dislocations can greatly influence the mechanical properties of heavily boron doped structures. Earlier work has already characterised these dislocations as edge type and they exist in (100) planes, with densities of 10^9 dislocations/cm^2, that are parallel to the wafer surface. The high concentration of boron in the surface of silicon affects the surface oxidation and changes the boron diffusion coefficient deep into the bulk silicon. This affect can be tens of micrometers away from the interface [94]. Ning's work shows that the as-diffused BSG-Si interface is rough in comparison to the SiO_2-Si interface, which is obtained when the BSG is removed and a thermal dry oxide is grown. Both of these interfaces are quite rough in comparison to a conventional oxidation of moderately doped silicon, where the interface can be atomically flat (This has been determined from AFM and TEM studies). With an oxygen concentration of 2 % the as-diffused boron saturation corresponds to a boronisation of silicon, while in the thermally oxidised case the oxygen is saturated and the boron concentration is 1% which represents a normal oxidation of p^+ silicon. No differences in density, configuration and

types of dislocation was found in the dislocation zones of the two interfaces studied. So in conclusion, the interface of BSG-p^+ Si is the main difference and the top surface of the p^+ diffusion shows the most roughness which is precisely the region that can change the buckling behaviour of silicon diaphragms as discussed in the last paragraph. Calculations by Ning show that the stress decreases nearly linearly from the interface surface (ie. the interface between BSG-p^+ Si or SiO_2-p^+ Si) of the wafer in to the first two thirds of the p^+ silicon profile depth. The shear stress at the surface is much greater than the yield stress at the diffusion temperature and so a high density of dislocations are preferentially generated in the surface of the diffused layer. Due to the stress gradient of the profile, the dislocations are forced down into the regions of lower boron concentration with correspondingly lower stress regions. A non uniform dislocation distribution therefore exists through the thickness of the diffusion profile. Dislocation interaction is complex and is detailed further in the reference.

All of these diffusion considerations make prediction of p^+ diaphragm characteristics for given fabrication parameters quite complicated, but a simple approximate model has been proposed by Tong et al. [95] He has found that by taking a Young's modulus of 140 GPa for the (110) direction of silicon, he could fit simulated with measured results for stress and doping profiles since the two are quite related. Tong's model will now be described since it was used for p^+ profile stress calculations.

The residual stress in a plane σ_i parallel to the wafer surface, with boron concentration N_B and background concentration N_{si} can be derived from Hooke's law, assuming no plastic deformation is involved in the process, and can be written as

$$\sigma_i = \frac{E(r_{Si} - r_B)}{(1-\nu) r_{Si} N_{si}} N_B \qquad (8.1)$$

where r_{Si} and r_B are the atomic radius of silicon and boron, respectively. From fig. 8.1 and for a diffusion depth Z, the residual stress distribution can be replaced by two linear functions of the form $\sigma = mZ + c$ with different gradients and intercepts. The first line AB is represented by:

$$\sigma_{AB} = \sigma_A + \frac{\sigma_B - \sigma_A}{Z_B} Z \qquad (8.2)$$

$$0 \le Z \le Z_B$$

where Z_B is the depth of the stress plane to be considered and

$$\sigma_A = \frac{E(r_{Si} - r_B)}{(1-\nu) r_{Si} N_{Si}} N_{BS} \qquad (8.3)$$

for a boron surface concentration N_{BS}. The line BC with a different slope is:

$$\sigma_{BC} = \sigma_B + \frac{\sigma_B}{h - Z_B} (Z - Z_B) \qquad (8.4)$$

$$Z_b \le Z \le h$$

where $Z-Z_B$ represents a y axis shift, h is the junction depth and the intercept is:

$$\sigma_B = \frac{E(r_{Si} - r_B)}{(1-\nu) r_{Si} N_{Si}} N_{B(ZB)} \qquad (8.5)$$

for the boron concentration $N_{B(ZB)}$ at Z_B. The average residual stress in the diffused layer, which is useful for membrane calculations (section A2.1), can be calculated by :

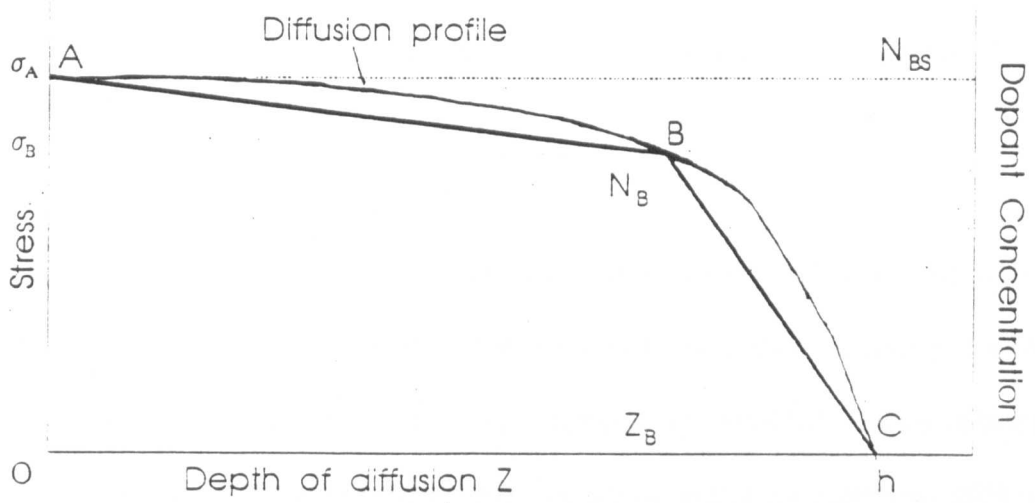

Figure 8.1 : Stress distribution and boron profile as a function of diffusion depth.

$$\sigma_i = \frac{1}{h}\int_0^{Z_B} \sigma_{AB} dz + \frac{1}{h}\int_{Z_B}^{h} \sigma_{BC} dz = \frac{\sigma_A Z_B + \sigma_B h}{2h} \qquad (8.6)$$

In a heavily boron doped silicon diaphragm the residual stress can range from 80MPa to 150 MPa.

It is quite clear that a p^+ diaphragm will have residual stress effects dependent on its processing conditions, which can result in large sensitivity reductions. A couple of techniques for characterisation and stress compensation, developed by Wise[96], can be indicated. He has developed an electrostatic technique involving boron doped microbridges [97] where a voltage is applied across a gap below a free standing bridge causing it to deflect. If the electrostatic force exceeds the reaction force, which is the normal component of the total axial force of the beam, then the bridge is pulled in and collapses. The test structures devised consist of a capacitive structure between p^+ silicon and a metal electrode, where the area of capacitance is kept constant. He uses two structures with different beam lengths which allow the force P_a, created by the axial stress, to be calculated and the Young's modulus, by the solution of two simultaneous expressions for the pull in voltage. The average intrinsic stress σ_i is given by (force/area):

$$\sigma_i = \frac{P_a}{bh} \qquad (8.7)$$

where b and h are beam width and thickness, respectively. For the calculations he assumes that the stress through the beam is uniform and in tension, the effect of Poisson's ratio is small, the deflection distance is small in comparison with the beam thickness and the beam does not distort when it pulls in.

The use of stress compensating dielectrics, where diaphragm dimensions cannot easily be changed (e.g use of a thicker membrane to reduce effects of internal membrane stress), can improve sensitivity substantially. However, to use such compensating techniques, the dielectric film must be characterised, which can be achieved with the afore mentioned technique. If it is assumed that for a composite beam composed of two different materials the beam is in tension, each layer has uniform stress and the composite structure does not bow then the stress relationship has been derived as follows[98]

$$\sigma_c t_c = \sigma_1 t_1 + \sigma_2 t_2 \qquad (8.8)$$

where σ_c is the total composite stress, t_c is the total thickness, $\sigma_{1,2}$ are the individual stresses for each layer, and $t_{1,2}$ is the respective thickness of each layer. If layer 1 represents a p^+ diffusion layer, then for layer 2 which is to be used for compensation, σ_2 can be set by fabrication of a suitable thickness t_2 for stress compensation of layer 1, after characterisation of the composite layer and the individual layers. Compensation dielectrics can include LPCVD silicon dioxide and LPCVD silicon nitride. An alternative stress compensation technique, indicated in section 4.6, would involve co-doping of germanium with boron. Wise [98] has developed a scaling theory for boron doped membranes which includes the intrinsic stress, and has used it to design ultra sensitive pressure sensors. He states that pressure sensitivity of diaphragms that have a thickness greater than 10 μm or a length less than 1mm are not significantly affected by the internal stress of the plate and can be considered stress free.

From the models for stress distribution that have been indicated and the well understood modelling of boron diffusion theory, it should be possible to fabricate diaphragms with precisely controlled stress profiles and hence control microphone sensitivity closely. For

example, using the diffusion modelling of section 4.11 and the stress profile model of this chapter, a program was written to numerically compute the average diaphragm residual stress for the range of diaphragm thicknesses and pre-deposition times shown in fig. 8.2. The results are displayed in fig. 8.3, where it can be seen that the average residual stress increases with pre-deposition time linearly. For this work, the pre-deposition time for the diaphragm was 1 hour which gave an etch stop diaphragm thickness of about 0.4μm. If this profile was driven in, the etch stop diaphragm could have been increased to a maximum, which is shown simulated in fig. 8.4, showing that the maximum diaphragm thickness for a drive in time between 8 and 14 hrs. is nearly 0.8 μm. After this maximum drive in time, the thickness is reduced as the profile concentration drops below the critical value. For these drive-in profiles, the average residual stress can be computed and plotted for the different diaphragm thicknesses as shown in fig. 8.5. From this figure it would appear that the etch stop diaphragm thickness increases to a maximum and then decreases due to the drive in process. The residual stress increases, for the maximum thickness of 0.8 μm and the stress ranges from 35 -45 MPa. From these simulated results it should be possible to select the pre-deposition and drive in conditions in order to fabricate a diaphragm with the desired average tensile stress in order to achieve a particular mechanical sensitivity. Experiments to investigate stress control of the diaphragm in order to verify calculations were not carried out in this thesis, because it was not feasible to design structures and techniques for residual stress measurement in the time available.

(Errors from the straight line are numerical in origin and are due to the number of models evaluated, finite word length and numerical integration) The values obtained from this model, for a given diaphragm thickness, can be substituted into the diaphragm deflection models (See

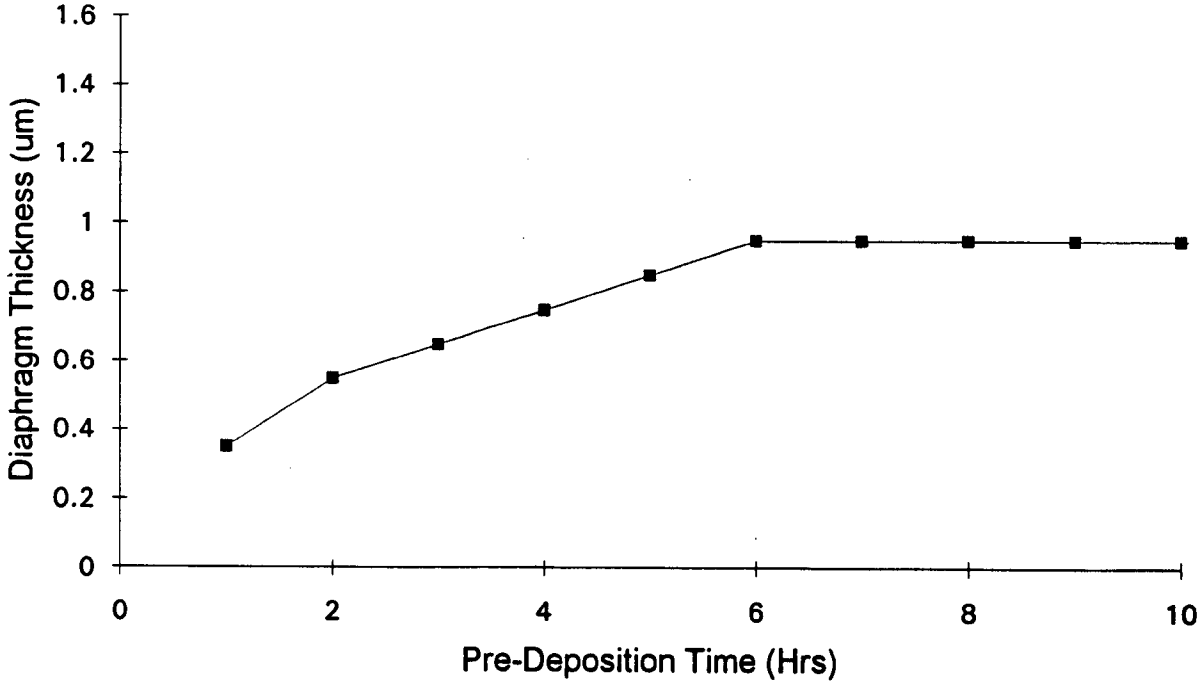

Figure 8.2 : Calculated diaphragm thickness as a function of pre-deposition time at a temperature of 1050 °C. (Calculations derived from equations in section 4.4)

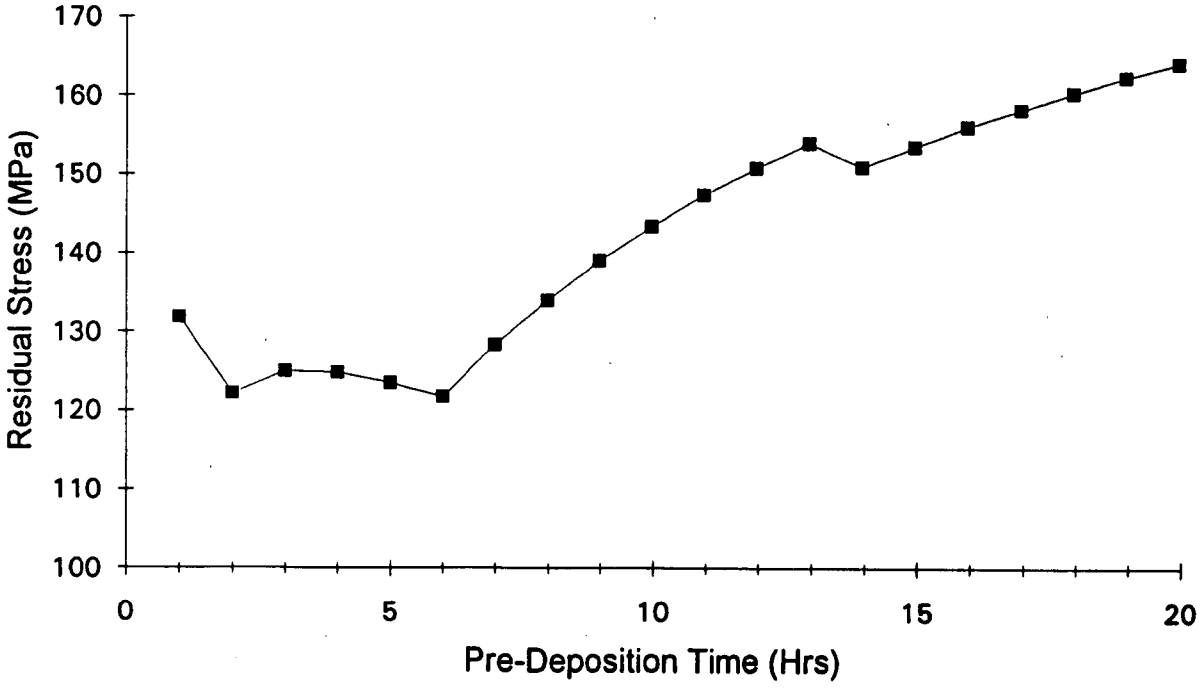

Figure 8.3 : Numerically calculated average diaphragm residual stress as a function of pre-deposition time for the diaphragm thicknesses given in figure 8.1. (Stress calculations from eqn. 8.6)

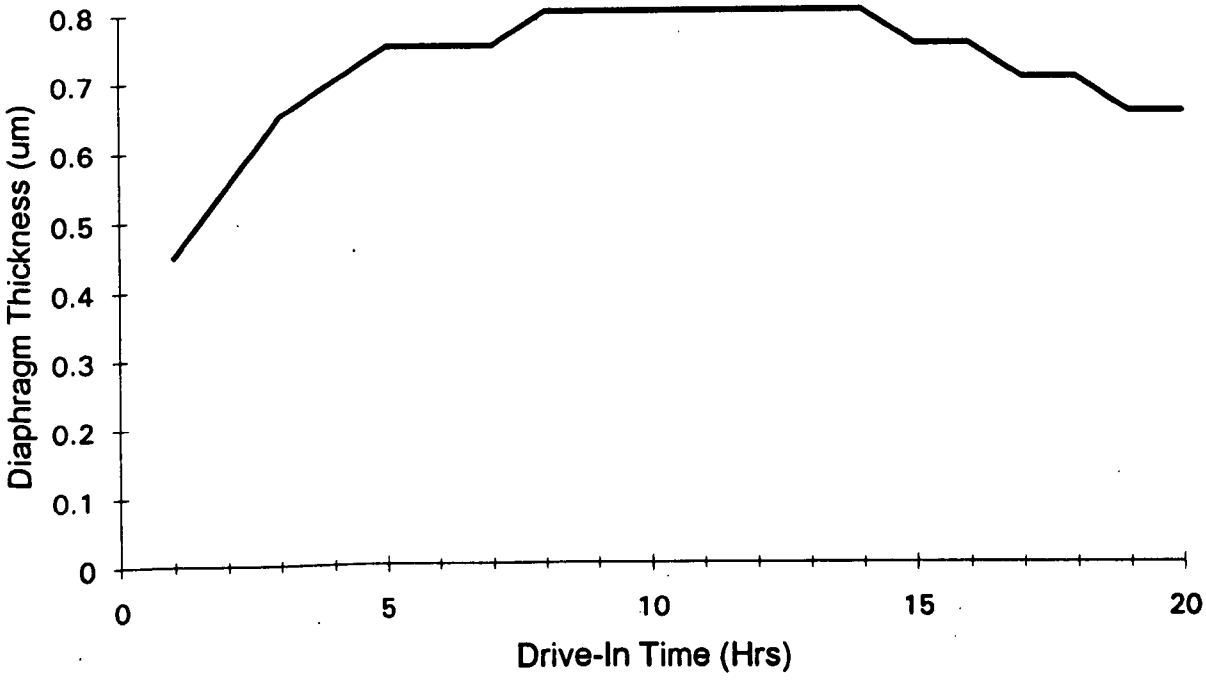

Figure 8.4 : Calculated diaphragm thickness as a function of drive-in time at a temperature of 1050 °C for an initial pre-deposition of 1 hr.(Calculations derived from equations in section 4.4)

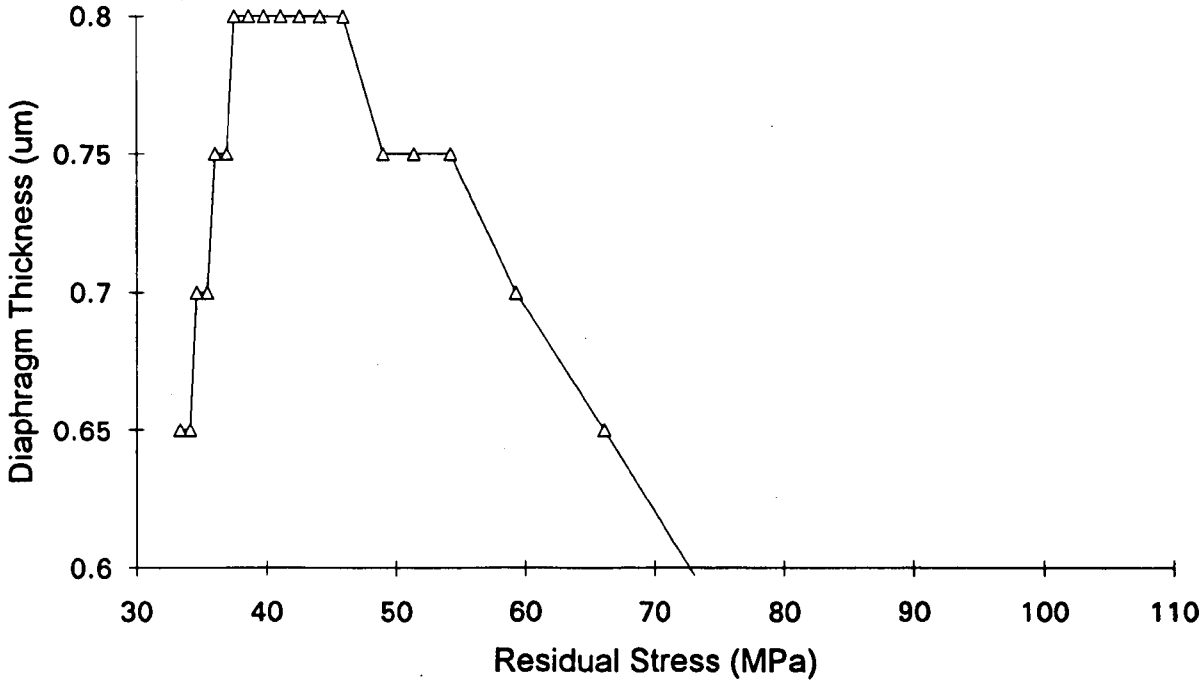

Figure 8.5 :Calculated diaphragm thicknesses derived from the diffusion conditions of fig.8.3 and their corresponding numerically calculated average diaphragm residual stress values.

section 3.1) to estimate microphone sensitivity.

8.2 Thin film properties of a gold/titanium multi layer on glass.

It is clear from results that there are many parameters such as deposition and annealing conditions that affect the metallisation properties. For this work, undesirable annealing introduced by the electrostatic bonding stage has, in many cases, caused gold ball bonding to fail. From the literature, more insight into thin film behaviour can be gained.

Properties of a vacuum deposited layer are influenced by impurities in the structure, such as absorbed gases, oxides and volatilized heater material and its structural form such as the texture and orientation of the crystallites. The structure and the purity are dependent on the conditions during the film formation such as rate of condensation, vapour incidence angle, gas pressure and substrate temperature etc. A vacuum deposited film is a product of its mode of deposition and environment and because the reproduction of experimental conditions is very difficult, each film is almost unique.

Very thin metal films condensed on non-metallic substrates can yield high specific resistivities. Further electrical conduction only becomes apparent when the film has reached an appreciable thickness. Thin metal films show with increasing thickness a continuous decrease in resistivity from higher than $10^{14}\,\Omega$. A thin metal film may possess a smooth continuous texture if the forces binding the condensed atoms to the substrate are greater or comparable to those between the condensed atoms. If the deposition is stopped, the films show a decay of conductivity with time, even though the surface is maintained at the temperature of deposition. The magnitude of this decay depends on the condition of the

surface on which the film is laid down, but becomes consistent after very vigorous heat treatment of the surface. It then decreases as the temperature of deposition is lowered, and provided the temperature is low enough may be completely arrested. Most experimental measurements of resistivity and film thickness are subject to errors which arise from the presence of unknown impurities in the film and the difficulties in measuring the thicknesses of deposits of a few atomic layers. Wilkinson [99] found that the resistivity of aged gold films as a function of thickness could be fitted to an equation by Planck

$$r_f = r_b\left(1+\frac{A}{t}\right) \tag{8.9}$$

where r_f and r_b are the resistivities of the film and bulk metal and A is Weale's constant given by

$$A = 4\frac{L_T}{\pi} \tag{8.10}$$

where L_T is the normal mean free path in the metal at temperature T. Choosing L_T = 970 Å, the curve of fig 8.6 can be used to fit Wilkinson's results, where gold was deposited on a glass substrate at 0°C. These results indicate that thicknesses greater than 10nm will approach the resistivity of the bulk gold metal. Very thin gold films on glass have extremely high resistivities. These values include an unknown resistivity term due to agglomeration of the film as well as shortening of conductor boundaries, since without the heat treatment, the resistivity is extremely difficult to predict.

A metal film can show an irreversible change in resistivity if maintained at or raised above the condensation temperature. When a freshly deposited layer of gold on glass is raised at a constant rate above that of its condensation temperature, the resistivity can first rapidly

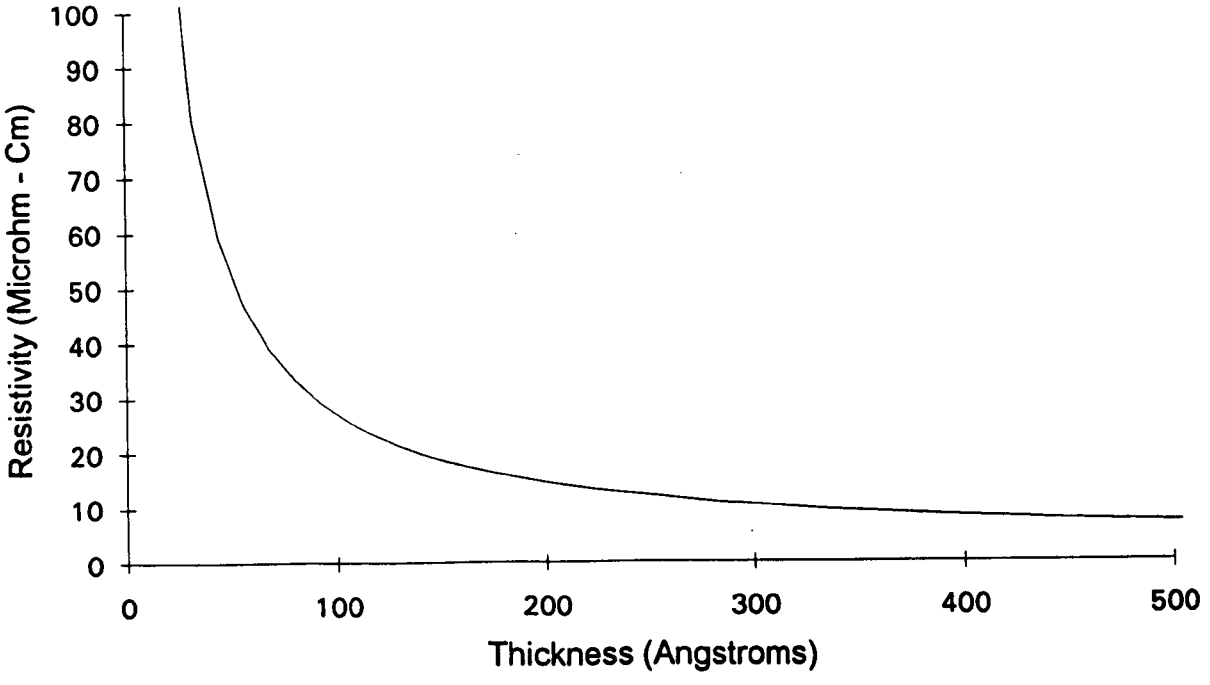

igure 8.6 : Curve fit of Wilkinson's results for the resistivity of sputtered gold as a function f thickness.

decrease to a minimum. If the temperature is raised further, a further decrease in resistivity can be observed. Finally after being maintained at a constant temperature for a long time, a low stable resistance is reached. Vand [100] explains that when a film has been raised in temperature for an appreciable period, a low stable resistance is reached, which exceeds the bulk value by virtue of the small thickness, traces of impurity atoms and undecomposed distortions.

If the texture of the deposit becomes granular consequent to the temperature rise, the irreversible decrease in resistance is not observed. Thus gold shows irreversible decrease after formation, but if the temperature is raised above 250 °C, the resistivity will irreversibly rise as the film becomes discontinuous due to the growth of isolated crystals. This increase can begin over 5 mins. of heating. This effect is less likely for thicker films.

From the preceding paragraphs and the results of section 6.8 it can be proposed that the electrostatic bonding stage could be causing the gold metallisation to recrystallise, since the bonding was carried out in the temperature range of 300 - 350°C for electrostatic bond times greater than 5 mins. The results of the gold ball bond tests (Section 6.7.3) on the metallisation films, annealed for different times, would indicate that the recrystallisation occurs between 15 and 30 mins of the anneal time, depending on temperature. If the specified 25 nm titanium layer is taken into consideration, which may not be continuous if the actual film thickness is not accurately known, then as the gold recrystallises, it may cluster between titanium islands. It was found from experiments that adhesion of gold film to glass was not high in comparison to its adhesion to a titanium inter layer, so when the gold ball bond was carried out, the gold clusters could have been pulled from the glass by

the gold ball. This reasoning could explain some of the failed gold ball bonds experienced for some of the completed structures, because there was insufficient titanium layer (ie only titanium islands present on the glass) to maintain a robust gold film adhesion.

It can be concluded that in order to achieve useful metallisation, a continuous titanium film of accurate thickness must be deposited and a thick accurate gold film must be employed to overcome recrystallisation effects. For this design, the maximum thickness should be greater than 10 nm but less than 75 nm. Additionally, deposition temperatures should be controlled carefully and the electrostatic bonding process should be carried out in under 15 mins at a low temperature. (300°C)

Ultimately, it was found that with the geometry and nature of the available deposition equipment shown in plate 8.2, that accurate thickness for thin films below 100nm was not reproducible for a multi layer metallisation. It is clear from the photograph 8.2(b) that the positioning of the titanium target, gold source and monitor crystal with respect to the substrate, which was clamped to the lid, were incompatible with uniform, controllable film deposition.

8.3 Effect of thin air film on the vibrations of a stretched circular membrane.

When the air thickness which is trapped behind a membrane is comparable with the size of the viscous and thermal boundary layer, which is in the range of 1-10 μm, the response will decrease with increasing frequency. This effect is due to the radial air flow causing large dissipative and reactive effects. Holes or furrows can be placed in the back electrode to minimise this effect. Wente indicated that the small air gap introduces a coefficient of

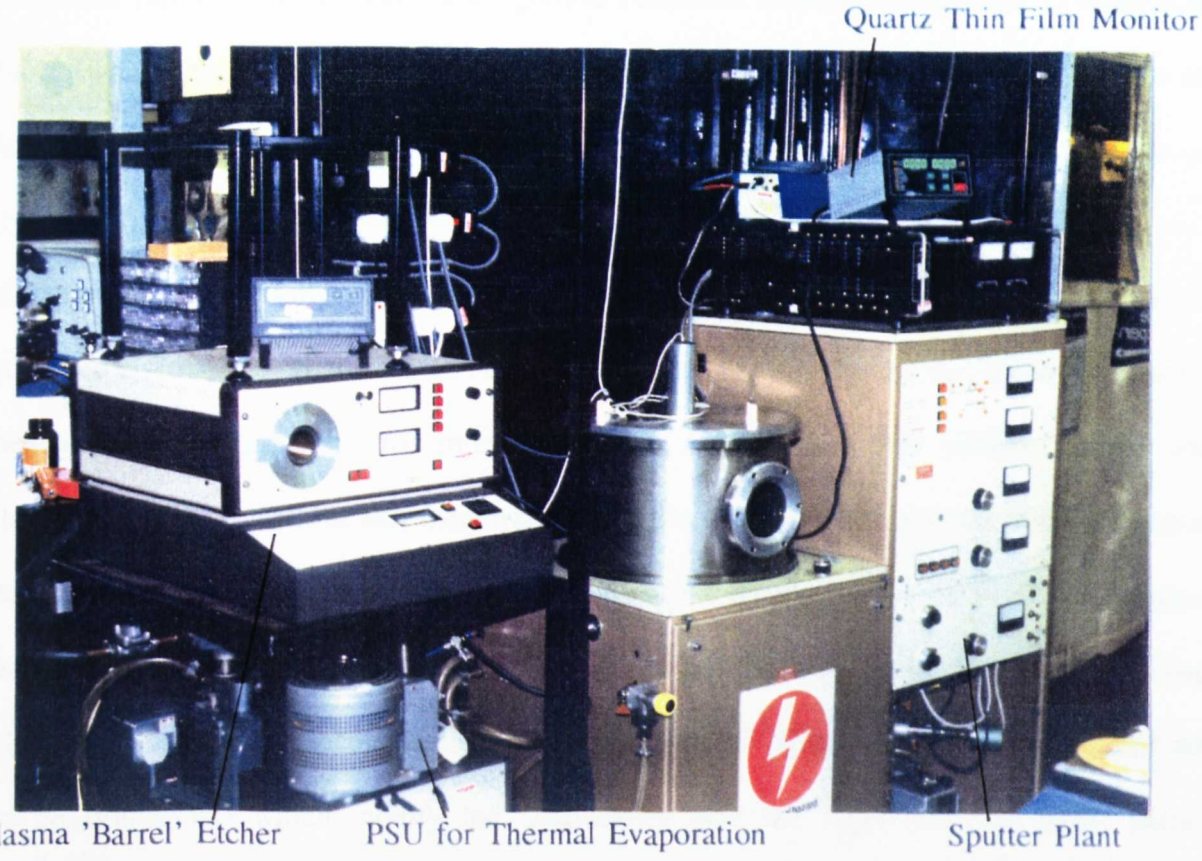

Plate 8.2(a) : Photograph showing the plasma etcher and sputter plant apparatus.

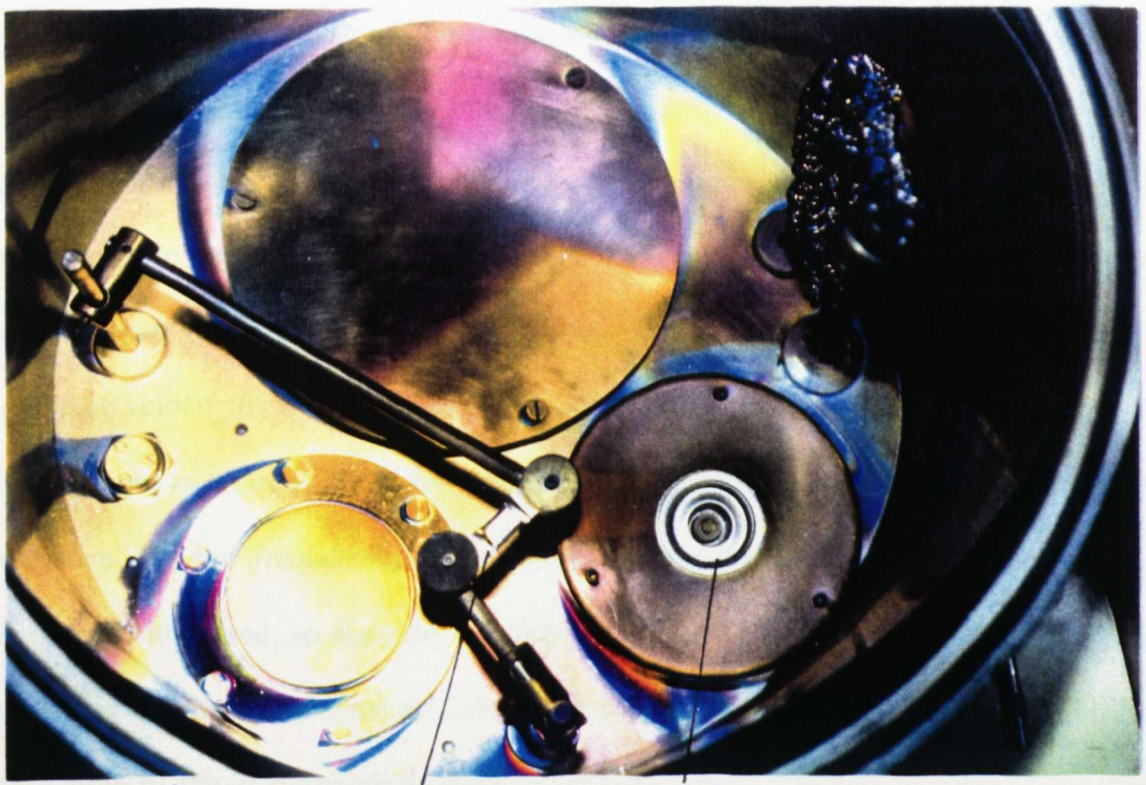

Plate 8.2(b) : Configuration of sputter plant metallisation apparatus with the lid removed.

resistance into the system, that is analogous to Poiseuille's coefficient for flow in small bore tubes, which leads to damping of the membrane. Additionally, the lateral motion of the air is prevented by its viscosity and contributes to the additional stiffness of the membrane.

A derivation, from fundamental fluid equations, for the effect of the thin air film on a stretched circular membrane is given by Robey[101] where gravity and non-linear terms were neglected because, for normal microphone use, a membrane will seldom exceed one thousandth of the electrode and membrane separation. The volume external to the air gap is considered infinite, in comparison to the volume of the air gap, which means that the excess pressure can be considered to be zero. A more recent derivation by Planter and Bruneau [102], which takes into account heat conduction effects of the gas (ie. process is assumed not to be isothermal) which modify the frequencies near the upper cut off point, shows correlation with Robey's work for a 25 μm air gap with a titanium diaphragm of radius 14 mm and 13μm thickness. The theory in the literature is only valid for a plate separation that is large in comparison to the mean free path of the gas. Robey details an explanation for the behaviour of the thin air gap where the large membrane area may be several hundred times the area where air exhausts into the external cavity or backchamber. When the membrane moves toward the back electrode, air jets out radially with a velocity that exceeds the membrane velocity by a factor of more than a hundred. The movement of this air, which can be considered as a viscous fluid for such a thin gap, introduces a mechanical resistance into the system. For low frequencies, this resistance is low and the air has time to escape, but as frequency is increased, so does the resistance to a point where the air is unable to overcome its own inertia. As a result, the air starts to compress until a frequency is reached where the transit time of the escaping air is equal to half the period. Beyond this frequency, the air

compresses further and the radial air flow is substantially reduced causing the membrane sensitivity to fall. For the example quoted, the stiffness at 20 kHz is 15 times the stiffness at 5 Hz, with a resonant frequency at an even higher frequency and stiffness. The average membrane amplitude changed from 40 to 2.5 angstroms which yields a drop in output voltage of 24 dB.

For the designs of this thesis it was not possible to determine the effects of the back chamber on frequency response by measurement because device yields were very low. The above discussion, in conjunction with evidence from recent microphone designs [29], suggests that the narrow air gap and absence of acoustic holes in the back electrode could severely reduce the upper cut off frequency to below 100 Hz. Further insight into the effects of small air gaps and the influence of backplate design can be found in literature relating to ultrasonic transducers.[103]

8.4 Conclusions

It has been shown in this thesis that silicon condenser microphone structures can be fabricated using basic microengineering techniques. The conclusion of the experimental research prevented development of the structures to the point where the fabrication was reproducible and yields were high, hence it was not possible to undertake a more detailed electrical characterisation. The main areas contributing to irreproducibility were

i) Silicon consumption and boron redistribution caused by the rim and diaphragm fabrication process, giving rise to reduced effective back chamber depth and diaphragm buckling respectively.

ii) Unpredictable stability of gold metallisation films, caused by anneal times, introduced by the electrostatic bonding process.

iii) Poor electrostatic bond stability in a prolonged low concentration room temperature KOH etch.

Suggestions for further work

Further work can be carried out to obtain higher yields of the devices and investigate the electrical characteristics. The developed processing schedule given in appendix A3.1 can be used as a basis for further research and development of the p^+ microphone structure. The following recommendations are given to assist with further research.

8.4.1 Modelling

For more detailed prediction of device behaviour and performance, the following computer aided modelling and simulation techniques could be used

i) Use the process modelling package SUPREM to determine the diffusion profiles more accurately and account for the influence of segregation and oxidation effects on the fabrication.

ii) Combine this profile information with stress modelling to predict intrinsic diaphragm stress accurately and its effects on sensitivity.

iii) Use the finite element analysis package Ansys in conjunction with electrostatic, air gap, profile stress and thermal stress modelling to predict the mechanical sensitivity and the resonant frequency of a given p^+ microphone structure geometry.

v) From the results of (iii), use an electro-mechanical model and a circuit simulator such

as SPICE to determine the frequency response, the electrical sensitivity and the noise of the silicon microphone for a given bias voltage.

vi) Develop advanced computer simulation models for silicon dissolution using anisotropic etchants in order to predict etch stops and predict etch stop etch rates, so that highly precise p^+ geometries can be fabricated and geometry specifications can be met.

8.4.2 Wafer Processing

i) High pressure oxidation could be investigated to achieve deeper back chambers in a shorter oxidation time.

ii) Ion implantation could be used instead of solid source diffusion for doping. This would eliminate unwanted borosilicate glass growth and silicon consumption.

iii) Silicon nitride masking could be used to eliminate dopant segregation and silicon consumption for rim and diaphragm masking.

8.4.3 Glass processing

To improve the glass processing, metallisation films should be deposited under highly controlled deposition conditions.

i) Rotate the substrate to achieve more uniform films.

ii) Use a cooled substrate holder to improve the lift off process by reducing the chance of the positive resist hard baking.

iii) Use moveable large diameter targets (In comparison to the substrate) with shuttering for sputtering the titanium and gold under the same vacuum, in order to achieve high

film uniformity.

iv) Sputter the gold immediately after sputtering the titanium layer.

A multiple target planetary sputter plant could be used to sputter the titanium and gold films. This type of equipment can have very accurate film thickness measurement facilities, which is important for thin films below 100nm thickness.

The substrate glass employed could be further investigated to find a metallisation substrate that is suitable for electrostatic bonding at temperatures below 300 °C, and has a very high alkali resistance, to eliminate problems with electrostatic bond deterioration for extended dissolution times. The manufacturer Hoya make some very advanced glass wafers designed for electrostatic bonding with silicon which have extremely low thermal mismatch.

8.4.4 Silicon dissolution

Silicon dissolution could be carried out using more advanced apparatus to achieve accurate etch times and sharp etch stops. Improvements that could be implemented include

i) An etchant recirculation system with a large volume reservoir to minimise the alteration of etch rate caused by byproducts (ie silicon) building up in the solution.

ii) Three term computer control (ie PID) of the etch bath temperature for etch rate control. This could be pre-programmable and linked to an etch rate model to determine temperature ramp and hold times.

iii) Concentration/Acidity(pH) measurement of solution and computer controlled IPA moderation to exercise control over etch stop behaviour. IPA would be removed by controlled evaporation.

8.4.5 Design improvements

The main area for improvement of the microphone design would be the provision of holes in the back chamber as in Bergqvist's designs. This could be achieved by using a thinner glass substrate with micromachined holes [20] or re-implementing the knowledge learned from the structure of this thesis to develop an improved design on a wafer with a p^+ backplate fig. 8.7. This design would allow the diaphragm to be fabricated with an electrochemical etch stop technique [104] to achieve a better diaphragm surface finish. Furthermore, such a design could be compatible with the fabrication of on chip electronics next to the microphone, on the back electrode wafer, which would give rise to improved output sensitivity and signal to noise ratio. The structure may even be suitable for fabrication of small microphone arrays on a single wafer. Some of the following advantages and disadvantages can be raised from this design

i) Trapped fluid would not be a problem since the two chips would be bonded after completion of wafer fabrication in a dry atmosphere either by electrostatic bonding of silicon to silicon dioxide, or investigation of low temperature silicon dioxide-titanium bonding [105].

ii) Diaphragms could be square or circular, the latter being possible if a square p^+ rim is fabricated for the anisotropic etch stop. Silicon dissolution would not require the removal of such a large quantity of high purity silicon since the silicon would be used to give the structure more strength and protection, with a structure thickness approaching 1mm.

iii) Gold metallisation would not be required since a standard $1\mu m$ aluminium electrode layer could be fabricated on the back chamber wafer.

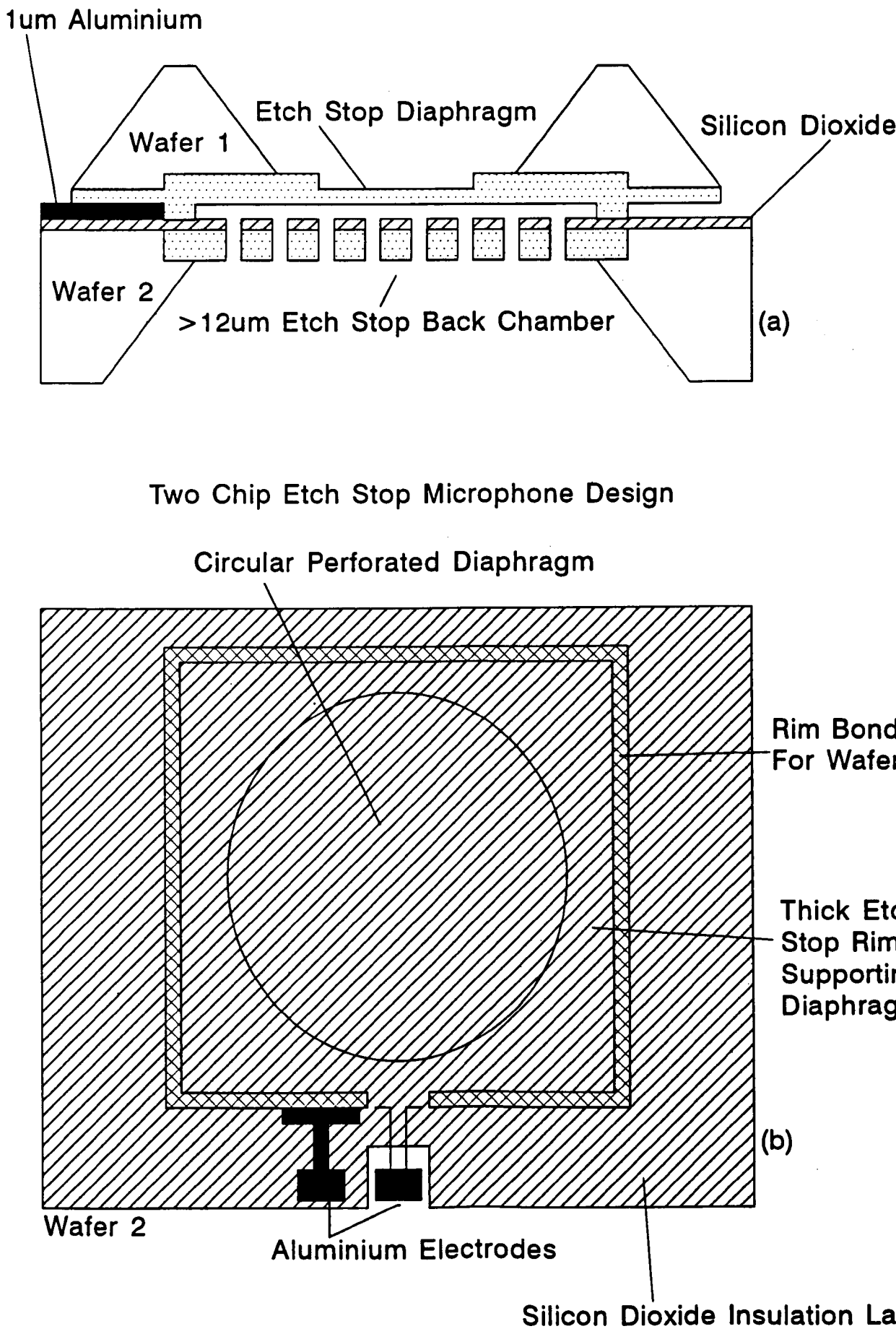

Figure 8.7 : A two chip p^+ etch stop microphone design. **(a)** Cross section of structure. **(b)** Plan view.

iv) More complicated alignment facilities would be required for the two chip monolithic structure and simple double sided wafer processing would have to be carried out for diaphragm fabrication.

v) Stray capacitance of the structure would be larger than for devices fabricated on glass, but thermal mis-match would be lower.

It is clear from this thesis that fabrication of a miniature silicon microphone structure was possible with limited fabrication resources and that further work, which utilises the above design improvements, could be conducted to obtain reproducible devices with characteristics that meet original design specifications, assuming that appropritae sophisticated modelling techniques are developed.

Further to the successful development of a single microphone, a future objective could be to realise small arrays of microphones, since there is a growing need for microphone arrays in acoustic imaging [106 , 107].

SUMMARY

This thesis details three years of research and development in silicon micromachining, which has led to the fabrication of a 2 x 2 mm^2 silicon microphone structure on a glass substrate.

Chapter 1 explains micromachining techniques, discusses the aims and objectives of this project and presents the different types of transduction techniques for microphones. This leads to presentation of silicon microphone structures in the literature survey of chapter 2.

Chapter 3 details the theoretical aspects of condenser microphones concerning deflections for stressed and unstressed diaphragms, electrostatics, microphone characteristics and aspects of silicon microphone fabrication for this project.

Chapters 4 explains all the fabrication theory and technology that was necessary to design and develop the miniature microphone structure and also supports the experimental work detailed in chapter 5. Chapter 6 summarises the main results and conclusions of the experimental fabrication work carried out .

Chapter 7 discusses some characterisation techniques that were investigated in addition to providing some results of preliminary electrical measurements.

The final chapter outlines advanced topics including control of diaphragm stress and doping profiles, thin metal film properties and microphone air gap behaviour. The thesis concludes by discussing possibilities for future research, with the presentation a new design.

Glossary

Due to the multidisciplinary nature of this thesis, a short glossary is provided to explain some of the terminology.

Activation Energy

The energy input required for a reaction to take place.

Anisotropic Etches

Etches that are capable of selectively producing a well defined etch trough with either a V- or a U-shaped cross section.

Arrhenius Relationship

For an activated process this relationship will produce a straight line connection between the log of an appropriate parameter (e.g. pressure, diffusion etc.) and the reciprocal of absolute temperature for any system obeying Boltzmann statistics.

CVD or Chemical Vapour Deposition

This is an important deposition technique which is regularly used for the deposition of silicon dioxide, silicon nitride and polycrystalline silicon (Polysilicon). The technique involves reacting a material at high temperature and depositing it on a crystal surface (e.g silicon wafer) with the aid of a carrier gas. Advanced methods of CVD such as plasma enhanced CVD (**PECVD**) and low pressure CVD (**LPCVD**) are available for specialised applications. CVD equipment is very expensive and involves the use of some very dangerous gases.

Ellipsometry

A measurement technique that can be employed for determining the thickness of transparent thin films such as silicon dioxide. It should be noted that the technique uses incident, circularly polarised light which becomes elliptically polarised on reflection from a thin film sample to be measured.

Ion Beam Etching (ion milling)

The surface of a substrate is eroded by using a high energy ion beam. Sometimes a focused ion beam is used (FIE - focused ion etching). Focused ion beams can also be used for sputtering the targeted material onto a substrate.

Miller Indices

Three numbers called Miller indices are used to describe the planes that are present in the unit cell of a given crystalline material.

These are detailed in most elementary engineering materials textbooks. For example the (100), (110) and (111) planes of silicon are the ones most referred to in this thesis.

Millipore or Reverse Osmosis water

The water used for silicon processing has to be very pure and has to be specially made using filtering and ion exchange technologies such as reverse osmosis. The millipore purification system used for this work removed particles, ions and bacteria from ordinary tap water. The purity of the water was determined by conductance measurements such that an extremely low conductivity indicated a low presence of ions in the water.

p^+ Etch Stop

When boron is diffused into a lightly doped n-type silicon wafer such that its concentration profile exceeds $3x10^{19}$ atoms/cm^3 the heavily doped, or p^+ silicon, can act as an etch stop to certain types of liquid etchants. For example, the etchant KOH will etch p^+ silicon much more slowly than n-type silicon. Hence the p^+ silicon is acting as an etch stop. (Note : An ideal p^+ etch stop would have a zero etch rate for the selective etchant used.)

Many factors can affect etch rate and etch stop properties - see chapter 4.

Plasma Etching

This is a form of dry etching that uses active ion species in a plasma to attack a

semiconductor surface. For example, an oxygen plasma can be used to remove photo resist from a wafer.

Poisson's Ratio ϑ

Consider a cube of material. The poisson's ratio can be defined as the amount by which the cube shrinks inwards when subjected to a tensile strain, and is given by the negative of the ratio of the inward lateral shrinkage strain to the original tensile strain:

ie Poisson's Ratio = - lateral strain/tensile strain

For silicon the constant $\vartheta = 0.3$ (Dimensionless quantity)

Roll Off

This is an engineering term used to describe the rate at which a frequency response is attenuated after the 3dB point, or corner frequency, of the amplitude versus frequency plot. e.g The upper corner frequency for a condenser microphone response might be 18 kHz with a 24dB/decade roll off. (Note this is second order roll off)

Sound

Sound consists of a wave motion of disturbances through a medium. In air, it is characterised by pressure disturbances superimposed on atmospheric pressure. These disturbances cause the accompanying air particles to oscillate. The air medium which transmits the disturbances does not travel out from the source it simply oscillates around a fixed point. The rate at which the disturbances travel is known as the speed of sound and has a value of 340 m/s in air at 20 °C

Sound Pressure Level (SPL)

The sound pressure level is usually expressed in dB and is given by $20\log(SP/2\times10^{-5})$. Where $SP/2\times10^{-5}$ is the ratio of the measured acoustic pressure SP to the average lower threshold of human audibility given as 2×10^{-5} Pa. Note : The acoustic pressure range of the human ear is from 2×10^{-5} Pa to 20 Pa(Threshold of pain) and would correspond to a sound pressure level (SPL) from 0 dB to 120 dB respectively.

Von Mises Stress

Von Mises yield criterion - Von Mises proposed that plastic deformation at a point initiates when the principal stresses at that point satisfy the relationship

$$\sqrt{0.5[(\sigma_1-\sigma_2)^2+(\sigma_2-\sigma_3)^2+(\sigma_3-\sigma_1)^2]}=\sigma_y$$

σ_y - Yield stress of the structural material under uniaxial tension

σ_1, σ_2, σ_3 - Principal stresses

The quantity on the left hand side of the equation is the Von Mises stress.

This expression is discussed more fully in any elementary finite element analysis engineering textbook.

VPE, LPE

Vapour phase and liquid phase epitaxy.

Wheatstone Bridge

A circuit configuration using four impedances. If one of the impedances in the bridge configuration is unknown, it can be compared with the other three known impedances for determination of its value. Further details can be found in any elementary physics text. A wheatstone bridge configuration is often used for electrical measurement in silicon strain gauges.

Appendix 1

A1.1 Mathematical models for circular condenser microphone

Static Behaviour of Condenser Microphones

Deflection of a stress free diaphragm

The relation between a homogeneous load P and the centre deflection w_o for a circular diaphragm with radius R, thickness h and Youngs's modulus E_d is

$$P=\frac{E_d h^3}{0.171R^4}[w_0+0.488\frac{w_o^3}{h^2}] \qquad \textbf{(A1.1)}$$

Deflection of a diaphragm with a large initial tensile stress σ_d

$$P=4\sigma_d\frac{h}{R^2}w_o+3.19E_d\frac{h}{R^4}w_o^3 \qquad \textbf{(A1.2)}$$

Deflection of a diaphragm with effective plate separation s_o and bias voltage V due to an electrostatic force for a stress free diaphragm

$$V^2=\frac{\frac{1}{3}\frac{s_a^2E_dh^4}{0.171R^4}[\frac{w_o}{h}+0.488\frac{w_o^3}{h^3}]}{\frac{\epsilon_o}{4w_o/s_a}[\frac{1}{1-w_o/s_a}-\frac{1}{2\sqrt{w_o/s_a}}\ln[\frac{1+\sqrt{w_o/s_a}}{1-\sqrt{w_o/s_a}}]]} \qquad \textbf{(A1.3)}$$

Deflection of a diaphragm due to an electrostatic force for a diaphragm with large initial stress

$$V^2 = \frac{\frac{2\sigma_d h w_o}{R^2} + 1.595 E_d h \frac{w_o^3}{R}}{\frac{e_o}{2w_o}\left[\frac{1}{s_a - w_o} + \frac{1}{w_o}\ln\left(1 - \frac{w_o}{s_a}\right)\right]} \qquad \textbf{(A1.4)}$$

The relation between the small signal pressure dP on the diaphragm and small signal movement dw_o of a diaphragm is determined by the mechanical sensitivity

$$S_m = \frac{dw_o}{dP} \tag{A1.5}$$

The relation between small signal movement and the small signal open circuit output voltage dV is determined by the electrical sensitivity

$$S_e = \frac{dV}{dw_o} \tag{A1.6}$$

Equilibrium of small signal forces leads to a mechanical sensitivity S_m expression for a stress free diaphragm

$$S_m = \frac{\frac{1}{3}}{\frac{dP_r}{dw_o} + \frac{dP_e}{dw_o}} \tag{A1.7}$$

where Pr is the normal reaction force per unit area and Pe is the electrostatic force per unit area. A similar equation can be derived for a diaphragm with large initial stress

$$S_m = \frac{\frac{1}{2}}{\frac{dP_r}{dw_o} + \frac{dP_e}{dw_o}} \tag{A1.8}$$

The following two expressions can be substituted into equation A1.7 to give an expression for the mechanical sensitivity for a stress free diaphragm

$$\frac{dP_r}{dw_o}=\frac{1}{3}\frac{E_D h^4}{0.171R^4}[\frac{1}{h}+1.464\frac{w_o^2}{h^3}] \qquad \textbf{(A1.9)}$$

$$\frac{dP_e}{dw_o}=\frac{\epsilon_o V^2}{2w_o^2}(\frac{2}{w_o}\ln(\frac{s_a}{s_a-w_o})+\frac{-2s_a+3w_o}{(s_a-w_o)^2}-2\pi\epsilon_o R^2\frac{(\frac{1}{s_a-w_o}+\frac{1}{w_o}\ln(1-\frac{w_o}{s_a}))^2}{C_i+\frac{\pi\epsilon o R^2}{w_o}\ln(\frac{s_a}{s_a-w_o})}) \qquad \textbf{(A1.10)}$$

The following two equations can be substituted into equation A1.8 to give an expression for the mechanical sensitivity for a diaphragm with large initial stress

$$\frac{d\overline{P_r}}{dw_o}=2\frac{\sigma_d h}{R^2}+4.785E_d h\frac{w_o^2}{R^4} \qquad \textbf{(A1.11)}$$

$$\frac{dP_e}{dw_o}=\frac{\epsilon_o V^2}{2w_o^2}[-\frac{3s_a-5w_o}{4(s_a-w_o)^2}+\frac{3}{8\sqrt{(s_a w_o)}}\ln(\frac{\sqrt{s_a}+\sqrt{w_o}}{\sqrt{s_a}-\sqrt{w_o}})-\frac{\frac{1}{2}\pi\epsilon_o R^2}{C_i+\frac{\pi\epsilon_o R^2}{2\sqrt{(s_a w_o)}}\ln\frac{\sqrt{s_a}+\sqrt{w_o}}{\sqrt{s_a}-\sqrt{w_o}}}[\frac{1}{s_a-w_o}-\frac{1}{2\sqrt{(s_a}}$$

(A1.12)

The electrical sensitivity for a stress free diaphragm

$$S_e = -\frac{V}{s_a - w_o}\left[\frac{\sqrt{\frac{s_a}{w_o}}}{\ln\left[\frac{\sqrt{s_a}+\sqrt{w_o}}{\sqrt{s_a}-\sqrt{w_o}}\right]} - \frac{s_a - w_o}{2w_o}\right] \qquad \textbf{(A1.13)}$$

The electrical sensitivity for a diaphragm with a large initial stress

$$S_e = -\frac{V}{s_a - w_o}\left[\frac{1}{\ln\left(\frac{s_a}{s_a - w_o}\right)} - \frac{s_a - w_o}{w_o}\right] \qquad \textbf{(A1.14)}$$

Finally, the total open circuit sensitivity for a stress free diaphragm, or one with large initial stress can be determined by using the following expression and the relevant equations defined earlier

$$S_{tot} = S_m S_e \qquad \textbf{(A1.15)}$$

S_{tot} is negative so sometimes the magnitude used.

Appendix 1

A1.2 Clamped diaphragm resonant frequency calculation

Formulae for calculation of the resonant frequency f_n of a plate with clamped edges.

$$f_n = \frac{2\pi}{3}\left[\frac{D}{\rho}\left(\frac{3}{a^4} + \frac{2}{a^2 b^2} + \frac{3}{b^4}\right)\right]^{1/2}$$

Properties for a 1mm^2 x $1\mu\text{m}$ thick silicon diaphragm.

Density of silicon $\rho = 2320\ \text{kg/m}^3$

Diaphragm area (a x b) dimensions $a = b = 1 \times 10^{-3}\ \text{m}$

where D is the flexural rigidity,

$$D = \frac{Eh^3}{12(1-\nu^2)}$$

Young's modulus for silicon $E = 3.12 \times 1011\ \text{N/m}^2$

Poisson's ratio $\upsilon = 0.3$

Diaphragm thickness $h = 1 \times 10^{-6}\ \text{m}$

For the above values the resonant frequency $f_n = 20.784\ \text{kHz}$

Appendix 2

A 2.1 Preliminary experimental work to formulate the processing for microphone structures.

Very early work involved investigation of masking and diaphragm etching by anisotropic and etch stop techniques. This section outlines the results and conclusions from this work.

Masking

Positive drawings (Actual size μm) for the masks were designed with Autocad using poly lines to construct the masking shapes Fig. A2.1 (Mask for M2 microphone). Each layer was plotted at a 4:1 ratio using a 0.01 mm dia draught pen and then photographed directly onto a 4" high resolution lithographic photographic plate with a 4:1 reduction ratio. Higher quality masks in terms of edge definition, quantity of devices and resolution could have been obtained using a step and repeat camera for mask generation, with a reduction of 16:1 for each individual pattern, however this facility was unavailable. To obtain a positive glass plate, the negative glass plate was contact printed onto a second glass plate. Care was taken with image reversal to avoid mask mismatch.

This method was not completely satisfactory since registration errors of a few hundred microns, from one mask to another, were evident due to non linearities of the plotter. Mask defects were also present in large numbers due to artwork defects, emulsion defects and particulate contamination. The reduction ratio was manually set up and incorrect ratios gave errors in mask geometries.

An improved technique was used where a 1:1 file was generated for each mask level and output as a postscript file. This file was then printed on acetate sheets using a 2400 dpi laser

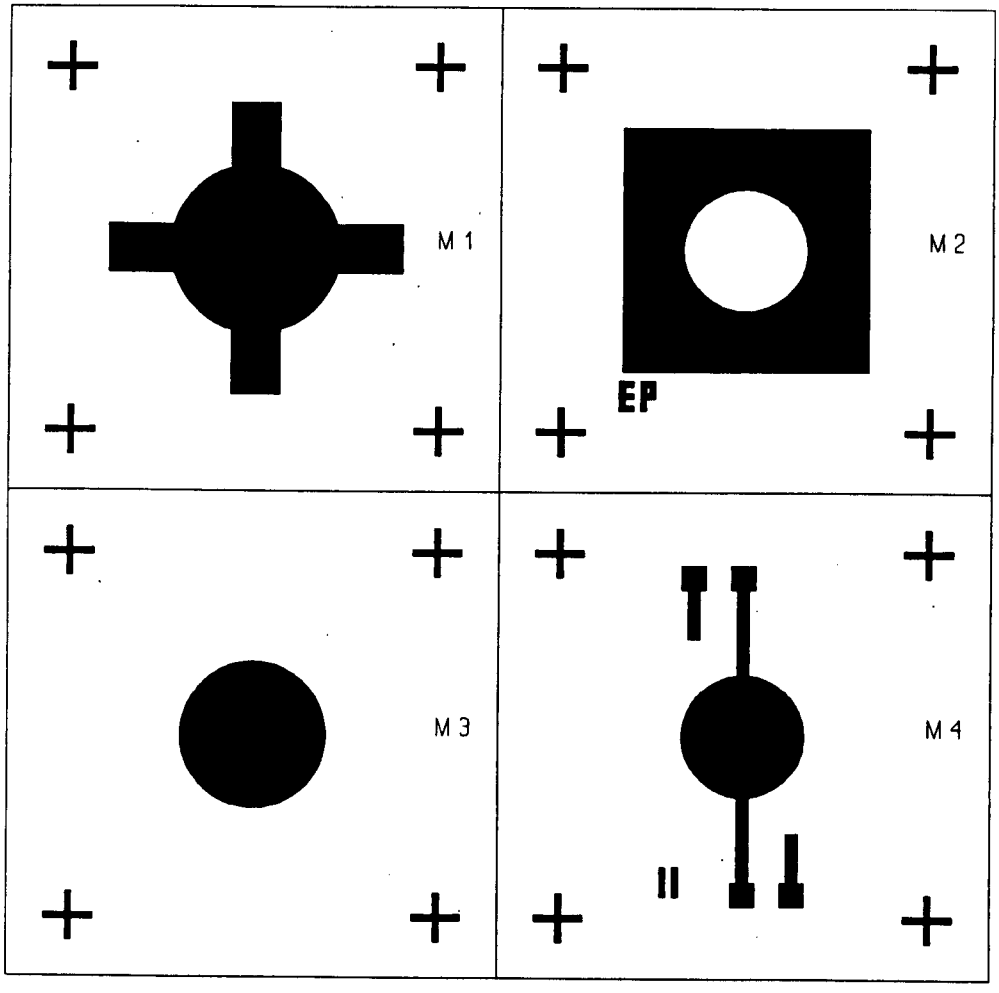

Figure A2.1 : Silicon processing masks M1-M3 and the metallisation mask M4 for fabrication of a circular silicon microphone on a glass substrate.

printer that used a semi photographic process. Negative or positive masks could be specified. To obtain the 4" glass plates, a simple contact print was carried out. A minimum resolution of 50 μm was obtainable with this procedure which was quite acceptable for the relatively large planar geometries that were implemented. The files generated by this method could be larger than 2MB for more than 50 devices, which necessitated large data storage facilities. Fig. A2.2 depicts a reduced resolution positive metallisation mask (Not to scale).

All contact printing for a mask set was carried out at room temperature on the same day and photographic materials were allowed to stabilise to this temperature before use to prevent thermal expansion effects leading to significant registration problems. (Especially for acetates) It was important for all contact printing, that the emulsion side of the mask faced the emulsion to be exposed, in order to prevent undesirable shadowing and lowered resolution of masks.

It was found, after optical microscope investigation, that the laser printed acetates had quite dense pitting defects ($<5\mu$m). This caused problems for the metallisation mask which was a negative glass plate, where the pitting defect was transferred to the metallisation in some places during processing.

The laser printer mask fabrication route was found to be low cost and quick. It generated masks with improved resolution, and cross mask registration, in comparison to the plotting/photographic process which could not be controlled as well. Commercial chrome masks which are very expensive could have been made once the microphone masks were satisfactory and the fabrication processing was reproducible.

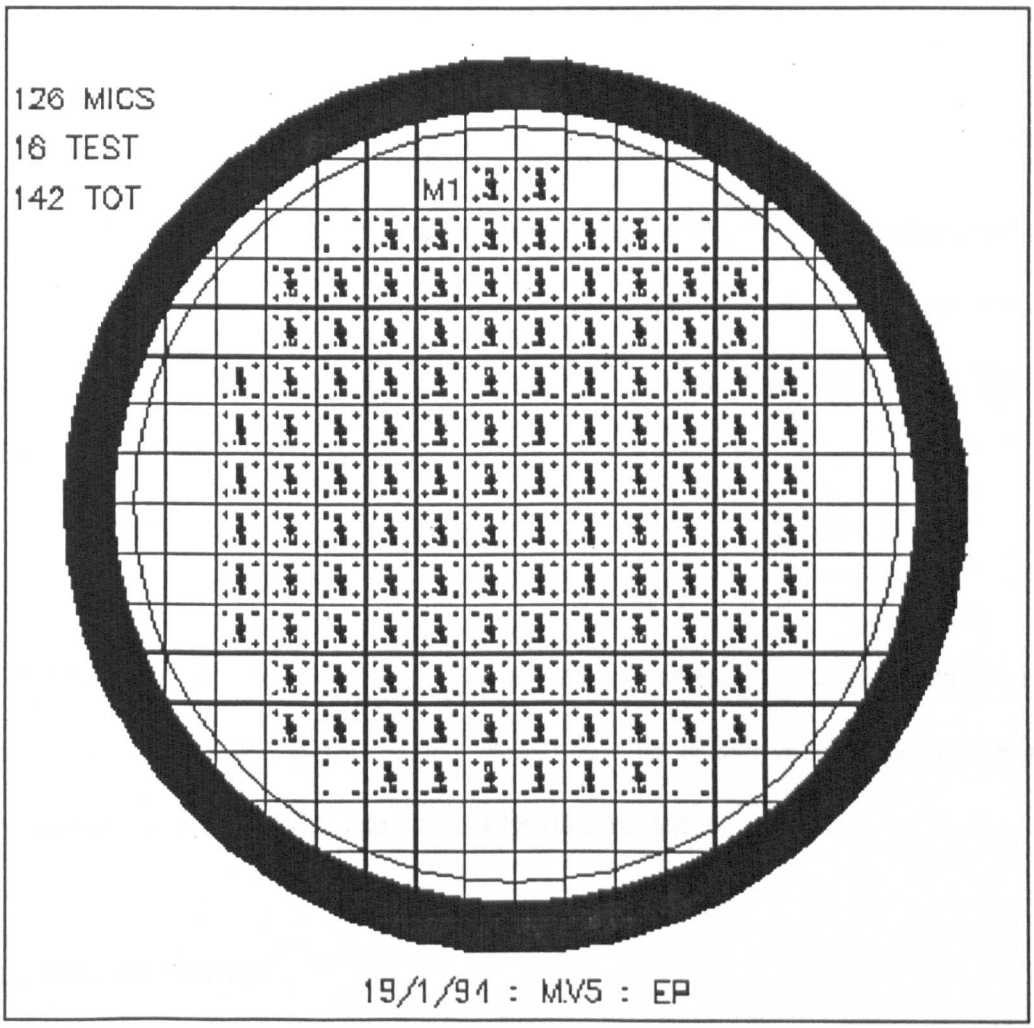

Figure A2.2 : Full metallisation mask (M4) for use in the fabrication of 126 metal patterns on a 3 " glass wafer. (The mask is on a 4" square glass wafer)

Anisotropic etching of silicon diaphragms

Thermal silicon dioxide grown by wet oxidation can be used as a mask for use in anisotropic etching of silicon diaphragms. The width of the diaphragm W_o and the width of the initial masking aperture W_{si} for a square diaphragm can be calculated from the following formula

$$W_o = W_{si} - \sqrt{(2t_{si})} \qquad \textbf{(A2.1)}$$

where t_{si} is the thickness of silicon to be etched fig. A2.3. Since the (111) plane etches upto 40 times slower than the (100) plane, W_{si} must be larger than W_o to obtain the desired diaphragm diameter. The approximate etch ratios for the different silicon planes are summarised as follows

(100)	:	(110)	:	(111)
40	:	30	:	1

To obtain $1mm^2$ x $1\mu m$ diaphragms, a $380\mu m$ thick wafer must be masked on the reverse side with $1.9mm^2$ windows. Before such a design can be implemented, the etch properties of silicon and the silicon dioxide mask must be determined.

Etch rate characterisation

Etch rate experiments were carried out to determine etch rates of lightly doped n-type silicon at different temperatures using 10 litres of KOH solution and 2.5 litres of IPA with thermostatically controlled temperature and continuous agitation. A chiller unit was employed to cool the lid of the etch bath to recondense IPA and prevent loss to the atmosphere. Two whole wafers were used as samples to obtain average values and the etch rate was determined by the following three techniques:

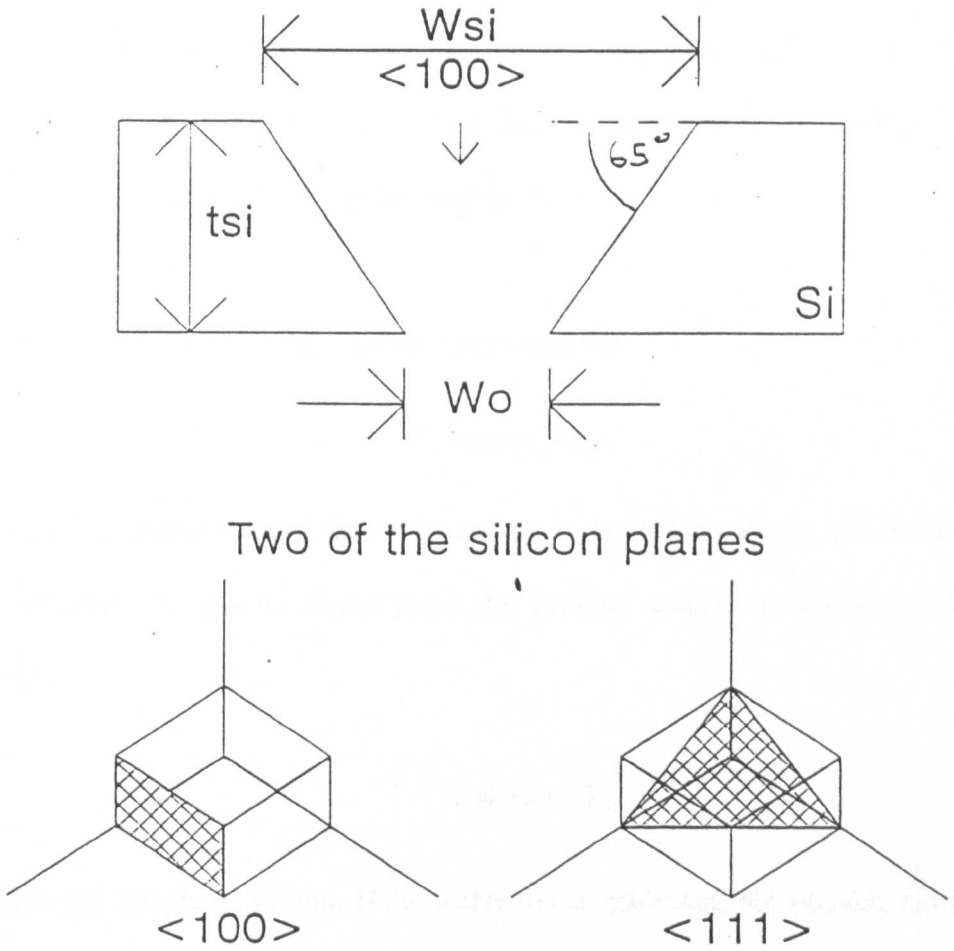

Figure A2.3 : Two crystal planes commonly exploited for timed anisotropic etching of silicon diaphragms.

i) Calculation of etch rate from mass loss measurements

This technique required the measurement of the mass of the wafer before and after etching. For these measurements, it was very important to ensure the wafers were free from any moisture, since mass errors yield inaccurate etch rate calculations. The electronic balance/scales used for measurement had a specified accuracy of +/- 0.01 g. The derivation for etch rate calculation will now be described.

The mass etched from a wafer can be determined by

$$\Delta m = m_o - m_e \qquad \textbf{(A2.2)}$$

where m_o is the initial mass of the wafer and m_e is the new mass. As the wafer is etched, the etched volume ΔV can be found from the average change in mass Δm which can be measured.

$$\Delta m = \rho * \Delta V \qquad \textbf{(A2.3)}$$

where ρ is the density of silicon. If the wafer flat is neglected, the volume etched for a wafer is

$$\Delta V = \pi r^2 h \qquad \textbf{(A2.4)}$$

where h is the thickness of silicon etched away. Substituting in eqn. 4.35 and re-arranging yields

$$h = \frac{\Delta m}{\rho \pi r^2} \qquad \textbf{(A2.5)}$$

Since 3" wafers were used and the density of silicon is 2.33g/cm^3, the etch rate R (μm/Hr) for a single side of the wafer is given by

$$R=47.04\frac{\Delta m}{t} \qquad \text{(A2.6)}$$

where t is the etch time in hours. This calculation is quite accurate while the geometry of the wafer remains circular, but gives increasingly artificial high etch rates as the wafer is etched, due to the altered geometry and etching of the edges of the wafer. From experiments, using 380 μm thick 3" wafers, it was found that for the first 50 μm of the wafer etched, the accuracy of eqn. A2.6 was better than 2% of the actual etch rate, but this increased to 10% when 300 μm was etched. The actual etch rate in this case was determined from talysurf experimental measurements and is discussed in (ii).

ii) Calculation of etch rate from Talysurf step height measurements

The talysurf is a commercial piece of apparatus for measuring step heights and surface roughness, of different materials, using a mobile precision stylus. For this work, the silicon wafer to be measured was secured in such a way that the stylus could be dragged over the edge of the wafer while recording a surface profile on a chart recorder. The etch rate is given by

$$R=\frac{w_t-h}{t} \qquad \text{(A2.7)}$$

where h is the measured thickness (or step height) of the wafer after etching, t is the etch time and w_t is the wafer thickness before etching. w_t and h can be determined from their respective talysurf recorded step height profiles. The probe scratches the wafer which may introduce some error, but the machine used had a specified accuracy of +/-1 μm, which could be maintained by careful calibration prior to measurement. (Note : For calibration, a manufacturer's sample with a series of accurately known 100μm, 50 μm and 10μm steps was used.)

iii) Calculation of etch rate from co-ordinate measuring machine (CMM) step height measurements.

The CMM consisted of a computer controlled robotic sensor tip that could be used to obtain automatic step height measurements from measured co-ordinate calculations. These measurements were obtained from a sample wafer that was firmly clamped to a smooth base table. Eqn. A2.7 can be used to determine the etch rate, where w_t is measured before etching and h is determined after etching. The specified accuracy of the CMM was +/- 3 μm and the machine carried out an auto calibration procedure before user measurement. It was found that measurement of silicon wafers less than 50 μm thick resulted in up to a 15% error in etch rate calculations compared to talysurf measurements. The reason for this was that the thin silicon wafers were very flexible and difficult to clamp rigidly to the measurement table of the CMM for determination of correct step height.

All three of the above techniques were used to obtain average values for etch rates. A 17% and a 40% KOH solution were investigated for determination of etch rates at different temperatures for n-type (100) silicon and silicon dioxide grown by wet oxidation at 1000°C using the apparatus and techniques outlined above. Average experimental etch rates compared with calculated values using the expressions in section 4.2 for the 40% KOH + IPA solution at different temperatures are shown in fig. A2.4(a). Close agreement with the model can be seen where any discrepancies could be attributable to the loss of IPA during the etching process. Similar agreement was found for the 17% KOH solution shown in fig. A2.4(b). Both graphs are shown for comparison in fig. A2.5 (Without IPA) where it can clearly be seen that the 17% solution has a higher etch rate for different temperatures. Both solutions show an exponential increase in the etch rate with temperature.

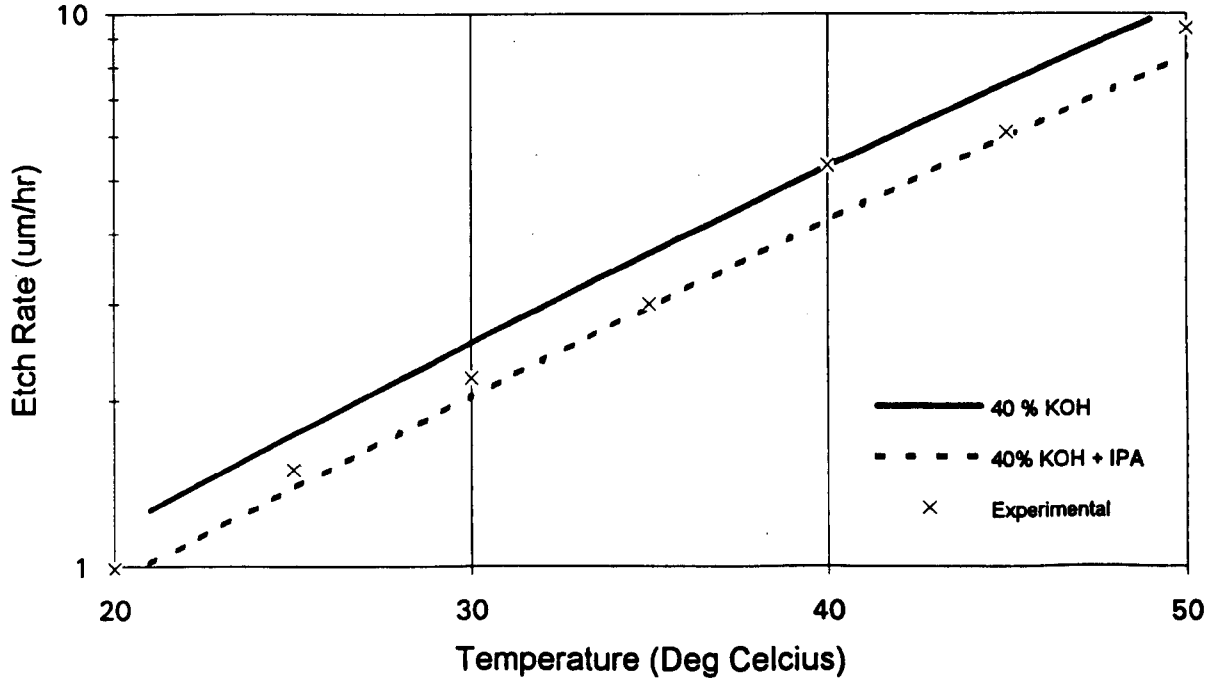

Figure A2.4(a) : Comparison of average experimental silicon (100) etch rates with calculated ones for a 40 % KOH + IPA solution as a function of temperature. (40 % KOH solution shown for reference, calculated values derived from eqn. 4.28)

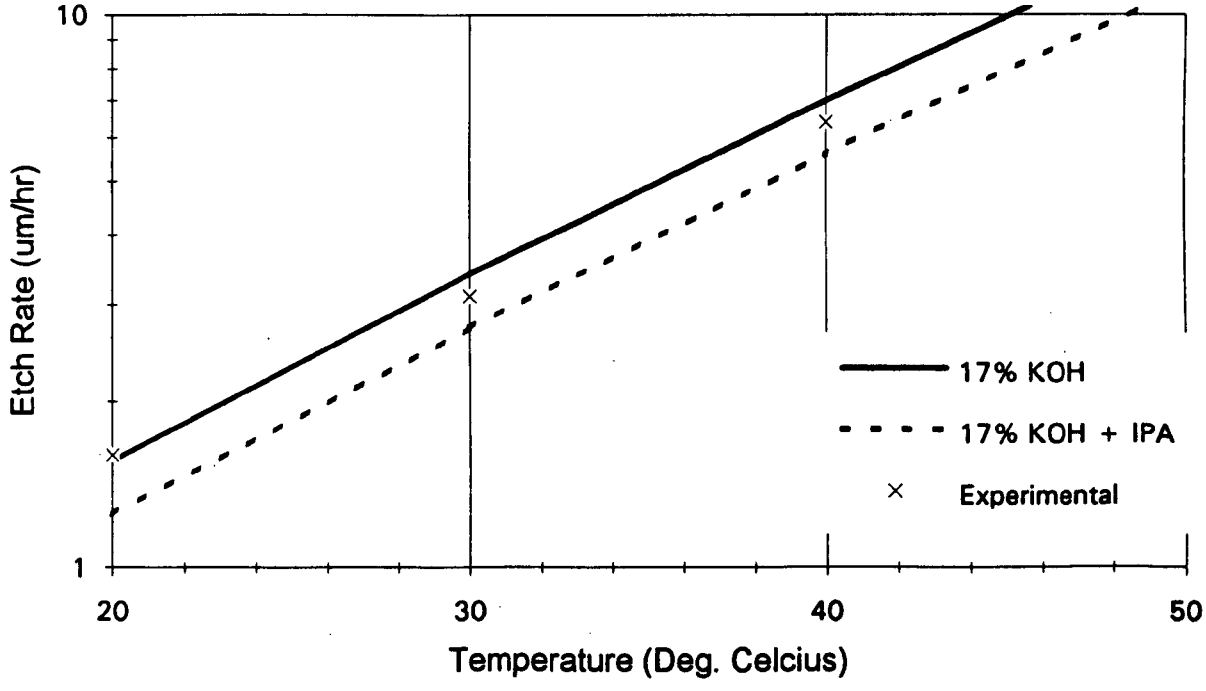

Figure A2.4(b) : Comparison of average experimental silicon (100) etch rates with calculated ones for a 17 % KOH + IPA solution as a function of temperature. (Calculated values derived from eqn. 4.28)

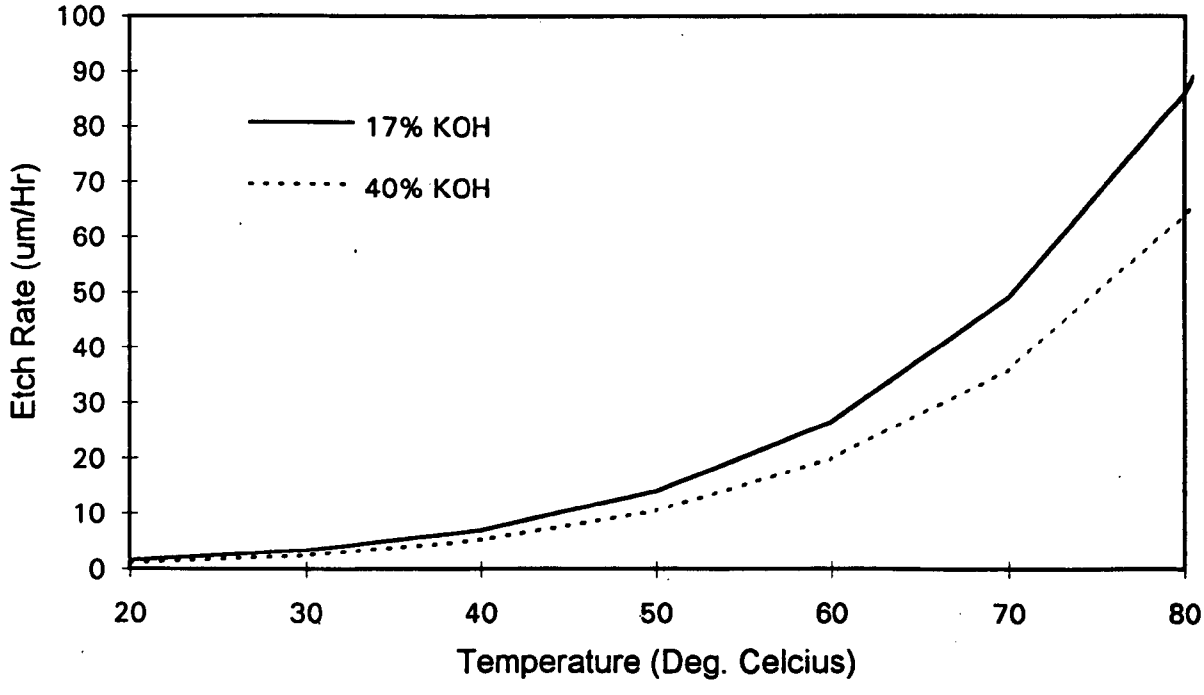

Figure A2.5 : Comparison of calculated silicon (100) etch rates for 17 % KOH and 40% KOH solutions as a function of temperature. (Calculations derived from eqn. 4.28)

The etch rate of a wet oxide grown at 1000°C on a (100) n-type wafer was also determined for different temperatures. Half of the oxide on the wafer was removed by suitable masking and etching to give a measurable step for profile measurements. Fig. A2.6 shows the results of etch rate with temperature for the two concentrations and shows that the more concentrated solution etches SiO_2 at a higher rate than the lower concentration for a given temperature and the etch rate increases exponentially for both solutions. The etch ratio of silicon to silicon dioxide can be calculated from figs. A2.5 and A2.6 and has been plotted for the 17% KOH concentration in fig. A2.7. This figure shows that at low temperatures the etch ratio is high and decreases exponentially with increasing temperature, the lower concentration having the highest etch ratios. It can also be shown by calculation, that as the concentration increases, the etch ratio decreases for a given temperature. Since the highest ratios are for lower temperatures, fig A2.8 shows etch ratio against concentration for 20 °C.

If a 4 hr wet oxide, which is approximately 1μm thick, grown at 1000°C is used as a mask then a minimum etch ratio of 380 would be required for a 380μm thick (100) n-type silicon wafer. To minimise etching time, it would be preferable to choose a high temperature for etching, in order to achieve the best etch rate for a given concentration. However, experimental work showed that the higher the temperature and concentration, the poorer the surface finish of the silicon surface. Best results were obtained for high etch ratios at low concentration and temperature but etch times were unacceptable. For example, a 17% solution at 20°C has an etch ratio of 2500 with a 1.56μm silicon etch rate. This would take 244 Hrs (Over 10 Days) to etch 380 μm of silicon while etching only 0.15μm of a 1μm wet oxide mask. Additionally, fabrication of a thin diaphragm, of 1μm thickness for a microphone, by a timed etch would be extremely difficult. Diaphragms of 50 μm thickness

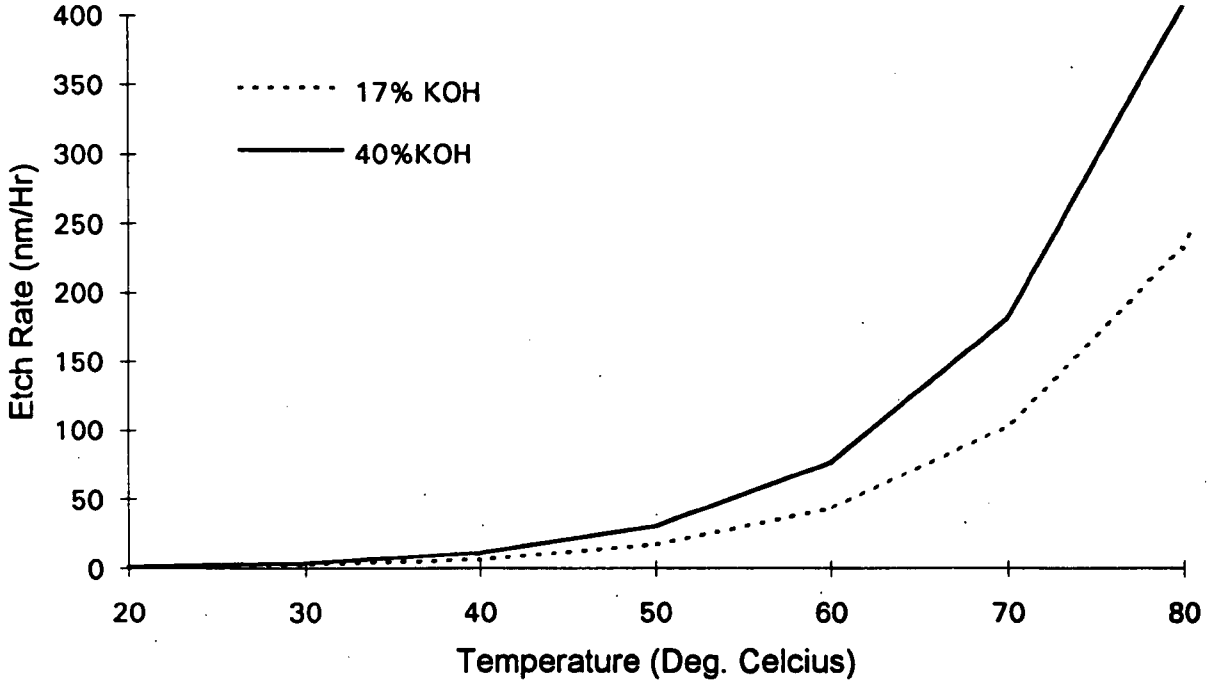

Figure A2.6 : Comparison of silicon dioxide etch rates for 17 % KOH and 40% KOH solutions as a function of temperature. (Calculations derived from eqn. 4.28)

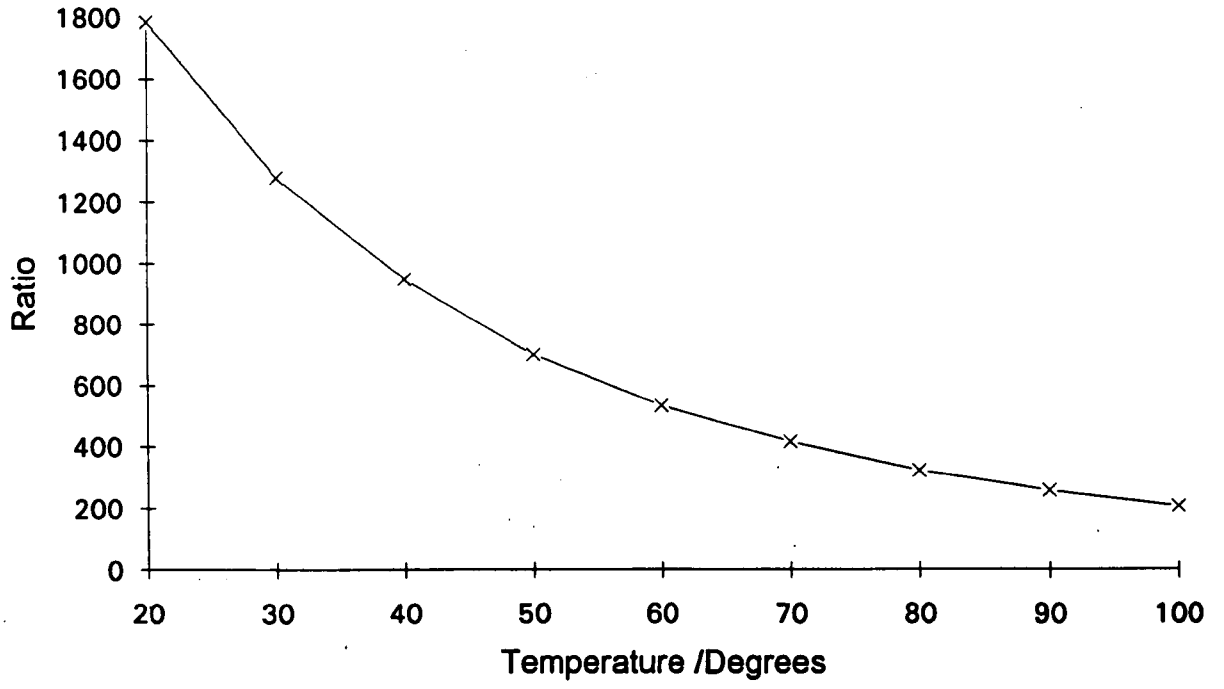

Figure A2.7 : Etch ratio for (100) silicon and silicon dioxide in a 17 % KOH solution as a function of temperature. (Graph derived from A2.5 and A2.6 for 17% KOH solutions)

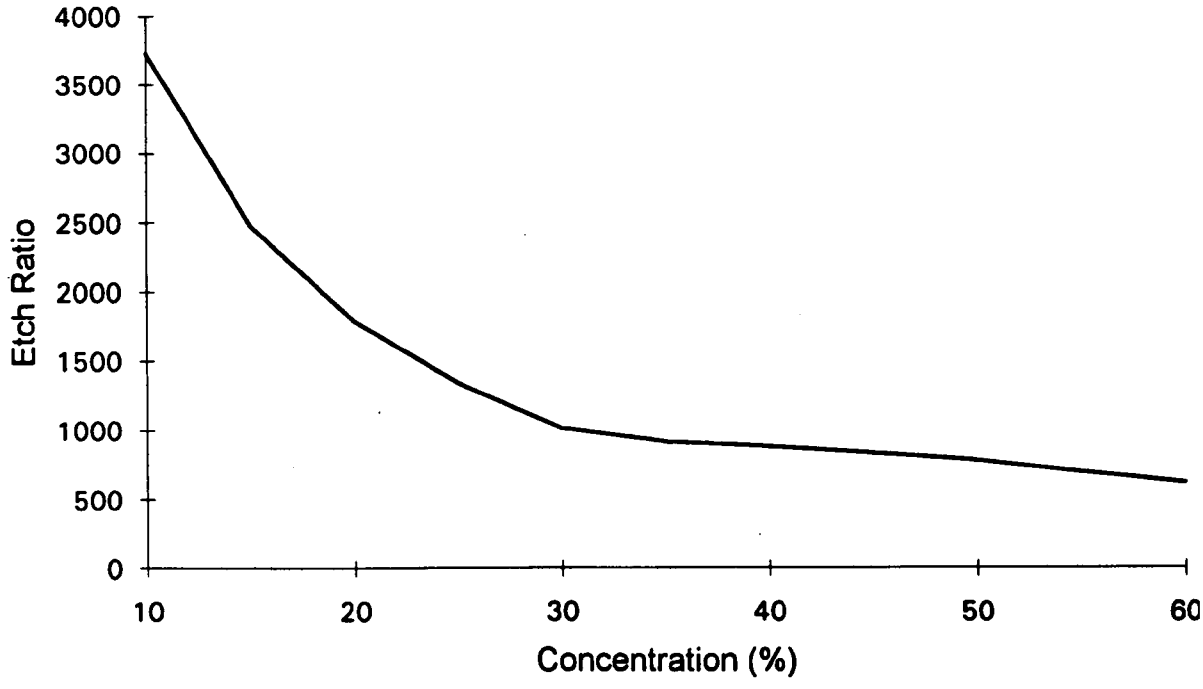

Figure A2.8 : Calculated etch ratio for (100) silicon and silicon dioxide as a function of % KOH concentration for a temperature of 20 °C .

are routinely fabricated for pressure sensors [108] by timed etching, but such diaphragms would require an unacceptably large area for a miniature microphone.

To achieve thin diaphragms, the etch stop technique that has been discussed in section 4.6 can be employed. Fig. A2.9 shows the basic steps of fabrication for a p^+ etch stop diaphragm by anisotropic etching. In section 4.6 it has been indicated that the best etch stop behaviour can be obtained for low concentration solutions at low temperature fig. 4.14.

A2.2 Process modelling

In order to minimise expense and time of unnecessary fabrication, programs were written using the theory developed in chapter 4.0 to investigate and predict the results of different processes. This was implemented by computer numerical evaluations of the models discussed. Examples of this are shown in figs. 4.4-4.6, figs. 4.14-4.18 and figs. A2.4-A2.8 where oxide thicknesses, back chamber depths, etch rates and etch selectivities have been calculated and plotted using computer programs written in Pascal. It was further required to try and predict diffusion profiles, resulting sheet resistances and etch stop depths for given diffusion parameters of time and temperature using the theory from sections 4.4 and 4.6. Initially the Gaussian and complementary profiles were evaluated so that pre-deposition and diffusion profiles could be displayed, Figure A2.10 shows the computed profile for a 16 hr. rim pre-deposition and a 1 hr. diaphragm pre-deposition at 1050 °C. For a critical boron concentration of $3x10^{19}$ atoms/cm^3, which is realistic for a low temperature/concentration KOH + IPA etch, the resultant diaphragm thickness will be 0.4μm thick and the rim will be just over 1.5 μm. The extra 15 hrs. for the rim diffusion does not appear to give a significant increase in etch stop depth. However, subsequent thermal steps to the rim

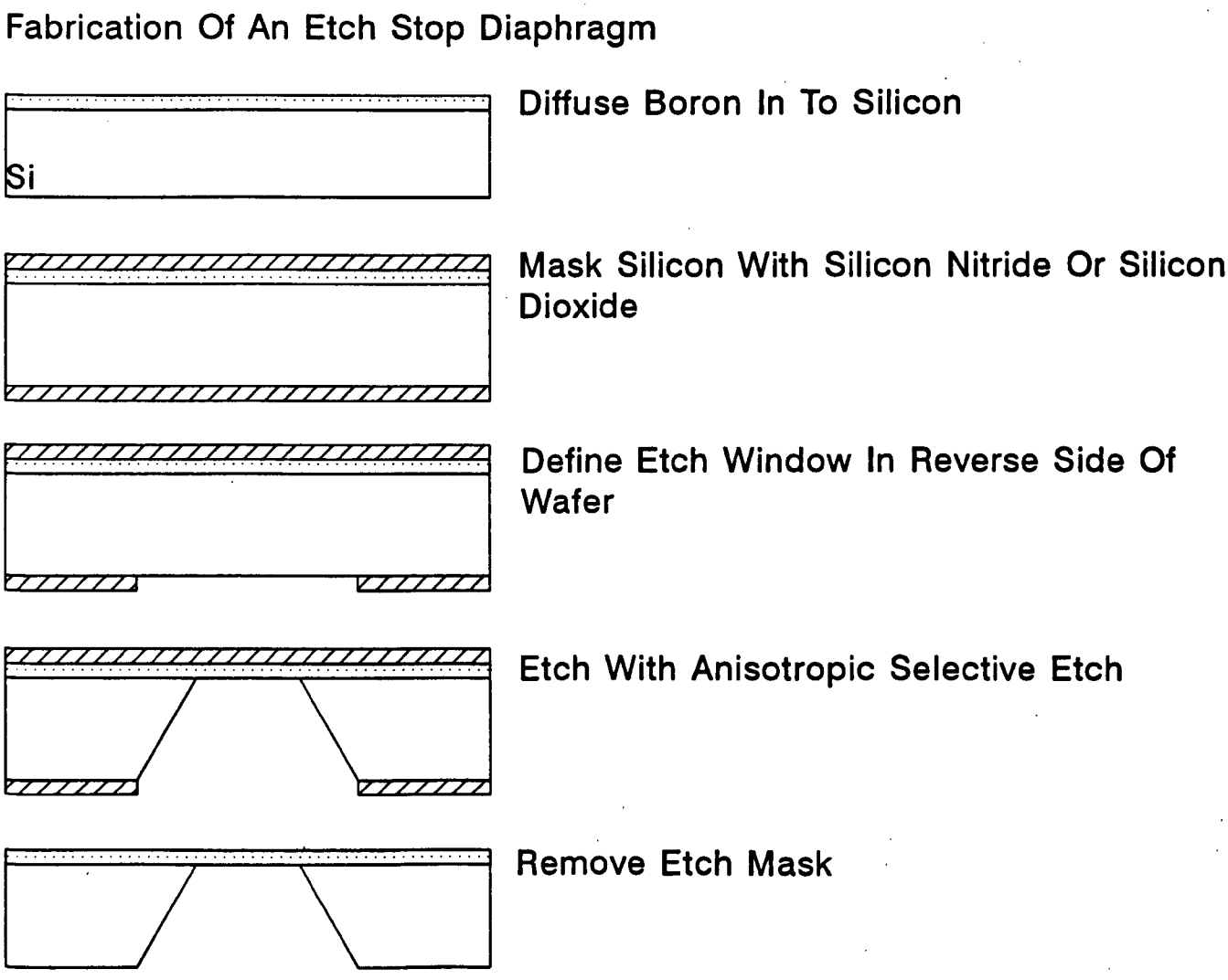

Figure A2.9 : Main steps for fabrication of an etch stop diaphragm by anisotropic etching of (100) silicon.

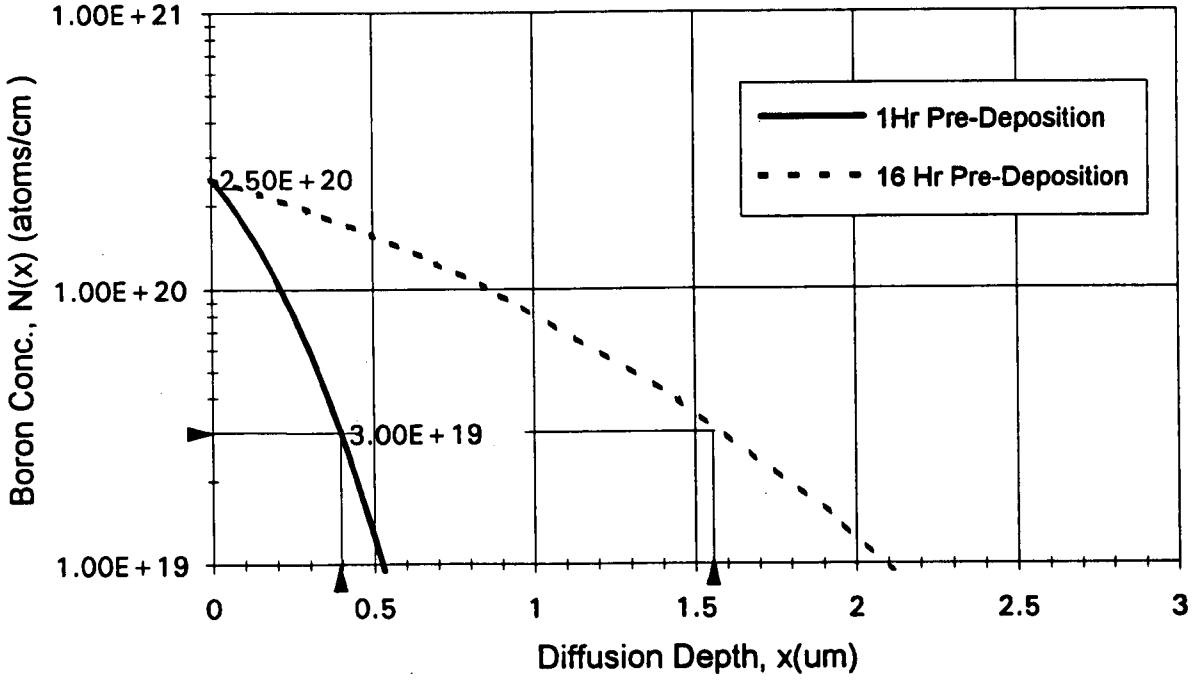

Figure A2.10 : Two calculated constant source diffusion profiles for a pre-deposition temperature of 1050 °C. (Calculations based on the models of section 4.4)

diffusion will serve to drive the boron deeper into the silicon, lowering the surface concentration, but increasing the etch stop depth. A limit is reached when the surface concentration approaches the critical boron concentration and the profile starts to loose its etch stop properties. Fig. A2.11 shows a 2 hr. diaphragm pre-deposition at 1050 °C, which gives an etch stop depth of nearly 0.6 μm. A subsequent 8 hr. drive in at 1050 °C can increase the diaphragm etch stop depth to 1 μm thus achieving a design target for the microphone structure. Fig. A2.12 shows calculations for the diffusion profile junction depth and the etch stop junction depth over a 20 hr. 1050 °C pre-deposition period. It shows that even for a 20 hr. pre-deposition, the junction depth will only just exceed 2 μm, clearly indicating the need for a drive-in process to obtain greater depths, the corresponding sheet resistance curve is shown in fig. A2.13 for these pre-deposition times. This curve is very useful for comparing the calculated sheet resistance for a given diffusion profile against that measured from a test wafer. For example, the sheet resistance for a 1 hr. pre-deposition is just over 10 Ω/□ and for 16 hrs. is 3 Ω/□, the latter indicating much lower resistivity and hence higher conductivity of the diffused profile.

It should be re-iterated that these computer simulations only used the simple models discussed and did not take into account segregation effects, concentration dependent diffusion etc. For more advanced computer modelling that incorporates models for these effects, the process modelling package SUPREM III[109] can be used.

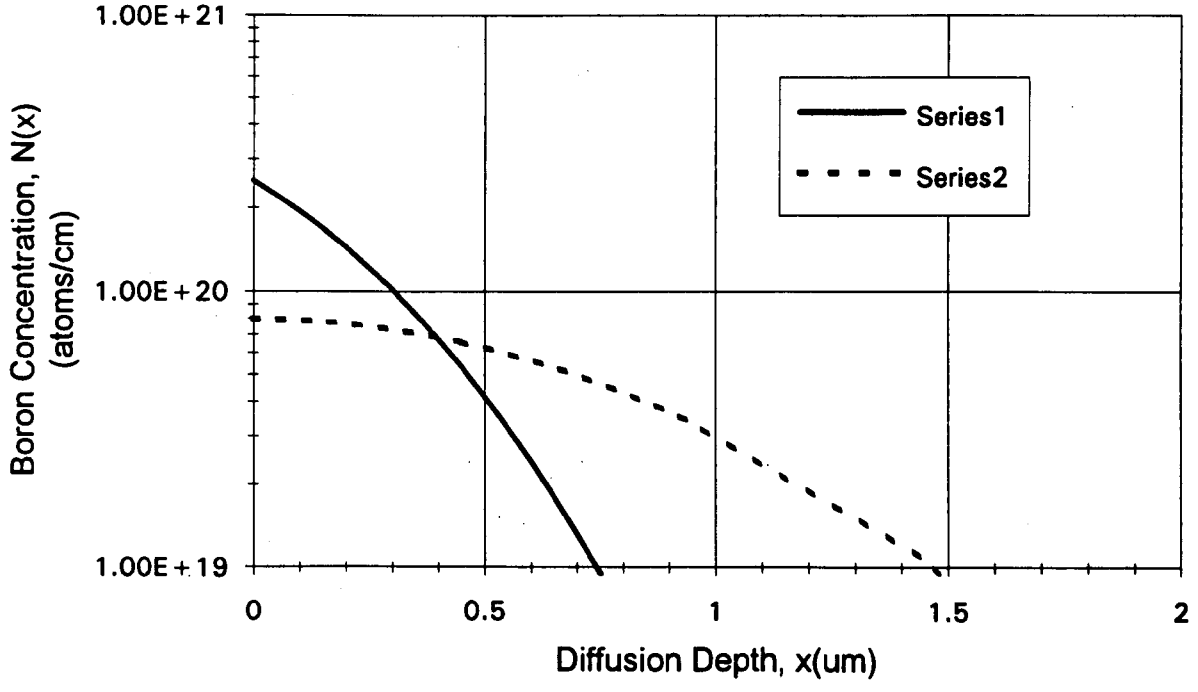

Figure A2.11 : A 2 hour constant source diffusion profile followed by an 8 hour drive in for a temperature of 1050 °C. (Calculations based on the models of section 4.4)
Series 1 : 2 Hr. Constant source diffusion.
Series 2 : 8 Hr. Drive in.

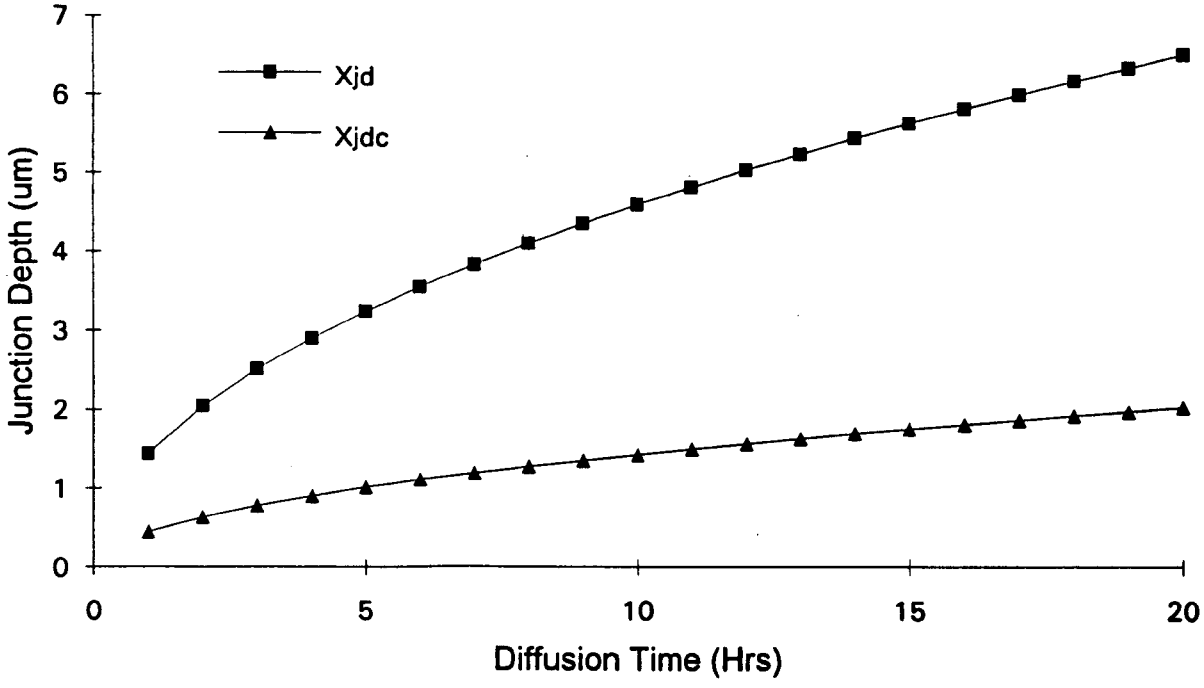

Figure A2.12 : Calculated diffusion profile and etch stop junction depths as a function of diffusion time for a pre-deposition temperature of 1050 °C. (Calculations based on the models of section 4.4)

Xjd :Diffusion profile junction depth.

Xjdc :Etch stop junction depth.

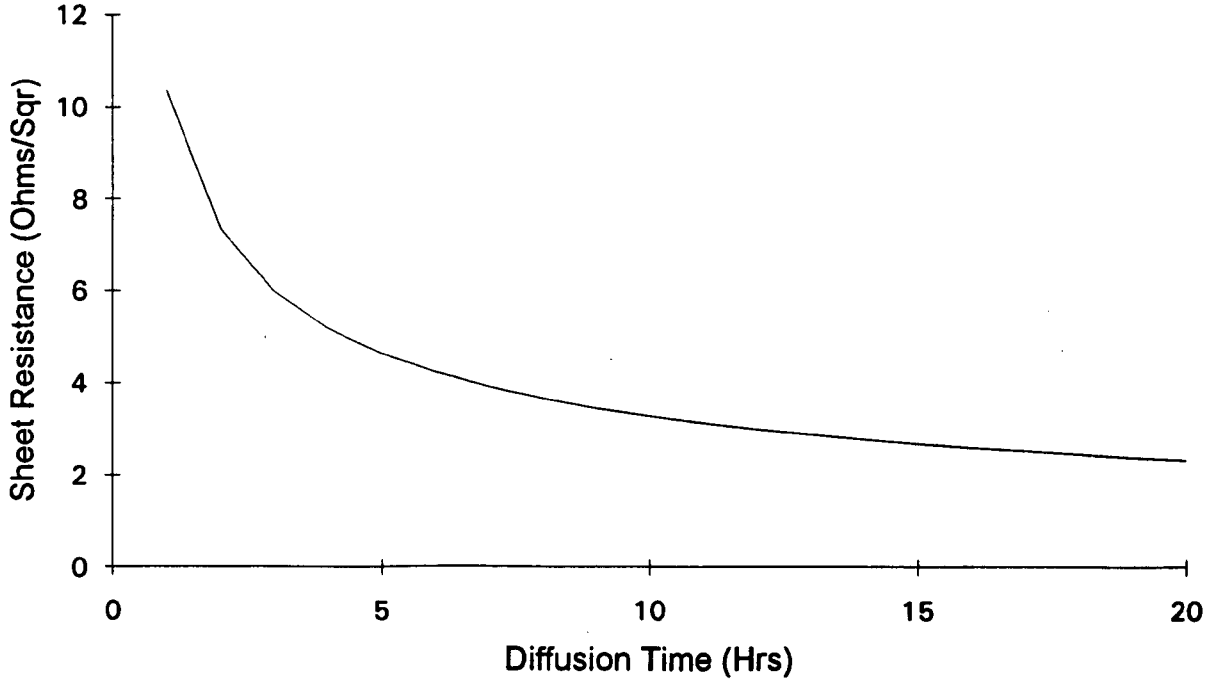

Figure A2.13 : Calculated sheet resistance values for the diffusion profile junction depth pre-deposition curve (Xjd) shown in fig. A2.12. (Note : This curve is useful for estimating junction depths from four point probe measurements of a diffused test wafer surface)

Appendix 3

A3.1 Finalised Processing Schedule for Silicon Microphones with a Circular Diaphragm.

Procedures indicated in italics are detailed after this schedule.

Wafer Processing

Stage 1 - Backchamber Formation

Use four 3" <100> virgin n-type wafers with a resistivity of between 1 and 3 Ohm-cm. Two of the wafers should be reserved for test purposes. Record the initial average sheet resistance of each test wafer T1 and T2 respectively. The other two wafers for device fabrication can be called D1 and D2. The wafers can be marked with these legends near the flat using a diamond scribe.

1. 1 min *contact etch* of all wafers.

2. *Dry all wafers* prior to an 8 Hr *wet oxidation* of all the wafers at 1100 °C with an oxygen flow rate of 3 l/min.

3. Pattern circular back chambers on two of the wafers using the ***negative lithography photoresist process***. Carry out a ***HF etch*** of wafers D1, D2 and T1, using the test wafer to determine when the silicon dioxide has been removed.

4. *Plasma etch* D1 and D2 to remove all photoresist.

5. Repeat step 2

6. Remove all the silicon dioxide on all wafers with a *HF etch* using the test wafer T1 as a guide. This should take a maximum of 20 mins. Examine the two patterned wafers for backchamber quality and characterise as appropriate. Record the average sheet resistance of T1 and T2. T2 represents continuous 16 h oxidation and T1 represents two separate 8 h oxidations.

Stage 2 - Rim Diffusion

1. *Dry all wafers* prior to a 4 Hr *wet oxidation* at 1000°C with an oxygen flow rate of 3l/min.

2. Pattern rims over backchambers on wafers D1 and D2 with the ***negative resist lithography process*** making sure the rear of the wafer is protected with photo resist. Then *HF etch* all the wafers except T1, using the test wafer T2 to determine when the silicon dioxide has been removed.

3. *Plasma etch* D1 and D2 to remove all the photoresist.

4. 1 min *contact etch* and *dry all wafers* prior to a 16 Hr ***pre-deposition*** at 1050 °C with a nitrogen flow rate of 3l/min and an oxygen flow rate of 7 ml/min. Immediately

followed by 15 min *dry oxidation*, in the same furnace, at 1050 °C with an oxygen flow rate of 3 l/min. The furnace should then be ramped down at 10 °C/min to 900 °C over 15 mins with 3l/min of nitrogen for subsequent removal. The sheet resistance of T2 should be measured prior to pre-deposition and T1 should not be placed near a source.

5. 45 Min *HF etch* to remove all masking oxide and borosilicate glass. If brown glassy appearance on test wafer, may require further etching. Record sheet resistance of T1 and T2. T1 should be n-type and T2 should be heavily p type.

Stage 3 - Diaphragm Diffusion

1. *Dry all wafers* prior to a 2 Hr *wet oxidation* at 1000°C with an oxygen flow rate of 3l/min.

2. Pattern diaphragms on wafers D1 and D2 with the *negative resist lithography* process making sure the rear of the wafers is protected with photoresist. Then *HF etch* all the wafers except T2, using the test wafer T1 to determine when the silicon dioxide has been removed.

3. *Plasma etch* D1 and D2 to remove all the photoresist.

4. 1 min *contact etch* and *dry all wafers* prior to a 1 Hr *pre-deposition* at 1050 °C with a nitrogen flow rate of 3l/min and an oxygen flow rate of 7 ml/min. Immediately

followed by 15 min *dry oxidation*, in the same furnace, at 1050 °C with an oxygen flow rate of 3 l/min. The furnace should then be ramped down at 10 °C/min to 900 °C over 15 mins with 3l/min of nitrogen for subsequent removal. The sheet resistance of T2 should be measured prior to pre-deposition and T1 should not be placed near a source.

5. 25 Min *HF etch* to remove all masking oxide and borosilicate glass. If brown glassy appearance on test wafer, may require further etching. Record sheet resistance of T1 and T2. T1 should be p type, with a sheet resistivity of 6-8 ohms/square and T2 should be more p type with a sheet resistivity range 0.5-1 ohms/square.

Stage 4 - Rim Protrusion

1. Etch each wafer separately in a solution, maintained at 20 °C, consisting of 1l of 17 % KOH and 250 ml of IPA in order to remove a thin layer of n-type silicon. The solution must be in a pyrex beaker and the wafer for etching must be immersed such that the polished side is parallel to the surface of the solution. 15 secs stirring with a glass rod should be carried out every 5 mins and the beaker must remain covered when stirring is complete.

2. Wash all wafers with running millipore water for 30 mins to remove all traces of etchant and IPA and allow to dry naturally under laminar flow conditions. Measure sheet resistance of test wafers T1 and T2 to monitor effect of etch on sheet resistance. Examine devices for signs of process problems.

Glass Processing

Stage 5 - Metallisation using a positive lift off process

1. Clean a glass wafer in 20 % Decon using an ultrasonic bath for 30 mins. Wash for 15 mins in running millipore water to remove all traces of detergent and then allow to dry naturally. *Plasma etch* for 30 mins to complete clean.

2. The following process is used to pattern the glass wafer with the electrode mask.

   i) Pre bake the wafer at 250 °C on a hot plate for 15 mins and allow 15 mins to cool.

   ii) Spin 1 ml of adhesion promoter at 4000 r.p.m. for 1 min followed by two coats of positive resist, using the same process, at 3000 rpm on the glass wafer to obtain a positive photo resist layer of 1-2 μm.

   iii) Soft bake wafer at 90 °C on a hot plate for 2 mins to remove excess solvent.

   iv) Pattern photoresist on wafer, with a negative glass mask of electrode pattern, using a UV exposure time of 30 secs.

   v) Develop patterned wafer for 15 mins and ensure all the unwanted photo resist is removed. Wash in millipore water for 15 mins and examine quality of masking under microscope.

3. *HF Etch* glass wafer for 10 mins to etch glass for metallisation adhesion promotion. Wash in millipore water and dry naturally.

4. Soft bake wafer on a hot plate at 90 °C for 1 min immediately prior to metallisation. RF Sputter 30 nm of titanium, in an argon atmosphere at a pressure of about 13.3 Pa, and ensure that the sputter rate is about 0.05 nm/sec which should take about 10 mins. To prevent oxidation of the titanium layer, immediately thermally evaporate 70 nm of gold at a pressure of 1.3×10^{-5} Pa, in the same plant, at a rate of 0.1 nm/sec. This will take about 12 mins. Allow the system 1 Hr to cool down before venting the chamber to air. Check that the metallised side of the wafer is gold coloured and that when viewed through the glass side the metal is silvery, indicating sufficient titanium coating. During the metallisation, the photo resist should not be allowed to exceed 150 °C in order to prevent it from hard baking and rendering the sample unusable. (The sample must not be brought up to air between metallisation depositions)

5. Place the metallised wafer, face up, at the bottom of a pyrex beaker containing 1 l of acetone. Stir the acetone while subjecting the acetone to 10 sec bursts of ultrasonic energy every minute. A 5 min period of this process should yield complete lift off of all unwanted metal and photoresist, leaving a glass wafer patterned with the microphone metallisation pattern. The wafer is then washed for 30 mins in millipore water to ensure removal of all traces of acetone and then dried naturally under laminar flow conditions.

Stage 6 - Preparation for etching

1. Ensure that glass and silicon wafer for bonding are clean, dry and completely free of particulate matter. This is achieved by drying on a hot plate at 150 °C for 15 mins, cooling for 5 mins and then blowing with nitrogen gas.

2. Align the glass wafer metallisation with the polished side of a wafer containing devices, such that the metal is flat against the silicon. Clamp the two wafers in position and heat upto 300 °C and then electrostatically bond the glass to the silicon with a voltage of 800 V. (See section 6.3) Remove the bonded wafers and allow to cool for 15 mins.

3. Etch the composite wafer in 500 ml of 5:2:2 silicon etch for 4 Hrs. The average etch rate should be 1.3 μm/hr. at room temperature which will remove over 300 μm of the 380 μm thick silicon wafer. Wash for 30 mins in millipore water and dry. (Note the glass will etch by 250 μm)

4. Diamond scribe the wafer on the silicon side in accordance with the scribe line indications on the wafer. Break the wafer along the scribing lines into individual devices of about a 5 mm^2 die ready for silicon dissolution.

Silicon Dissolution

Stage 7 - Realisation of single microphone structures.

1. Etch each individual die in a 1l solution of 17% KOH and 250ml of IPA at 40 °C+/-0.5°C for 11 hrs to remove about 60 μm of silicon at a rate of 5.5 μm/hr.

2. Transfer the die to another 1l solution of 17% KOH and 250ml of IPA maintained at 20°C+/-0.5°C. Etch for at least 15 hours, at a rate of about 1.3 μm/hr, to remove the remaining silicon and visually observe the appearance of devices. When all the n-type silicon has been removed, the p+ etch stop microphone is complete and should be carefully removed to a slow flow millipore water system. This complete step can take between 15 and 30 Hrs depending on accuracy of previous etching stages.

3. Wash the microphone in millipore water for 1 hr. and transfer to a petri-dish containing 100 ml of electronic grade IPA. Store structure(s) at 0°C with a lid on the petri-dish for at least 8 hours before further processing.

4. Examine the microphone, while in the IPA solution, for defects in the structure such as fracture, mask faults, unwanted silicon, etch finish defects etc, metallisation damage etc. and keep if it appears to be testable.

Removal of water from back chambers

Stage 7 - Preparation for test

1. Carefully transfer the microphone directly from the IPA into 100ml of fresh uncontaminated cleanroom grade chloroform and leave for 4 hrs.

2. Remove microphone from chloroform and place microphone with the substrate on a liniment free cloth for 30 mins for all the chloroform to evaporate.

3. Put microphone in oven with mounting header for 15 mins at a temperature of 80 °C. Remove and allow to cool for 15 mins.

4. Araldite the microphone onto the header using the minimum of glue.

5. Place header in aluminium block and heat up to 150 °C on a gold ball bonding machine. Gold ball bond 25 μm wire from the microphone pads to the header pads to establish connections to microphone. Remove the aluminium block and allow the header to cool naturally over 30 mins.

6. Test the microphone structure

The following notes detail the processes indicated in bold for the above schedule.

Etching and Lithography

The contact etch and HF etch involve the use of hydrofluoric acid which is extremely dangerous and should be handled with care using the proper facilities and user protection. PTFE or polythene holders must be used for the etch and wafer handling.

All work must be carried out in laminar flow conditions with fume extraction for etchant vapours. A wet chemical etch station was used.

Contact Etch

The contact etch bath is a 10:1 mixture of 48 % HF and de-ionized reverse osmosis water and should be operated at room temperature. It has an etch rate of about 300 angstroms/min of dry thermal silicon dioxide. The procedure for use is

1. Immerse the wafers into the etch for 1 min.

2. Remove and wash in a cascade millipore water system for 15 mins.

3. Allow to drain for 15 mins.

4. Allow wafers to dry naturally of use a dry nitrogen supply to blow dry.

Silicon Dioxide Etch (or HF ETCH)

The HF etch consists of a suitable mixture of 40% ammonium fluoride and 48% hydrofluoric acid (10:1) and de-ionized reverse osmosis water and should be operated at room temperature. The etch rate is about 100nm/min for an undoped thermal oxide. A test wafer can be used to determine when etching is complete since the etch is hydrophillic towards silicon dioxide and hydrophobic towards silicon. This is observed by wetting on the silicon dioxide surface and de-wetting on the silicon.

1. Make sure a test wafer is employed with the same oxide growth conditions as the wafers to be etched. The shiny side of the wafer should be placed in the holder such that it is at the front facing the operator for monitoring purposes.

2. Immerse the wafers into the etch for 10 min.

3. Remove the wafers out of the etch a small distance to see if the test wafer has started to de-wet with the etch.

4. When the wafer has fully de-wet, remove the wafers and wash in a cascade millipore water system for 20 mins.

5. Allow to drain for 15 mins.

6. Allow wafers to dry naturally or use a dry nitrogen supply to blow dry.

Dry All Wafers

Before many 'dry' processes can be carried out it is important that the wafers are free from any moisture.

1. Pre-bake all the wafers at 250 °C for 15 mins in an oven or on a hot plate.

2. Allow wafers 15 mins to cool in wafer holder in laminar flow conditions.

Negative Lithography Photo Resist Process

This is a very important process used to transfer a pattern from a mask to a wafer using ultraviolet sensitive photoresists. All work must be carried out in safelight and laminar flow conditions with fume extraction for solvent vapours. Appropriate safety precautions must be taken when working with lithography chemicals. The following technique is only suitable for patterning oxidised wafers.

1) Pre - bake wafers at 250 °C for 15 mins and allow to cool for 15 mins.

2) Apply 1ml of negative photo resist to the centre of a wafer and spin at 4000 r.p.m. for 1 min to give about 0.8 μm thick layer of resist.

3) If the resist coating is not uniform the wafer cannot be used and should be put in photo resist thinner immediately.

4) Soft-bake the wafer at 90 °C for 1 min.

5) The spinner should be cleaned with thinner for subsequent use.

6) Transfer wafer to mask aligner. Using a positive mask (e.g Microphone backchamber, rims and diaphragm.) with the emulsion side facing towards the shiny side of the wafer, expose with 10 secs of UV.

7) Develop wafers in the following solutions at room temperature for the given times using continuous agitation. 1l of each solution is used in a pyrex beaker.

Chemical	Development Time /s
Developer	30
Developer	30
n-Butyl Acetate (1:1)	15
n-Butyl Acetate	30
n-Butyl Acetate	30

8) Blow dry wafers to remove excess solvent using a dry nitrogen gas supply.

9) Hard bake developed wafers at 250 °C for 15 mins

10) The wafers are now ready for subsequent processing which usually entails a HF etch

to transfer the pattern from the photo resist into the oxide.

If a wafer was unusable stage (3) it should be cleaned in the photoresist solvent for 10 mins, washed for 15 mins and dried ready for reuse in this process. Any resist that cannot be removed should be plasma etched.

Plasma Etch

A barrel etcher is used with an RF generated oxygen plasma to remove positive or negative photo resists.

1) Make sure wafers a completely dry and load in to barrel etcher with shiny side towards the etcher window.

2) Establish the plasma at a pressure between 0.1 and 0.3 torr and leave wafers for 1 hr.

3) Examine wafer through etcher window to see photo resist removal progress. When all colour banding of the etched photoresist (Interference effects caused by different thicknesses of photoresist) has disappeared, the photo resist should all be removed and the process is complete.

The time scale for this process depends on the thickness of the photoresist, the baking parameters and how many wafers are to be etched simultaneously. Ensure wafers do not

overheat during the process since this can bake the photoresist onto wafers harder and increase the process time.

A contact etch usually follows a plasma etch to remove any native oxide formed on the silicon wafers by the process.

Thermal Processes

The following are thermal processes carried out in a 3 zone closed loop controlled quartzware furnace. See fabrication lab notes for more details of quartzware handling and operator procedure.

Wet Oxidation

This process is usually used to grow a general purpose masking oxide that is faster growing and less dense than a dry oxide. It is grown in an ambient atmosphere of steam and oxygen.

1) Ramp the furnace upto 900 °C and set the gas flow rate to 3l/min of nitrogen.

2) Load wafers, in a quartzware sled, at a rate of 10 cm per minute, for 4 mins until the sled sits in the furnace in the correctly profiled zone of the furnace. It is important that the wafers are placed in the sled such that the shiny side faces away from the gas flow, in order to prevent any particulate contamination on the device fabrication surface.

3) Ramp the furnace up to 1000 °C which will take 9 mins at a rate of 10°C/min. For higher oxidation temperatures such as those used for back chamber fabrication the ramp up time will be longer.

4) Begin the oxidation at the stabilised temperature by introducing steam into the furnace using a nitrogen carrier gas with a flow rate of 0.5l/min. An Oxygen flow rate of 3l/min should be set.

5) Carry out the oxidation process for the specified time while ensuring a continuous supply of steam. (The steam must be generated from a temperature regulated pyrex vessel containing millipore water.)

6) At the end of the oxidation period, stop oxygen and steam flow, and introduce dry nitrogen at 3l/min. Ramp the furnace to 900 °C for removal of the wafers at 10 cm/min over 4 mins.

7) Allow 30 mins for the wafers to cool before further processing.

Dry Oxidation

This process is the same as wet oxidation except water vapour with a nitrogen carrier is not used for the oxidation. An oxygen flow rate of 3l/min should be used at the oxidation temperature.

For this work dry oxidation is carried out at the end of pre-deposition processing. (See schedule above)

Pre-Deposition

Boron solid sources are used for a constant source diffusion. Before a pre-deposition process is carried out, the sources have to be aged as follows.

i) Set nitrogen gas flow to 3l/min and ramp up the furnace to 900°C. This will take 1.5 hours at 10°C/min.

ii) Load wafer protected sources in a quartzware sled, at a rate of 10 cm per minute, for 4 mins until the sled sits in the furnace in the correctly profiled zone of the furnace.

iii) Ramp up the furnace to 1050 °C and age the sources for 4 hours.

iv) Ramp the furnace to 900°C and remove the sources at rate of 10 cm/min.

v) Allow 30 mins for boat to cool.

vi) Exchange wafers to be diffused with source protection wafers such that the shiny side faces the source. The sled of sources with wafers is ready for pre-deposition.

vii) Ensure the furnace is at 900°C, the nitrogen flow rate is 3l /min and that oxygen is admitted through a needle valve at 7ml/min. Load the furnace with the sled at 10 cm/min for 4 mins. Ramp the furnace up to 1050°C at 10 °C/min which will take 15 mins.

viii Continue with the diffusion parameters stated in the main processing schedule.

iv) Always remove the sources at 900°C from the furnace with a nitrogen flow rate of 3l/min at a rate of 10 cm/min for 4 mins in order to avoid thermal shock to the wafers and the sources.

A3.2 Fabrication Timescale

Guide to processing times		Days
a)	**Silicon wafer processing (max of 4 wafers)**	
1)	Making backchambers (2 oxidations, 1 lithography step)	4
2)	Rim pattern (1 oxidation, 1 lithography step)	2
3)	Deep diffusion and BSG removal (1 pre-deposition, Long HF etch, short oxidation)	2
4)	Diaphragm pattern (1 oxidation, 1 lithography step)	2
5)	Shallow diffusion (1 pre-deposition, short HF step)	1
b)	**Glass wafer processing (max of 1 wafer)**	
1)	Glass clean and patterning	1
2)	Metallisation and lift off	1
c)	**Final stages**	
1)	Electrostatic bonding (+ Wafer dicing)	1
2)	Silicon dissolution (Depends on technique) (Apparatus for etching simultaneously only 2 x 1cm dies) (Also freeze dry after etch)	5
3)	Packaging	1

From phase (a) and (b) there is potential for over one hundred devices/wafer to be made if stage (c) is successful.

Total time for uninterrupted complete fabrication is a minimum of 20 working days or 4 weeks.

A3.3 Facilities

Film deposition (Not planetary systems, thus film thickness difficult to control)

Electron beam evaporation plant (5kV).
Ar^+ Sputter plant

3" Furnaces

Wet, dry silicon dioxide
Aluminium Anneal
Boron and phosphorus solid source diffusion

Lithography

Oxygen barrel type plasma etcher for photo resist stripping
Yellow room with humidity and temperature control equipped with:-
Kasper single sided mask aligner
Positive and negative photo resist spinners
Beaker development system
Hot plates

Wet Chemical Etching

Wet chemical etch station with cascaded weir system supplied with millipore and R/O water. Laminar flow conditions with humidity and temperature controlled environment. Facilities for handling extremely hazardous chemicals such as HF, HNO_3 and H_2SO_4

Etch station designed for handling 3" wafers safely in order to etch SiO_2 and Si while wearing appropriate safety clothing.

Characterisation

Veeco four point probe
Ellipsometer for oxide thickness measurements
C-V mercury probe for oxide quality measurements

Device Test and Packaging

3" Wafer probe system
Gold ball bonding apparatus purchased for this project.

Appendix 4

A4.1 Computer program implementation of microphone models

```
{PROGRAMMER :EDWARD PALLETT}
{DATE       :15/02/92}
{VERSION    :2.2}
{LANGUAGE   :TURBO PASCAL VER 4.0}

PROGRAM microphone_calcs;
USES crt,graph,menu5,dos;    {UNITS CONTAINING LIBRARY ROUTINES}
CONST v=0.3;  {Poissons ratio for silicon}
      E=1.6e11; {Youngs modulus for si NM-2}

TYPE  mat=array[0..70] of real;
      norm=array[0..70] of integer;
      cv1=array[0..650,0..4] of real;
      cv2=array[0..650,0..4] of integer;
      s=string[7];
VAR   m1:mat;
      c_v:cv1;
      c_v_g:cv2;
      scn_dat:norm;
      mx,my,max:integer;
      data:file of real;
      temp:s;
      data2:file of s;
      filename1,filename2:string[15];
      a,b,q,r,h,d,defl,xf,yf,max_defl,vbias,wo,sigma_d,wmax:real;
      p_max:integer;
      select,param1,param2,param3,param4,param5,nm:integer;

{-------------------------------------------------------------------------}
PROCEDURE header;
{TOP MESSAGE}
BEGIN
  highlight;
  cursor_off;
  nondestruct2;  {TOP WINDOW}
  writeln('Circular Diaphragm Calculations Ver 4.2 c1994');
  gotoxy(15,1);
END;
{-------------------------------------------------------------------------}
{Mathematical functions}

function sinh(x:real):real;
BEGIN
 sinh:=(exp(x)-exp(-x))/2;
```

```
END;

function cosh(x:real):real;
BEGIN
 cosh:=(exp(x)+exp(-x))/2;
END;

function tanh(x:real):real;
BEGIN
 tanh:=sinh(x)/cosh(x);
END;

{-------------------------------------------------------------------------}
function power(x:real; y:integer):real;   {Integer power calculation x^y}
var
z:real;
i:integer;
BEGIN
z:=1.0; i:=y;
while i>0 do
   BEGIN
      if odd(i) then z:=z*x;
      i:=i div 2;
      x:=sqr(x);
    END;
  power:=z;
END;
{-------------------------------------------------------------------------}
function sm_c(a,r,sep:real):real;  {Capacitance For Circular Diaphragm}
CONST   Eo=8.85e-12;    {permittivity of air}
VAR     area:real;
BEGIN
   Area:=(pi*(sqr(a)-sqr(r)));
   sm_c:=(Eo*Area)/sep;
END;
{-------------------------------------------------------------------------}
```

```
Procedure read_valf;
BEGIN
  writeln('*** Parameters For Deflection/Electrostatic Calcs ***');
  writeln;
  write('Enter Bias Voltage      ');
  readln(vbias);
  write('Enter max deflection μm ');
  readln(wmax);
  write('Enter diaphragm stress (Pa) : ');
  readln(sigma_d);
  wmax:=wmax/1e6;
  clrscr;
END;
{-------------------------------------------------------------------------}
function Pr(wo,a,h:real):real; {Calc reaction force per unit area on diaphragm}
{Unstressed diaphragm}
const Ed=1.5e11;  {Young's modulus of diaphragm}
VAR t1,t2:real;
BEGIN
   t1:=(wo/h)+0.488*((sqr(wo)*wo)/(sqr(h)*h));
   t2:=(Ed*sqr(h)*sqr(h))/(0.171*sqr(a)*sqr(a));
   Pr:=(1/3)*t2*t1;
END;
{-------------------------------------------------------------------------}
function Pe(wo,sep,V:real):real; {Calculate electrostatic force per unit area}
{Unstressed diaphragm}
CONST Eo=8.85e-12;
     Em=100;  {rel permit of silicon}
VAR t1,t2,t3,t4,sa:real;
BEGIN
    sa:=sep+(h/Em);{ea/em - rel perm diaph em}
    t1:=wo/sep;          {sa effective air gap}
    t2:=sqrt(wo/sep);
    t3:=(Eo/(4*t1))*sqr(V/sep);
    t4:=((1/(1-t1))-((1/(2*t2))*ln((1+t2)/(1-t2))));
    Pe:=t3*t4;
END;
{-------------------------------------------------------------------------}
```

```
Procedure e_stat;
{Calculate net force on diaphragm per unit area for increasing applied pressurs}
{Unstressed diaphragm}
VAR Prf,Pef,Pdf,wmin,range:real;
    lp:integer;
BEGIN

    writeln('Diaphragm Deflection -  Stress Free   *** Electrostatic Calcs***');
    writeln;
writeln('Vbias :',vbias:0:3,' V ',' Max Defl : ',wmax*1e6:0:3,' μm ');
writeln;
  wmin:=0.0001e-6;
  range:=(wmax-wmin)/15;
  wo:=0;
  for lp:=1 to 15 do
    BEGIN
     wo:=wo+range;
     Prf:=Pr(wo,a,h);        {d- plate separation}
     Pef:=Pe(wo,d,Vbias);        {a- diaphragm radius }
     Pdf:=Pef-Prf;             {h- diaphragm thickness}
     write('wo: ',wo*1e6:3:2,' μm ','Pr: ',Prf:3:2,' Pa  ');
     writeln('Pe: ',Pef:3:2,'Pa ','Pd: ',Pdf:3:2,'Pa');

    END;
END;
{-------------------------------------------------------------------------}
function Prs(wo,a,h,sigmad:real):real;
{Reaction force per unit area for stressed diaphragm}
const Ed=1.5e11;
VAR t1,t2:real;
BEGIN
   t1:=(2*sigmad*h*wo)/sqr(R);
   t2:=1.595*Ed*h*(power(wo,3)/power(R,4));
   Prs:=t1+t2;
END;
{-------------------------------------------------------------------------}
function Pes(wo,sep,V:real):real;
{Electrostatic force per unit area for unstressed diaphragm}
CONST Eo=8.85e-12;
     Em=100;
VAR t1,t2,t3,t4,sa:real;
BEGIN
    sa:=sep+(h/Em);{ea/em - rel perm diaph em}
    t1:=(eo*sqr(v))/(2*wo);        {sa effective air gap}
    t2:=1/(sa-wo);
    t3:=(1/wo)*ln(1-(wo/sa));
    Pes:=t1*(t2+t3);
END;
```

```
Procedure e_stat_s;
{Calc net force on diaphragm with built in stress}
VAR Prf,Pef,Pdf,wmin,range:real;
    lp:integer;
BEGIN
writeln('Diaphragm Deflection - Large Initial Tensile Stress   ***Electrostatic Calcs**');
writeln;
writeln('Vbias :',vbias:0:3,' V ',' Max Defl : ',wmax*1e6:0:3,' μm ','Init Stress :
',sigma_d/1e6:0:3,' Mpa');
writeln;
  wmin:=0.0001e-6;
  range:=(wmax-wmin)/15;
  wo:=0;
  for lp:=1 to 15 do
    BEGIN
     wo:=wo+range;
     Prf:=Prs(wo,a,h,sigma_d);        {d- plate separation}
     Pef:=Pes(wo,d,Vbias);        {a- diaphragm radius }
     Pdf:=Pef-Prf;              {h- diaphragm thickness}
     write('wo: ',wo*1e6:3:2,' μm ','Pr: ',Prf:3:2,' Pa  ');
     writeln('Pe: ',Pef:3:2,'Pa ','Pd: ',Pdf:3:2,'Pa');

    END;
END;

{-------------------------------------------------------------------------}
```

```
function  c_sum:real;
{Calculate capacitance for deflected diaphragm}
VAR step,delta_a,cap_sum,sx,tmp:real; {Fraction of side}
    px,py,mx:integer;
BEGIN
sx:=a;
mx:=0;
step:=abs(sx)/(max);
sx:=0;
cap_sum:=0;
for mx:=0 to max do
  BEGIN
     cap_sum:=cap_sum+sm_c(sx+step,sx,d-(m1[mx]/1e6));
     sx:=mx*step;

  END;
    if abs(max_defl*1e-6)>=d then
     BEGIN
       cap_sum:=-1;
     END;

  c_sum:=cap_sum;
END;
{-------------------------------------------------------------------------}
function  c_diff:real;
{Calc change in capacitance for a deflected diaphragm}
VAR  tot_cap:real;
BEGIN
  tot_cap:=sm_c(a,0,d);    {zero pressure cap}
  c_diff:=c_sum-tot_cap;
  if abs(max_defl*1e-6)>=d then
     BEGIN
       gotoxy(40,12);
       c_diff:=-1;
     END;
END;
{-------------------------------------------------------------------------}
function  pc_diff:real;
{Percentage change in capacitance}
BEGIN
 pc_diff:=(c_diff/sm_c(a,0,d))*100;
 if c_diff=-1 then pc_diff:=-1;
END;

{-------------------------------------------------------------------------}
```

```
PROCEDURE g_setup; {Set up graphics mode}
VAR graphdriver:integer;
    graphmode:integer;
    errorcode:word;
BEGIN
   graphdriver:=detect;
   initgraph(graphdriver,graphmode,'');
   errorcode:=graphresult;
   if errorcode<>grok then
    BEGIN
      writeln('GRAPHICS ERROR: ',graphErrorMsg(errorcode));
      writeln('(You probably dont have a graphics card)');
      halt(1);
    END;
END;
{-------------------------------------------------------------------------}
PROCEDURE pause_g;      {Pause graphics screen}
VAR g:integer;
BEGIN
   moveto(300,400);
   outtext('Press Any Key To Continue   ');
   g:=ord(readkey);
END;
{-------------------------------------------------------------------------}
PROCEDURE info;
VAR  l,m:integer;
BEGIN;
   l:=wherex;
   m:=wherey;
   gotoxy(50,1);
   writeln('File : ',filename1);
   gotoxy(27,22);
   write('Current Circular Diaphragm ');
   gotoxy(15,23);
   write('r:',a*1e6:3:3,'μm  ');
   write('h:',h*1e6:3:3,'μm  ');
   write('d:',d*1e6:3:3,'μm ');
   write('q:',q:3:3,'Pa ');
   write('Vb:',vbias:1:0,'V');
   write('      ');
   gotoxy(48,12);
   write(h*1e6:3:3,'   ');
   gotoxy(48,12);
   write(d*1e6:3:3,'   ');
   gotoxy(48,12);
   write(q:3:3,'  ');
   gotoxy(l,m);
END;
```

```
PROCEDURE r_out(b:integer);  {Erase a line of text}
VAR  l,m,n:integer;
BEGIN;
   l:=wherex;
   m:=wherey;
   for n:=1 to b do
   write(' ');
   gotoxy(l,m);
END;
{-------------------------------------------------------------------------}
PROCEDURE calc_ind;   {Calculation indicator}
VAR j,k,l:integer;

BEGIN
   j:=wherex;
   k:=wherey;
   if (nm>31) or (nm<0) then
    BEGIN
       nm:=0;
       gotoxy(20,5);
       r_out(50);
    END;
   nm:=nm+1;
   gotoxy(nm+20,5);
   write('#');
END;
{-------------------------------------------------------------------------}
PROCEDURE wipe;       {Remove calculation indicator when complete}
BEGIN
   gotoxy(20,5);
   r_out(60);
   nm:=0;
END;
{-------------------------------------------------------------------------}
```

```
PROCEDURE default;   {Read in variables}
BEGIN
  gotoxy(35,16);
  write('Enter Radius (μm) Of Diaphragm   : ');
  cursor_on;
  readln(a);
  a:=a/1e6; {side of square}
  info;
  xf:=0; {Centre Of Diaphragm}
  yf:=0;
  gotoxy(35,17);
  write('Enter Thickness (μm) Of Diaphragm : ');
  readln(h);
  h:=h/1e6;
  info;
  gotoxy(35,18);
  write('Enter Plate Separation  (μm)      : ');
  readln(d);
  d:=d/1e6;
  info;
  gotoxy(35,19);
  write('Enter Pressure    (Pa)          : ');
  readln(q);

  gotoxy(35,20);
  write('Enter Bias Voltage (V)          : ');
  readln(Vbias);
  cursor_off;
  info;
 {Enter No Of Points 1-64)}
  max:=64;                {Set point size for area integration}
  gotoxy(35,20);
  writeln('Please Wait.... Calculating');
END;
{-------------------------------------------}
{The following five procedures are for file handling}
PROCEDURE Putlead(I:integer);
BEGIN
  if I>=10
  then write(I:2)
  else write('0',I:1);
END;
{-------------------------------------------}
```

```
PROCEDURE PutDateTime(DT:datetime);
VAR
  H:integer;
  ch:char;
BEGIN
   with dt do
     BEGIN
        write(Month:2,'-');
        putlead(day);
        write('-');
        putlead(year mod 100);
        write(' ');
        if hour>=12
        then ch:='p'
        else ch:='a';
        H:=hour mod 12;
        if h=0 then h:=12;
        write(h:2,':');
        putlead(min);
        write(ch);
     END;
 END;
{-----------------------------------------------}
PROCEDURE PutName(Name:string);
VAR
Dotpos:integer;
Ext:string[3];
BEGIN
   Dotpos:=pos('.',Name);
   if dotpos<>0 then
    BEGIN
       ext:=copy(name,dotpos+1,length(name)-dotpos);
       delete(name,dotpos,1+length(name)-dotpos)
    END
   else EXT:='';
   write(Name,' ':(10-length(name)),ext,' ':(5-length(ext)))
END;
{-----------------------------------------------}
```

```
PROCEDURE PutSrec(SRec:SearchRec);
VAR  DT:DateTime;
BEGIN
 with srec do
   BEGIN
      PutName(name);
      if (Attr and Directory) < > 0
      then write('    <DIR>')
   else
   BEGIN
      write(size:10,'    ');
      unpacktime(time,dt);
      putdatetime(dt)
   END;
      writeln;
  END;
END;
{-----------------------------------------------}
```

```
PROCEDURE GetDirectory;
VAR path:string;
    srec:searchrec;
    v:integer;
BEGIN
   co_ord_ipt;
   v:=0;
    gotoxy(15,8);
    Write('Enter path name: ');
    readln(path);
    writeln;
    if path<>'' then
       BEGIN
          FindFirst(path,anyfile,srec);
          while doserror=0 do
             BEGIN
               gotoxy(17,v+10);
               putsrec(SRec);
               FindNext(SRec);
                v:=v+1;
               if v=8 then
                  BEGIN
                     pause1;
                    v:=0;
                  END;
             END;
            writeln;
            if v<8 then
               BEGIN
                  repeat
                     gotoxy(17,v+10);
                     r_out(45);
                     v:=v+1;
                     until v=8;
             END;
       END;
     pause1;
     restore;
END;
{-----------------------------------------}
```

```
Function w(r,a,q,h:real):real;
{Calculate deflection for given diaphragm parameters}
VAR w1,b,wt1,wt2,k,w2,mp,Em,t1a,t2a,t3a,t4a,t1b,t2b,t3b,D,yd,am,xd:real;
    jk,m,n,pow:integer;
BEGIN
  d:=(E*power(h,3))/(12*(1-sqr(v)));
  w1:=(q/(64*d))*sqr((sqr(a)-sqr(r)));
  w:=w1;
END;

{-------------------------------------------------------------------------}
function ToStr(i:real;a,b:integer):string;
BEGIN
  str(i:a:b,temp);
  ToStr:=temp;
END;
{-------------------------------------------------------------------------}
function xc(cap,freq:real):real;
{Calculate the reactance of the microphone at different frequencies}
BEGIN
  xc:=1/(2*pi*freq*cap);
END;
{-------------------------------------------------------------------------}

PROCEDURE results;
{Output results of calculations}
VAR ta1,ta2,ta3,d_p:real;
CONST p1=2e-5;  {Pa}
      p2=1;
      p3=20;
BEGIN
  gotoxy(14,8);
  write('*** Circular Silicon Diaphragm Calculations ***');
  gotoxy(14,10);
  write('Type a (μm)                    : ',a*1e6:3:4);
  gotoxy(14,11);
  write('Thickness                      : ',h*1e6:3:4);
  gotoxy(14,12);
  write('Pressure (Pa)                  : ',q:3:4);
  defl:=w(0,a,p1,h)*1e6;
  gotoxy(14,15);
  write('Deflection (μm) @ 2e-5 Pa (0dB)   : ',defl:3:4);
  defl:=w(0,a,p2,h)*1e6;
  gotoxy(14,16);
  write('Deflection (μm) @ 1 Pa    (93dB)  : ',defl:3:4);
  defl:=w(0,a,p3,h)*1e6;
  gotoxy(14,17);
  write('Deflection (μm) @ 20 Pa   (120dB  : ',defl:3:4);
```

```
  pause1;
  restore;{results opt}

  co_ord_ipt;
  gotoxy(14,8);
  write('Plate Separation (μm)                    : ',d*1e6:3:3);
  gotoxy(14,9);
  write('Max Deflection ',max_defl:3:3,' μm For P Of  ',q:3:4,'  Pa');
  gotoxy(14,10);
  write('Capacitance With No Applied Pressure pf  : ',sm_c(a,0,d)*1e12:3:3);
  gotoxy(14,11);
  ta1:=c_sum;
  if ta1<>-1 then
  write('Capacitance For Applied Pressure     pf  : ',ta1*1e12:3:3);
  gotoxy(14,12);
  ta2:=c_diff;
  if (ta1<>-1) and (ta2<>-1) then
  write('Change In Capacitance For ',q:3:3,' Pa is ',ta2*1e12:3:3,' pF');
  gotoxy(14,13);
  ta3:=pc_diff;
  if (ta1<>-1) and (ta2<>-1) and (ta3<>-1) then
  write('% Change In Capacitance Delta_C/Co       : ',ta3:3:3);

  if (ta1=-1) or (ta2=-1) or (ta3=-1) then
     BEGIN
        gotoxy(20,15);
        write('Deflection Exceeds Plate Separation ! ');
     END
    ELSE
     BEGIN
       gotoxy(14,15);
       writeln('For capacitance of ',ta1*1e12:3:2,' pF');
       gotoxy(14,16);
       writeln('Reactance at 50 Hz 3db point : ',xc(ta1,50)/1e6:3:1,' MOhms');
       gotoxy(14,17);
       writeln('Reactance at 500 Hz          : ',xc(ta1,5e2)/1e6:3:1,' MOhms');
       gotoxy(14,18);
       writeln('Reactance at 5 kHz           : ',xc(ta1,5e3)/1e6:3:1,' MOhms');
       gotoxy(14,19);
       writeln('Reactance at 50 kHz          : ',xc(ta1,5e4)/1e6:3:1,' MOhms');
     END;
END;
{---------------------------------------}
```

```
PROCEDURE section;
CONST   p2=100;
        samples=128; {No of samples Of profile}
VAR t:integer;
    x,step,inc:real;
BEGIN
  {r:=1000/1e6;}
 {Steps Across Diaphragm Profile}
   t:=samples;
   inc:=samples;
        {For half of diaphragm}

   step:=abs(a)/samples;
   writeln(a*1e6:3:3,'    ',step*1e6:3:3);
   pause;
   x:=0;
   gotoxy(1,19);
   writeln('Steps : ',samples:4);
   gotoxy(1,20);
   write('Cross-section Of Diaphragm At Pressure ',p2:3,'Pa: Deflection : ');
   gotoxy(1,21);
   write('X Position      : ');
   gotoxy(1,22);
   write('Steps Remaining : ');
REPEAT
   x:=x+step;
   defl:=w(x,a,p2,h)*1e6;
   delay(300);
   gotoxy(65,20);
   write(defl:3:4,'    μm  ');
   gotoxy(20,21);
   write(x*1e6:3:3, '   μm  ');
   gotoxy(20,22);
   write(t:4);
   t:=t-1;
UNTIL x>=r;

END;
{-------------------------------------------}
```

```
PROCEDURE write_cv;
{Save file of calculations}
VAR s,t:integer;
BEGIN
  c_v[0,0]:=a;
  c_v[1,0]:=h;
  c_v[2,0]:=d;
  c_v[3,0]:=q;
  c_v[4,0]:=p_max;
  gotoxy(15,17);
  write('Enter Filename : ');
  r_out(17);
  readln(filename2);
  gotoxy(15,18);
  Write('Writing Data....');
  assign(data,filename2);
  rewrite(data);
 for t:=0 to 4 do
 BEGIN
   for s:=0 to p_max do
     BEGIN
         write(data,c_v[s,t]);
     END;
  END;
   close(data);
END;
{-----------------------------------------------}
PROCEDURE zero;
{Clear c_v array}
VAR t,s:integer;
BEGIN
  for t:=0 to  4 do
 BEGIN
   for s:=0 to 650 do
     BEGIN
         c_v[s,t]:=0;
     END;
  END;
 END;
{-----------------------------------------------}
```

```
PROCEDURE read_cv;
{Retrieve file}
VAR s,t,iocode:integer;
    tr:real;
BEGIN
   zero;
   filename2:='spod.dat';
   gotoxy(40,17);
   write('Enter Filename : ');
   r_out(17);
   {$I-}
   cursor_on;
   readln(filename2);
   cursor_off;
   if filename2='' then filename2:='spod.dat';
   gotoxy(40,19);
   write('Retrieving Data...');
   assign(data,filename2);
   reset(data);
   iocode:=ioresult;
   if iocode<>0 then
                BEGIN
                 writeln('File Not Found !');
                 pause1;
                 exit;
                END;

   for s:=0 to 4 do {Locate size of array}
    BEGIN
       read(data,c_v[s,0]);
    END;
   p_max:=trunc(c_v[4,0]);

   reset(data);
   for t:=0 to 4 do
    BEGIN
       for s:=0 to p_max do
        BEGIN
           read(data,c_v[s,t]);
        END;
    END;
   close(data);
   a:=c_v[0,0];
   h:=c_v[1,0];
   d:=c_v[2,0];
   q:=c_v[3,0];
END;
{-------------------------------------------------------------}
```

```
PROCEDURE plot_cv(sel:integer);
{Plot calculated parameters}
CONST     yax=50;
          x_no=500;
VAR n,x_inc,x_co,l,p,sig_y:integer;
    xgi,ygi,xgis,ygis,min_no,max_no,data,scale:real;
BEGIN
  min_no:=c_v[0,sel];
  max_no:=c_v[0,sel];
  data:=0;
  x_co:=0;

      x_inc:=trunc(x_no/p_max);   {scale for screen width}
      for n:=0 to p_max do
       BEGIN
           data:=c_v[n,sel];
           if abs(data)>max_no then max_no:=abs(data);
           if abs(data)<min_no then min_no:=abs(data);
       END;
       if max_no=0 then max_no:=1e-11; {protect against div by zero}
scale:=150/max_no;              {scale for screen height}
 for n:=0 to p_max do
       BEGIN
           c_v_g[n,sel]:=(175-trunc(c_v[n,sel]*scale));
       END;
g_setup;
moveto(240,2);
outtext('+++ Circular Diaphragm Microphone Calculations +++');
moveto(0+yax,10);  {plot axis}
lineto(0+yax,175);
moveto(0+yax,175);
lineto(640+yax,175);
l:=0;
ygi:=0;
ygis:=max_no/10; {get y axis inc}
repeat                          {plot lines and values on y axis}
   moveto(0+yax,175-l);
   lineto(10+yax,175-l);
   moveto(0,172-l);
   outtext(tostr(ygi,3,2));
   l:=l+15;
   ygi:=ygi+ygis;
until l>=175;

xgi:=0;
xgis:=c_v[p_max,1]/10; {get pressure inc}
xgi:=xgis;
l:=50;
```

```
if (xgis*p_max)>100 then sig_y:=0; {decimal places display control for x-axis}
if ((xgis*p_max)<100) and ((xgis*p_max)>10) then sig_y:=1;
if (xgis*p_max)<10  then sig_y:=2;
repeat                  {plot lines and values on x axis}
  moveto(l+yax,170);
  lineto(l+yax,180);
  moveto(l+yax-15,185);
  outtext(tostr(xgi,3,sig_y));
  l:=l+50;
  xgi:=xgi+xgis;
until l>=x_no+50;

moveto(0+yax,175); {plot curve}
for n:=0 to p_max do
    BEGIN
      lineto(x_co+yax,(c_v_g[n,sel]));
      x_co:=x_co+x_inc;
    END;
    moveto(600,180);
    outtext('/Pa');


    case sel of
     2:BEGIN
        moveto(48,0);
        outtext('Cap /pF');
       END;

     3:BEGIN
        moveto(48,0);
        outtext('% Cap');
       END;

     4:BEGIN
        moveto(48,0);
        outtext('W(0,0) /μm');
       END;
     END;

     moveto(50,240);
     outtext('Diaphragm Radius (μm)    : ');
     moveto(300,240);
     outtext(tostr(a*1e6,3,3));

     moveto(50,255);
     outtext('Diaphragm Thickness (μm) : ');
     moveto(300,255);
     outtext(tostr(h*1e6,3,3));
```

```
      moveto(50,270);
      outtext('Plate Separation (μm)    : ');
      moveto(300,270);
      outtext(tostr(d*1e6,3,3));

      moveto(50,285);
      outtext('Final Value On Graph     : ');
      moveto(300,285);
      outtext(tostr(c_v[p_max,sel],3,3));
    pause_g;
    restorecrtmode;
END;
{-----------------------------------------------------------------}
PROCEDURE plot_graphs;
VAR z:integer;
BEGIN
for  z:=2 to 4 do
  BEGIN
   plot_cv(z);
  END;
END;
{-----------------------------------------------------------------}
```

```
PROCEDURE write_data;
VAR x,y:integer;
   value:real;
BEGIN
  m1[max+1]:=a;
  m1[max+2]:=h;
  m1[max+3]:=d;
  m1[max+4]:=q;
  m1[max+5]:=max;

  gotoxy(57,1);
  write('                    ');
  gotoxy(57,1);
  readln(filename1);
  {Write('Writing Data');}
  assign(data,filename1);
  rewrite(data);
  for y:=0 to max-1 do
   BEGIN
     for x:=0 to ((max-1))+5 do
       BEGIN
         write(data,m1[x]);
       END;
   END;
  close(data);
  writeln;
END;
{-----------------------------------------------}
PROCEDURE write_string;
VAR x,y,i:integer;
BEGIN
  write('Writing Data');
  assign(data2,filename1);
  rewrite(data2);
  for y:=0 to max-1 do
   BEGIN
     for x:=0 to max-1 do
       BEGIN
         temp:=ToStr(m1[x],3,3);

        write(data2,temp);
        writeln(temp);
       END;
       write('.');
   END;
  close(data2);
  writeln;
END;
```

```
PROCEDURE read_string;
VAR x,y:integer;
    value:real;
BEGIN
  write('Retrieving Data');
  assign(data2,filename1);
  reset(data2);
  for y:=0 to max-1 do
   BEGIN
     for x:=0 to max-1 do
       BEGIN
         writeln(ToStr(m1[x],3,3));
       END;
       write('.');
   END;
  close(data2);
  writeln;
END;
{-----------------------------------------------}
PROCEDURE empty;
VAR x,y:integer;
    value:real;
BEGIN
  for y:=0 to max-1 do
   BEGIN
     for x:=0 to (max-1)+5 do
       BEGIN
         m1[x]:=0;
         scn_dat[x]:=0;
       END;
   END;

END;
{-----------------------------------------------}
PROCEDURE read_data;
VAR x,y:integer;
    value:real;
BEGIN
  gotoxy(50,1);
  writeln('File : ');
  gotoxy(57,1);
  r_out(17);
  gotoxy(57,1);
  {$I-}
  cursor_on;
  readln(filename1);
  cursor_off;
  assign(data,filename1);
```

```
  reset(data);
  for y:=0 to max-1 do
   BEGIN
     for x:=0 to (max-1)+5 do
       BEGIN
          read(data,m1[x]);
       END;
  END;

  close(data);
  {$I+}
  if IOresult<>0 then
                BEGIN
                  gotoxy(1,1);
                  write('File Not Found ! ');
                  delay(1000);
                  gotoxy(1,1);
                  r_out(18);
                  gotoxy(57,1);
                  r_out(17);
                  exit;
                END;
  writeln;
  a:=m1[max+1];
  h:=m1[max+2];
  d:=m1[max+3];
  q:=m1[max+4];
  max:=trunc(m1[max+5]);

END;
{-----------------------------------------------}
```

```
PROCEDURE plot;
{Plot deflection data}
VAR x,y,value,offset,xc,yc:integer;
const x_shift=100;
BEGIN
   g_setup;
   offset:=0;
   moveto(270,10);
   outtext('Diaphragm Radius (μm)    : ');
   moveto(500,10);
   outtext(tostr(a*1e6,3,3));

   moveto(270,20);
   outtext('Diaphragm Thickness (μm) : ');
   moveto(500,20);
   outtext(tostr(h*1e6,3,3));

   moveto(270,30);
   outtext('Applied Pressure (Pa)  : ');
   moveto(500,30);
   outtext(tostr(q,3,3));

   moveto(270,40);
   outtext('Maximum Deflection (μm)  : ');
   moveto(500,40);
   outtext(tostr(max_defl,3,3));

if q>20 then
   BEGIN
      moveto(270,50);
      outtext('Pressure>20 Pa - No Scale For Graphics ! ');
    END;

     value:=-scn_dat[0];
    y:=0;
      moveto(x_shift,(175-(value)));

     for x:=0 to max-1 do
       BEGIN
          value:=-scn_dat[x];;
          ellipse(350,175-(value),0,360,(x*4),(x));
          y:=y+5;
       END;
     pause_g;
restorecrtmode
END;
{-----------------------------------------------------------------}
```

```
PROCEDURE normalise;
{Scale deflection data for plotting on screen}
VAR  x,y:integer;
     scale,data,max_no,min_no,np:real;
BEGIN

 min_no:=m1[0];
 max_no:=m1[0];
 y:=0;
  for x:=0 to max-1 do
        BEGIN
            data:=m1[x];
            if abs(data)>max_no then max_no:=abs(data);
            if abs(data)<min_no then min_no:=abs(data);
        END;
    max_defl:=max_no;
    if max_no=0 then max_no:=1e-12; {Protect against divide by zero}

   writeln('Max Defl : ', Max_no:3:3,' μm ',' Displ Sens : ',Max_defl/q:3:3,' μm/Pa');


    scale:=(175) /(max_no);      {screen res} {scaling fiddle}

    if q>20 then np:=20 else np:=q;  {scale x 1}

    scale:=scale*np/20;{Scaling For graphics only up to 20 pa}


y:=0;
  for x:=0 to max-1 do
        BEGIN
            scn_dat[x]:=trunc(m1[x]*scale);
        END;
END;
{-----------------------------------------------}
```

```
PROCEDURE store;
{Store diaphragm deflections}
CONST   Samples=64;
        {P2=1;}
VAR     inc,step,sx,sy,temp:real;
BEGIN
 {Steps Across Diaphragm Profile}
                {For half of diaphragm}
              {a  side of diaphragm}
sx:=a;
mx:=0;
my:=0;
step:=abs(sx)/max;
sx:=0;
sy:=0;
for mx:=0 to max-1 do
   BEGIN
        m1[mx]:=w(sx,a,q,h)*1e6;  {Store in microns}
      calc_ind;
       sx:=mx*step;
   END;
   wipe;
END;
{-------------------------------------------------------------------------}
PROCEDURE     cap_v_press;
{Calculate change in capacitance for applied pressure - static clculations}
VAR p,r:integer;
    cc,dc,df,p_m,press_inc,ta1,ta2,ta3:real;
BEGIN
   max_defl:=0;  {has own max defl detection}
   zero;
   cc:=0;
   dc:=0;
   p_m:=0;
   p_max:=50;
   press_inc:=0;
   gotoxy(14,8);
   write('Enter Max Pressure (Pa)    : ');
   readln(p_m);
   gotoxy(14,9);
   write('Enter no of steps  (5<s<500) : ');
   readln(p_max);
   press_inc:=p_m/p_max;

   gotoxy(14,11);
   writeln('        ***** Running *****');
   q:=0;
   for p:=0 to p_max do
```

```
    BEGIN
      store;
      cc:=c_sum*1e12;
      dc:=pc_diff;
      df:=w(0,a,q,h)*1e6;
      if df>=d*1e6 then
        BEGIN
          gotoxy(14,15);
          write('Deflection Exceeds Plate Separation ! ');
          cc:=0;
          dc:=0;
        END;
      c_v[p,1]:=q; {pressure mmHG}
      c_v[p,2]:=cc; {capacitance inc}
      c_v[p,3]:=dc; {capacitance change}
      c_v[p,4]:=df; {Deflection}
      gotoxy(14,13);
      write('Pa   Cinc(pF)   % Delta C   Defl (μm) ');
      gotoxy(14,14);
      write(q:3:3,'  ',cc:3:3,'     ',dc:3:3,'       ',df:3:3);
      q:=q+press_inc;
    END;
  writeln;
END;
{-------------------------------------------------------------}
PROCEDURE text1;
{MAIN MENU OUTPUT}
BEGIN
  gotoxy(15,7);
  writeln('***** Parameter Control Menu *****');
  {gotoxy(10,22);
  write('Select Desired Option With Funtion Keys.');
  gotoxy(10,23);
  writeln('Enter Integers Using Arrow Keys After Function Selection.');
  gotoxy(10,24);
  writeln('If No Integers Are Entered Default Values Are Used.');}
  gotoxy(15,9);
  writeln('F1  Diaphragm Parameters          ');
  gotoxy(15,10);
  writeln('F2  Adjust Thickness  (μm)      : ');
  gotoxy(15,11);
  writeln('F3  Adjust Plate Separation (μm): ');
  gotoxy(15,12);
  writeln('F4  Adjust Pressure (Pa)        : ');
  gotoxy(15,13);
  writeln('F5  Results & Plot                ');
  gotoxy(15,14);
  writeln('F6  Read Deflections From Disk    ');
```

```
  gotoxy(15,15);
  writeln('F7  Save Deflections To Disk      ');
  gotoxy(15,16);
  writeln('F8  Variable Versus Pressure      ');
   gotoxy(15,17);
  writeln('F9  Read F8 Info From Disk        ');
  gotoxy(15,18);
  writeln('F10 Directory Of Disk');

  gotoxy(15,19);
  writeln('E   Exit');
END;
{-------------------------------------------------------------------------}
PROCEDURE menu_control;
{THIS PROCEDURE CONTROLS THE PROGRAM SELECTION AND FLOW}
{INTEGERS READ FOR SELECTIONS 1,2,3,6 & 7 START WITH DFAULT
PARAMETERS AND
ARE ALWAYS REMEMBERED AT THE LAST VALUE ENTERED IF CHANGED
WITH ARROW KEYS}
VAR decno:integer;
   a,b,t:integer;
BEGIN

  select:=0;
  info;
  repeat;
  keyboard(a,b);          {GET A FUNCTION KEY SELECT VALUE}
  fkeys(a,b,select); {DRIVE FUNCTION KEY SELECT MENU IN EXTERNAL
PROCEDURE}
  if a=1 then
    BEGIN
      case select of  {TASKS PERFORMED BEHIND EACH FUNCTION KEY
SELECTION}

         1:BEGIN
           info;
           nondestruct3;
           default;
           restore;
           info;
          END;

         2:BEGIN
           info;
           gotoxy(48,10);
           r_out(10);
           cursor_on;
           readln(h);
```

```
    cursor_off;
    h:=h/1e6;
    info;
    writeln;
  END;

3:BEGIN
    info;
    gotoxy(48,11);
    r_out(10);
    cursor_on;
    readln(d);
    cursor_off;
    d:=d/1e6;
    info;
    writeln;
  END;

4:BEGIN
    info;
    gotoxy(48,12);
    r_out(10);
    cursor_on;
    readln(q);
    cursor_off;
    info;
    writeln;
  END;

5:BEGIN
    store;
    normalise;
    restore;
    co_ord_ipt;
    results;
    pause1;
    restore;
    restore;
    clrscr;
    read_valf;
   e_stat; {diaph with stress}
    pause1;
    clrscr;
    e_stat_s;
    pause1;
    plot;
    header;
    co_ord_ipt;
```

```
        text1;
        info;
      END;

    6:BEGIN              {NO OF STEPS}
        read_data;
        normalise;
      END;

    7:BEGIN
        write_data;
        normalise;
      END;

    8:BEGIN
        info;
        restore;
        co_ord_ipt;
        cap_v_press;
        gotoxy(14,16);
        write_cv;
        restore;
        restore;
        plot_graphs;
        header;
        co_ord_ipt;
        text1;
      END;

    9:BEGIN
        restore;
        co_ord_ipt;
        text1;
        nondestruct3;
        read_cv;
        restore;
        plot_graphs;
        header;
        co_ord_ipt;
        text1;
      END;

   10:BEGIN
        getdirectory;
      END;
    END;
END;
```

```
if a=0 then   {normal keys}
  BEGIN
  case select of
     11:BEGIN              {SAFE EXIT PROCEDURE}
          select:=0;
          quit(t);
          if t=1 then exit;
          if t=0 then
             BEGIN
               resetfunc;
             END;
          END;
        END;
    END;
  until select=12;
  cursor_on;
END;
{-------------------------------------------------------------------------}
BEGIN
   restore;
   restore;
   clrscr;
   a:=500/1e6;   {default values}
   r:=a;
   h:=1/1e6;
   d:=1/1e6;
   q:=5;
   xf:=0;
   yf:=0;
   vbias:=1;
   p_max:=10;
   max:=64;
   filename1:='a:scratch.dat';
   filename2:='a:default.dat';

   clrscr;
   empty;
   nm:=0;   {calc counter}
   clrscr;
   header;
   co_ord_ipt;
   text1;
   info;
   menu_control; {Start menu control of procedures}
   clrscr;
 END. {Of program}
```

```
{Functions for calculation of deflection of square diaphragms}

{The following functions and procedures can be used in place of
those in the main program for calculation of the deflection of
square diaphragms}
{-------------------------------------------------------------------------}
function  c_sum:real;
{Total capacitance for given deflection for square diphragm}
VAR delta_a,cap_sum:real; {Fraction of side}
    px,py:integer;
BEGIN
  delta_a:=(a/2)/max;   {allow for only 1/4 of diaphragm}
  cap_sum:=0;
    for py:=0 to max-1 do
      BEGIN
        for px:=0 to max-1 do
          BEGIN
            cap_sum:=cap_sum+sm_c(delta_a,(d-(m1[px,py]*1e-6)));
          END;
      END;

   cap_sum:=cap_sum*4;
     {*4 For all quadrants}
   c_sum:=cap_sum;
  if abs(max_defl)>=d*1e6 then
       BEGIN
         c_sum:=-1;
       END;
END;
{-------------------------------------------------------------------------}

Function w(x,y,a,q,h:real):real;
{Calculation of deflection for an unstressed diaphragm - See Timoshenko}
CONST v=0.3;  {Poissons ratio for silicon}

VAR t1,t2,t3,t4,D,m,n,p:real;
BEGIN
  if y<1e-36 then
                BEGIN
                 y:=1e-36;
                 {writeln('Number Underflow');}
                END;
  if y>1e36 then
                BEGIN
                y:=1e36;
               {  writeln('Number Overflow');}
                END;
  t1:=sqr((2*x)/a);
```

```
   t2:=sqr((2*y)/a);
   gotoxy(1,1);

   D:=(E*power(h,3))/(12*(1-sqr(v)));
   t3:=(q*power(a,4))/(16*d);
   m:=sqr(1-t1);

   n:=sqr(1-t2);
   t4:=(sqr(1-t1)*sqr(1-t2))*
   ((0.02023*t3)+(0.00535*t3*(t1+t2))+(0.00625*t3*(t1+t2)));
   w:=t4;
END;
{-------------------------------------------------------------------------}
PROCEDURE plot;
VAR x,y,value,y_shift,offset,xc,yc:integer;
const x_shift=100;
BEGIN
    if max_defl>0 then y_shift:=300;
    if max_defl<0 then y_shift:=175;
   {writeln('Max Deflection (μm): ',tostr(max_defl));}

   g_setup;
   offset:=0;
   moveto(10,20);
   outtext('Deflection');
   moveto(45,y_shift-130);
   outtext('0');
   moveto(40,y_shift-128);
   lineto(20,y_shift-128);
   lineto(20,349);
          moveto(270,10);
      outtext('Diaphragm Side (μm)      : ');
      moveto(500,10);
      outtext(tostr(a*1e6,3,3));

      moveto(270,20);
      outtext('Diaphragm Thickness (μm) : ');
      moveto(500,20);
      outtext(tostr(h*1e6,3,3));

      moveto(270,30);
      outtext('Applied Pressure (Pa)  : ');
      moveto(500,30);
      outtext(tostr(q,3,3));


   value:=-scn_dat[1,1];
   moveto(20,(y_shift-(value+offset)));
```

```
  lineto(40,(y_shift-(value+offset)));
  outtext(tostr(max_defl,3,3));

  for y:=0 to max-1 do
   BEGIN
    value:=-scn_dat[0,y];

     moveto(x_shift+0+offset,(y_shift-(value+offset)));
    for x:=0 to max-1 do
      BEGIN
         value:=-scn_dat[x,y];
         lineto(x_shift+(x*4)+offset,(y_shift-(value+offset)));
      END;
      offset:=offset+2;
   END;
    pause_g;
restorecrtmode
END;
{-------------------------------------------------------------------}
PROCEDURE store;
CONST   Samples=64;
       {P2=1;}
VAR     inc,step,sx,sy,temp:real;
BEGIN
 {Steps Across Diaphragm Profile}
                {For half of diaphragm}
sx:=-a/2;           {a  side of diaphragm}
step:=abs(sx)/max;
for my:=0 to max-1 do
  BEGIN

    for mx:=0 to max-1 do
     BEGIN
       sx:=mx*step;
       m1[mx,my]:=w(sx,sy,a,q,h)*1e6;  {Store in microns}
     END;
     writeln(mx:3,'  ',sx*1e6:3:3,'    ',my:3,'    ',sy*1e6:3:3,' Def: ',m1[0,my]:3:3);}
     calc_ind;
     sy:=my*step;
  END;
  wipe;
END;
{-------------------------------------------------------------------}
```

```
PROGRAM doping_calcs_erfc;
{Programmer       : Edward Pallett}
{Version          : 1.1}
{Turbo Pascal Ver.: 4.0}
{Procedures to calculate boron diffusion profiles for pre-deposition and drive in}
{$N+}

USES crt;
CONST
     Ea=3.69; {(eV)}
     k=1.38e-23;
     Dpr=10.5; {cm2/s}
     No=2.5e20;
     NB=2e15;
TYPE mat=array[1..100,1..4] of real;
VAR  D,xj,temp1,temp2:real;
     t1,t2,X,rconst,B:real;  {B parabolic rate constant}
     hrs:integer;
     t:longint;
     dpth:mat;
{-------------------------------------------------------}


PROCEDURE pause;
VAR ch:char;
BEGIN
  writeln('Press Any Key To Continue');
  ch:=readkey;
END;
{-------------------------------------------------------}
FUNCTION dc(temp:real):real;
BEGIN
  dc:=Dpr*exp(-(Ea/((273+temp)*8.614e-5)));
END;
{-------------------------------------------------------}
FUNCTION q(t1:real):real; {Calculate dose}
VAR f,dose:REAL;
BEGIN
  f:=2*sqrt((dc(temp1)*t1)/pi);
  dose:=No*f;
  q:=dose;
END;
{-------------------------------------------------------}
Function tx(x:real):real;
VAR f:real;
BEGIN
  tx:=x/(2*sqrt(dc(temp1)*t1));
END;
```

```
{-------------------------------------------------------}
Function NoErfc(t:real):real;
VAR g:real;
BEGIN
  if t=0 then t:=1e-7; {Prevent div by zero but get value for small t}
  g:=No*(1/sqrt(pi))*(exp(-sqr(t))/t);
  if g>No then g:=No; {Fudge Factor}
  NoErfc:=g;
END;
{-------------------------------------------------------}
Function ep(z:real):real;
BEGIN
  ep:=exp(-sqr(z));
END;
{-------------------------------------------------------}

Function erfc(z:real):real;  {Numerical Integration To Solve ERF}
CONST k=100; {no of strips}
VAR h,pta,ptb,pm,erfz:real;
    i:integer;
BEGIN
  h:=z/k;
  pta:=0.5*(ep(0)+ep(z));
  pm:=2/(sqrt(pi));
  ptb:=0;
  for  i:=1 to k-1 do
    BEGIN
      ptb:=ptb+ep(i*h);
    END;
  ptb:=ptb;
  erfz:=pm*h*(pta+ptb);
  erfc:=1-erfz
END;
{-------------------------------------------------------}
Function Gauss(t:real):real;
VAR f,g:real;
BEGIN
  if t=0 then t:=1e-7;
  f:=sqr(t/(2*sqrt(dc(temp2)*t2))); {Second diff drive in time and temp}
  g:=(Q(t1)/(sqrt(pi*dc(temp2)*t2)));
  {writeln('Surface conc ',g:3);}
  gauss:=g*exp(-f);
END;
{-------------------------------------------------------}
PROCEDURE Erfc_Profile;
VAR x:real;
   cnt:integer;
BEGIN
```

```
  x:=0;
   for cnt:=1 to 40 do
   BEGIN
     dpth[cnt,1]:=x;{tx(x*1e-4);}
     dpth[cnt,2]:=No*erfc(tx(x*1e-4));    {converts to μm}
     dpth[cnt,3]:=0; dpth[cnt,4]:=0;
     writeln(tx(x*1e-4):3:3,' Concentration At ',x:3:3,'μm  ',No*erfc(tx(x*1e-4)):3,'
Atoms/cm3');
     if cnt=20 then pause;
     if No*Erfc(tx(x*1e-4))>1 then
       BEGIN
            if cnt<20  then  x:=x+0.05;
            if cnt>=20 then x:=x+0.5;
       END;
   END;
END;
PROCEDURE Gauss_Profile;
VAR x:real;
    cnt:integer;
BEGIN
  x:=0;
   for cnt:=1 to 40 do
   BEGIN
     dpth[cnt,1]:=x;   {tx(x*1e-4);}
     dpth[cnt,2]:=Gauss(x*1e-4);      {converts to μm}
     dpth[cnt,3]:=0;
     dpth[cnt,4]:=0;
     writeln('Concentration At ',x:3:2,'μm  ',Gauss(x*1e-4):3,' Atoms/cm3');
     if cnt=20 then pause;
     if gauss(x*1e-4)>1 then
     BEGIN
       if cnt<20  then  x:=x+0.05;
       if cnt>=20 then x:=x+0.5;
     END;
   END;
END;
{-------------------------------------------------}
PROCEDURE profile_test;
VAR dt1,dt2:Real;
BEGIN
  dt1:=Dc(Temp1)*T1;
  dt2:=Dc(Temp2)*T2;
  writeln('D1T1 ',dt1:3,' cm2');
  writeln('D2T2 ',dt2:3,' cm2');
  writeln('If D2T2>>D1T1 then profile assumption valid');
  if dt2>(5*dt1) then writeln('Profiles Will Be Valid !') else
  writeln('*** Drive In Profile Invalid ! ***');
END;
```

```
{-------------------------------------------------}
PROCEDURE manual_inp;
VAR x,sc:real;
BEGIN
  write('Pre-deposition Temperture oC ');
  readln(temp1);
  write('Diffusion Coefficient : ');
  writeln(dc(temp1):3,' cm2/sec');
  write('Pre Deposition Time hrs ');
  readln(t1);
  t1:=t1*3600;
  Writeln('---------------------------------');
  write('Drive-in Temperture oC ');
  readln(temp2);
  write('Diffusion Coefficient : ');
  writeln(dc(temp2):3,' cm2/sec');
  write('Drive In Time hrs ');
  readln(t2);
  t2:=t2*3600;
  writeln('---------------------------------');
  writeln('Dose ',q(t1):3,' atoms/cm2');
  sc:=(Q(t1)/(sqrt(pi*dc(temp2)*t2)));
  writeln('Drive In Surface Concentration ',sc:3,' atoms/cm3');
  profile_test;
  writeln('---------------------------------');
  pause;
END;
{-------------------------------------------------}
 BEGIN
    clrscr;
    manual_inp;
    writeln('*** Pre-Deposition Profile ****');
    writeln;
    Erfc_profile;
    pause;
    writeln('*** Drive-In Profile ****');
    writeln;
    Gauss_profile;
    writeln;
    Pause;
END.

{This code will run, but is an extract from a larger program
for process calculations}
```

List Of References

1. K. Petersen, Silicon as a mechanical material, Proc. IEEE, vol. 70, no. 5, pp. 420-457, May 1982.

2. Microsensors 1990, IEEE Press, USA

3. H. Reichl, Micro System Technologies 92, 3 rd International Conference on Micro Electro, Opto, Mechanic Systems and Components Berlin, Oct 21-23, 1992.

4. Elliott, Integrated circuit fabrication technology.

5. Ernest Bassous, Fabrication of Novel Three-dimensional microstructures by the anisotropic etching of (100) and (110) silicon, IEEE Trans Electron ED-24, No. 10, Oct 1978

6. P. Scheeper, J. Voorthuyzen and P.Bergveld, PECVD silicon nitride diaphragms for condenser microphones, Sensors and Actuators B, 4(1991) 79-84

7. O. Brosze, Aufbau und Wirkungsweise elektroakustischer Wandler, Der Fernmelde Ingenieur, 35. Jahrgang (1981) Heft 6, 1-36, Heft 7, 1-35

8. W. Lukosz abd P. Pliska, Integrated optical interferometer as a light modulator and microphone., Sensors and Actuators, A25-27(1991) 337-340.

9. D. Garthe, A fibre-optic microphone, Sensors and Actuators A, 25-27 (1991) 341-345

10. R. Schellin and G. Hess, A silicon subminiature microphone based on piezoresistive polysilicon strain gauges, Sensors and Actuators A, 32 (1991) 555-559

11. D. Hohm and R. Gerhard-Multhaupt, Silicon-dioxide electret transducer, J Acoust. Soc. Am., 75 (1984) 1297-1298.

12. S. M. Sze, Physics of Semiconductor Devices, Chapter 7, 2nd ed.,John Wiley & Sons, 1981.

13. R. Williams and M. H. Woods, High electric fields in silicon dioxide produced by corona charging, J. Appl. Phys., Vol 44, No 3, March 1973

14. D. Hohm and G. Hess, A subminiature condenser microphone with silicon nitride membrane and silicon back plate, J.Acoustic. Soc Am., 85 (1989) 476-480.

15. W. Kuhnell and G.Hess, Micromachined subminiature condenser in silicon, Sensors and Actuators A, 32 (1992) 560-564.

16. W. Kuhnel and G. Hess, A silicon condenser microphone with structured back plate and silicon nitride membrane, Sensors and Actuators A,30 (1992) 251-258.

17. A. J Sprenkels, R. A. Groothengel, A. J. Verloop and P. Bergveld, Development of an electret microphone in silicon, Sensors and Actuators, 17 (1989) 509-512.

18. A. J. Sprenkels, A silicon subminiature electret microphone, University of Twente, 1988, Thesis.

19. P. Murphey, K. Hubschi, N. De Rooij and C. Racine, Subminiature silicon integrated electret capacitor microphone, IEEE Trans. Electr. Ins, 24 (1989) , 495-498.

20. J. Bergqvist and F. Rudolf, A new condenser microphone in silicon, Sensors and Actuators A,21-23 (1990) 123-125.

21. J. Bergqvist and F. Rudolf, J. Maisano, F. Parodi and M. Rossi, A silicon condenser microphone with a highly perforated backplate, Proceedings of Transducers '91, San Francisco, USA, 266-269.

22. W. Kuhnel Silicon condenser microphone with integrated field effect transistor, Sensors and Actuators A, 25-27 (1991) 521-525.

23. E. S. Kim, R. S. Muller, and P. R. Gray, Integrated microphone with CMOS circuits on a single chip, IEDM Tech Dig, June 1992, Vol 39, No. 6, Pg 1385.

24. E. S. Kim, J. R. Kim and R. S. Muller, Improved IC-compatible piezo-electric microphone and CMOS process, Proceedings of Transducers '91, san francisco, USA, 270-273

25. R. Schellin and G. Hess, A silicon subminiature microphone based on piezoresistive polysilicon strain gauges, Sensors and Actuators A, 32 (1991) 555-559

26. K. D. Wise, Samaun and J. B. Angell, An IC piezoresistive pressure sensor for biomedical instrumentation, IEEE trans. Biomed. Eng., vol. BME-20, pp.101-109, Mar. 1973

27. P. R. Scheeper, W. Olthiuss and P. Bergveld, Fabrication of a subminiature silicon condenser microphone using sacrificial layer technique, Proceedings of Transducers '91, San Francisco, USA, 408-411.

28. P. R. Scheeper, W. Olthius and P. Bergveld, A silicon condenser microphone with a silicon nitride diaphragm and backplate, Proceedings of Michromechanics Europe 1992 (MME '92), Leuven, Belgium, 110-113.

29. J. Bergqvist, J. Gobet, Capacitive microphone with a surface micromachined backplate using electroplating technology, submitted for publication in J. of Microelectromechanical Systems. 1994

30. D. Wise and Kukjin Chun, A high performance silicon tactile imager based on a capacitive cell, IEEE Trans. Elect. Dev., Vol. ED-32, No 7, July 1985

31. T. Cho, K. Najafi, C. Lowman and K. Wise, An ultrasensitive silicon pressure based microflow sensor, IEEE Trans. On Electron Dev, Vol 39, No. 4,April 1992.

32. T. Bourouina, S. Spirovitch, F. Baillieu and C. Vauge, A new silicon condenser microphone with a p^+ silicon membrane, Sensors and Actuators A, 31 (1992) 149-152.

33. E. Frederiksen, N. Eirby and H. Mathiasen, Prepolarized condenser microphones for measurement purposes, Noise and Vibration Control Worldwide, March (1980) 88-96.

34. A. J. Sprenkels, A silicon subminiature electret microphone, Thesis, Twente University, 1988.

35. S. Timoshenko and S. Woinowski-Krieger, Theory of plates and shells, 2nd edn., McGraw-Hill, New York, 1959.

36. P. Morse and K. U. Ingard, Theoretical acoustics, 1st Edn., McGraw-Hill, New York, 1968.

37. F. Friam and P. Murphy, Miniature electret microphones, J. Audio Eng. Soc. Am, 18 (1970) 511-517.

38. A. J. Sprenkels, A silicon subminiature electret microphone, Thesis, University of Twente, 1988.

39. H. Chau, K. D. Wise, Noise due to brownian motion in ultrasensitive solid-state pressure sensors, IEEE. Trans. on Electron Dev. ED-34, No. 4, April 1987.

40. K. Chun, A high performance silicon tactile imager based on a capacitive cell, Ph.D. dissertation, The University Of Michigan, Ann Arbor, May, 1986.

41. L. Kinseler, A. R. Frey, A. B. Coppens, J. V. Sanders, Fundamentals of acoustics, Third Ed. John Wiley & Sons 1982

42. P. R. Scheeper, J. A. Voorthuyzen and P. Bergveld, PECVD Silicon nitride diaphragms for condenser microphones, Sensors and Actuators B, 4(1991) 79-84

43. B. E. Deal, Thermal oxidation kinetics of silicon in pyrogenic H_2O and 5% HCL/H_2O mixtures, Journal of the Electrochemical Society, 125, 576-579 (April 1978).

44. D. Morgan, An introduction to semiconductor microtechnology, Open University, John Wiley & Sons. 1983.

45. R. B. Fair, Boron Diffusion in Silicon - Concentration and orientation dependence, background effects, and profile estimation, Journal of the Electrochemical Society, 122, 800-805 (June, 1975).

46. N. Harris. Modern vacuum practice, McGraw Hill 1989

47. Edwards FTM5 thickness monitor reference guide

48. S. M. Sze, Semiconductor devices physics and technology, Wiley, 1985

49. L. Holland, Vacuum deposition of thin films, Chapman & Hall, 1966.

50. Fetz, H., Z. Phys., 119 (1942), 590

51. Wehner, GG. K., Phys. Rev.,93 (1954), 633

52. Kenneth J. Klabunde, Thin films from free atoms and particles, Academic Press 1985.

53. W. H. Ko, J. T. Suminto, and G. J. Yeh, Bonding techniques for microsensors, Elsevier Science Publishers, B. V., 1985.

54. H. Seidel, L. Csepregi, A. Heuberger, H. Baumgartel, Anisotropic etching of crystalline silicon in alkaline solutions, I. Orientation dependence and behaviour of passivation layers, Electrochemical Society, Vol 137, No 11, Nov 1990

55. H. Seidel, L. Csepregi, A. Heuberger, H. Baumgartel, Anisotropic etching of silicon in alkaline solutions, II. Influence of dopants, Electrochemical Soc, Vol 137, No 11, Nov 1990

56. B. Kloek, D. Collins, Nico F, De Rooij and R. L. Smith, Study of electrochemical etch stop for high precision thickness control of silicon membranes, IEEE Trans. Elec Dev. Vol 36, No 4, Apr 1989.

57. J. M. Crishal and A. L. Harrington, J. Electrochem. Soc., 111,202 (1962), Abs. 89

58. R. M. Finne and D. L. Klein, J. Electrochem. Soc., Vol 114, 965 (1967)

59. L. D. Clark, Jr., J. L. Lund, and D. J. Edell, in "Technical Digest," IEEE Solid-State Sensor and Actuator Workshop, Hilton Head Island, SC, June 6-9, 1988.

60. M. Asano, T. Cho, and H. Muraoka, Abstract 354, p. 911, The Electrochemical Society Extended Abstracts, Vol. 76-2, Las Vegas, NV, Oct. 17-22, 1976.

61. M. M. Abu-Zeid, D. L. Kendall, G. R. de Guel, and R. Galeazzi, Abstract 275, p. 400, The Electrochemical Society Extended Abstracts, Vol. 85-1, Toronto, Ont., Canada, May 12-17, 1985.

62. A. Reisman, M. Berkenblit, S. A. Chan, F. B. Kaufman, and D. C. Green, J. Electrochem. Soc., Vol 126, 1406 (1979).

63. E. Bassous, U.S. Pat. 3,921,916 (1975).

64. O. Tabata, R. Asahi, H. Funabashi and S. Sugiyama, Anisotropic etching of silicon In TMAHW solutions, IEEE 1991

65. U. Schnakenberg, W. Benecke, P. Lange, TMAHW Etchants for silicon micromachining, IEEE 1991

66. J. B. Price, in "Semiconductor Silicon, " H. R. Huff and R. R. Burgess, Editors, p. 339, The Electrochemical Society Softbound Proceedings Series, Princeton, NJ (1973).

67. E. D. Palik, H. F. Gray, and P. B. Klein, J. Electrochem. Soc., Vol 130, pg. 956 (1983).

68. J. B. Price , Anisotropic etching of silicon with KOH-H_2O-Isopropyl alcohol, Electrochem. Soc. Vol. ED29 No. 1. Jan 1982

69. H. Seidel, L. Csepregi, A. Heuberger, H. Baumgartel, Anisotropic etching of crystalline silicon in alkaline solutions, J. Electrochem. Soc., Vol. 137, No. 11, Nov. 1990.

70. O. Tabata, R. Asaha, H. Funabashi, S. Sugiyama, Anisotropic etching of silicon in $(CH_3)_4NOH$ solutions, Proceedings of Transducers '91, san Francisco, USA, 811-814.

71. U. Schnakenberg, W. Benecke, P. Lange, TMAHW etchants for silicon micromachining, Proceedings of Transducers '91, San Francisco, USA, 815-818.

72. A. Bogh, ibid., vol 118, 401 (1971).

73. J. B. Price, in "Semiconductor silicon, "H. R. Huff and R. R. Burgess, Editors, p. 339, The Electrochemical Society Softbound Proceedings Series, Princeton, NJ (1973)

74. N. F. Raley, Y. Sugiyama, and T. van Duzer, ibid., Vol. 131, 161(1984).

75. H. K. Charles, G. V. Clatterbaugh and J A. Weiner, the ball bond shear test : Its methodology and application, American Society for testing materials 1984.

76. David J. Elliot, Integrated circuit fabrication technology, McGraw-Hill book company.

77. E.Pallett, An innovative method for etching backchambers accurately, to be published, De Montfort University 1995.

78. W. H. Ko, J. T. Suminto and G. J. Yeh, Bonding techniques for microsensors, 1985, Micromachining and Micropackaging of Transducers.

79. P. R. Scheeper, J. A. Voorthuyzen, W. Olthuis and P. Bergveld, Investigation of attractive forces between PECVD silicon nitride microstructures and an oxidised silicon substrate.

80. N. Takeshima et al., Electrostatic Parallelogram Actuators, IEEE 1991

81. T. Inoue and H. Osatake, A new drying method of biological specimens for scanning electron microscopy : The t-butyl alcohol freeze-drying method, Arch. Histol. Cytol., Vol. 51, No. 1, 1988, pp. 53-59

82. K. Suzuki, K. Najafi, K. Wise, A 1024 element high performance silicon tactile imager, IEEE Trans On Elec. Dev. Vol. 37. No 8, Aug 1990.

83. K. Chun, K. Wise, High Performance silicon tactile imager based on a capacitive cell, IEEE Trans. On Elec. Dev., Vol ED 32, No 7, July 1985

84. O. Tabata, R. Asahl, H. Funabashi, S. Sugiyama, Anistotropic etching of silicon in $(CH_3)_4(NOH)$ solutions, Transducers and actuators 91.

85. W. Chu and M. Mehregany, A study of residual stress distribution through the thickness of p+ silicon films, IEEE Trans. On Electron Dev. Vol 40, No. 7, July 1993

86. R. Huster and A. Stoffel, Vertically structured silicon membranes by electrochemical etching, Sensors and Actuators, A21-A23 (1990) 899-903.

87. L. J.Van der Pauw. Philips Research Reports 13, 1-9 (1958).

88. Dror Sarid, Scanning force microscopy with applications to electric, magnetic and atomic forces, Oxford series in optical and imaging sciences, Oxford University press 1991.

89. Fariborz Maseeh and Stephen D. Senturia, Plastic deformation of highly doped silicon, Sensors and Actuators, A21-A23 (1990) 861-865

90. Xiaoyi Ding, Wen H. Ko and Joseph M. Mansour, Residual stress and mechanical properties of boron-doped p^+-silicon films, Sensors and Actuators, A21-A23 (1990) 866-871

91. Xiaoyi Ding and Wen H. Ko, Buckling behaviour of boron doped p^+ silicon diaphragms, IEEE 1991

92. Wen-Hwa Chu and Mehran Mehregany, A study of residual stress distribution through the thickness of p^+ silicon films., IEEE Trans. Ob Elec. Dev. Vol. 40, No. 7, July 1993

93. X. J. Ning, P. Pirouz, M. Mehregany, and W. Chu, Cross-sectional TEM studies of heavily boron doped silicon, Sensors and Actuators, 1991

94. Charles P. Ho, James D. Plummer, Stephen E. Hansen, Robert W. Dutton, VLSI Process modelling - Suprem III, IEEE Trans. on Elect. Dev., Vol. ED-30, No. 11, Nov. 1983.

95. Lijun Tong, Jen-Tai Hsu, Wen H. Ko, Xiaoyi Ding, The analysis of capacitive pressure sensors with large deflection. , IEEE 1991

96. Steve T. Cho, Khalil Najafi, and Kensall D. Wise, Internal stress compensation and scaling in ultrasensitive silicon pressure sensors, IEEE Trans. On Elect. Dev. Vol. 39, No. 4, April 1992.

97. K. Najafi and K. Suzuki, A novel technique and structure for the measurement of intrinsic stress and Young's modulus of thin films, Proc. IEEE Workshop on Microelectromechanical Systems, Feb. 1989, pp. 96-97.

98. O. Tabata, K. Kawahata, S. Sugiyama, and I. Igarashi, Mechanical property measurements of thin films using load-deflection of composite rectangular membrane, Proc. IEEE Workshop on Microelectromechanical Systems, Feb. 1989, pp 152-156.

99. Wilkinson, P. G. , J. Appl. Phys.,22 (1951), 419

100. Vand. V., Proc. phys. Soc., Lond., 55 (1943), 222.

101. D. H. Robey, Theory of the effect of a thin air film on the vibrations of a stretched circular membrane, Journal of the Acoustic Society Of America, Vol. 26, No 5. Sept. 1954.

102. G. Plantier and M. Bruneau, Heat conduction effects on the acoustic response of a membrane separated by a very thin air film from a backing electrode, J. Acoustique 3 (1990) 243-250

103. H. J. Carr, Electrostatic transducers for airborne ultrasonics, Ph.D. thesis, University of Nottingham, Oct. 1989.

104. Wu. Chong-ruo, An investigation of p-n junction etch stop, Sensors and actuators A, 35(1993) 181-187

105. L. J. Brillson et. al., Titanium-silicon and silicon dioxide reactions controlled by a low temperature thermal annealing., J. Vac. Sci. Technol. A, 4(3) (1986), pp. 993-997.

106. L. A. Brown, J. A. G. Knight, Review of current developments in nearfield acoustic holography, De Montfort University.

107. L. A. Brown, J. A. G. Knight, A. Croft, M. Hargreaves, Acoustic imaging using nearfield holography, De Montfort University Leicester.

108. H. Tanigawa, T. Ishihara, M. Hirata, and K. Suzuki, MOS Integrated silicon pressure sensor, IEEE Trans. Electron Dev., vol. ED-32, no. 7, pp. 1191-1195, July 1985.

109. C. P. Ho, J. D. Plummer, S. E. Hansen, R. W. Dutton, VLSI Process modeling-Suprem III, IEEE Trans. on electron devices, Vol. ED-30, No. 11, Nov 1983